On slope stabilization by piles

Centrifuge tests, Numerical simulation and Analytical method

Guoping Lei

Institut für Geotechnik (IGT)

Universität für Bodenkultur Wien

Dissertation zur Erlangung des akademischen Titels

Doctor naturalium technicarum (Dr.nat.techn.)

N° 39

August 2018

On slope stabilization by piles: Centrifuge tests, Numerical simulation and Analytical method

---

Guoping Lei

Betreuer:
Univ.Prof. Dr.Ing. Wei WU

Acknowledgements

I would like to acknowledge all the people who has provided help and advices during my doctoral study at the Institute of Geotechnical Engineering (IGT) at the University of Natural Resources and Life Sciences (BOKU) in Vienna, Austria.

I am very grateful to my supervisor, Univ.Prof.Dr.Ing. Wei Wu, for his guidance, encouragement and patience throughout this period.

I also wish to express my gratitude to Prof. Tang Huiming and Prof. Li Changdong from China University of Geosciences (Wuhan), with whom I started my academic adventure. They have also supported my research after I went abroad.

Special appreciation goes to the China Scholarship Council and Otto Pregl Foundation for Geotechnical Fundamental Research, whose financial support has made it possible to carry out this research.

I would like to thank Dr. Gregor Idinger and Dr. Miguel Cabrera for the training and guidance in the early stage of my centrifuge experience. Their pursuit of high-level experiments was always inspiring me whenever I encountered difficulties in the laboratory. Many thanks to Rick Veenhof, who has shared the most centrifuge journey with me and was always open for discussion, and Martin Grogger, who has been a good friend and has offered help whenever I needed it. During the centrifuge tests, many colleagues have provided help for which I am very thankful and they are: Dr. Markus Rauchecker, Sara Usai, Francisco Gavilán Expósito, Dr. Pouyan Abbasimaedeh, Dr. Cui Deshan, and Nader Moussaei.

I would also like to thank Marco Camusso and Man-Huy Tran from ITASCA Consultants. s.a.s. for helping me solve the problems in the numerical modelling.

I am very grateful to be one of IGT. It is a place with great academic atmosphere and full of bright individuals, who has made my time at BOKU joyful and unforgettable. It was my pleasure to work with them: Dr. Acharya Madhu Sudan, Dr. Lin Jia, Jenny Allen, Christine Lang, Dr. He Xuzhen, Dr. Wang Shun, Wang Jingxiu, Sandra Alvarez, Dr. Peng Chong, Dr. Switala Barbara, Dr. Xu Guofang, and Dr. Guo Xiaogang.

Finally, I would like to thank my parents Lei Yinquan and Wang Youyun, my brother Dr. Lei Guoqing and my lovely wife Liu Shan for their endless love and support.

Abstract

Rows of discrete piles are widely used to stabilize slopes. This stabilizing technique is influenced by many factors, e.g., pile spacing, pile bending stiffness and pile slenderness. While the effect of pile spacing has been extensively studied in the literature, little work has been done on the effect of pile bending stiffness and pile slenderness. However, they also have a significant influence on the pile behaviour and the effectiveness of prevention. In this study, the pile-soil interaction is studied through centrifuge tests and numerical simulation. Centrifuge tests were conducted on a 45° slope reinforced by a row of piles. Four different failure modes are identified and their relations with pile spacing, bending stiffness, slenderness and up-slope soil length have been revealed. For piles with a low bending stiffness, the top part of the pile becomes ineffective and the overall slope stability is reduced. With higher relative pile stiffness, which can be achieved by reducing the pile slenderness, more effective reinforcement and relative higher soil pressure are obtained. The application of deep-buried piles is proven to be a good alternative when flexible piles are used in deep-seated landslide. Numerical simulations are carried out on piles installed in two horizontal soil layers with relative movement. The lateral force on the pile increases rapidly in the early stage of soil movement due to the quick mobilisation of soil pressure in the deep soil. The critical pile spacing is found to be between 3 and 4 times the pile diameter, which agrees well with the observation in the centrifuge tests. The observations of flexible pile behaviour and its relationships to pile slenderness and pile bending stiffness are also confirmed by the numerical simulation. An increase in flexible pile behaviour is observed when a stronger sliding soil layer or weaker stable soil layer is used. According to the analysis of soil stresses around the piles, the plastic deformation theory for the ultimate soil pressure on the pile is modified to be applicable to a larger pile spacing range. Lastly, a generalized strain wedge model for flexible piles subjected to lateral soil movement is introduced. The modified plastic deformation theory is applied in the large pile spacing cases to consider the flow failure between the piles. The ability of the proposed method to capture the flexible pile behaviour is verified by comparing it with the numerical models and two reported case studies.

Kurzfassung

Aufgelöste Pfahlreihen werden häufig verwendet um Böschungen zu stabilisieren. Diese Stabilisierungstechnik wird von vielen Faktoren beeinflusst, z. B. Pfahlabstand, Pfahlbiegesteifigkeit und Pfahlschlankheit. Während die Wirkung des Pfahlabstandes in der Literatur eingehend untersucht wird, ist die Wirkung der Pfahlbiegesteifigkeit und der Pfahlschlankheit noch wenig geforscht worden. Sie haben aber auch einen wesentlichen Einfluss auf das Pfahlverhalten und die Wirksamkeit der Präventionsmaßnahme. In dieser Studie wird die Pfahl-Boden-Wechselwirkung durch Zentrifugenmodellversuche und numerische Simulation untersucht. Zentrifugenversuche wurden an einer 45° geneigten Böschung durchgeführt, die durch eine Reihe von Pfählen verstärkt wurde. Vier verschiedene Versagensarten wurden identifiziert und ihre Beziehungen zu Pfahlabstand, Biegesteifigkeit, Schlankheit und Hanglänge wurden aufgezeigt. Bei Pfählen mit einer geringeren Biegesteifigkeit wird der obere Teil des Pfahls unwirksam und die Gesamtstabilität der Böschung wird reduziert. Bei einer höheren relativen Pfahlsteifigkeit, die durch Verringerung der Pfahlschlankheit erreicht werden kann, werden eine effektivere Verstärkung der Böschung und ein höherer Bodendruck hervorgerufen. Die Anwendung von in der Tiefe vergrabenen Pfählen erweist sich als eine gute Alternative, wenn flexible Pfähle in tiefsitzendem Erdrutsch verwendet werden. Im weiteren wurden numerische Simulationen mit Pfählen durchgeführt, die in zwei horizontalen Bodenschichten mit relativer Bewegung installiert sind. Der Bodendruck auf den Pfahl steigt im frühen Stadium der Bodenbewegung aufgrund der schnellen Mobilisierung des Bodendrucks in der tiefen Bodenschicht schnell an. Der kritische Pfahlabstand liegt zwischen 3 und 4-fachem Pfahldurchmesser, was gut mit den Ergebnissen aus den Zentrifugenvesuchen übereinstimmt. Die Beobachtungen des flexiblen Pfahlverhaltens und seine Beziehungen zur Pfahlschlankheit und Pfahlbiegesteifigkeit werden ebenfalls durch die numerische Simulation bestätigt. Eine Zunahme des flexiblen Pfahlverhaltens wird beobachtet, wenn eine stärker gleitende Bodenschicht oder eine schwächere stabile Bodenschicht verwendet wird. Gemäß der Analyse der Bodenspannungen um die Pfähle herum wird die Theorie der plastischen Verformung für den endgültigen Bodendruck auf dem Pfahl modifiziert, um auf einen größeren Pfahlabstandsbereich anwendbar zu sein. Schließlich wird ein verallgemeinertes Verformungskeilmodell für flexible Pfähle eingeführt, die einer

seitlichen Bodenbewegung ausgesetzt sind. Die Theorie der modifizierten plastischen Verformung wird für große Pfahlabstände angewendet, um das Strömungsversagen zwischen den Pfählen zu berücksichtigen. Die Fähigkeit der vorgeschlagenen Methode, das flexible Pfahlverhaltens zu erfassen, wird durch Vergleiche mit numerischen Modellen und zwei dokumentierten Fallstudien verifiziert.

Table of contents

List of figures

List of tables

Nomenclature

The notation employed in this thesis is presented in the following lists. For all the symbols or abbreviations, their interpretations are always given in the text. Some symbols may have different meanings in different chapters. In this case, only the commonly used meaning is listed here. The actual interpretation of the symbol should follow the definition in the corresponding chapter.

Abbreviations

A*i*P	test with *i* Aluminium Piles
A*i*PB	A*i*P with deep Buried piles
A*i*PSS	A*i*P with Shallow soil layer and Short soil length
A*i*PSM	A*i*P with Shallow soil layer and Middle soil length
A*i*PSL	A*i*P with Shallow soil layer and Long soil length
BD	Boundary Displacement
CCD	Charge-Coupled Device
DFD	Diversity Factor of Displacement
DS	Dense Sand
FDM	Finite Difference Method
$FLAC^{3D}$	Fast Lagrangian Analysis of Continua in three dimensions
LS	Loose Sand
NP	test with No Piles.
OCR	Over Consolidated Ratio
P*i*P	test with *i* Plastic Piles
P*i*PB	P*i*P with deep Buried piles
P*i*PSS	P*i*P with Shallow soil layer and Short soil length
P*i*PSM	P*i*P with Shallow soil layer and Middle soil length
P*i*PSL	P*i*P with Shallow soil layer and Long soil length
rpm	Revolutions Per Minute

RK	Rock
SG	Strain Gauges
SL	Stress Level
SR	Soft Rock
SSE	Sum of Squares due to Error

Roman Symbols

A	[-]	the ratio of pile resistance to the weight of up-slope soil
B_{mob}	[-]	equivalent pressure mobilised on the pile
c	[kPa]	soil cohesion
d	[mm]	pile diameter
D	[m]	pile diameter
D_1	[m]	pile axis-to-axis distance
D_2	[m]	the clear interval between piles
D_r	[-]	soil relative density
E	[GPa]	pile elastic modulus
e	[-]	soil void ratio
EI	[kNm^2]	Bending stiffness of pile
E_s	[MPa]	modulus of elasticity of soil
F	[kN]	concentrate force
F_s	[-]	slope safety factor
f_p	[-]	group factor for p_u
g	[m/s^2]	earth's gravity constant
h	[mm]	thickness of the sliding soil
h_1	[mm]	buried depth of the pile top
h_p	[mm]	length of pile in the sliding soil
h_w	[m]	thickness of the stabilized wedge
I	[m^4]	sectional moment of inertia
I_{v0}	[kN/m]	integration of the initial vertical stress along depth
i	[-]	number of piles
k	[kN/m^3]	soil stiffness from the $p-y$ relation
K_0	[-]	at-rest lateral earth pressure coefficient
K_a	[-]	active lateral earth pressure coefficient
K_f	[-]	coefficient for the lateral soil stress at the pile line
K_p	[-]	passive lateral earth pressure coefficient

K_R	[-]	pile flexibility factor
l	[mm]	up-slope soil length
M	[kNm]	pile bending moment
N	[-]	scaling factor of centrifuge
N_p	[-]	lateral capacity factor of pile in clay soil
P	[kN]	total force on pile
p	[kPa]	soil pressure on pile
P_u	[kN]	ultimate force on pile
p_u	[kPa]	ultimate soil pressure on pile
R	[-]	rotation matrix between two Cartesian coordinate systems
S	[kN]	pile cross-sectional shear force
s	[mm]	pile axis-to-axis distance
sx, sy	[mm]	surface coordinate system
S_u	[kPa]	Undrained shear strain of clay
Sxx, Syy, Szz	[kPa]	normal stresses along x, y, z directions, respectively
T	[mm]	translation vector between two Cartesian coordinate systems
u, v	[pixels]	image coordinate system
w	[%]	water content
W	[kN]	weight of the soil block in the up-slope
x, y, z	[mm]	Cartesian coordinate system

Greek Symbols

α	[-]	factor for friction from the boundaries
β	[°]	wedge angle or the inclination angle of the slip surface
δ	[-]	wedge shear strain
Δx	[mm]	x displacement
Δy	[-]	y displacement
γ	[kN/m^3]	unit weight of soil
μ	[-]	Poisson's ratio
ω	[mm]	beam middle displacement in a simple supported beam bending test
ϕ	[°]	soil internal friction angle
ρ	[g/cm^3]	bulk density of soil
ρ_d	[g/cm^3]	soil dry density
σ_v	[kPa]	vertical soil stress
σ_{v0}	[kPa]	initial overburden pressure

τ	[kPa]	shear stress
ε	[-]	wedge horizontal strain
φ	[°]	soil internal friction angle
ζ	[m]	relative pile-soil displacement

Subscripts, Superscripts, Accents and Other

$(\cdot)'$	effective value of the variable
$(\cdot)^N$	normalised value of the variable
$(\cdot)^T$	transposition of the vector or matrix
$(\cdot)_{\max}$	maximum value of the parameter
$(\cdot)_{\min}$	minimum value of the parameter
$(\cdot)_r$	rest value of the parameter

Chapter 1

Introduction

Piles are widely used to stabilize natural and engineered slopes. Piles, which penetrate through the unstable soil mass and embed in the stable layer underneath, are usually installed discretely with a certain spacing. The essence of piling is to transfer the sliding force from the failing mass to the stable soil layer. Each pile behaves as a single vertical beam, which interacts with adjacent piles giving rise to the arching effect. The stabilizing piles are designed by maximizing the pile spacing for cost effectiveness while still enabling the formation of arches. Numerous studies have been conducted for the analysis of slopes stabilized by piles. However, the stabilizing mechanism is still unclear due to the complexity of the pile-soil interaction. The aim of this thesis is to reveal the mechanism of stabilizing piles by using various techniques and provide some help for engineering practice.

1.1 Current practice and limitation

In practice, a conventional slope stability analysis (e.g., using the methods of Bishop (1955), Janbu (1957), Morgenstern and Price (1965), Spencer (1967), or Sarma (1973)) is performed to evaluate the required lateral resisting force to increase the slope safety factor to the desired value. Subsequently, a pile configuration which can provide the required resisting force and serves appropriately in the work duration is selected. The major challenge of the design process lies at the evaluation of the driving force applied on the pile by the moving soil mass. The pile usually works as a flexible cantilever beam and will deform under the lateral load from the soil, which in return will affect the deformation of the failing soil mass and therefore the driving force itself. This complex coupled problem must be solved simultaneously.

Analytical methods, such as the pressure-based method and the displacement-based method, are usually adopted in the primary design. The pressure-based method uses the ultimate soil pressure, which is usually estimated empirically, as an external load to calculate

the internal forces in the pile. Therefore the pressure-based method is more suitable for rigid piles subjected to large soil movement. For free-headed slender piles, large pile deformation is usually expected. The use of the ultimate soil pressure leads to over conservative design. As an alternative to the pressure-based method, the displacement-based method calculates the soil pressure on the pile based on the lateral soil reaction due to the pile-soil interaction ($p-y$ relationship), which can be estimated empirically or through field tests. The displacement-based method has incorporated the soil-pile relative displacement into the pile response analyses. However, the application of the analytical methods relies highly on the accuracy of the prediction of the lateral soil reaction, which is usually difficult to obtain. As a result, a conservative design with larger pile diameter, closer pile spacing and deeper socketed length is usually adopted in practice.

Three-dimensional numerical analyses, such as the finite element method or the finite difference method, can produce the most realistic solutions of the pile-soil interaction when appropriate constitutive models are applied and the correct soil state is considered. Therefore numerical simulation is also used to validate the analytical method or empirical predictions. However, the mesh-relied numerical methods could produce unreliable result when extremely large deformation, tension failure or separation of contacts occur in the model. It is necessary that the numerical model is validated by field measurements or laboratory experiments.

Slope stabilized by a row of vertical discrete piles is a complex problem involving many factors, in which pile spacing is extensively studied in the literature. Less research is carried out for the effect of pile bending stiffness and slenderness, which, however, also has significant influence on the pile behaviour and the effectiveness of prevention. In this thesis, the mechanism of slope stabilized by piles is studied by centrifuge modelling and numerical simulation. Based on the numerical and experimental studies, an analytical method based on the strain wedge method is proposed for the flexible piles subjected to lateral soil movement.

1.2 Layout of the Thesis

The layout of the thesis is listed as follows:

Chapter 2 summarizes previous studies related to the stabilizing piles including three aspects: the failure modes, the pile response and the ultimate soil pressure on the pile.

Chapter 3 describes the centrifuge modelling methodologies in IGT laboratory. The monitoring system and data processing methods are presented in detail.

Chapter 4 presents the centrifuge tests of a 45° unstable slope reinforced by a row of piles. The observed failure modes, the effect of the pile spacing, pile stiffness, pile slenderness, relative up-slope soil length and the behaviour of the buried piles are discussed.

Chapter 5 presents a series of idealised numerical simulations. The modelling procedure is described in detail. The effect of pile spacing, pile slenderness, pile bending stiffness, soil properties and the ultimate lateral soil pressure are discussed.

Chapter 6 introduces a strain wedge model to calculate the response of flexible piles subjected to lateral soil movement.

Chapter 7 gives conclusions and suggestions for further study.

Chapter 2

Literature review

The topic of stabilising piles has been extensively investigated in the past half century. These studies can be divided into several subtopics: (1) the failure modes of the piled slope; (2) the pile response and the soil pressure distribution; and (3) the ultimate soil pressure and the arching effect.

2.1 The failure modes and the slope safety factor

Viggiani (1981) identified six different failure modes depending on the geometry of the problem, on the yield moment of the pile section and on the strength of the stable and sliding soil. Three failure modes are possible for a rigid pile, as shown in figure 2.1a, when the pile yield moment is higher than the bending moment acting upon it. In mode A the pile-soil interaction attains the yield value only below the slip surface; the whole pile translates together with the sliding soil. In mode B soil failure occurs both above and below the slip surface. The pile undergoes a rigid rotation. In mode C the pile is fixed in the firm soil and the sliding soil 'flows' around it. Figure 2.1b illustrates three failure modes depending on the number and location of plastic hinges occurring on the pile section. The failure mode B2 seems to be the most common in practice because the corresponding combination of parameters is most likely to occur. This classification has included almost all the possibilities of failure in the soil and the pile based on the two-layer model with a fixed slip surface. However, other failure modes refer to the change of slip surface are not considered.

Yoon (2008) performed a series of centrifuge tests of an unstable slope reinforced by a row of discrete piles. Four types of soil behaviour were observed by varying the up-slope soil length ratio (l/h) and the pile spacing (s/d) (figure 2.2): (1) 'Up-slope failure' with passive wedge and probably potential up-slope slip above the wedge at large l/h and small s/d; (2) 'Flow' through the piles with large deformation at large l/h and s/d; (3) 'Stable'

condition with small deformation at small l/h and s/d; (4) 'Potentially shallow surface failure' passing through the piles or 'ravelling' between the piles at small l/h and large s/d. His observations have revealed some failure possibilities refer to the formation of other slip surfaces considering, however, only rigid piles in relatively shallow slides.

The slope safety factor or stability factor is usually evaluated by implementing limit equilibrium analysis or numerical analysis.

Ito et al. (1981) proposed a design method for the stabilizing piles against landslide with a fixed sliding surface. The lateral force exerted on the piles was estimated through the plastic deformation theory developed by Ito and Matsui (1975). Factors (such as the interval between piles, the pile head condition, the pile length above sliding surface, the pile diameter and the stiffness of the steel pipe pile) on the stability of a piled slope were investigated.

Hassiotis et al. (1997) modified the friction circle method for slope stability to take into account the force exerted by the piles. The plastic deformation theory developed by Ito and Matsui (1975) was used to estimate the pressure acting on the piles. The methodology is able to consider the variations in the critical surface due to the presence of piles.

Hayward et al. (2000) performed four centrifuge tests to investigate the use of a row of spaced piles for the stabilization of a cutting slope. Failure was observed in the tests without piles and with piles having a spacing of 6 times the pile diameter.

Wei and Cheng (2009) analysed the stability of a slope with one row of piles using strength reduction method in $FLAC^{3D}$. The critical slip surface was divided into two parts at the pile row when the pile spacing was small. With the increase of pile spacing, the two parts tended to merge together into a clear critical slip surface, which was also observed to be shallower than the unreinforced slope.

Zhang and Wang (2010) developed a simplified method by extending the simplified Bishop slice method to analyse the stability of a piled strain-softening slope. It was concluded that the slope geometry and the pile layout (pile spacing, location and depth) had a significant effect on the safety factor and the critical slip surface.

Yamin and Liang (2010) developed a slices-based limit equilibrium method to calculate the global factor of safety of a slope with a row of drilled shafts. A load transfer factor was introduced to take into account the arching mechanisms of the drilled shafts. By searching for the highest load transfer factor, the optimum shaft location can be determined. The load transfer factor was further studied through finite element method (Liang and Yamin (2010)) and the influence of the pile configurations and the soil properties was investigated.

Ashour and Ardalan (2012a) used the modified Bishop method of slices to calculate the safety factor of a piled slope. The soil pressure and its distribution along the pile segment

above the slip surface was evaluated by a strain wedge method. Parameters such as pile position, pile spacing, soil type and pile diameter were also studied.

Wang and Zhang (2013) conducted centrifuge tests and finite element analysis on the reinforcement mechanism of piles in a slope. The influencing area was divided into three zones by two critical surfaces obtained by comparing the displacement distribution between the reinforced and the unreinforced slopes. Two concepts, compression effect and shear effect, were proposed to describe the pile reinforcement mechanism. Several factors such as pile spacing, pile location, pile end restriction and slope inclination were further investigated.

Zhou et al. (2014) applied limit equilibrium method and finite element method with shear strength reduction to estimate the lateral force acting on the stabilizing piles in a landslide in the Three Gorges Reservoir in China. The slope was modelled two dimensionally in both of the methods.

In the limit equilibrium analysis, the contribution of the piles to the slope stability is simplified into an additional resistance force which is usually estimated by using the ultimate soil pressure on the pile p_u. However, p_u may not be reached along the whole pile length in many cases, depending on the relative pile rigidity. Numerical analysis, on the other hand, can overcome this shortcoming and produces more reliable results.

2.2 The pile response and the soil pressure distribution

The pile response becomes the primary concern when the piles are used as a foundation for the superstructure. Lateral soil movement can also be caused under several circumstances: piled bridge abutment constructed on soft clay, pile foundation in liquefied or lateral spreading ground, piles nearby excavations, etc.

2.2.1 Stabilising piles and pile foundation

Poulos (1973) considered the lateral soil movement phenomenon as a lateral load similar to the negative friction developed on piles by the vertical movement of the surrounding soil. The analysis method for laterally loaded piles (Poulos (1971)) was extended to calculate the case of lateral soil movement. The soil was assumed to be an ideal elasto-plastic material and the pile was assumed to be a thin vertical strip. The horizontal soil movement, the soil elastic modulus, the yield soil pressure and its distribution with depth were required as input in the theory. It was concluded that the relative flexibility of the pile, the boundary conditions at the pile head and the pile tip, and the distribution of soil movement with the depth along

the pile were the most important factors affecting the magnitude of lateral movement and bending moment developed in the pile.

By adopting the analysis method above, Poulos (1995) had discussed the design of stabilizing piles. Four modes of pile response, namely 'flow mode', 'intermediate mode', 'short-pile mode' and 'long-pile mode', were proposed according to the pile length arrangement. In the 'flow mode' (figure 2.3a), the maximum moment occurs below the slip surface, in the stable soil layer. The pile movement is considerably less than the soil movement. In the 'short-pile mode' (figure 2.3c), the maximum moment occurs well above the slip surface in the unstable soil. The soil and pile movements are similar. In the 'intermediate mode' (figure 2.3b), large moments are developed both above and below the slip surface and the pile head movement can exceed the soil movement. The 'long pile mode' refers to the pile failure when the yield bending moment of the pile section is reached, which can be associated with any of the three modes above. The flow mode creates the least damaging effect of soil movement on the pile, if protection of the piles is being attempted, efforts should be made to promote this mode of behaviour. The intermediate mode develops the largest shear force and bending moment in the pile, if piles are being used to stabilize a slope, they should be designed so that the intermediate mode of behaviour occurs.

Subgrade reaction method is a common approach to calculate the pile response under lateral load. The extension of this method for piles under lateral soil movement has been discussed by many researchers (Byrne et al. (1984); Reese et al. (1993); Chow (1996); Cai and Ugai (2003); Guo (2006); Frank and Pouget (2008); White et al. (2008); Cai and Ugai (2011)). In the subgrade reaction method the soil is replaced by a series of independent nonlinear springs continuously distributed along the pile axis. The response of the spring is usually described by a series of specified p-y curves, therefore it is also called the p-y method. The pile flexure equation for pile subjected to a free-field lateral soil movement with no axis or external lateral loads is

$$EI\frac{d^4y}{dz^4} - k(y - y_s) = 0 \tag{2.1}$$

where EI is the bending stiffness of the pile; k is the soil stiffness from the p-y relationship; y is the lateral pile deflection and y_s is the free-field soil displacement. This is a typical uncoupled method to calculate the pile response. The p-y relationship is either obtained empirically or through field tests. The connection between the p-y relation and the basic soil properties is usually poor.

The pile response under lateral soil movement has been intensively investigated through laboratory model tests (Fukuoka (1977), Chen (1994), Poulos (1995), Chen and Poulos (1997), Pan et al. (2000), Pan et al. (2002b), Tsuchiya et al. (2001), White et al. (2008), etc.).

Chen (1994) conducted laboratory model tests on a single pile and a pile group subjected to lateral soil movements, which was achieved by imposing a triangular movement profile at the soil boundary. The effect of pile head condition, pile embedded length, pile diameter and pile stiffness on the maximum bending moment in a single pile was investigated. The group effect, depending on the pile arrangement, pile spacing, pile head fixity condition and pile position, was found to have a significant effect on the maximum bending moment of a pile in a group.

Model experiments were also conducted to investigate the response of vertically loaded piles subjected to lateral soil movement (Guo and Ghee (2006), Guo et al. (2006),Guo and Qin (2010)). The effect of pile diameter, soil movement profiles, sliding depth and the magnitude of axial load on the piles in sand or clay were examined.

White et al. (2008) conducted large-scale load tests on relatively slender piles subjected to a free-field lateral soil movement which was induced by a uniform translation of the model shear box. Negative soil reaction was observed at the head of slender piles. It was concluded that pressure-based methods might overestimate the passive resistance provided by slender piles while displacement-based methods (such as the *p*-*y* method by Reese et al. (2000)), on the other hand, could offer analysis considering relative soil movement and provide predictions that agreed well with experimental tests especially at low relative soil displacements.

Li et al. (2016) performed model tests to study the influence of embedment conditions on the response of stabilizing piles. The pile was embedded in a stable bedrock, including an upper hard layer and a lower weak layer. The optimum percentage of the hard layer in the embedment was investigated.

The pile response has also been studied using numerical methods.

Kourkoulis et al. (2011) proposed a hybrid method for the design of slope stabilizing piles, in which the lateral resisting force needed from the piles was calculated by a conventional slope-stability analysis and the pile response was analysed through finite element simulation including only a limited region of soil around the piles. It was concluded that the method was especially suitable to the cases of pre-existing potential sliding interfaces within slopes. Parametric study (Kourkoulis et al. (2010)) was performed on the pile spacing (s), the thickness of the unstable soil mass (h), the depth of pile embedment, the pile diameter (d) and the pile group configuration. It was concluded that $s = 4d$ was the most cost-effective

pile spacing and the critical embedment depth to achieve fixity conditions at the base of the pile ranged from $0.7h$ to $1.5h$.

Kanagasabai et al. (2011) carried out three-dimensional finite difference analyses to investigate the behaviour of a single stabilizing pile. The study confirmed some failure mechanisms for stabilizing piles categorized by Viggiani (1981) and studied the influence of the slip plane strength and the inclination of the ground surface on the pile behaviour.

Field tests also describe the pile behaviour. Namely,

Esu and D'Elia (1974) described a field test of a reinforced concrete pile installed into a clay-shale earthflow with a thickness varying between 5.0 and 7.5 m. The pile was instrumented with three pair pressure cells and an inclinometer. Measurements were carried out for 8 months until a plastic hinge was formed below the slip surface. The bending moment, shear force and pile deflection were able to be derived from the measured data. This test has been extensively analysed (Chow (1996); Chen and Poulos (1997); Cai and Ugai (2003)). In the study of Chen and Poulos (1997), some other field tests (Beer and Wallays (1972), Carrubba et al. (1989), Kalteziotis et al. (1993)) were also analysed.

Smethurst and Powrie (2007) reported the measurements of a number of discrete piles used to stabilize a railway embankment. Strain gauges were installed in three adjacent piles to measure the bending moments in the piles induced by the slope movements. Inclinometer tubes were installed both inside the strain-gauged piles and in the slope midway between each pair of the instrumented piles to measure any difference in the movement of the piles and the soil midway between the piles. The mechanism of slope and pile movement and the pile loading based on the relative pile and soil displacements were identified. The pile responses were well compared with a calculation based on a simple beam-on-spring model using non-linear $p-y$ curves.

Frank and Pouget (2008) reported a 16-year measurement of an instrumented steel pipe pile installed in an experimental embankment. Long-duration $p \sim \Delta y$ ($\Delta y = y - y_s$, is the relative displacement, y is the pile displacement and y_s is the free displacement of the soil) lateral reaction curves were constructed through pre-bored pressuremeter tests and self-boring pressuremeter tests. It was concluded that the presuremeter methods yielded overestimated pile responses compared to the measured pile displacement and bending moment.

Song et al. (2012) investigated the behaviour of stabilizing piles installed in two cut slopes located at a highway construction site. Four rows of stabilizing piles were installed and monitored. The measurements show that the deflection of the stabilizing piles and the deformation of the slope are significantly affected by the heavy rainfall.

Lirer (2012) reported a well instrumented field trial consisting of five piles installed in an active mudslide. The piles had been monitored for 3 years. The experiment was back

analysed by a three dimensional numerical analysis ($FLAC^{3D}$) to gain a deeper insight on piles' structural behaviour and stabilizing effectiveness. The predicted lateral loads on piles were in good agreement with those deduced from the measurements.

2.2.2 Piled bridge abutment constructed on soft clay

The problem of piles under lateral soil movement is encountered when the piled bridge abutment is constructed on soft clay. Springman (1989), Stewart (1992), Bransby and Springman (1997) and Ellis and Springman (2001) conducted centrifuge tests and also numerical analyses to study the pile response.

Springman (1989) proposed a parabolic-shaped pressure distribution estimated on the basis of an approximate relative soil-pile displacement.

Stewart et al. (1994) proposed a displacement based method to estimate the maximum pile bending moment and the pile cap deflection without attempting to reproduce the distribution of bending moment with depth. The method was based on a simple soil deformation mechanism suggested by Springman (1989) and the lateral pressure acting on the pile was related to the approximate relative soil-pile displacement. The method was also extended to consider the non-linear stress-strain behaviour of the soft stratum and the correction of embankment geometry.

Martin and Chen (2005) performed three dimensional finite difference analysis on the pile responses to lateral soil movement caused by embankment loading. It was observed that the relative stiffness between the pile and the soil was an important factor to determine the failure modes of the pile and the pressure on the pile.

2.2.3 Pile foundation in liquefied and lateral spreading ground

Pile foundation could suffer from lateral soil movement when the piles penetrate through liquefiable soil layers.

Wilson et al. (2000) performed bask-analysis of *p-y* behaviour from dynamic centrifuge tests of pile-supported structures. The observed *p-y* behaviour showed characteristics that were consistent with the undrained cyclic loading behaviour of saturated sand.

Abdoun et al. (2003) reported the results of eight centrifuge model tests of vertical single piles and pile groups subjected to earthquake-induced liquefaction and lateral spreading. It was observed that the maximum permanent bending moments occurred at the boundaries between the liquefied and nonliquefied layers. Strain softening of the soil around the piles was confirmed by the observation that the bending moments first increased and then decreased during the shaking. Dobry et al. (2003) used these centrifuge tests to calibrate two limit

equilibrium methods to evaluate the bending response and the safety factor against the bending failure of the pile. After the calibration, the two methods were used to calculate the pile response in the Niigata Family Court House building during 1964 Niigata earthquake with good agreement.

Finn (2005) evaluated the general engineering practice for estimating the response of pile foundations in liquefiable and non-liquefiable soils during earthquakes based on results from field tests, centrifuge tests and comprehensive non-linear dynamic analyses.

Bhattacharya et al. (2005) proposed an alternative mechanism for the pile failure in liquefiable deposit during earthquakes based on pile buckling. The slenderness ratio of the pile was introduced to classify the pile performance. The analysis was verified by case histories and centrifuge tests.

Brandenberg et al. (2007) used the beam on nonlinear Winkler foundation methods to analyse a series of centrifuge tests of pile foundations embedded in a soil profile with liquefaction-induced lateral spreading during earthquake shaking. It was concluded that certain guidelines and assumptions in engineering practice could produce significant conservative or unconservative prediction and therefore some guidelines were recommended in the study.

2.2.4 Piles nearby excavations

Lateral soil movement could happen to piles near an excavation. Leung et al. (2000) carried out centrifuge model tests to investigate the influence of deep excavation on an adjacent single pile foundation behind the retaining wall. It was observed that the induced bending moment and pile deflection decreased exponentially with the increasing distance between the pile and the wall. A plane failure was observed in the case of wall collapse. With the pile installed in the failure zone, large lateral soil movement and significant bending moment were observed. Using the same experimental apparatus of Leung et al. (2000), the influence of excavation on pile groups (Leung et al. (2003)), on a single pile in clay with stable or unstable retaining wall (Ong et al. (2006), Leung et al. (2006)) and on pile groups in clay (Ong et al. (2009)) were further studied. All the centrifuge tests were also well back analysed using a finite element program. Besides that, the effect of tunnelling on the piles nearby is also reported in the literature (Bezuijen and van der Schrier (2005), Hong et al. (2015), Chiang and Lee (2007), Ng and Lu (2013), Ng et al. (2015),.etc).

2.3 The ultimate soil pressure and the arching effect

The ultimate soil pressure on the pile p_u is of great importance in the design of stabilizing piles. The evaluation of p_u is usually based on the analysis of soil arching between the piles.

Wang and Yen (1974) developed a method to analysis the soil arching in slopes. Their theory assumes that the soil behaves like a rigid-plastic solid with a firm underlying base upon which the soil slides and into which piles are rigidly embedded in a single row. The theory predicts an optimal relative width at which the arching is most effective and also a critical relative width at which piles placed in a slope at any larger spacing will be of little use for stabilization. The theory also indicates a relationship between the slope length and the arching potential. The necessary slope length to develop the arching fully is approximately 5-6 times the spacing of the piles.

Ito and Matsui (1975) proposed a plastic deformation theory to estimate the lateral force acting on the piles. It was developed by assuming a plastic state satisfying Mohr-Coulomb's yield criterion in the surrounding ground just around piles. Referring to figure 2.4, a row of piles with diameter d and center-to-center distance D_1 was considered. The lateral force acting on a pile is calculated by:

$$
\begin{aligned}
p =& cD_1\left(\frac{D_1}{D_2}\right)^{(N_\varphi^{\frac{1}{2}}\tan\varphi+N_\varphi-1)} \\
&\times\left\{\frac{1}{N_\varphi\tan\varphi}\left\{\exp\left(\frac{D_1-D_2}{D_2}N_\varphi\tan\varphi\tan(\frac{\pi}{8}+\frac{\varphi}{4})\right)-2N_\varphi^{\frac{1}{2}}\tan\varphi-1\right\}\right. \\
&\left.+\frac{2\tan\varphi+2N_\varphi^{\frac{1}{2}}+N_\varphi^{-\frac{1}{2}}}{N_\varphi^{\frac{1}{2}}\tan\varphi+N_\varphi-1}\right\} \\
&-c\left\{D_1\frac{2\tan\varphi+2N_\varphi^{\frac{1}{2}}+N_\varphi^{-\frac{1}{2}}}{N_\varphi^{\frac{1}{2}}\tan\varphi+N_\varphi-1}-2D_2N_\varphi^{-\frac{1}{2}}\right\} \\
&+\frac{\gamma z}{N_\varphi}\left\{D_1(\frac{D_1}{D_2})^{(N_\varphi^{\frac{1}{2}}\tan\varphi+N_\varphi-1)}\exp\left(\frac{D_1-D_2}{D_2}N_\varphi\tan\varphi\tan(\frac{\pi}{8}+\frac{\varphi}{4})\right)-D_2\right\}
\end{aligned}
\tag{2.2}
$$

where D_2 is the clear interval between the piles; c and φ are the cohesion and the internal friction angle of the soil, respectively; γ is the unit weight of soil and z is the depth from the ground surface. N_φ is given by

$$
N_\varphi=\tan^2(\frac{\pi}{4}+\frac{\varphi}{2}) \tag{2.3}
$$

The theory was applied to some case studies in the typical tertiary landslide areas of Niigata in Japan, in which the theoretical results were in approximately the same order of magnitude as the measured results. Because the pile deformation was not considered, it was suggested that the lateral force under pile top restrained condition might be estimated by the theory of plastic deformation. It is argued that equation 2.3 is only valid over a limited range of spacings because the mechanism of flow through the piles is not the critical mode at large spacings or at very close spacings (Poulos (1995)). He et al. (2015) modified the theory with the active earth pressure at the down-slope side calculated by a theory extended from the method of Paik and Salgado (2003). The modification had taken the effect of slope angle into consideration, but showed limited accuracy in the predictions. There was another theory also proposed by Ito and Matsui (1975) in the same paper based on the theory of plastic flow. However, its application is limited due to the high requirement of accurate soil constants.

Chen (1994) performed a numerical study using the finite and infinite element method to investigate the ultimate soil pressure on piles subjected to lateral soil movements in both cohesive and cohesionless soils. Chen and Poulos (1997) proposed a dimensionless group factor f_p, which was the ratio of p_u of a pile in a group and p_u of an isolated pile. In the study, p_u was calculated by a finite-element analysis of a two dimensional pile-soil system in the horizontal plane.

Pan et al. (2000) conducted laboratory tests on single piles in soft clay subjected to lateral soil movements to determine the ultimate soil pressure. In the tests both the pile head and tip were fully fixed against movement and rotation. It was observed that the ultimate soil pressure on single passive piles was about $10S_u$ (S_u is the undrained shear strength of clay) and the soil movements required to fully mobilize the soil pressure was approximately 0.4 times the pile diameter. The same tests were also carried out for two piles with various arrangements (Pan et al. (2002b)). It was observed that the ultimate soil pressures with pile spacing of three and five times the pile width were lower than those in the case of single piles, which implied that group effects existed even with a pile spacing of five times the pile width. Different distribution of p_u along the pile were developed for the single and coupled piles. Pan et al. (2002a) performed three dimensional finite element analysis on the behaviour of a single pile subjected to lateral soil movements, and concluded that the maximum ultimate soil pressure is $10S_u$ and $10.8S_u$ for a stiff pile and a flexible pile, respectively.

Liang and Zeng (2002) studied the soil arching mechanism quantitatively through two dimensional finite element analysis. It was observed that the ratio of pile spacing to the pile diameter had the greatest influence on the development and intensity of soil arching. Parametric study showed that the smaller the pile spacing ratio and the higher the friction angle, the more soil stresses were transferred to the drilled shafts due to soil arching.

Chen and Martin (2002) adopted a plain strain finite difference model to simulate the arching effect between the piles. Drained and undrained soil conditions, soil dilatancy, interface roughness were considered. It was observed that the soil dilatancy had considerable effects on the formation of the arch, since higher soil dilatancy would cause an increase in the soil volume around the piles.

Durrani et al. (2008), Yoon and Ellis (2009), Ellis et al. (2010) had analysed the ultimate soil pressure on the pile through different methods and claimed that the pile spacing that produced the most effective soil arching was $s/d = K_p^2/(K_p - K_a)$, where K_a and K_p were active and passive lateral earth pressure coefficients, respectively.

Pan et al. (2012) carried out three dimensional finite difference analyses on the ultimate lateral pressure p_u of a friction soil with an effective internal friction angle of 20°. It was observed that the depth, to which the unconfined ground surface affected the ultimate lateral pressure, was about five times the pile diameter. Commonly used empirical distributions of the limiting pressure were found to be either larger or smaller than the numerical results for a frictionless pile-soil interface and they were found to be smaller than the numerical results for a full-strength pile-soil interface.

Li et al. (2013) performed numerical tests on a horizontal soil-pile slice subjected to horizontal thrust at the boundary of the numerical model and found that the thrust was shared by three parts: the soil arch behind the piles, the soil arch between the piles, and the sliding mass in front of the piles.

2.4 Summary

Slope stabilizing by piles is a complex geotechnical topic involving many parameters such as pile spacing, diameter, embedded length, pile and soil properties, slope geometry and ground profile. From the analysis and observations in the literature, some useful conclusions can be drawn:

1. In a piled slope, the following failure forms are most likely to occur: (1) soil failure below the slip surface, piles move along with the sliding soil; (2) plastic hinge in the pile below the slip surface; (3) soil 'flows' between the piles.

2. Soil arching between the piles becomes more effective with the decrease of pile spacing. The critical pile spacing, beyond which the arching effect tends to reduce, is about 3 to 4 times the pile diameter.

3. The ultimate soil pressure becomes larger with higher internal friction angle in sand and higher shear strength in clay.

4. The resistance of a stabilizing pile becomes larger for piles with higher pile stiffness, fixed pile head, larger pile diameter, more competent embedment, and rougher pile-soil interface.

Even though the understanding of the stabilizing piles has been improved by the reported studies, several aspects of the mechanism deserve further study, which are the focuses of this thesis:

1. Failure modes of a slope reinforced by relatively flexible piles or deep-buried piles.
2. Ultimate soil pressure on piles and its relation to pile spacing.
3. The soil pressure distribution along the pile depth, the possibility of a fully mobilised p_u and its relation to the pile configurations.

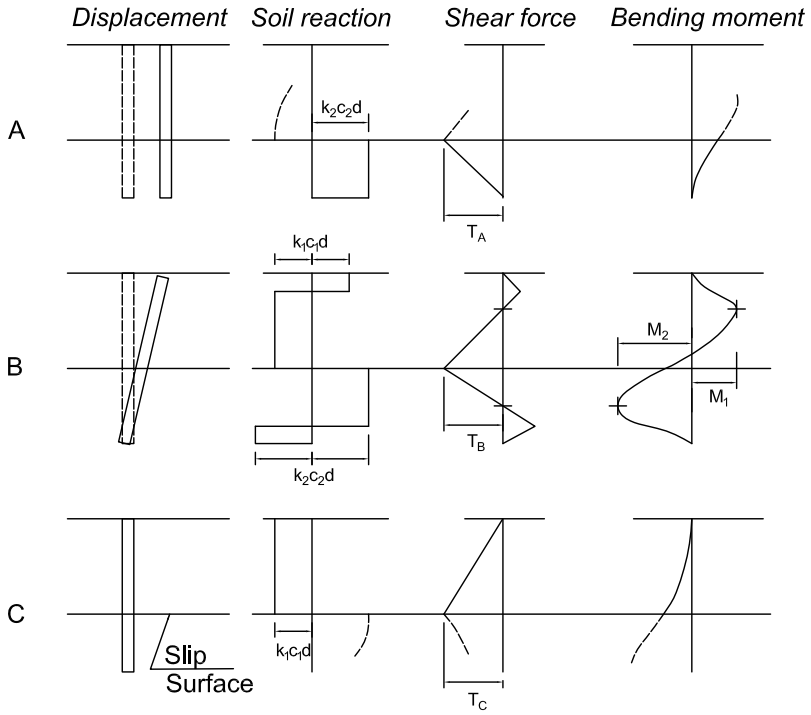

(a) rigid pile

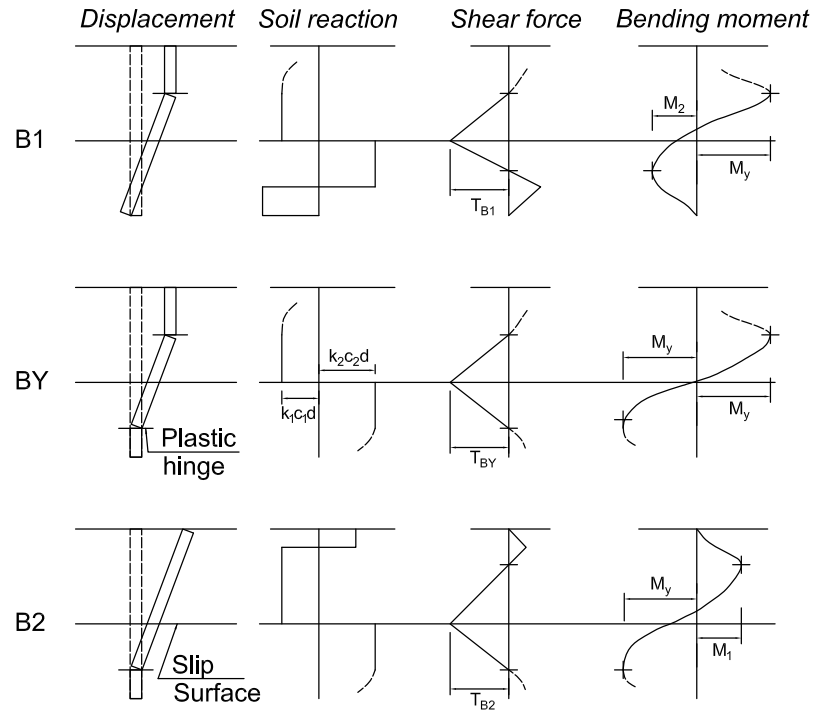

(b) with plastic hinges

Fig. 2.1 Failure modes of stabilizing pile (Viggiani (1981)). K_1 and K_2 are the pile bearing capacity factor for the sliding and stable layers, respectively; c_1 and c_2 are the soil shear strength for the sliding and stable layers, respectively; d is the pile diameter; T is the maximum shear force in the pile; M_1 and M_2 are the maximum pile bending moment above and below the slip surface, respectively; M_y and T_{BY} correspond to the ultimate values of the pile internal forces.

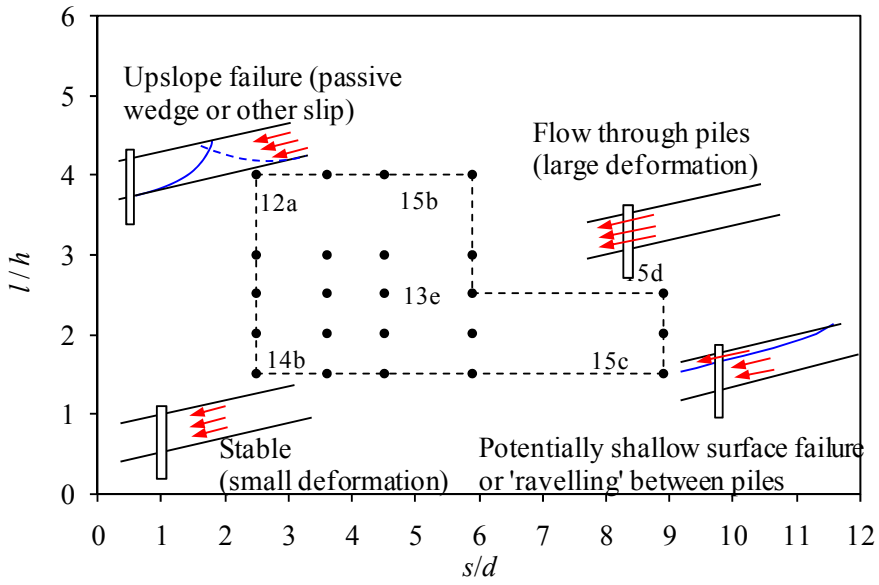

Fig. 2.2 Typical soil behaviour for piled slope (Yoon (2008)). s/d is the ratio of the pile axis-to-axis distance (s) to the pile diameter (d); l/h is the ratio of the horizontal distance from the pile location to the slope crest (l) to the pile length in the sliding soil (h).

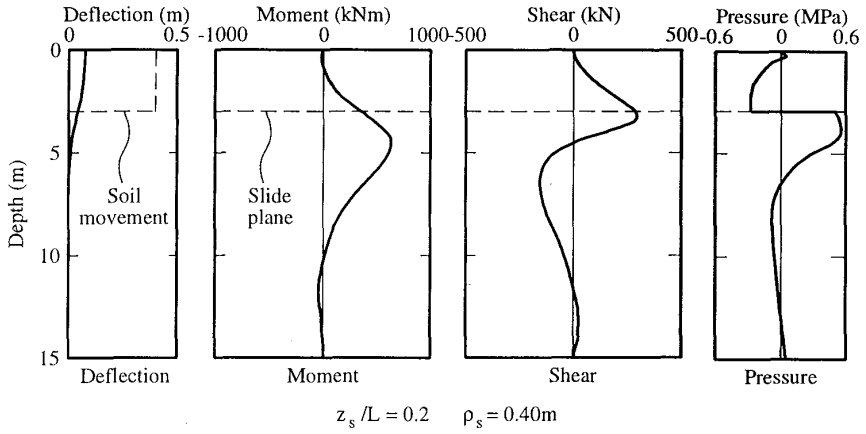

(a) Flow Mode

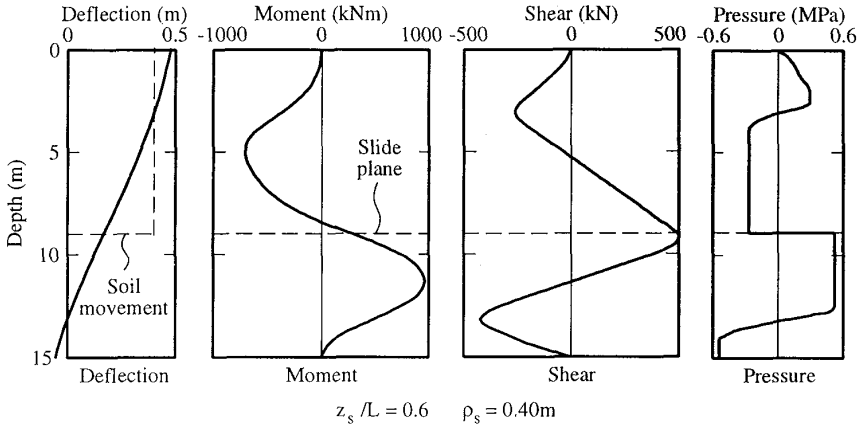

(b) Intermediate Mode

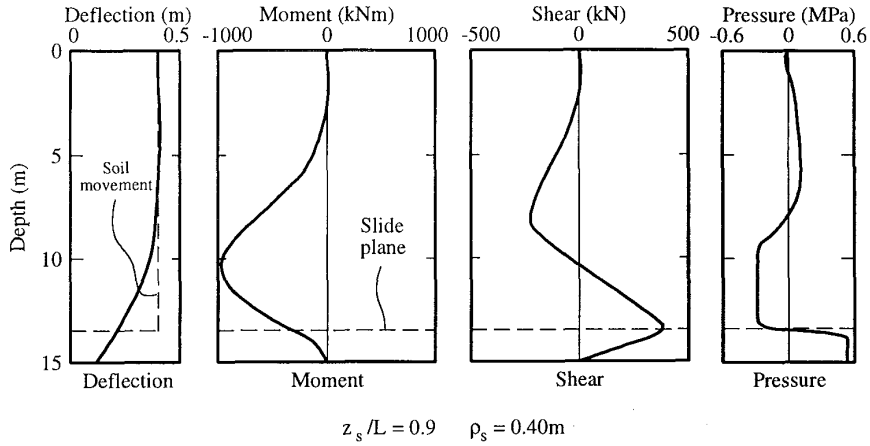

(c) Short Pile Mode

Fig. 2.3 Pile behavior characteristics for various modes (Poulos (1995)). z_s is the depth of the slip surface; L is the embedded length of the pile; ρ_s is the soil movement.

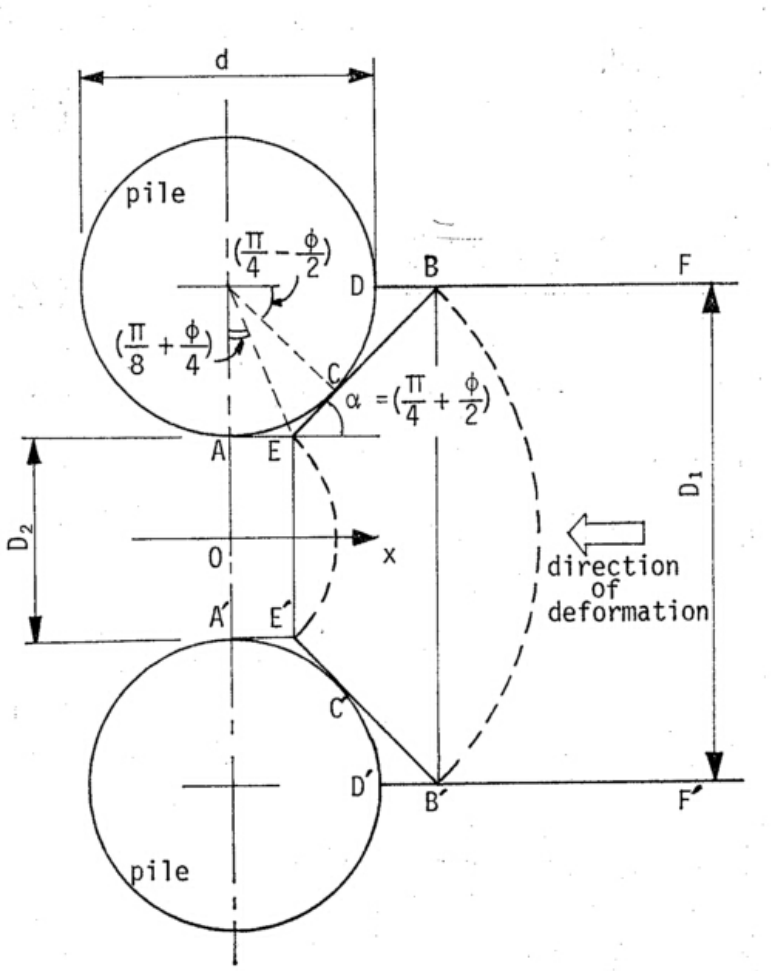

Fig. 2.4 State of plastic deformation in the ground just around piles (Ito and Matsui (1975))

Chapter 3

Methodology of Centrifuge Experiments

3.1 Introduction to geotechnical centrifuge

The mechanical behaviour of soil varies with confining pressure. To test a geotechnical object in laboratory scale, the confining pressure must reach the same level in the field. Centrifuge test, which produces an enhanced gravitation field for the soil, is one of the solutions to achieve this. For a soil column in prototype and its $1/N$ reduced mode at 1 g (Figure 3.1), the vertical stress increases linearly with depth at the same rate of ρ g. When the centrifugal force of N g is applied on the model, the stress profile of the model is amplified N times so that the soil stress at the bottom of both the model and its prototype are identical. This means that the a model scaled down in size by $1/N$ in centrifuge will behave like the prototype. Some basic scaling laws relevant to this study are listed in Table 3.1.

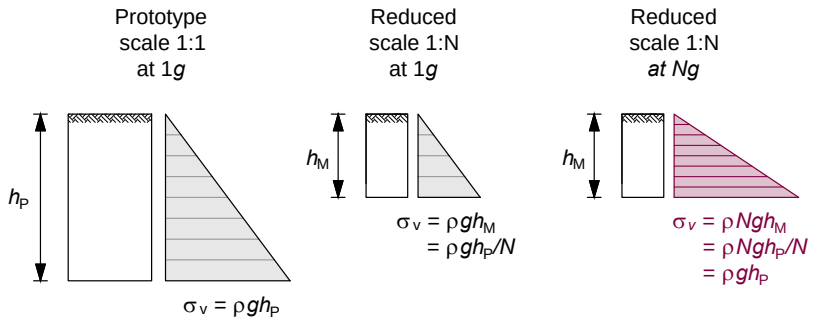

Fig. 3.1 Schematic presentation of the principle of centrifuge modelling (Idinger (2016)). ρ is soil bulk density. g is earth's gravity constant.

However, some shortcomings of centrifuge modelling require attention:

Table 3.1 Summary of selected scaling laws.

Properties	Full-scale prototype	Centrifuge model at $N \times g$
Gravity / Acceleration $[m/s^2]$	1	N
Stress / Pressure $[kg/ms^2]$	1	1
Distance $[m]$	1	$1/N$
Strain [-]	1	1
Shear strain rate $[1/s]$	1	N
Volume $[m^3]$	1	$1/N^3$
Density $[kg/m^3]$	1	1
Unit weight $[kN/m^3]$	1	N
Mass $[kg]$	1	$1/N^3$
Elastic modulus / Young's modulus $[Pa]$	1	1
Time (dynamic) $[s]$	1	$1/N$
Velocity (dynamic) $[m/s]$	1	1

1. *Increase of soil density during centrifuge spin-up*. Additional compaction of the model soil is inevitable. Corrections should be made if the tests are designed to perform with a specific soil density.

2. *Non-linearity of vertical stress*. The centrifugal acceleration is proportional to the distance between the soil element and the centrifuge axis, which results in the non-uniform distribution of acceleration in the model. For a slope model, the soil at the crest has less acceleration than the soil at the toe.

3. *Boundary conditions*. For plane strain problems, the boundaries parallel to the plane should be frictionless. Any resistance along these planes could lead to the reduction of stress and deformation in the soil and therefore the delay of soil failure.

4. *Coriolis effect*. Soil particles, which moves at a high velocity relative to the model container, will experience an additional Coriolis acceleration.

In this study, the thickness of the soil layer in the model is relatively small compared with the beam length of the centrifuge. During the centrifuge spin-up, the soil experiences mainly overall movement with a low velocity relative to the model container. Therefore, only the boundaries conditions are considered in the analysis of the test results.

Table 3.2 Specifications of the geotechnical centrifuge at BOKU

Diameter of Centrifuge [mm]	3,000
Radius to the base of swinging platform, r_{max} [mm]	1,308.5
Radia acceleration [g]	0 to 200
Angular velocity [rpm]	0 to 400
Deviation in angular velocity [%]	+/-0.1
Maximum load capacity [g-kg]	9,070
Maximum payload [kg]	90.7
Maximum model dimensions $w \times d \times h$ [mm]	$538 \times 556 \times 540$

3.2 Geotechinical centrifuge at BOKU

All the centrifuge tests in this thesis were carried out on the beam centrifuge in the Institute of Geotechnical Engineering at the University of Natural Resources and Life Sciences, Vienna (BOKU). Figure 3.2 is the schematic illustration of the beam centrifuge. Two swinging platforms are located at both sides of the symmetrical beam with a radius of 1.3 m. One platform contains the model box and the other the counterweight. The increase of angular velocity can be controlled via a software in the control room. Other specifications are listed in Table 3.2.

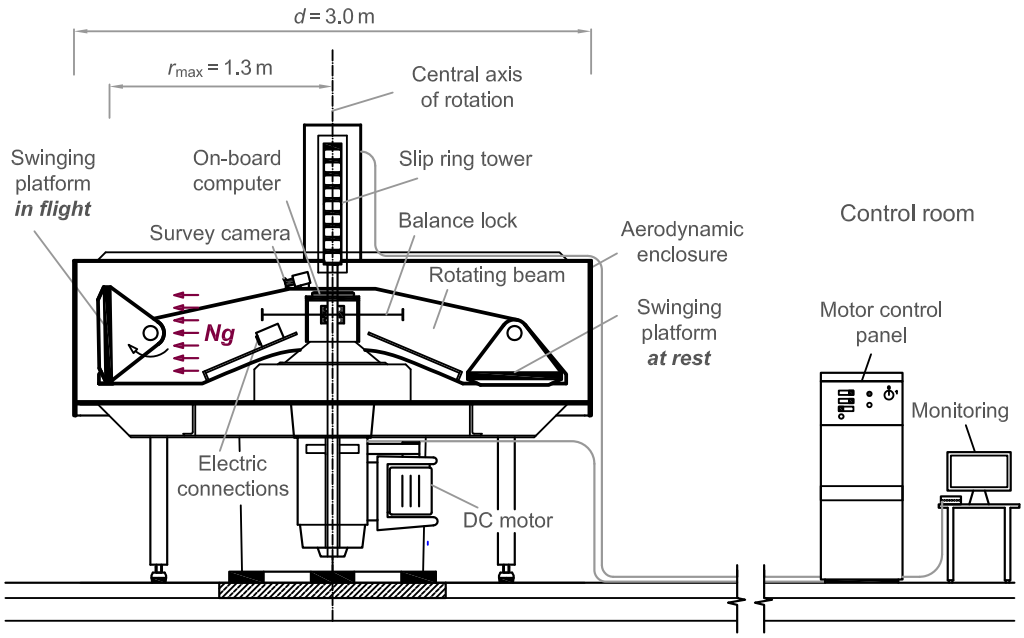

Fig. 3.2 Schematic presentation of the centrifuge testing facility at BOKU.

3.3 Model soil

The soil used in the centrifuge tests was taken from a landfill excavation site in Fischamend, Lower Austria. The soil characteristics and mechanical properties were investigated by Idinger (2016). Figure 3.3 shows the grain size distribution curve. According to ÖNORM-EN-ISO-14688-2 (2013), the soil sample is classified as a well-graded, uni-modal, medium-fine sand with a minor fraction of silt ($mfSa$, si'). The relative density (D_r) of the soil sample used for all the experiments is 0.55, which lies in the range of medium dense. The corresponding dry density (ρ_d) and void ratio (e) are 1.53 g/cm^3 and 0.74, respectively. The initial water content for all the tests is 11.5%.

Figure 3.4 shows the failure surface, Mohr circles for peak stresses, and stress paths of drained triaxial tests on unsaturated soil samples with the suction $s = 10$ kPa. The effective internal frictional angle (ϕ') is 31.8° and the cohesion (c) is 6.0 kPa, which is common in practice.

All the soil parameters related to this study are summarized in Table 3.3.

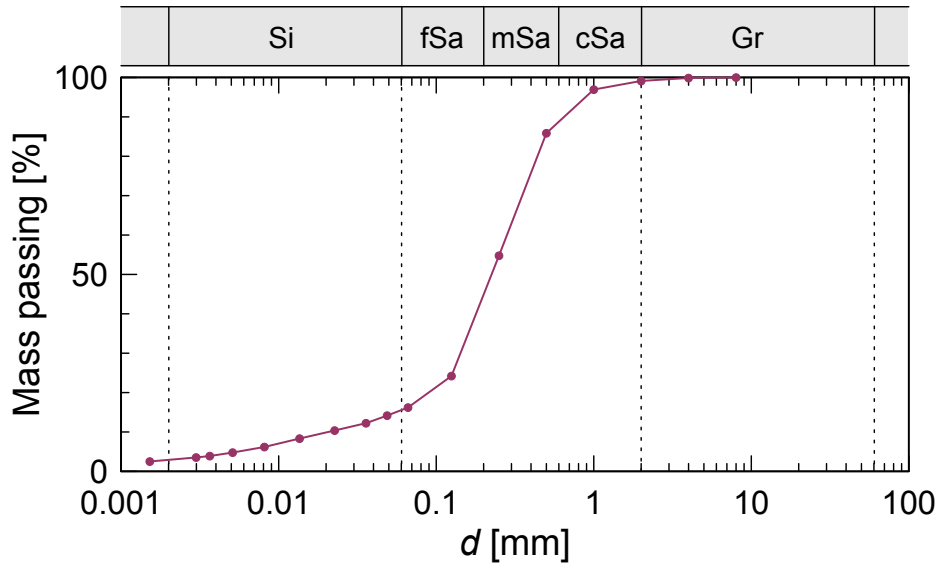

Fig. 3.3 Grain size distribution curve of the granular model soil: mfSa - medium fine sand (Idinger (2016)). Si - silt, fSa - fine sand, mSa - medium sand, cSa - course sand, Gr - gravel.

3.4 Model piles and bending tests

Two different kinds of model piles with bending stiffness of 18.21 $MNmm^2$ and 1.53 $MNmm^2$ are used to represent relative rigid and flexible piles, respectively. Both piles have a diameter of 10 mm. The stiff piles are made of an aluminium tube with a wall thickness of 1 mm

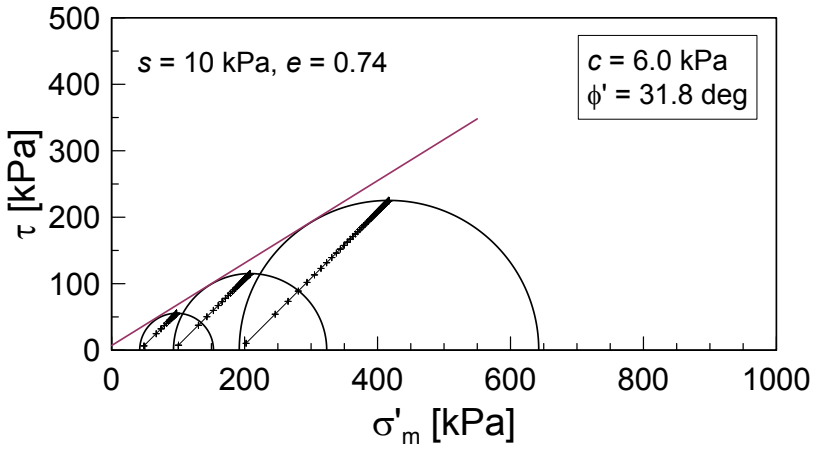

Fig. 3.4 Shear strength analysis (Idinger (2016)). σ'_m is mean effective stress; τ is shear stress; s is matric suction; e is void ratio; c is cohesion; ϕ' is effective friction angle.

Table 3.3 Soil properties. (ρ_d - dry density, e - void ratio, D_r - relative density, w - water content, E_s - elastic modulus, ϕ' - effective friction angle, c - cohesion.)

ρ_d (g/cm^3)	e (-)	D_r (-)	w (%)	E_s (MPa)	ϕ' (deg)	c (kPa)
1.53	0.74	0.55	11.5	16.0	31.8	6.0

while the flexible piles are made of an acrylic tube with a wall thickness of 3 mm. The corresponding prototype diameter at 50 g is 0.5 m. The prototype bending stiffness at the same target g-level is 113.8 MNm^2 for the aluminium pile and 9.54 MNm^2 for the acrylic pile, which respectively correspond to the stiffness level of bored concrete pile (171 MNm^2 with a diameter of 0.6 m as reported by Smethurst and Powrie (2007)) and steel tube pile (28.82 MNm^2 with a diameter of 0.4 m as reported by Lirer (2012)).

3.4.1 Bending test

As shown in Figure 3.5, a series of bending tests was performed on an uni-axial compression test device. The distance between the two supporting points is 30 cm. Three kinds of piles were tested: aluminium piles with outer diameters of 10 mm and 15 mm, acrylic piles with an outer diameter of 10 mm. For each pile type, two tests were conducted. A vertical load was applied in the middle of the simply supported beam. The magnitude of the load and the vertical displacement at the beam middle were recorded through the compression device. The results are plotted in Figure 3.6.

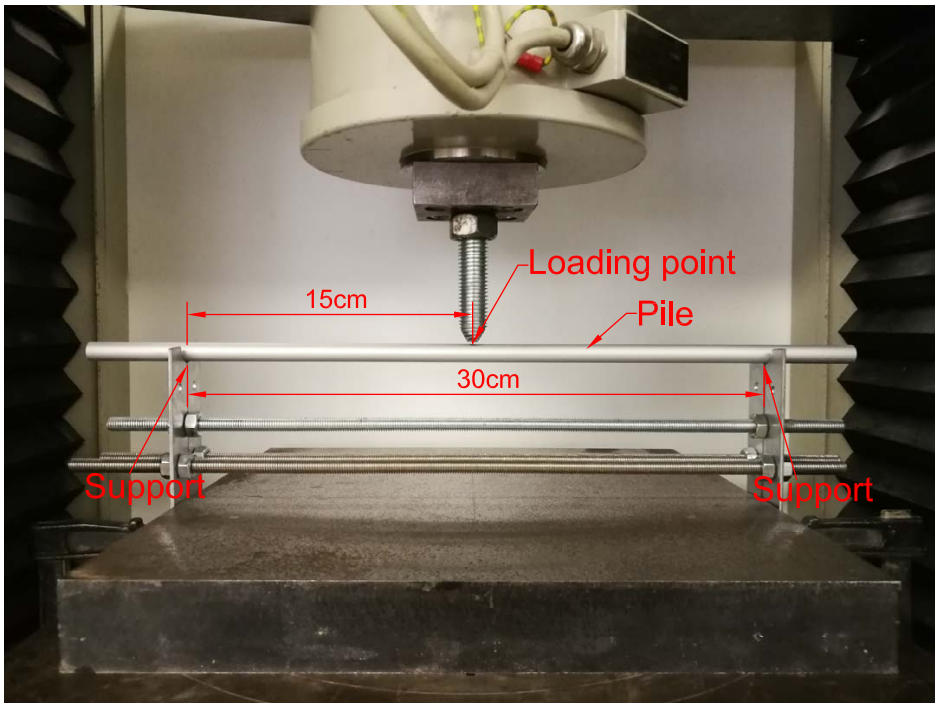

Fig. 3.5 Bending test of the aluminium pile.

In a simply supported horizontal beam, the vertical displacement of the middle point and the magnitude of the vertical concentrated load at the middle point have the following relationship:

$$\omega = \frac{Fl^3}{48EI} \tag{3.1}$$

where ω is the vertical displacement of the middle point; F is the vertical concentrated load; l is the beam length between the two supporting points; E is the elastic modulus of the beam and I is the sectional moment of inertia.

Linear fitting is applied to the linear part of each curve in Figure 3.6. The calculations of elastic modulus are given in Table 3.4. The difference between the elastic moduli for the aluminium piles of different diameter is less than 1%, which also confirms the reliability of the bending tests.

3.4.2 Bending test with strain gauges

Bending tests with two aluminium piles instrumented with strain gauges were conducted in order to test the strain gauges. As shown in Figure 3.7, the pile is instrumented with two strain gauges locating at the exterior of the same cross-section. A vertical load is applied at a distance of 130 mm to cause a known bending moment at the measuring cross-section. The

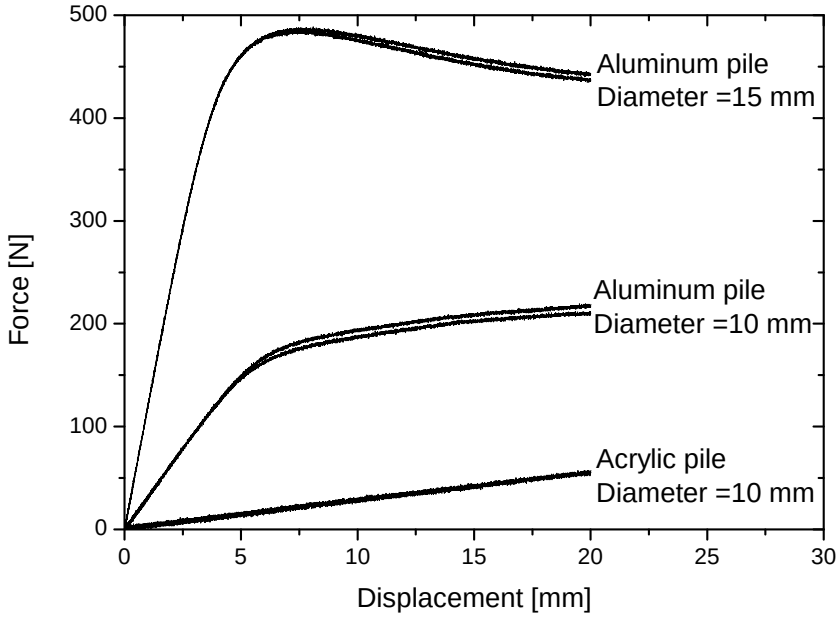

Fig. 3.6 Bending test results of different piles.

load vector should be perpendicular to the pile axis and parallel to the line that connects the strain gauges.

Figure 3.8 shows the signal of the two strains gauges obtained in a cantilever bending test including 5 steps of loading and 5 steps of unloading. The relationship between the strain and bending moment can be described by:

$$\varepsilon = \frac{Mc}{EI} \tag{3.2}$$

Table 3.4 Calculation results of the bending tests

Pile material	Aluminium	Aluminium	Acrylic
Outer diameter (mm)	10	15	10
Inner diameter (mm)	8	13	4
Beam length (mm)	300	300	300
Fitting slope $\frac{F}{\omega}$ (N/mm)	31.67	119.33	2.71
EI ($MNmm^2$)	17.81	67.12	1.53
I (mm^4)	289.81	1083.06	478.31
E (GPa)	61.46	61.98	3.19

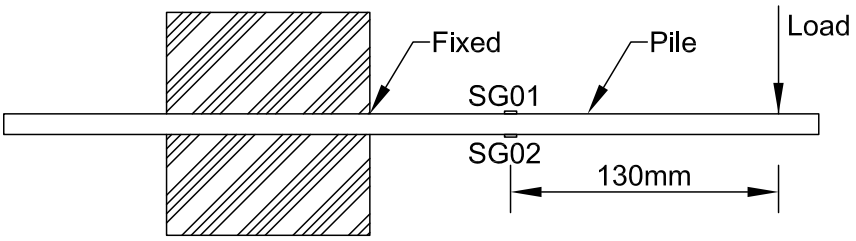

Fig. 3.7 Cantilever bending test with strain gauges (SG: strain gauge).

where ε is the strain; M is the bending moment and c is the distance from the pile axis to the point where the strain is being measured (here half of the diameter). Figure 3.9 shows the scatter plot of the bending tests. Linear fitting is applied to obtain the bending stiffness (EI). The average EI of all the tests is 18.21 $MNmm^2$, with a difference of 2.3% from the bending test on the uni-axial compression test device. For further calculation of bending moment in the centrifuge tests, the EI value of 18.21 $MNmm^2$ is adopted.

3.4.3 Strain gauge arrangements on the model piles

Figure 3.10 shows the distributions of strain gauges on the model piles. Different distributions are adopted according to the test purpose. Model pile $P1$ is designed for the tests with a thick sliding layer. In this case, we are interested in the distribution of the driving force. 5 pairs of strain gauges are arranged above the sliding surface with an interval of 20 mm. Model pile $P2$ is designed for the tests with deeply buried piles in a thick sliding layer. With the experience of pile $P1$, the most part of driving force is exerted by the lower part of the sliding layer. For this reason, 5 pairs of strain gauges are installed above the sliding surface with an interval of 15 mm. The 5^{th} pair is located at the sliding surface. Model pile $P3$ is designed for the cases with a thin sliding layer. It is concluded from the analysis of pile $P1$ and $P2$ that the bending moment at the top part of the pile is very small compared with the maximum bending moment. Therefore, in this case, one pair of strain gauges is moved to the embedded part of the pile to improve the measurement accuracy below the sliding surface.

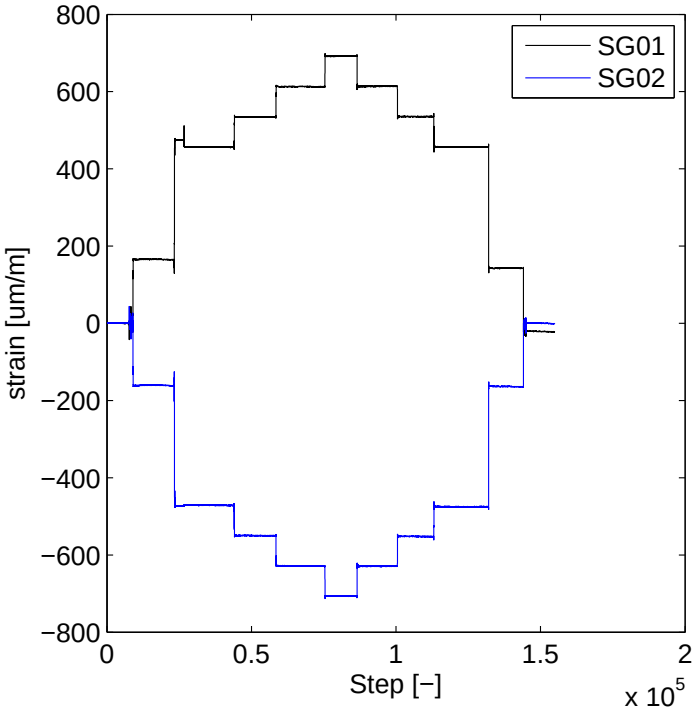

Fig. 3.8 Signal of strain gauges in the bending test. The step value is the number of the recorded signal.

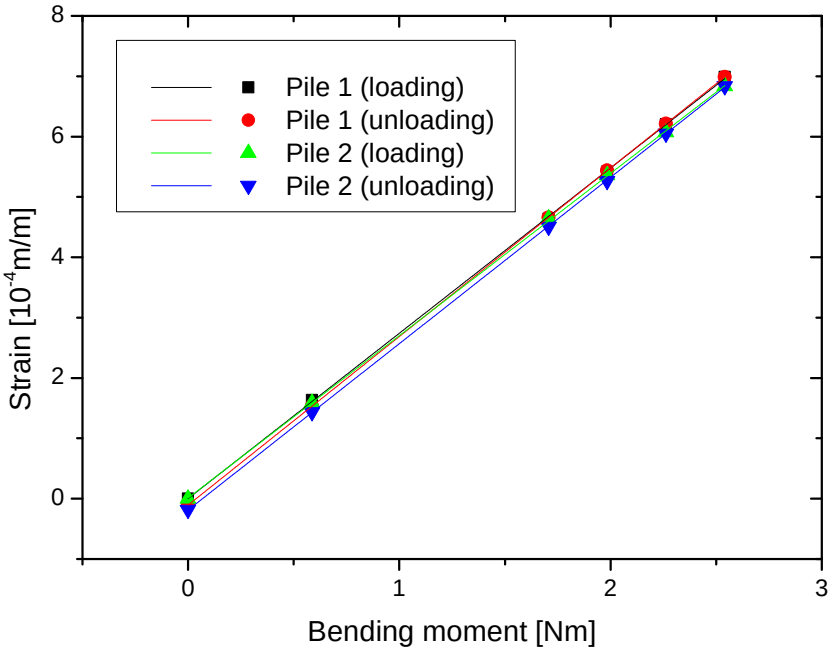

Fig. 3.9 Linear fitting of the strain ε and the bending moment M from the bending test.

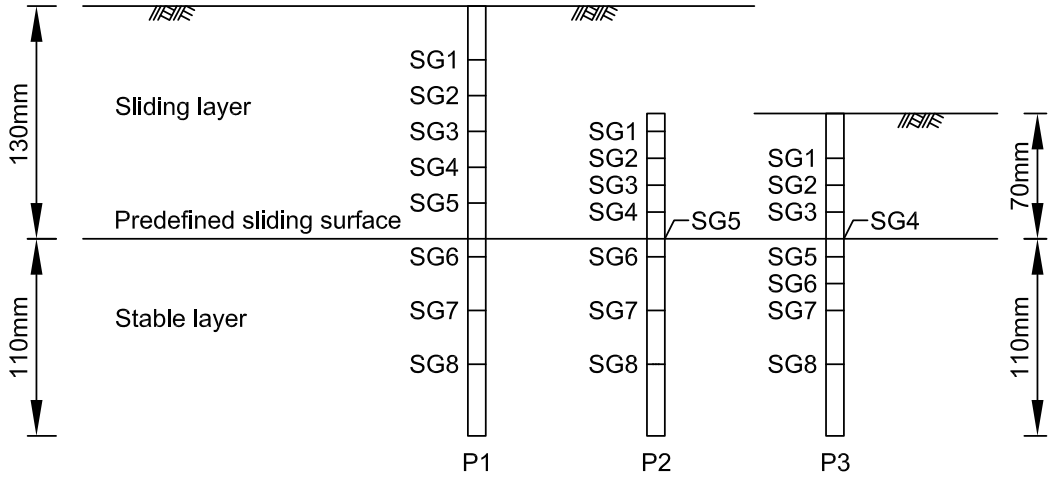

Fig. 3.10 The distribution of strain gauges (SG) for different pile settings in the centrifuge tests. P1: pile in thick sliding soil; P2: short pile in thick sliding soil; P3: pile in thin sliding soil.

3.5 Data processing for the instrumented pile

The sliding force is applied on the upper part of the pile while an anti-sliding force, which points to the opposite direction, is applied on the pile just below the sliding surface due to the stable layer. Another force is applied at the pile bottom by the stable layer to maintain the equilibrium of horizontal forces. A segmented curve fitting method is required to analyse the measurements of bending moment due to the discontinuity of lateral force distribution on the pile at the sliding surface.

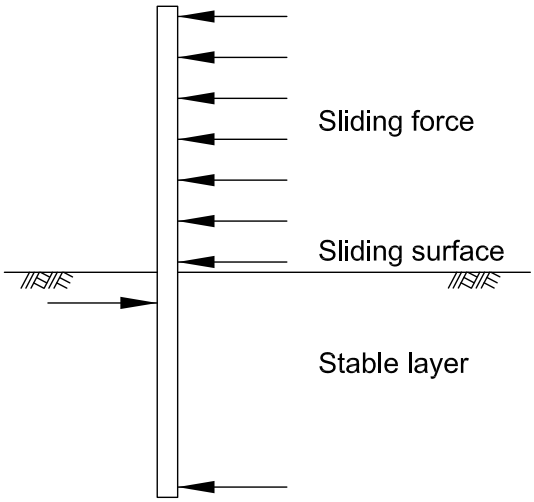

Fig. 3.11 Schematic diagram of forces on the pile

As illustrated in Figure 3.11, for the upper part of the pile, the sliding force is supposed to be continuously distributed in the sliding layer. For the lower part of the pile, due to the poor contact between the pile surface and wood structure, concentrated forces near the slip surface and the pile tip are the most possible interactions. Curve fitting using 4^{th} degree polynomials and linear fitting are employed for the upper and lower parts of the pile, respectively. The following boundary and continuity conditions are used:

1. zero bending moment and shear force at the pile head and tip;

2. zero soil pressure at the pile head;

3. continuity of bending moment and shear force at the slip surface.

The vertical coordinate z is set to point downwards with the origin at the pile top. Implement the boundary conditions at the pile head, the fitting functions for the upper part of the pile can be given as follows:

$$M(z) = a_4 z^4 + a_3 z^3 \quad \text{(Bending moment)} \tag{3.3a}$$

$$S(z) = \frac{\mathrm{d}M(z)}{\mathrm{d}z} = 4a_4 z^3 + 3a_3 z^2 \quad \text{(Shear force)} \tag{3.3b}$$

$$p(z) = \frac{\mathrm{d}M^2(z)}{\mathrm{d}z^2} = 12a_4 z^2 + 6a_3 z \quad \text{(Pressure)} \tag{3.3c}$$

In the lower part of the pile, the concentrated force near the sliding surface changes the direction of shear force in the pile, where the bending moment reaches the maximum (M_{max}). The depth of this concentrated force (h_c) is set as a variable that needs to be determined in the fitting process. The second concentrated force is set at the pile tip. The fitting of bending moment measurements includes the following steps:

1. The maximum moment (M_{max}) usually locates between the strain gauge which gives the maximum measured data (SG_{max} at 1 cm below the sliding surface) and the strain gauge below it. Therefore, the range of h_c is fixed.

2. Implement linear fitting for the measurements from the strain gauges below SG_{max} using the pile tip boundary condition. The fitting result is applied from h_c to the pile tip.

3. Use dichotomy method to search for h_c. For every try of h_c, the M_{max} is calculated from the linear fitting and the shear force at the sliding surface S_s is calculated by

$$S_s = \frac{M_{max} - M_s}{h_c - h_s} \tag{3.4}$$

   where M_s and h_s are the bending moment and depth at the slip surface, respectively.

4. Implement polynomial fitting for the upper part of the pile using the measurements above and at the sliding surface and the shear force at the sliding surface S_s. Least square technique is adopted to obtain the coefficients a_4 and a_3 in equation 3.3a. As there is no external force between h_s and h_c, the bending moment should increase linearly from M_s at h_s to M_{max} at h_c.

5. Calculate the sum of squares due to error (SSE), which measures the total deviation of the fitted values ($\hat{M}_i$) from the measured values (M_i):

$$SSE = \sum_{i=1}^{n} (\hat{M}_i - M_i)^2 \tag{3.5}$$

where n is the number of measured values which locates above the maximum point. SSE is calculated for every given h_c. Step 3 to 5 is repeated until the optimal value of h_c which gives the minimum value of SSE is found. The dichotomy process ends when the search zone is reduced to a narrow range (10^{-4} m).

3.6 Model container and slope construction

Figure 3.12 shows the sketch of the model container. It consists of three aluminium walls with a thickness of 15mm, a transparent front wall made of acrylic with a thickness of 30mm, an aluminium frame to protect the acrylic when mounting it with the side walls, and an aluminium base plate with a thickness of 12mm. Camera installation is possible at the top of the container for the top-view and on the other side of the base plate opposite to the container for the cross-sectional view (side-view). On the inner surface of the front and rear wall, a thin film of transparent silicon oil is applied prior to each test to reduce the wall friction.

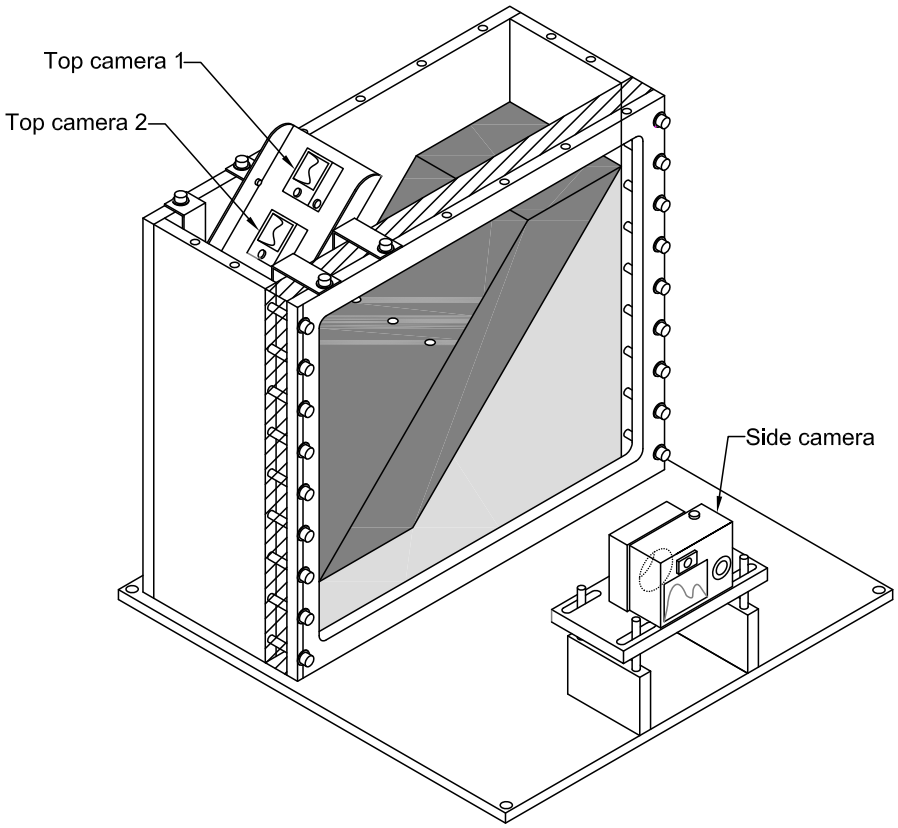

Fig. 3.12 Sketch of the model container.

Figure 3.13 shows the geometry of a slope model. The slope, which is reinforced by a row of discrete piles, has an inclination angle of 45°. The slope consists of two layers: a sliding soil layer and a stationary layer underneath modelled by wood. A slip surface with low friction is installed between the unstable and stable layers. The slip surface consists of three layers which from top to bottom are a 2 mm thick rubber sheet with a smooth surface, a sprayed silicon oil layer and a 1 mm thick aluminium sheet. The pile head and tip line

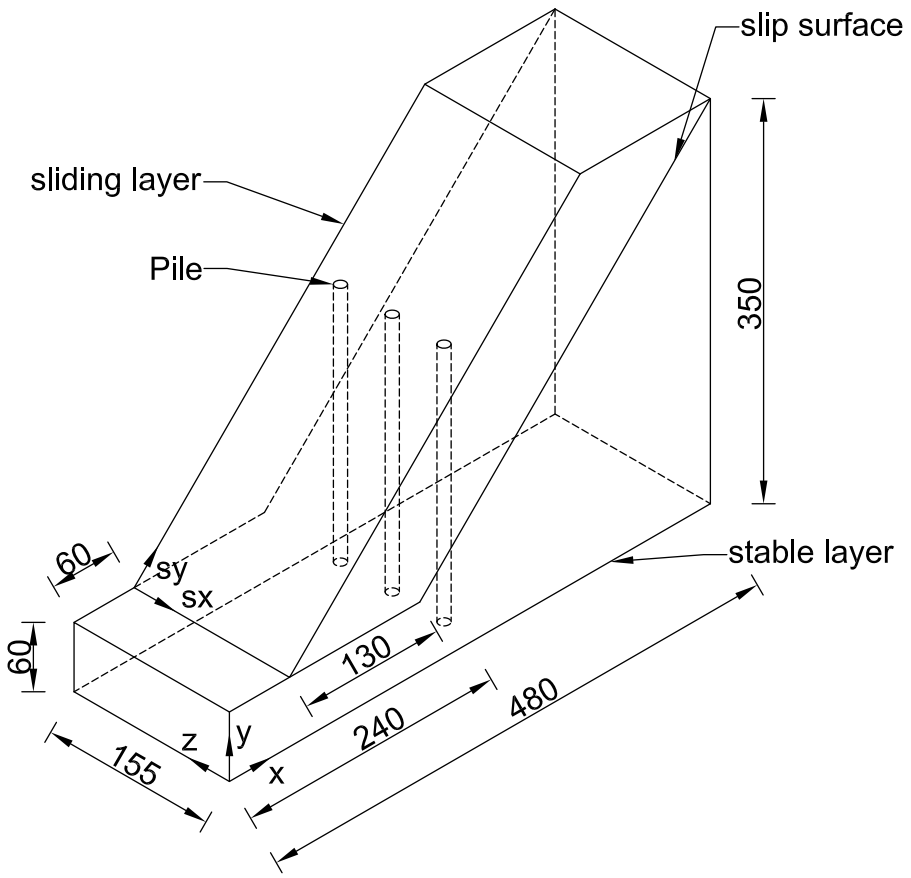

Fig. 3.13 Model geometry of the test with a thick sliding layer (Unit: mm). *x*, *y*, *z*: global Cartesian coordinate system; *sx*, *sy*: local surface coordinate system.

up with the ground surface and the bottom of the wooden structure, respectively. The total length of the model pile is 24 cm with an embedded length of 11 cm. For the cases with different pile length, the embedded length remains unchanged.

Figure 3.14 shows the construction procedure:

- Firstly, the stable layer is modelled by wood slices with the thickness ranging from 3 mm to 12 mm to allow for adjustment of pile spacing. The piles are installed before the soil compaction in order to ensure a tight soil-pile contact.

- Secondly, The wood structure is covered by an aluminium sheet with silicon oil applied on the upper surface. The aluminium sheet is fixed on the wood structure. Between the soil and the aluminium sheet, a smooth rubber sheet is placed. Both the rubber and aluminium sheets are perforated at the pile locations. The perforated areas are extended in both down-slope and up-slope directions to enable the relative movement

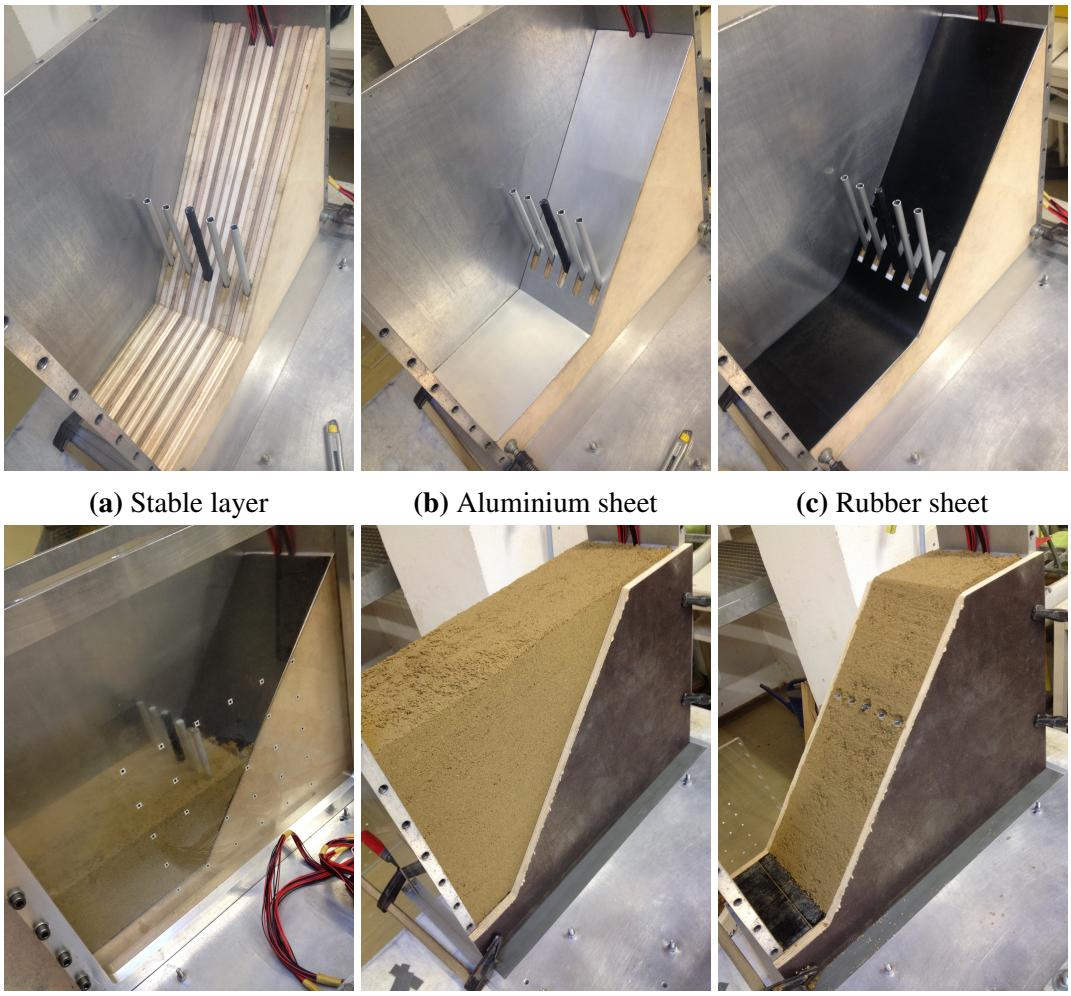

(a) Stable layer **(b)** Aluminium sheet **(c)** Rubber sheet

(d) Compaction every 25mm **(e)** Shaping **(f)** After shaping

Fig. 3.14 Model preparation procedure. (Note: only the middle pile is instrumented with strain gauges.)

between the pile and the two sheets. The maximum displacement of the soil layer on the aluminium sheet is 35 mm.

- Finally, the premixed soil sample is compacted to the required density via moist tamping. Divided horizontal sub-layers with the thickness of 25 mm is adequate to produce a uniform density distribution in the soil. After the compaction, the soil is trimmed to the model dimensions using two wooden templates. A rubber piece with a width of 40 mm in the slope toe area is removed before the test to enable soil layer movement.

3.7 Boundary effect

Two boundaries are critical in the centrifuge tests in this study: the interface between the sliding soil and the side walls (side boundaries), and the predefined slip surface. In theory, the side boundaries are symmetry planes of the model, on which the shear force should be zero. Therefore, measures should be taken to minimize the effect of side boundaries on the soil movement. For the purpose of the centrifuge test, low friction is also required in the predefined slip surface so that more sliding force from the soil can be transferred to the piles. The measure that is taken to reduce the interface friction is to apply silicon oil on the side walls and between the rubber and aluminium sheets. To determine the friction parameters of the interfaces, the direct shear box is modified. Figure 3.15 shows the modified shear box for the slip surface. The same aluminium surface is used to test the side boundary. For the side boundary, in which the sliding soil contacts the side window, the same frictional parameters with the other side wall are adopted.

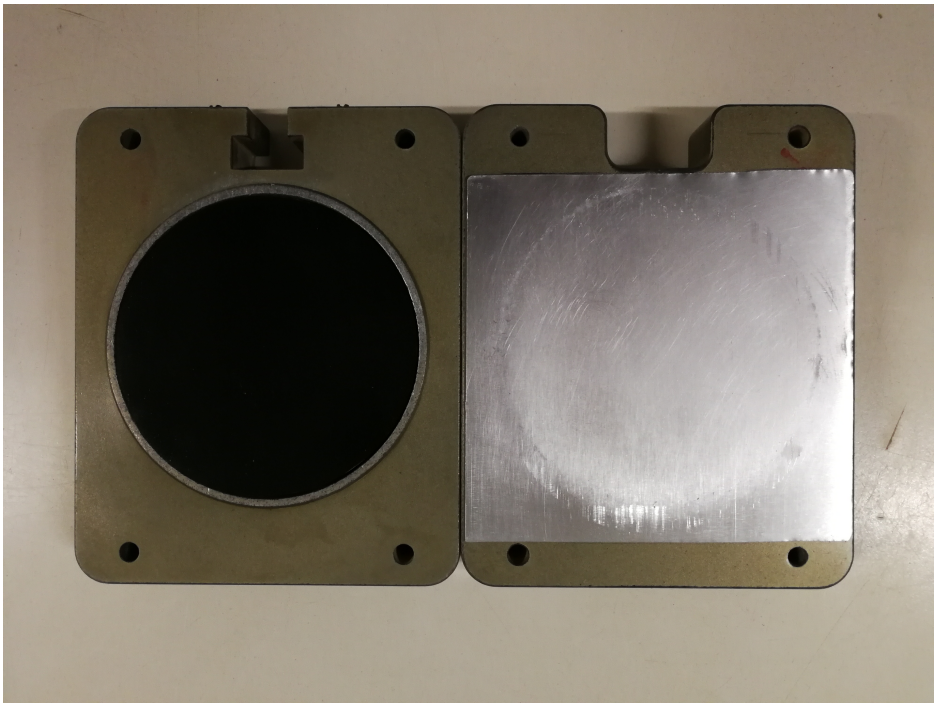

Fig. 3.15 Modified direct shear box for testing the interface between the rubber disc (left) and the aluminium sheet (right).

The results of the direct shear tests are presented in Figure 3.16. Since large soil movement is expected, the interface parameters obtained using the rest values (φ_r and c_r) are adopted for further analysis. For the slip surface, the friction angle is 6.06° and the cohesion is 4.78 kPa. For the side boundaries, the friction angle is 27.8° and the cohesion is 0 kPa. Compared

with the soil internal friction angle, φ_r of the side boundary is relatively high. However, our centrifuge tests show that the soil movement is not affected by the side walls.

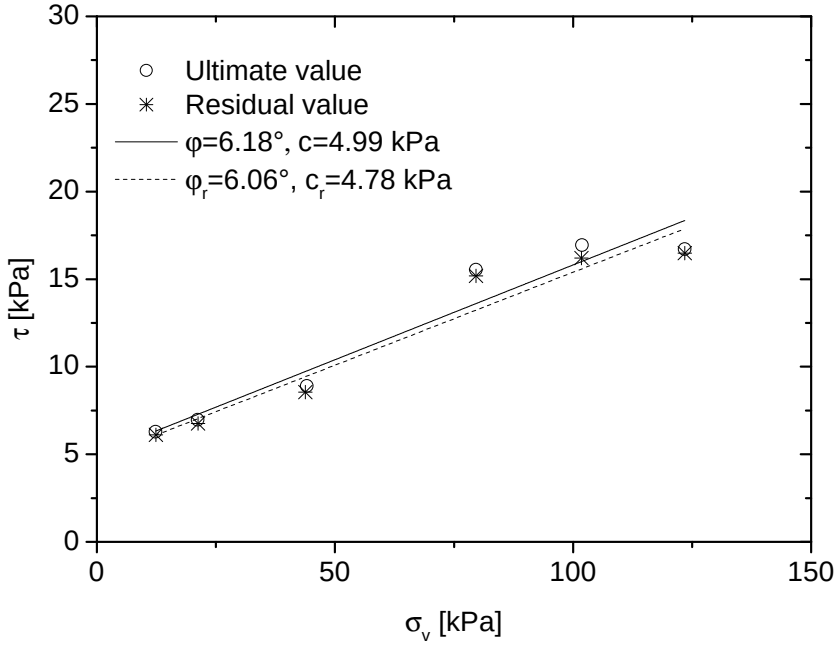

(a) Interface of aluminium and rubber with silicon oil in between

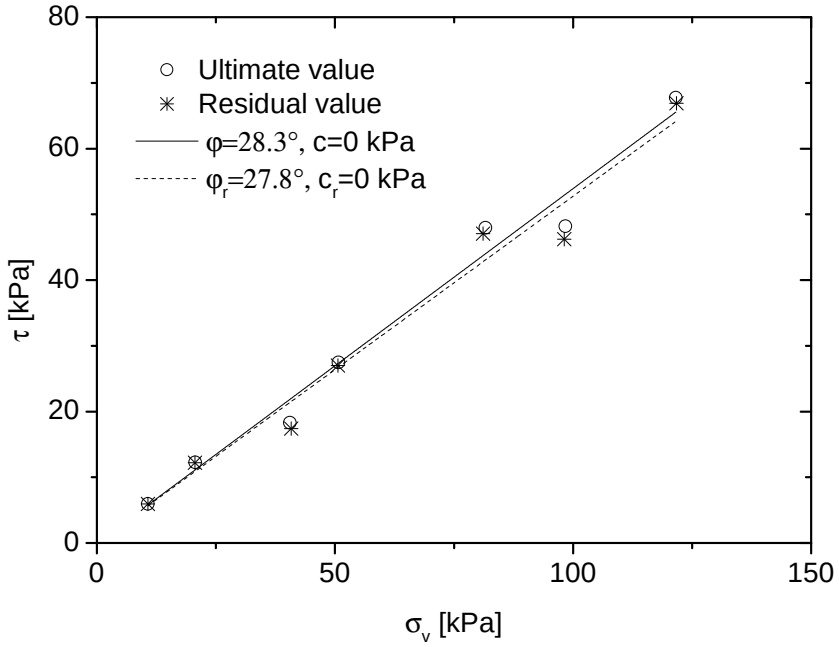

(b) Interface of aluminium and sand with silicon oil in between

Fig. 3.16 Results of the direct shear tests. σ_v is vertical stress; τ is shear stress; φ and φ_r are peak and residual friction angle, respectively; c and c_r are peak and residual cohesion, respectively.

3.8 Image-based deformation analysis

Image-based deformation analysis is applied both on the side-view and the top-view.

3.8.1 GeoPIV for the side-view

Particle Image Velocimetry (PIV) is a velocity measuring technique that was originally developed in the field of experimental fluid mechanics. Based on PIV and close-range photogrammetry, White et al. (2003) developed a deformation measurement system (GeoPIV) for geotechnical tests. The soil sample used in this study is natural sand, which has its own texture in the form of different-coloured grains and the light and shadow formed between adjacent grains when illuminated. Figure 3.17 shows the analysis procedure in GeoPIV. The first image, which is normally the image before any deformation, is divided into a grid of test patches. Each test patch, $I_{test}(U)$, consists of a sample of the image matrix, $I(U)$, of size $L \times L$ pixels. For each test patch, a search patch $I_{search}(U+s)$ is extracted from the second image, which is usually taken after soil deformation. This search path extends beyond the test patch by a distance s_{max} in both u and v directions. The new coordinates of the test patch in the second image are evaluated by applying cross-correlation of $I_{test}(U)$ and $I_{search}(U+s)$. The image-space deformation of the soil sample is formed when all the test patches have been searched in the second image. To convert the image-space deformation into object-space deformation, in GeoPIV, a 14-parameter transformation following Heikkila and Silven (1997) was extended to include distortion due to the observation through a viewing window. In the transformation, the non-coplanarity of the CCD (Charge-coupled device) and object planes, the radial and tangential lens distortion, the refraction through a viewing window, and the CCD pixel non-squareness are considered. The software package is widely used in geotechnical laboratory tests.

The precision of PIV is strongly influenced by the patch size and the image content (soil texture). The effect of the patch size is studied using an image of the sand sample. Four patch sizes (8, 16, 32, 64 pixels) are chosen and the identical area of image content is used. Figure 3.18 shows the image texture of the model sand and the area that is selected. To consider the influence of the magnitude of soil movement or the independence of image texture, the image is compared with itself after several artificial translations of the image content. The results are shown in Figure 3.19. It is seen that high precision is obtained when the patch size is larger than 30 pixels and no influence from the soil movement is observed. In the PIV analysis hereafter, patch size 30×30 is adopted.

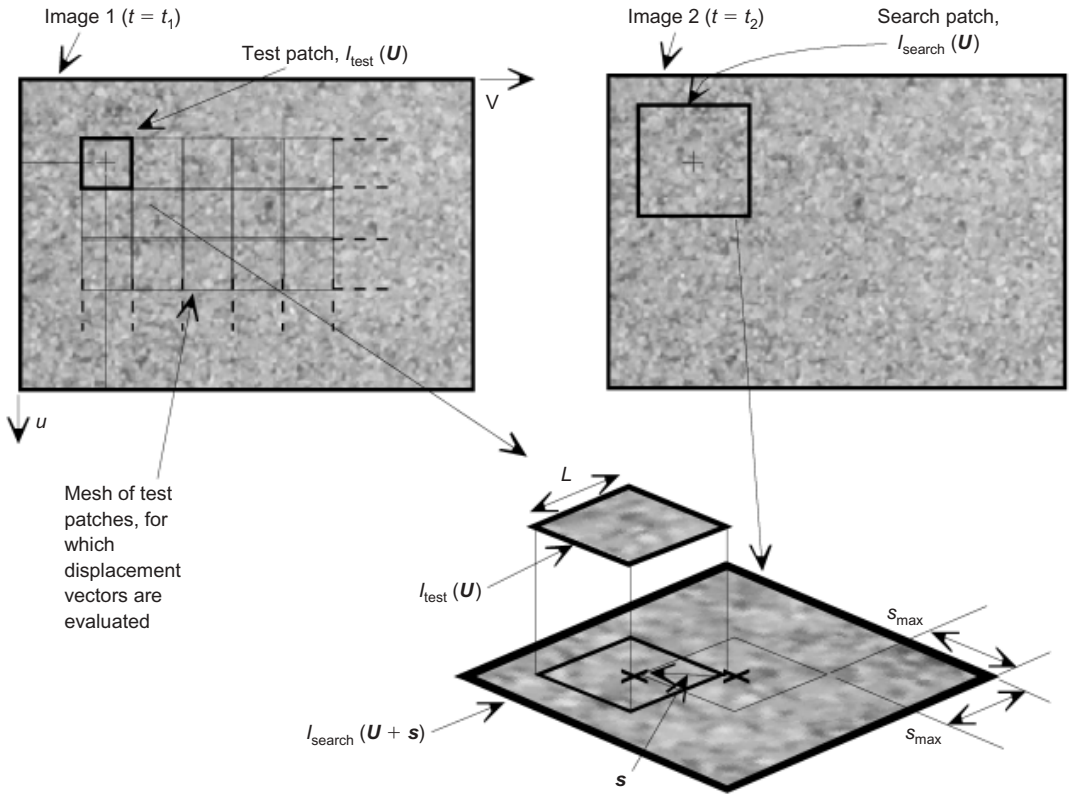

Fig. 3.17 Image processing in PIV the analysis (taken from White et al. (2003)). $I(U)$ is the image matrix of the patch with the center at the image coordinate U; s is the vector of the patch movement.

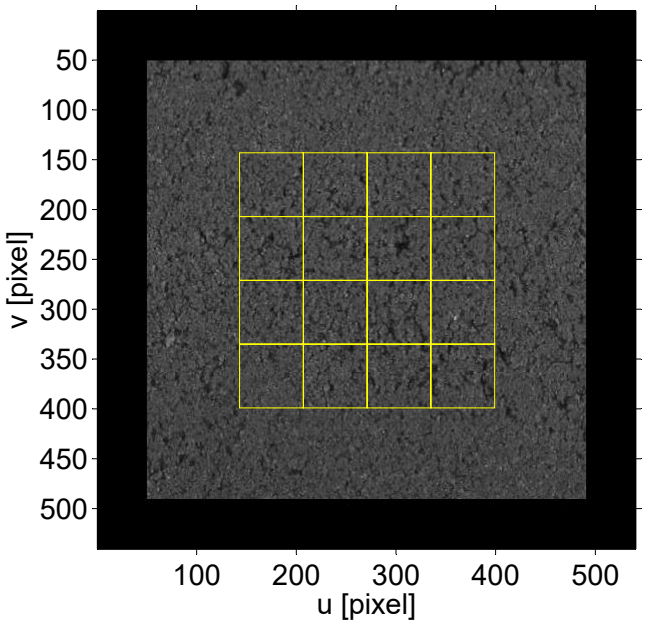

Fig. 3.18 Image texture of the model sand and trial patches (64×64 pixels).

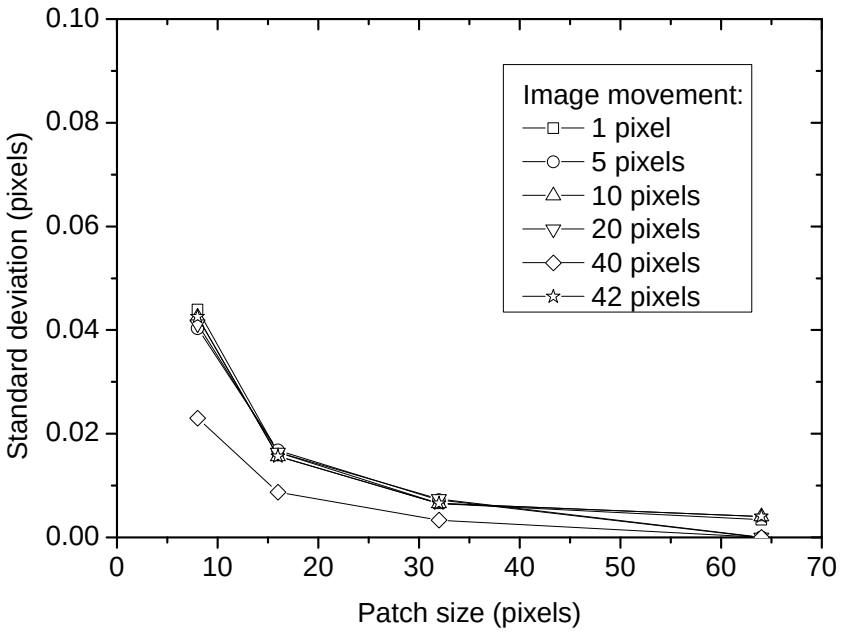

Fig. 3.19 Precision of PIV as a function of patch size for various image-space translation.

3.8.2 StereoPIV analysis on the slope surface

GeoPIV is a conventional PIV system working on the soil deformation analysis on a two-dimensional plane. In order to measure the deformation of a free surface, a stereo system consisting of 2 or more cameras is essential. Yuan et al. (2011) have reported an application of two open software packages to perform StereoPIV on a geotechnical object. The basic theory is to construct a three-dimensional displacement field using the image-space displacements, the physical camera locations as well as the camera parameters. In this study, a new MATLAB toolbox is developed to implement the StereoPIV analysis with the correction of lens movement during the centrifuge test. The analysis includes three parts:

Camera calibration

The procedure of camera calibration provided by Heikkila and Silven (1997) is adopted. A short introduction to the theory is given below.

Physical camera parameters are divided into extrinsic and intrinsic parameters. Extrinsic parameters refer to the transformation from the object coordinates to the camera coordinates or the transformation between camera coordinates in a multi-camera system. Intrinsic parameters include the effective focal length f, scale factor s_u, and the image center or the principal point (u_0, v_0). The pin-hole model (Figure 3.20), in which each point in the object space is projected by a straight line through the projection center into the image plane, is the basis of the theory.

An arbitrary object point (X_i, Y_i, Z_i) is transformed to its corresponding camera coordinate (x_i, y_i, z_i) through the following equation:

$$\begin{bmatrix} x_i \\ y_i \\ z_i \end{bmatrix} = \begin{bmatrix} m_{11} & m_{12} & m_{13} \\ m_{21} & m_{22} & m_{23} \\ m_{31} & m_{32} & m_{33} \end{bmatrix} \begin{bmatrix} X_i \\ Y_i \\ Z_i \end{bmatrix} + \begin{bmatrix} X_0 \\ Y_0 \\ Z_0 \end{bmatrix} \tag{3.6}$$

where (X_0, Y_0, Z_0) is the coordinate of the origin of the camera coordinate system in the object coordinate system, which is also the projection center; and

$$\begin{bmatrix} m_{11} & m_{12} & m_{13} \\ m_{21} & m_{22} & m_{23} \\ m_{31} & m_{32} & m_{33} \end{bmatrix} = \begin{bmatrix} \cos\varphi\cos\kappa & \sin\omega\sin\varphi\cos\kappa - \cos\omega\sin\kappa & \cos\omega\sin\varphi\cos\kappa + \sin\omega\sin\kappa \\ \cos\varphi\sin\kappa & \sin\omega\sin\varphi\sin\kappa + \cos\omega\cos\kappa & \cos\omega\sin\varphi\sin\kappa - \sin\omega\cos\kappa \\ -\sin\varphi & \sin\omega\cos\varphi & \cos\omega\cos\varphi \end{bmatrix}$$

where ω, φ and κ are Euler angles used to define a sequence of three elementary rotations around x, y and z axis, respectively.

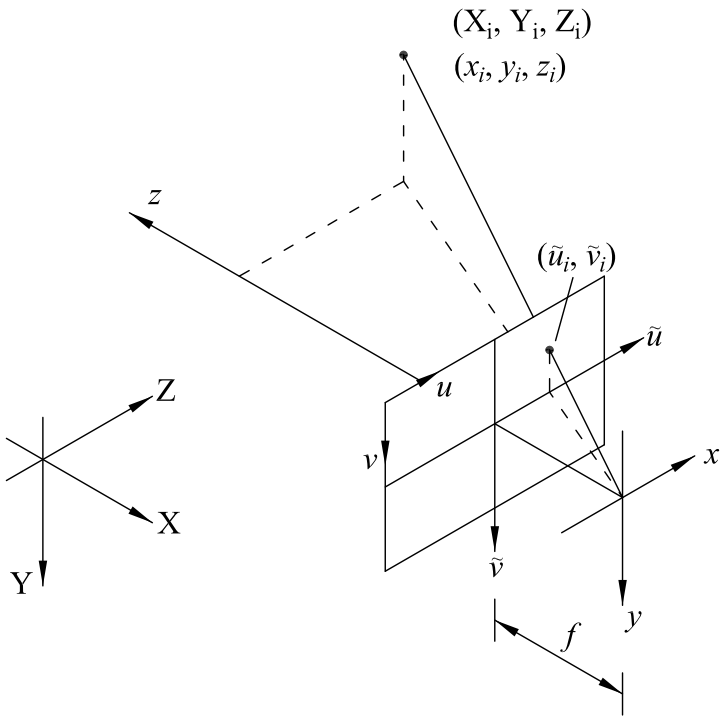

Fig. 3.20 Schematic diagram of the pinhole model.

The projection of point (x_i, y_i, z_i) to the image plane is expressed as

$$\begin{bmatrix} \tilde{u}_i \\ \tilde{v}_i \end{bmatrix} = \frac{f}{z_i} \begin{bmatrix} x_i \\ y_i \end{bmatrix} \tag{3.7}$$

Two additional coefficients D_u and D_v are required to change the metric units to pixels, as

$$\begin{bmatrix} u_i \\ v_i \end{bmatrix} = \begin{bmatrix} D_u s_u \tilde{u}_i \\ D_v \tilde{v}_i \end{bmatrix} + \begin{bmatrix} u_0 \\ v_0 \end{bmatrix} \tag{3.8}$$

When high accuracy is required, the simple pinhole model is extended with some corrections for the systematically distorted image coordinates. The image distortion includes radial distortion and tangential distortion. The radial distortion can be approximated using the following expression:

$$\begin{bmatrix} \delta u_i^{(r)} \\ \delta v_i^{(r)} \end{bmatrix} = \begin{bmatrix} \tilde{u}_i (k_1 r_i^2 + k_2 r_i^4 + ...) \\ \tilde{v}_i (k_1 r_i^2 + k_2 r_i^4 + ...) \end{bmatrix} \tag{3.9}$$

where k_1, k_2 ,... are coefficients for radial distortion, and $r_i = \sqrt{\tilde{u}_i^2 + \tilde{v}_i^2}$. It is suggested that one or two coefficients are adequate to compensate for the distortion.

The tangential distortion is defined by:

$$\begin{bmatrix} \delta u_i^{(t)} \\ \delta v_i^{(t)} \end{bmatrix} = \begin{bmatrix} 2p_1\tilde{u}_i\tilde{v}_i + p_2(r_i^2 + 2\tilde{u}_i^2) \\ p_1(r_i^2 + 2\tilde{v}_i^2) + 2p_2\tilde{u}_i\tilde{v}_i \end{bmatrix} \tag{3.10}$$

where p_1 and p_2 are coefficients for tangential distortion.

With the correction of distortion, equation 3.8 can be rewritten as:

$$\begin{bmatrix} u_i \\ v_i \end{bmatrix} = \begin{bmatrix} D_u s_u(\tilde{u}_i + \delta u_i^{(r)} + \delta u_i^{(t)}) \\ D_v(\tilde{v}_i + \delta v_i^{(r)} + \delta v_i^{(t)}) \end{bmatrix} + \begin{bmatrix} u_0 \\ v_0 \end{bmatrix} \tag{3.11}$$

Equation 3.11 indicates that the forward-projection problem is non-linear. The parameters must be estimated simultaneously using an iterative algorithm. The direct linear transformation (DLT) is adopted to produce a solution for the parameters, which are used as initial values for the optimization. Several electronic publications (Heikkilä (2000), Bouguet (2015)) are available for this camera calibration process.

PIV analysis

The image-space displacement of the soil surface from each camera is calculated using the same theory with GeoPIV. In order to perform triangulation in the next step, image-space coordinates of the identical points in both cameras are essential. Therefore, it is of great importance that the patch centers in the PIV analysis for both cameras are identical. A checked pattern with square size 5mm×5mm is printed on paper, which is laminated to avoid damage from the water in the soil. The checked pattern is placed on the soil surface with no gap in between. The image-space locations of the checked pattern corners, which can be captured from both views, are the patch centers used in the PIV analysis. The checked pattern should be removed before the soil deformation. The error due to the thickness of the checked pattern is neglected in this study.

Triangulation

Figure 3.21 shows the schematic diagram of the triangulation, which computes the 3D location of a set of points (patch centers) given their image projections (denoted by $U_{il} = [u_{il}, v_{il}, 1]^T$ and $U_{ir} = [u_{ir}, v_{ir}, 1]^T$ for left and right images, respectively). By applying the reverse of equation 3.11, the normalised coordinates of the image points in the corresponding

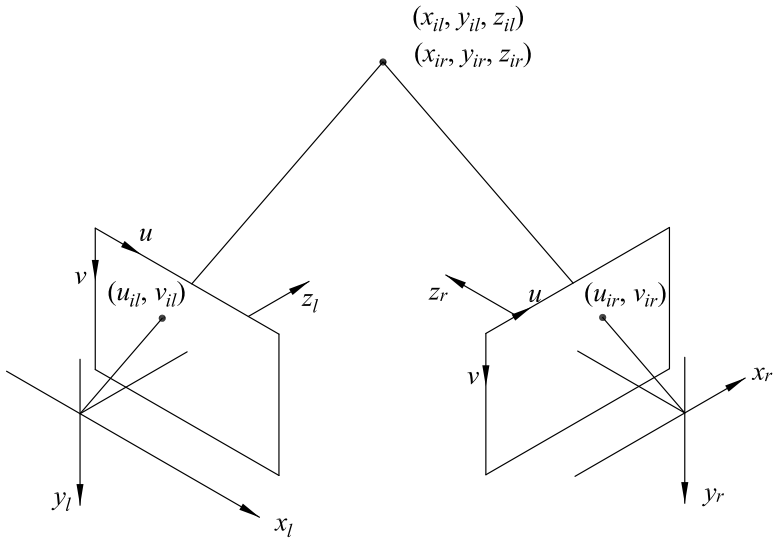

Fig. 3.21 Schematic diagram of triangulation

camera coordinate system ($\tilde{U}_{inl} = [\tilde{u}_{inl}, \tilde{v}_{inl}, 1]^T$ and $\tilde{U}_{inr} = [\tilde{u}_{inr}, \tilde{v}_{inr}, 1]^T$) can be obtained. An iteration is needed since the lens distortion is considered in the step of camera calibration. According to the pinhole model, the relationship of the normalised image coordinate and the object coordinate in the same camera coordinate system is given by:

$$\tilde{U}_{inl} = \begin{bmatrix} \tilde{u}_{inl} \\ \tilde{v}_{inl} \\ 1 \end{bmatrix} = \frac{1}{z_{il}} \begin{bmatrix} x_{il} \\ y_{il} \\ z_{il} \end{bmatrix} \tag{3.12}$$

$$\tilde{U}_{inr} = \begin{bmatrix} \tilde{u}_{inr} \\ \tilde{v}_{inr} \\ 1 \end{bmatrix} = \frac{1}{z_{ir}} \begin{bmatrix} x_{ir} \\ y_{ir} \\ z_{ir} \end{bmatrix} \tag{3.13}$$

Assuming that the coordinate system of left camera is the world coordinate, the object coordinate in the right camera system can be transformed to the left camera system through the following equation:

$$\begin{bmatrix} x_{il} \\ y_{il} \\ z_{il} \end{bmatrix} = R \begin{bmatrix} x_{ir} \\ y_{ir} \\ z_{ir} \end{bmatrix} + T \tag{3.14}$$

where R is the 3×3 rotation matrix and T is the 3×1 translation vector.

There are only two unknowns z_{il} and z_{ir} in equation 3.14. Least-squares approximation technique is adopted to solve this overdetermined problem. The values of z_{il} and z_{ir} are given by:

$$z_{il} = \frac{(\tilde{U}_{inr}^T R\tilde{U}_{inl})T^T\tilde{U}_{inr} - (\tilde{U}_{inr}^T\tilde{U}_{inr})T^T(R\tilde{U}_{inl})}{(\tilde{U}_{inl}^T\tilde{U}_{inl})(\tilde{U}_{inr}^T\tilde{U}_{inr}) - (\tilde{U}_{inr}^T R\tilde{U}_{inl})^2} \tag{3.15}$$

$$z_{ir} = \frac{(\tilde{U}_{inl}^T\tilde{U}_{inl})T^T\tilde{U}_{inr} - (\tilde{U}_{inr}^T R\tilde{U}_{inl})T^T(R\tilde{U}_{inl})}{(\tilde{U}_{inl}^T\tilde{U}_{inl})(\tilde{U}_{inr}^T\tilde{U}_{inr}) - (\tilde{U}_{inr}^T R\tilde{U}_{inl})^2} \tag{3.16}$$

where the superscribe T means the transposed vector or matrix. The coordinates of the object in each camera system can then be easily calculated using equation 3.12 and 3.13.

The StereoPIV System

A new MATLAB toolbox for the StereoPIV analysis of centrifuge tests is developed based on the work of Bouguet (2015) and White et al. (2003). The user interface of the toolbox is shown in Figure 3.22. The StereoPIV analysis of a centrifuge test includes the following 5 steps:

1. *Camera calibration*. After the installation of the two cameras, a small rigid checked pattern (10×10 grid with a grid size of 10 mm) is placed above the measuring surface at various positions with various angles (10∼20 in this study) inside the common view of the cameras. The camera parameters, the rotation matrix R and the translation vector T of the right camera to the left camera are calculated. Figure 3.23 shows the relative position of the cameras and all the positions of the checked pattern.

2. *Mesh generation*. Before the soil deformation, a thin printed checked pattern is placed on the soil surface of interest. Grid corners are extracted from both views and are used as patch centres for the image space PIV analysis (n denotes the patch numbers). Figure 3.24 shows the extracted grid corners (red cross) from the left view.

3. *PIV analysis in both views*. After a centrifuge test, several images (m denotes the number of the image couples) are selected from both views to represent different stages of the test. The initial patches (u_{il}^j, v_{il}^j, u_{ir}^j and v_{ir}^j, $i = 1...n$, $j = 1$) are already obtained in the last step. PIV analysis is performed separately in each view to obtain the displaced patches in the rest stages of the test (u_{il}^j, v_{il}^j, u_{ir}^j and v_{ir}^j, $i = 1...n$, $j = 2...m$). Figure 3.25 shows the patches before and after the test in the left view.

4. *Camera movement monitoring*. A checked pattern is placed on the side wall as a reference to the camera movement (Figure 3.26). At each stage of the test (image

couple j), certain grid corners in the left view (blue circles in Figure 3.26) are extracted. The rotation matrix R_j and the translation vector T_j of the left camera to the reference plane are calculated. The relative movement between the cameras is not considered.

5. *Triangulation*. Triangulation is performed on each image couple to obtain the soil surface coordinates $[x_{il}^j, y_{il}^j, z_{il}^j]^T$ $(i = 1...n,\ j = 1...m)$, which are further transformed into the reference coordinate system to take into account the camera movement. The soil movement at the soil surface is obtained by calculating the difference between the current coordinates and the initial coordinates. Figure 3.27 shows the soil surface before and after the test. The out-of-plane movement of the soil surface is well captured.

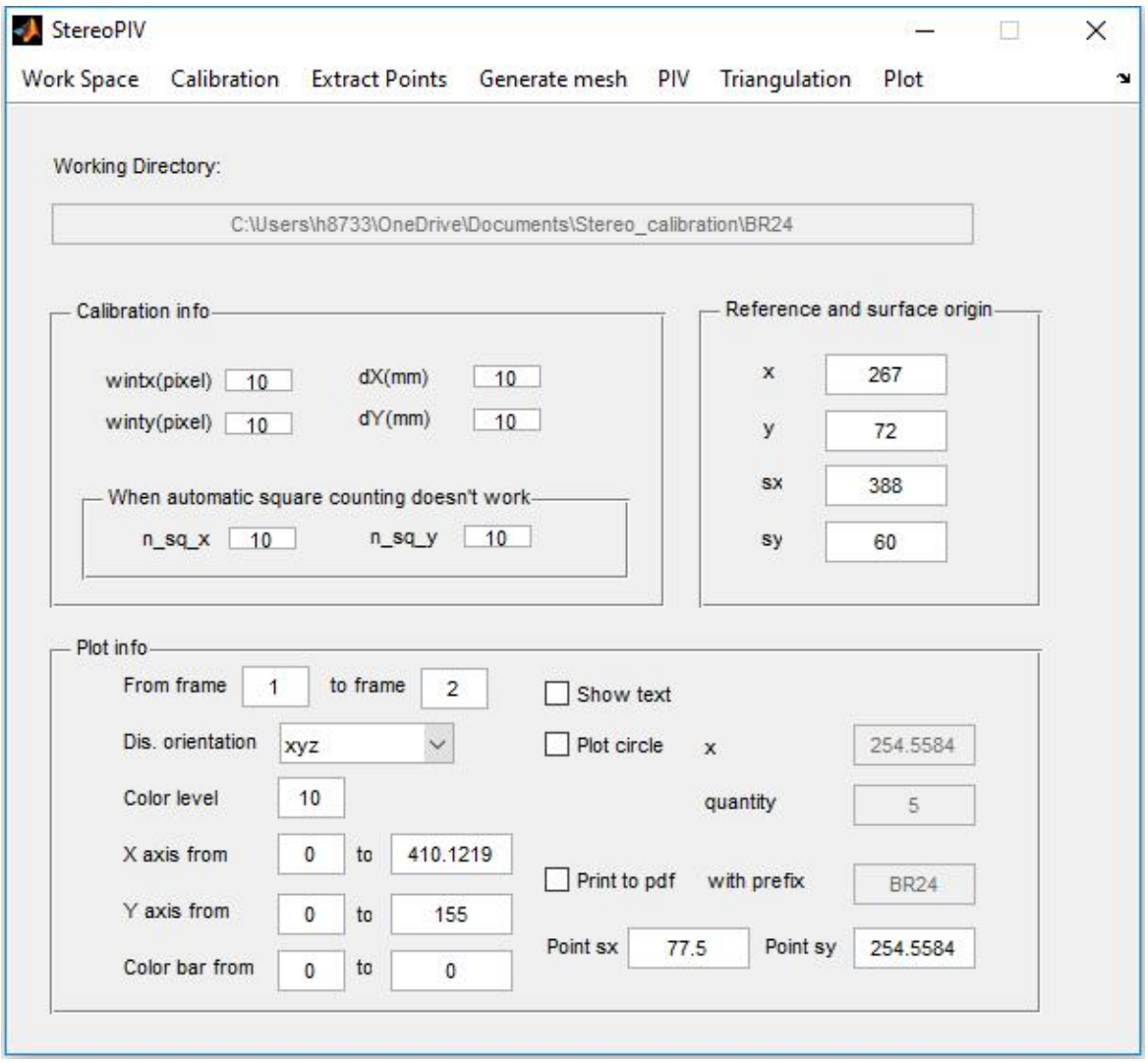

Fig. 3.22 The user interface of the MATLAB toolbox for StereoPIV

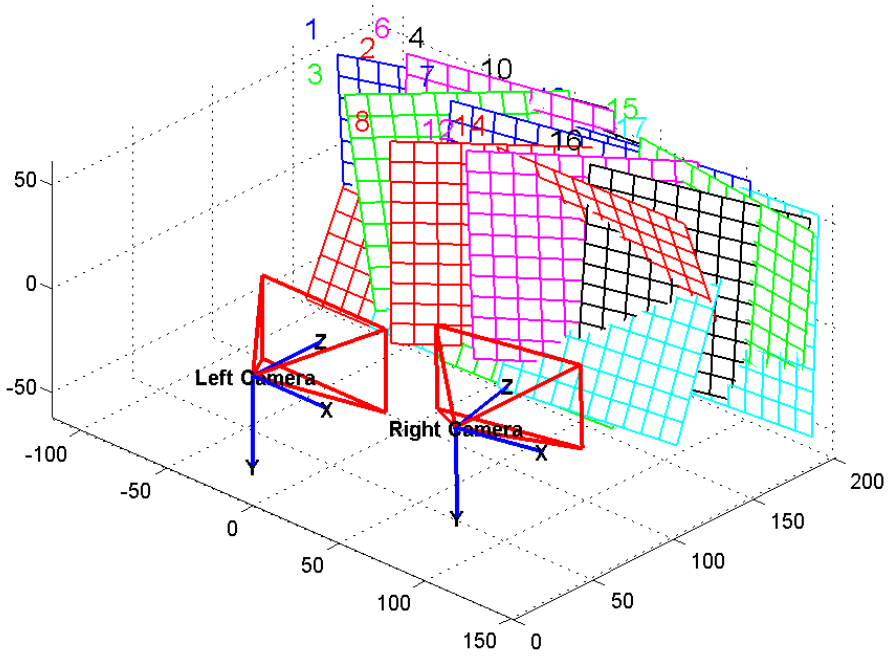

Fig. 3.23 Extrinsic relation of the cameras and the calibration grids (unit: mm).

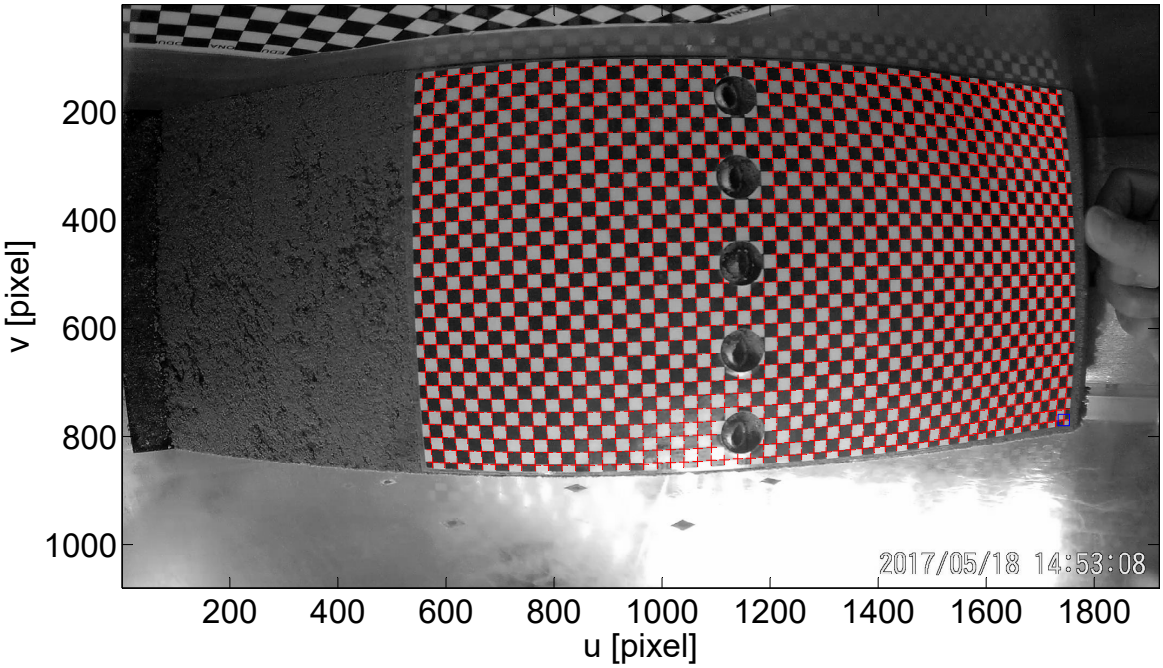

Fig. 3.24 Generation of patch centers

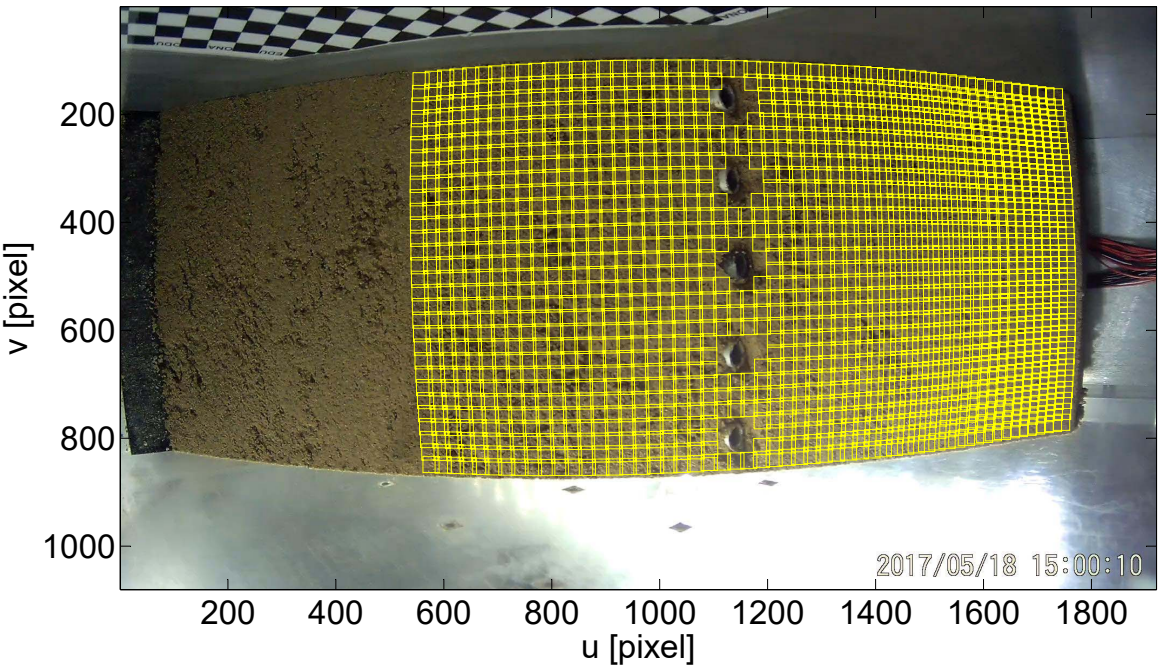

(a) The patches before the soil movement

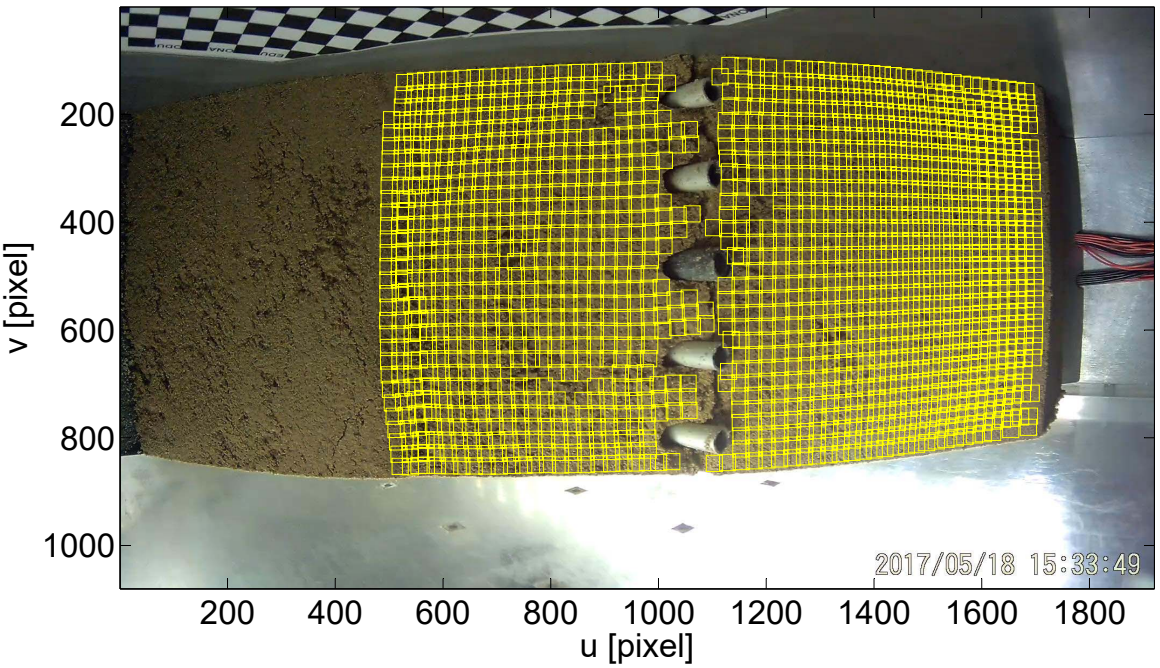

(b) The patches after the soil movement

Fig. 3.25 Image space PIV analysis

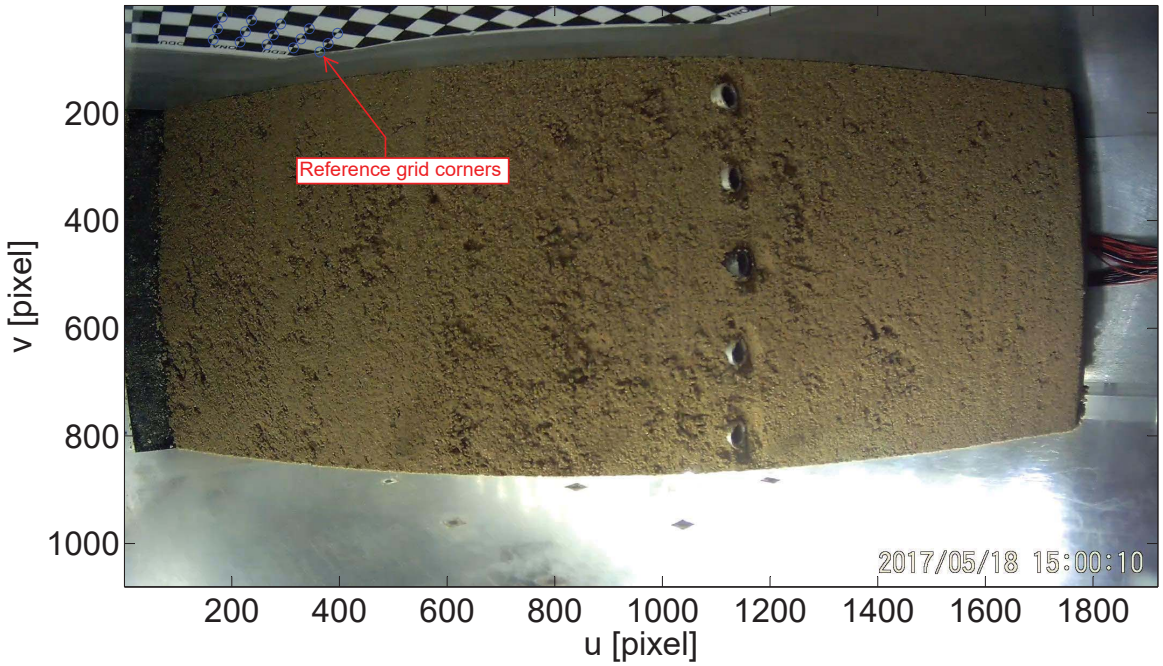

Fig. 3.26 Reference grid corners in the left camera view. (Note: corners in the small circles are selected.)

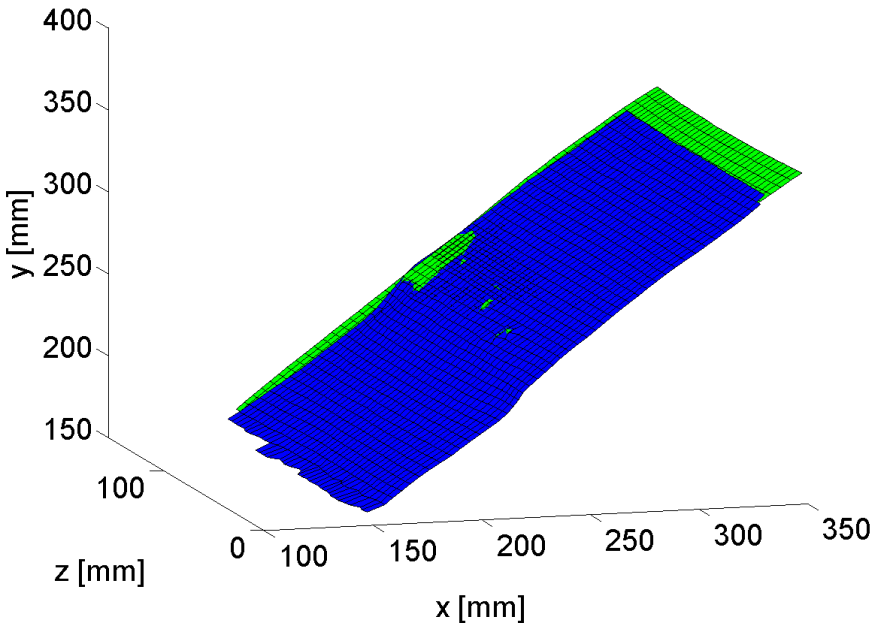

Fig. 3.27 Triangulation result of the soil surface before (green) and after (blue) the soil movement.

Chapter 4

Results and analysis of centrifuge tests

4.1 Overview of the tests

In total, 29 cases are considered. All the centrifuge tests are listed in Table 4.1. Five parameters, namely, the pile material or bending stiffness EI, the spacing ratio s/d, the pile slenderness h/d, the relative length of the up-slope soil l/h and the pile length above the sliding surface h_p, are considered in this chapter. The only triggering factor is gravity. A g-up test procedure is employed by continuously increasing the gravity-induced stress field. The increase of stresses in the model slope corresponds to the increase of the prototype slope height. The g-up test procedure is ended when the soil movement reaches the limit or the test reaches 50g. The increase of the centrifugal acceleration (rpm) is conducted at a rate of 0.1 per second.

4.2 Soil movement without pile reinforcement

A test without pile reinforcement (NP) was performed to validate the system. Figure 4.1 shows the soil displacement in the sliding layer at 2.7 g, at which the soil starts to move at a high velocity. The slope toe area, where the slip surface approaches the horizontal, is the only anti-sliding part of the unstable layer. When the sliding force in the soil exceeds the anti-sliding force, the toe area starts to move horizontally and a uniform soil movement is produced for the inclined part (see Figure 4.2), which enables the pile-soil interaction to be studied in a generic way.

Table 4.1 Pile configurations for all the tests. s/d is the pile spacing (ratio); h is the vertical thickness of the sliding soil; h_p is the pile length in the sliding soil (usually = h). l/h is the ratio of the up-slope length to the soil layer thickness.

Test code	Test NO.	Pile material	s/d	h (mm)	h_p (mm)	l/h
NP	BR09	-	-	130	-	-
A2P	BR15, BR27(SG)	Aluminium	7.75	130	130	0.85
A3P	BR10, BR26(SG)	Aluminium	5.17	130	130	0.85
A4P	BR12, BR25(SG)	Aluminium	3.88	130	130	0.85
A5P	BR18, BR24(SG)	Aluminium	3.10	130	130	0.85
A2PSL	BR46(SG)	Aluminium	7.75	70	70	2.43
A3PSS	BR42(SG)	Aluminium	5.17	70	70	2.43
A3PSM	BR41(SG)	Aluminium	5.17	70	70	2.43
A3PSL	BR39(SG)	Aluminium	5.17	70	70	2.43
A4PSL	BR17, BR38(SG), BR40(SG)	Aluminium	3.88	70	70	2.43
A5PSS	BR35(SG), BR45(SG)	Aluminium	3.10	70	70	0.85
A5PSM	BR36(SG), BR44(SG)	Aluminium	3.10	70	70	1.56
A5PSL	BR37(SG), BR43(SG)	Aluminium	3.10	70	70	2.43
A2PB	BR31(SG)	Aluminium	7.75	130	70	0.85
A3PB	BR30(SG)	Aluminium	5.17	130	70	0.85
A4PB	BR29(SG)	Aluminium	3.88	130	70	0.85
A5PB	BR28(SG)	Aluminium	3.10	130	70	0.85
P2P	BR14	Acrylic	7.75	130	130	0.85
P3P	BR11	Acrylic	5.17	130	130	0.85
P4P	BR13	Acrylic	3.88	130	130	0.85
P5P	BR19	Acrylic	3.10	130	130	0.85
P4PSL	BR16	Acrylic	3.88	70	70	2.43
P5PSS	BR21	Acrylic	3.10	70	70	0.85
P5PSM	BR23	Acrylic	3.10	70	70	1.56
P5PSL	BR20	Acrylic	3.10	70	70	2.43
P2PB	BR34	Acrylic	7.75	130	70	0.85
P3PB	BR33	Acrylic	5.17	130	70	0.85
P4PB	BR32	Acrylic	3.88	130	70	0.85
P5PB	BR22	Acrylic	3.10	130	70	0.85

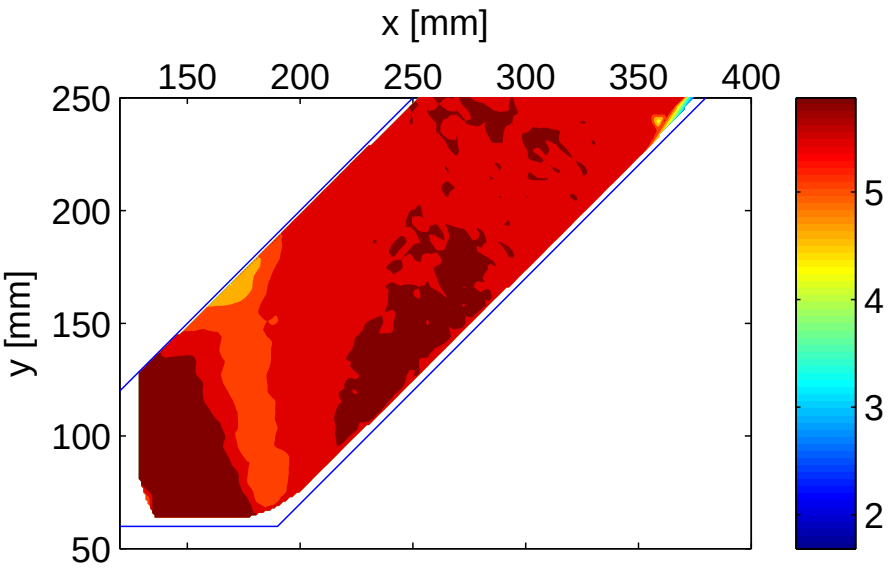

Fig. 4.1 Soil displacement at 2.7g for test NP. (Unit: mm)

4.3 Failure modes with pile reinforcement

Four failure modes (namely, flow failure, down-slope failure, over-top failure, and pile structural failure) are identified and their relations to pile stiffness, pile slenderness and pile spacing are discussed here.

To combine the effect of pile stiffness and pile slenderness, Poulos and Davis (1980) introduced a non-dimensional parameter called the pile flexibility factor K_R:

$$K_R = \frac{EI}{E_s h^4} \tag{4.1}$$

where EI is the pile stiffness, E_s is the elastic modulus of soil and h is the thickness of the sliding layer. In this thesis, K_R is also described as the relative pile rigidity because a higher K_R value corresponds to a more rigid pile behaviour.

Figure 4.3 shows the general relationship between failure modes and test configurations (K_R and s/d). The relative up-slope length l/h is another parameter which can significantly affect the failure mode. In this study, low K_R value refers to the case of acrylic piles with high slenderness ratio (test series P*i*P). The pile spacing s/d is found to be a decisive factor for a successful reinforcement. With large s/d, the up-slope is prone to 'flow failure' at the pile row. In the upper-left zone of the figure (small s/d and large K_R), two failure modes are possible depending on the relative length of up-slope soil l/h: down-slope failure and over-top failure. The down-slope failure is formed due to the strong separation effect of the

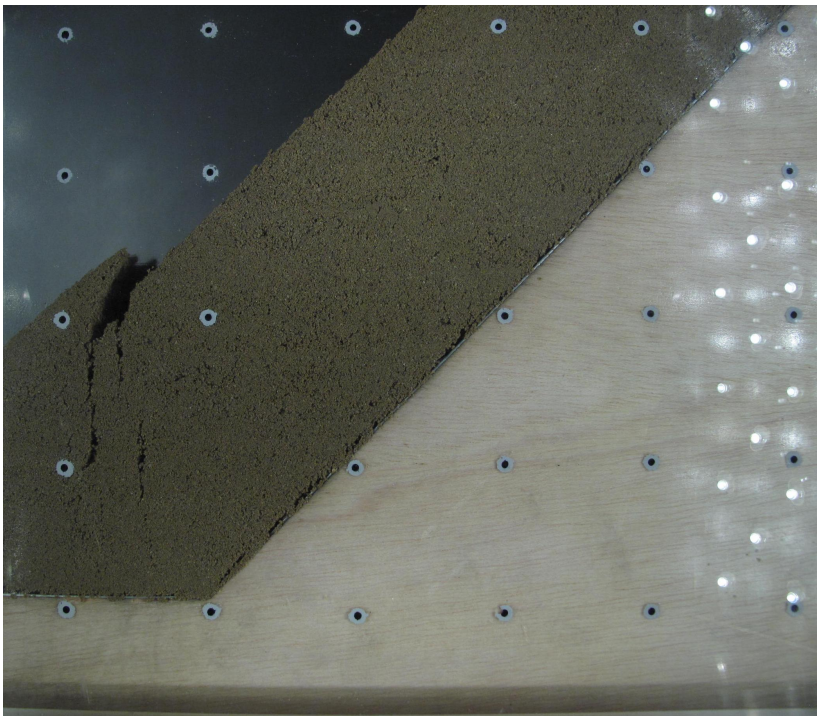

Fig. 4.2 Large soil movement after the test.

pile row. When l/h is large, the up-slope tends to move over the pile top (over-top failure). In the lower-left zone of the figure (small K_R), due to the large pile deformation, the over-top and the down-slope movements merge at the pile row. In all the experiments presented in Table 4.1, the structural failure of the pile is observed in the test series P*i*P and tests A2P, A2PB, P3PB and P2PB.

4.3.1 Flow failure

The mode 'flow failure' refers to the failure of soil arching between the adjacent piles. In this mode, the soil flows through the pile row. Figure 4.4 shows the top view of test A2P at 50 g. The up-slope soil has bypassed the piles and therefore a gap is formed in the down-slope direction of the piles. In this case, the runout is stopped by the lateral wall in the model box. The horizontal displacements of the pile top and the soil in between the piles (Figure 4.5) gives a clear indication that the piles have failed to prevent the soil movement.

4.3.2 Down-slope failure

The down-slope is prone to failure when the up-slope is well stabilised. This failure mode is clearly observed in test A5PSS (Figure 4.6), in which l/h is very small. In the tests belonging

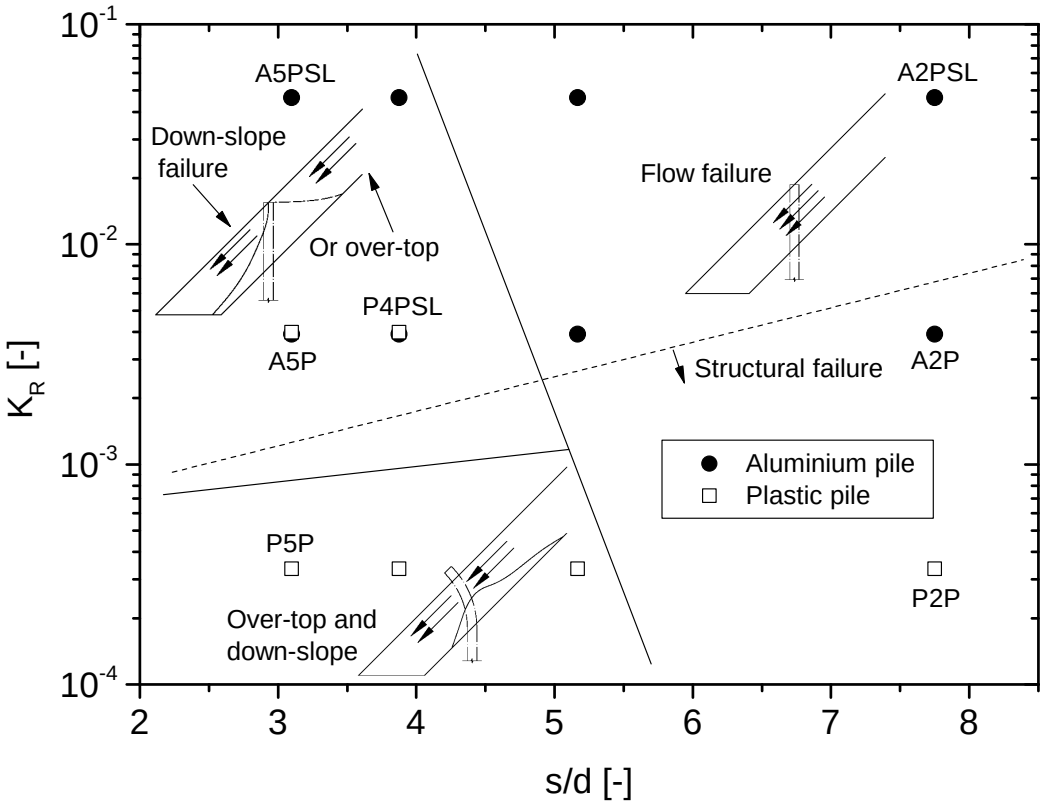

Fig. 4.3 Overview of the tests and their corresponding failure modes. K_R: relative pile rigidity; s: pile axis-to-axis distance; d: pile diameter.

to the same failure category (Figure 4.3), only some minor indications can be observed, such as cracks at the pile row (Figure 4.7). Soil movement in the up-slope has significant influence on the down-slope movement. When the displacement of the up-slope is large, which is usually due to the large up-slope length l, the down-slope soil is pushed to slide forward. However, the pattern of local failure in the down-slope can still be captured by the digital image processing.

Figure 4.8 shows the side-view soil displacement at 50 g of test A5P. Note that only a part of the slope is analysed by PIV (the PIV analysed region is marked by the dotted rectangle in Figure 4.14). Because of the plain strain assumption, in test NP, the soil displacements in xy cross-sections throughout the longitudinal direction z (see Figure 3.13) are similar to the side-view soil displacement. For the tests with piles, the pile installation has resulted in variations along the longitudinal direction. The side-view only represents the movement of the cross-sectional plane in the middle of two adjacent piles. It is seen in the figure that

Fig. 4.4 Top view of test A2P at 50 g.

the up-slope is successfully stabilized after a certain amount of soil compaction while the largest movement takes place in the down-slope which could result in a local failure. The maximum shear strain shows that a vertical shear band along the pile axis is formed allowing a separation between the up- and down-slope soil masses.

4.3.3 Over top failure

The mode 'over-top failure' refers to the soil in the up-slope region that moves above the stabilising piles, occurring when the up-slope is long. Figure 4.9 shows the displacement of the side-view of test A5PSL, which has the largest l/h value of 2.43. It is seen that a certain zone in the up-slope is well stabilized while the rest of the up-slope tends to move above this zone. The maximum shear strain of this test at 45 g and 50 g are displayed in Figure 4.10. A shear band is formed, which starts at the pile top and extends into the up-slope until the predefined slip surface. However, this failure can hardly be observed by bare eye. The reason is that the soil layer is attached to a rubber layer, which provides a slippery surface but also restricts the relative soil movement at the soil bottom. As a result, a second and shallower shear band is formed at a higher g-level (as shown in Figure 4.10b). The over-top failure has transformed into a shallow failure.

As mentioned previously the over-top failure can also merge with the down-slope failure when K_R is small. Figure 4.11 shows the side-views of test P5P before and after failure. The pile top has moved along with the soil. A clear slip surface can not be easily detected because the soil movement is a combination of translation of the whole entity and deformation inside the sliding soil. PIV analysis (Figure 4.12) shows that the lower part of the up-slope soil is

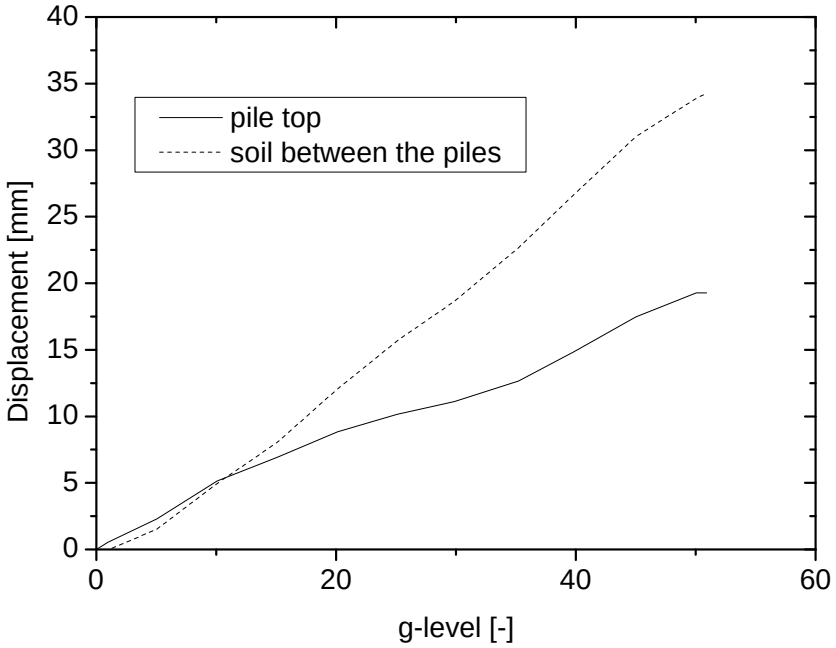

Fig. 4.5 Horizontal displacement of the pile top and the soil between the piles for test A2P.

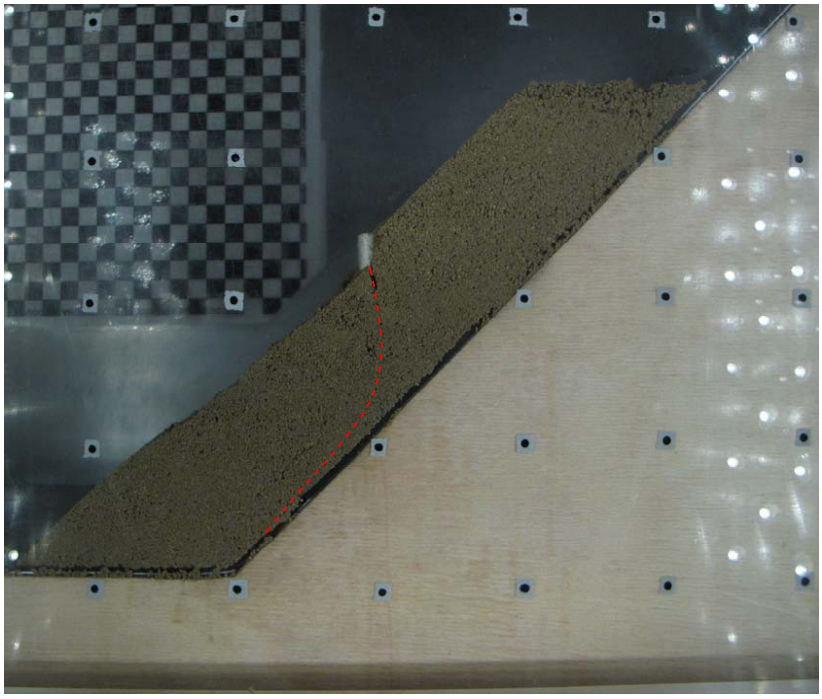

Fig. 4.6 Side-view of test A5PSS at 50 g. The red dashed line depicts the inferred local slip plane.

Fig. 4.7 Top-view of test A5P at 50 g.

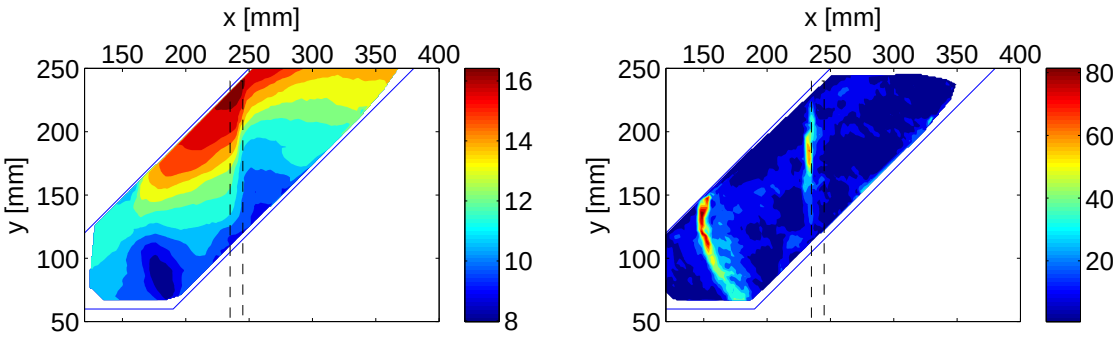

(a) displacement [mm] **(b)** maximum shear strain [%]

Fig. 4.8 PIV results of test A5P at 50 g.

stabilized while the upper part moves above the lower part, pushing the down-slope soil. The maximum shear strain shows that the vertical shear band, which is induced by the down-slope soil movement, and the shear band parallel to the slip surface, which is due to the over-top movement, have intersected and merged at the pile row.

4.3.4 Pile structural failure

The structural failure of the piles takes place when the bending moment has reached the ultimate value: breakage for the acrylic piles and plastic hinge for the aluminium piles. Below the dashed line in Figure 4.3 are the tests with structural failure (without the tests with deep-buried piles). The pile material (or the ultimate pile bending moment) is the key factor. All the tests with long acrylic piles (series PiP) are observed with structural failure

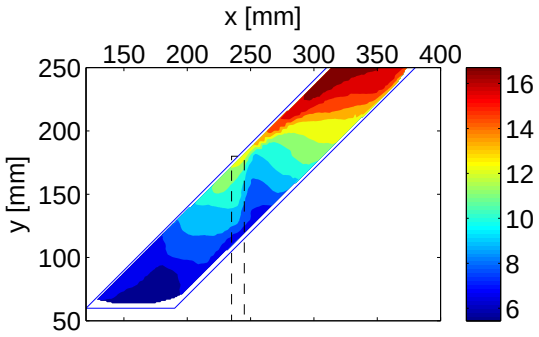

Fig. 4.9 PIV computed soil displacement (unit: mm) of test A5PSL at 50 g.

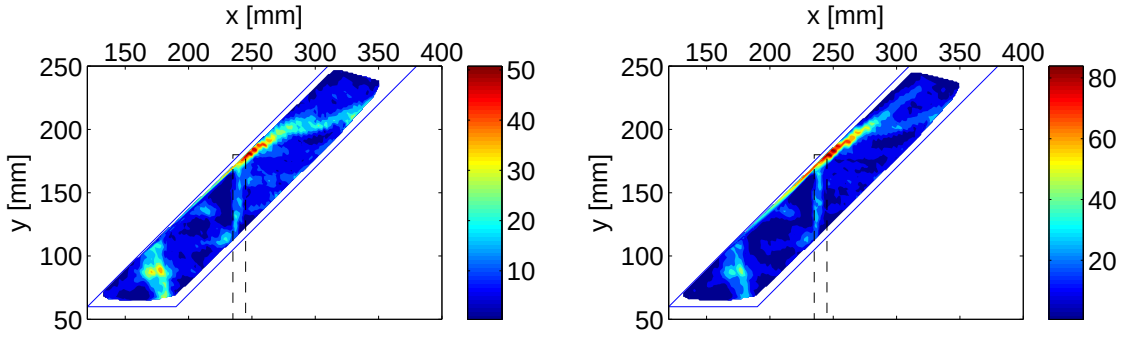

(a) 45 g **(b)** 50 g

Fig. 4.10 PIV computed maximum shear strain (unit: %) of test A5PSL. Shear band changes direction from 45 g to 50 g.

while only the test A2P in the test series AiP is observed with a plastic hinge failure. Pile spacing is another important factor for the pile structural failure and will be discussed in the following section. The breakage or plastic hinge occurred at about 1 cm below the predefined slip surface as shown in Figure 4.13.

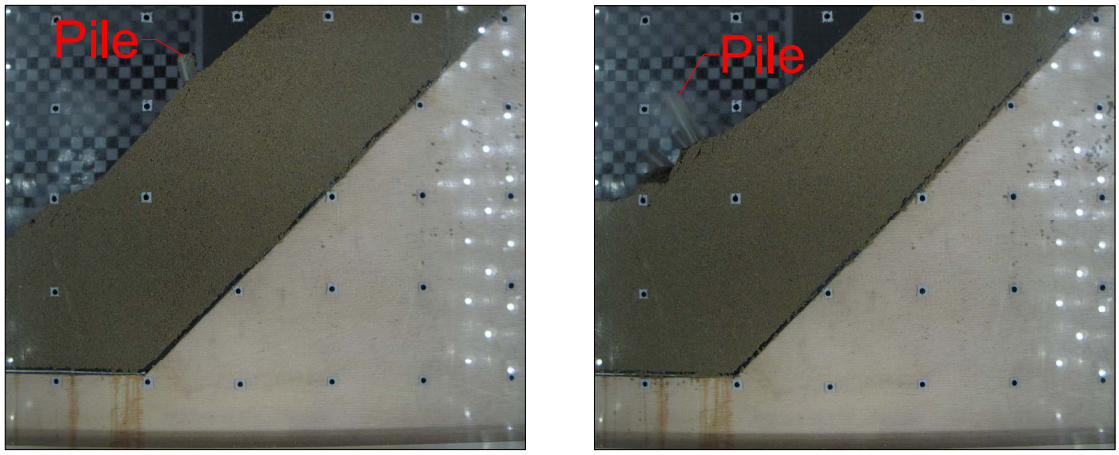

(a) before failure (50.3 g) **(b)** after failure

Fig. 4.11 Side-view of test P5P.

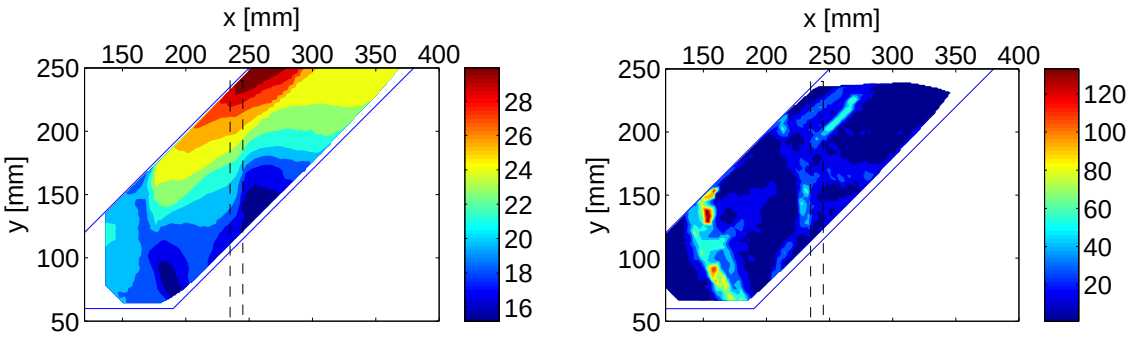

(a) displacement (unit: mm) **(b)** maximum shear strain (unit: %)

Fig. 4.12 PIV results of test P5P before failure (50.3 g).

Fig. 4.13 Broken piles after the tests. Left side is the pile head. The breakage of acrylic piles and the plastic hinge in aluminium piles occurred at about 14 cm measured from left (about 1 cm below the slip surface).

4.4 The role of pile spacing s/d

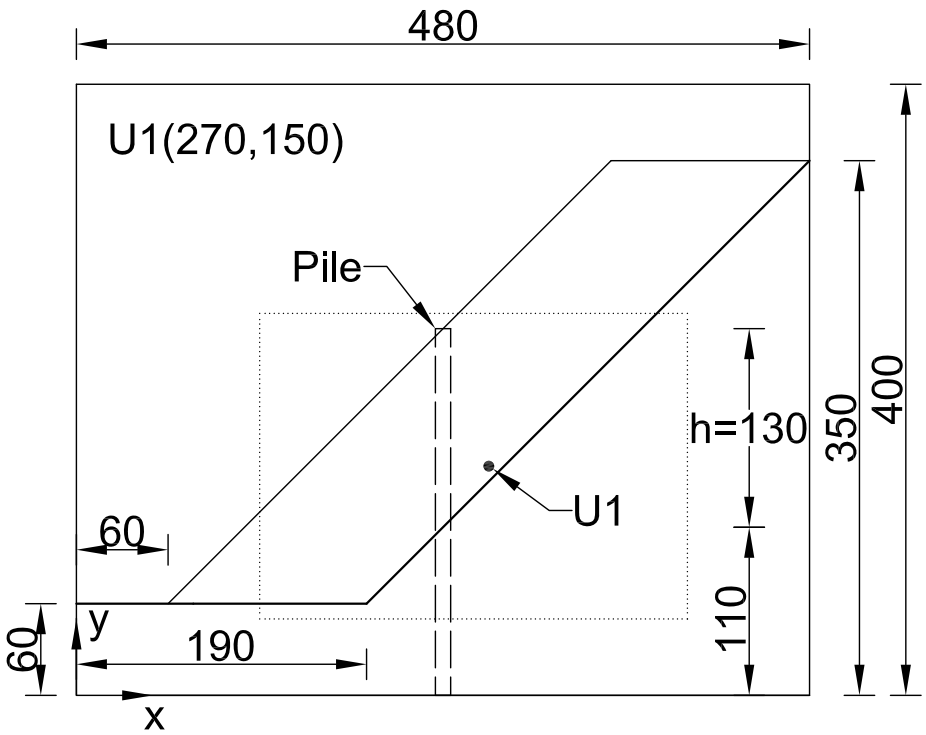

Fig. 4.14 Geometry of the model in cross-sectional view (unit: mm). The dotted rectangle indicates the area where PIV analysis is applied. U1 is a monitoring point whose displacement is used to represent the movement of the rubber sheet.

Four pile spacing ratios are considered in the centrifuge tests. The test series AiP using long aluminium piles is analysed here to reveal the role of pile spacing, where i = 2, 3, 4 or 5, are the number of piles used in each test and correspond to s/d = 7.75, 5.17, 3.88 and 3.10 ratios, respectively. Figure 4.14 shows the cross-sectional geometry of this test series. The overall movement of the unstable layer is generated by the sliding between the rubber sheet and the aluminium sheet. For test NP, the movement of the soil layer is limited by the model container. For the tests with piles, which penetrate through all the layers, the soil movement is limited by the perforated area in the rubber sheet. In this study, limit of 35 mm is predetermined.

Displacement analysis

The displacement of the point U1 with coordinates (270 mm, 150 mm) is used to determine whether the unstable layer has reached its limit displacement or not. Figure 4.15 shows the soil displacement at U1 for the test series AiP. The displacements for test NP and the test

series A*i*P(SG), which has the same configuration with A*i*P but with an instrumented pile, are also plotted in the figure. For test NP, the displacement at U1 reached 5.9 mm at a very early loading stage of 2.7 g and its movement afterwards was not captured due to the high velocity of soil movement.

As seen in Figure 4.15, the soil displacement at U1 increases almost linearly with g-level. No sudden acceleration is observed. The displacement level increases with the pile spacing. For tests A2P and A3P, the soil movement has reached the limit and is much higher than tests A4P and A5P. For the test series with an instrumented pile, the displacements of tests A2P(SG) and A3P(SG) are much smaller than the corresponding tests without instrumentations. The reason could be that the instrumented pile has a larger diameter and higher surface friction than the original pile. Since only one pile is instrumented, when an even number of piles (2 and 4) are applied, the asymmetry of pile could lead to further resistance from the side walls. Note that the influence of the instrumentation is not considered in the analysis. Although the displacements are reduced by the instrumented piles, the patterns of failure remain the same.

Figure 4.16 shows the displacement of the side-view at 50 g. The displacement level of the sliding soil increases with the increase of s/d. In tests A4P and A5P, conspicuous soil separation between the up-slope and down-slope soil is observed, while in tests A2P and A3P the displacement is continuous at the pile row. Even though some local excessive displacements are observed in tests A2P and A3P, the soil mass has bypassed the piles considering the large magnitude of displacements. These observations from the side-view are confirmed by the top-view. Figure 4.17 presents the displacement of the soil surface corresponding to Figure 4.16. Note that Figures 4.17b and 4.17c are produced from a single-camera system while the other two are from a double-camera system, which brings a difference in the accuracy of the measured displacements especially at the slope toe. Nevertheless, the displacement discontinuity at the pile row for tests A4P and A5P is clearly visualized. Figure 4.18 shows the surface displacement for the test series A*i*P(SG). Similar to A*i*P, the soil movement tends to maintain consistent at the pile row for large pile spacing and tends to separate at the pile row for small pile spacing.

Deformation analysis

The displacement analysis shows that soil deformation exists in the sliding soil mass. Figure 4.19 shows the maximum shear strain of the side-view at 50 g. Large strains or for some cases even the highest value of the maximum shear strain are observed in the slope toe area, where the slip surface turns horizontal. This can be an interference when we analysis the soil strain at the pile row. Therefore, the sub-figures for the 4 tests in the test series A*i*P are not plotted in the same range of strain value. The shear band in the soil is well revealed. When

the pile spacing is small (A4P, A5P), clear strain concentrations are obtained at the pile row. A vertical shear band is formed along the pile length. On the contrary, such shear band does not appear in the cases with a larger pile spacing (A2P and A3P). In test A2P, a shear band parallel to the slip surface is observed. It is induced by the further increasing of the g-level after the maximum soil layer displacement (35mm) is reached. This phenomenon is not observed in test A2P(SG), in which the displacement limit for the soil layer is not reached.

To better understand the soil deformation in the slope, Zhang and Wang (2016) proposed an index termed the *Diversity Factor of Displacement* (DFD), which is calculated by:

$$DFD = \frac{n \sum_{i=1}^{n} w_i^2 - (\sum_{i=1}^{n} w)^2}{an(n-1)} \tag{4.2}$$

where a is the area of the analysis zone, w is the horizontal or vertical displacement of the measured points, and n is the number of the measured points in the analysis zone. The advantage of DFD over strain in the deformation analysis is that DFD can consider all the displacement information inside a target zone and the calculation does not depend on the mesh as in the PIV analysis.

Figure 4.20 presents the DFD for horizontal (x) and vertical (y) displacements (Δx and Δy) along a vertical line at $x = 240$ mm (the pile row location) in the side-view. Large differences of DFD can be observed with the change of pile spacing. For the small spacing cases (A4P and A5P), DFD for Δy increases rapidly with the increase of g-level while DFD for Δx remains unchanged, which also confirms that the soil shear deformation is vertical along the depth. Between these two tests, the rapid increase of DFD in test A5P (35 g) occurs later than test A4P (25 g). This is reasonable since a certain amount of relative pile-soil displacement is needed to mobilise the pile-soil interaction. For the large spacing cases (A2P and A3P), the increase of DFD is small in both directions. For test A3P, DFD for Δy has increased at the early stage, but it remains unchanged after about 35 g. Obviously the piles are only effective at the beginning before the flow failure between the piles occurs. For test A2P, DFD remains unchanged for most of the vertical line except a small increase at about $y = 190$ mm in both x and y directions. This location corresponds to the shear band in Figure 4.19a. It can be seen that the increase of DFD starts at about 35 g, at which the soil displacement has almost reached its limit. Apparently the shear band detected in test A2P is not due to the pile-soil interaction.

Another observation is that the pile plastic deformation is only observed in test A2P, which implies that the piles have experienced more force than in the other tests with more piles. This agrees with observations from the literature (Kourkoulis et al. (2010)).

Analysis of strain gauge measurements

The aforementioned analysis of soil displacement and deformation is based on the test series A*i*P. The following analysis of soil pressure on piles makes use of the measurements from the strain gauges (SG) on one of the piles in the test series A*i*P(SG), which has the same configuration with A*i*P. Even though smaller soil displacement is obtained for A*i*P(SG), the observations from A*i*P are also applicable to A*i*P(SG). Figure 4.21 shows the internal forces and soil pressure of test A5P(SG) at different g-levels. The bending moment above the slip surface (at the depth of about 0.13 m) increases exponentially from the pile top to the slip surface and so is the shear force but with a lower order of magnitude. The soil lateral pressure increases almost linearly with depth. Figure 4.22 shows the internal forces and soil pressure of the test series A*i*P(SG) at 50 g. The results of tests A2P(SG) and A4P(SG) are very close to tests A3P(SG) and A5P(SG), respectively. The soil pressure is closely related to the soil movement. Because of the pile asymmetry due to the instrumentation, the soil movements of the tests with an even number of piles are smaller than the corresponding tests without instrumentation. It is believed that the measured soil pressure in tests A2P(SG) and A4P(SG) is smaller than the value that can be reached theoretically.

Figure 4.23 shows the analysis of the sliding force on the pile. The pile shear force at the depth of the slip surface, which is regarded as the total sliding force exerted on the pile, increases with the g-level (Figure 4.23a). Before about 20 g, the sliding force increases slightly with the g-level. Afterwards, the sliding force increases almost linearly with a higher increasing rate.

To further analyse the sliding force on the pile, two parameters proposed by Yoon (2008), A and B_{mob}, are adopted. The first parameter A describes the ratio of the resistance of the piles to the weight of the up-slope soil. The calculation of A is given in Appendix A. The second parameter B_{mob} expresses the equivalent pressure mobilised on the pile due to the interaction with soil, relative to the nominal overburden stress at the equivalent depth:

$$B_{mob}(z) = \frac{p(z)}{\sigma'_v(z)} \tag{4.3}$$

where z is the depth; $p(z)$ is the load per unit length divided by the pile diameter; $\sigma'_v = \gamma z$ where γ is the soil unit weight, the pore pressure is not considered. The soil pressure increases linearly with depth giving rise to a triangular pressure distribution, therefore B_{mob} can be assumed to be constant with depth. Hence an average value of B_{mob} along the pile section

above the slip surface (average B_{mob} in the following text) can be calculated by:

$$B_{mob}(z) = \frac{S_p}{\gamma h^2 d/2} \tag{4.4}$$

where S_p is the pile shear force at the depth of the slip surface; h is the thickness of the unstable soil layer; d is the pile diameter.

In some cases the measured soil pressure deviates from the linear distribution. The B_{mob} value at the middle of the pile upper section above the slip surface (middle B_{mob} in the following text), which is less affected by the upper and lower boundary of the soil layer, is also used in the analysis.

The variations of A and B_{mob} throughout the test are plotted in Figure 4.23b, 4.23c and 4.23d. In theory, both parameters should be approximately constant throughout the test. However, the resistance from the side walls and the slip surface could be relatively large at low g-level. There must be a time period at the early stage of the test (here from 1 g to about 20 g), in which A and B_{mob} increase with the g-level. At a high g-level, both parameters tend to stay constant. It is observed that the middle B_{mob} is more stable during the test than the average B_{mob}. The use of the middle B_{mob} could be more meaningful.

The maximum values of A and B_{mob} in the stable period are plotted in Figure 4.23e and 4.23f, respectively. The horizontal line CL2 in Figure 4.23e represents the theoretical estimation of the maximum value of A. It is calculated by $A_{max} = (1-\alpha)\sin\beta$, where α is the factor for friction from the boundaries and β is the inclination angle of the slip surface. It is seen that the measured A values of test A5P ($s/d = 3.10$) and A3P ($s/d = 5.17$) are very close to CL2, while the other two are far below. As discussed previously, the reason for that could be the extra resistance from the boundaries due to the asymmetry when an even number of piles are adopted. As commonly adopted in the literature (Yoon (2008)), a soil failure criteria, $B_{max} = {K_p}^2$, is used here as a theoretical estimation of the maximum B_{mob}, as shown by the line CL1 in Figure 4.23f. CL1 in Figure 4.23e and CL2 in Figure 4.23f are respectively derived from CL1 in Figure 4.23f and CL2 in Figure 4.23e through the equation $B_{max} = A_{max} 2(s/d)(l/h)$. It is seen that CL1 is above CL2 in the current s/d range, which implies that theoretically the maximum soil pressure on pile is not likely to be reached under the given s/d range and l/h value. In Figure 4.23f, both average and middle B_{mob} values are plotted and their differences are small because of the linear distribution of soil pressure in this test series. The middle B_{mob} has slightly increased with the increase of s/d. However, the measured B_{mob} has not reached the soil failure line (CL1: $B_{max} = {K_p}^2$), which is also expected since CL2 is far below CL1. According to the measured soil pressure on the pile, the flow failure between the piles is not likely to take place. However, observations from

some tests (A2P and A3P without instrumentation) have shown opposite conclusions which support another failure mechanism: with the current pile slenderness h/d, even though the pile can still be considered as a rigid pile, the pile top has experienced large displacement along the down-slope direction. When s/d becomes larger, the soil arching between the piles becomes less effective, especially in the pile top region, in which the arching effect may not form. Losing the support of the top region, the soil movement develops further to cause the failure of the whole layer. In the next section, a more flexible pile will be adopted. The ineffectiveness of the top part of the pile will be more apparent and its influence on the pile-soil interaction will be confirmed in another independent test series using shorter piles deeply buried in the slope.

Summary

Based on the test series A*i*P and A*i*P(SG), it can be obtained that, as the pile spacing s/d becomes larger (from 3.1 to 7.75), the overall soil displacement and the sliding force on the piles becomes larger, the failure mode changes from the down-slope failure to flow failure.

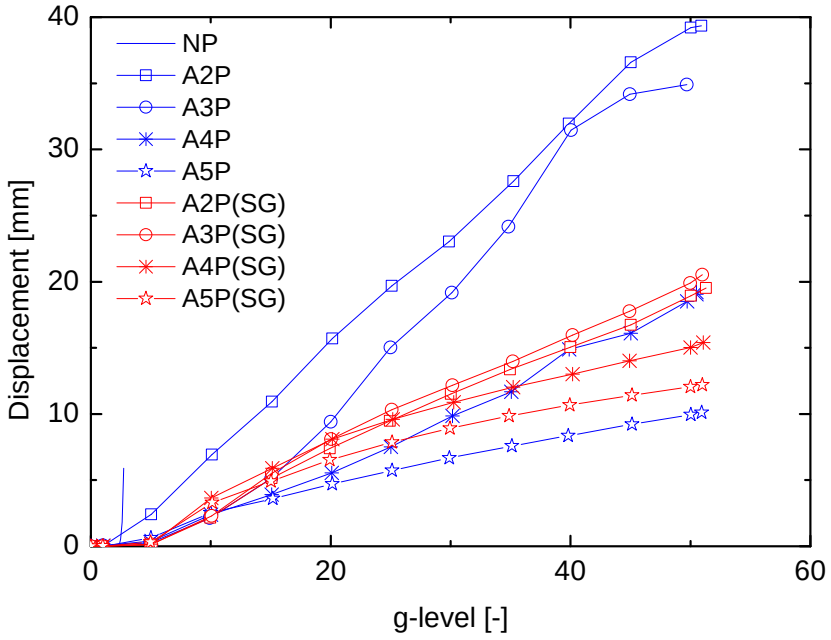

Fig. 4.15 PIV computed soil displacement at U1.

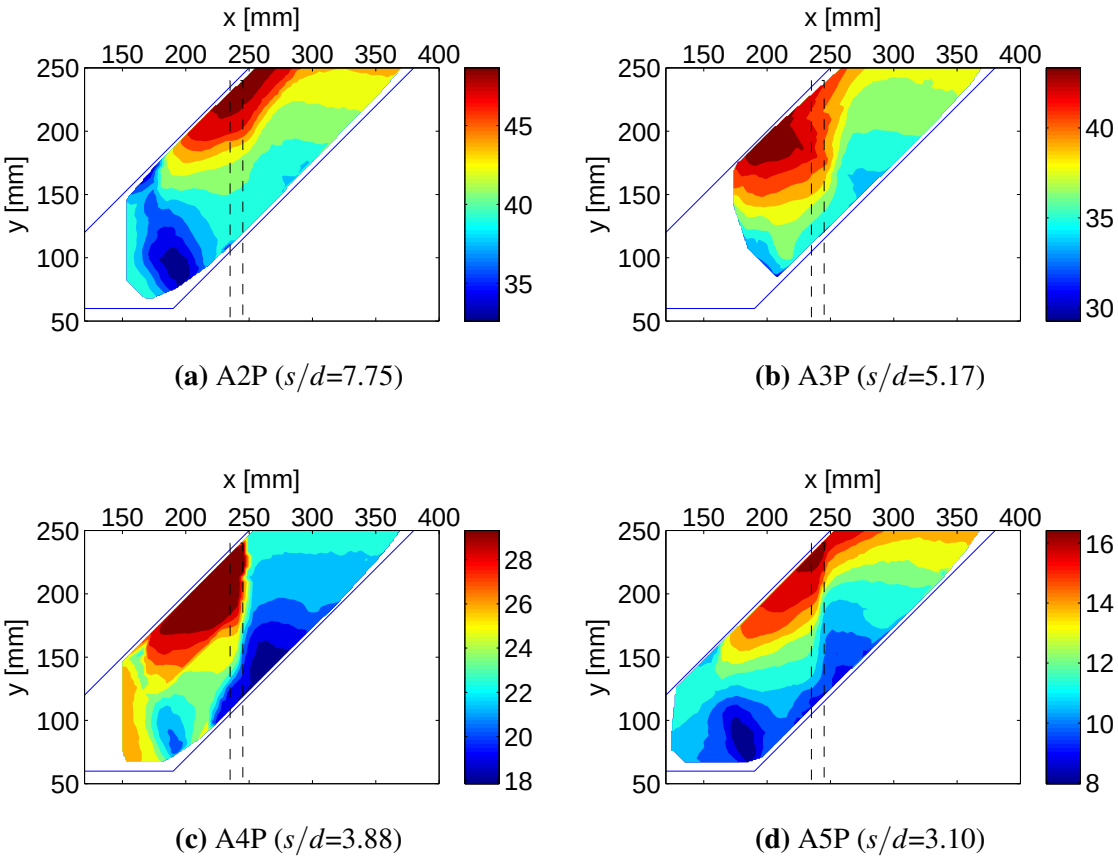

(a) A2P (s/d=7.75)

(b) A3P (s/d=5.17)

(c) A4P (s/d=3.88)

(d) A5P (s/d=3.10)

Fig. 4.16 PIV computed displacement (unit: mm) of the side-view at 50 g. Different displacement patterns: (a) and (b) are flow failure, (c) and (d) are down-slope failure. Note that the figures are not plotted in the same displacement range, the overall displacement in (a) and (b) is much higher. The initial pile location is marked by the dashed rectangle.

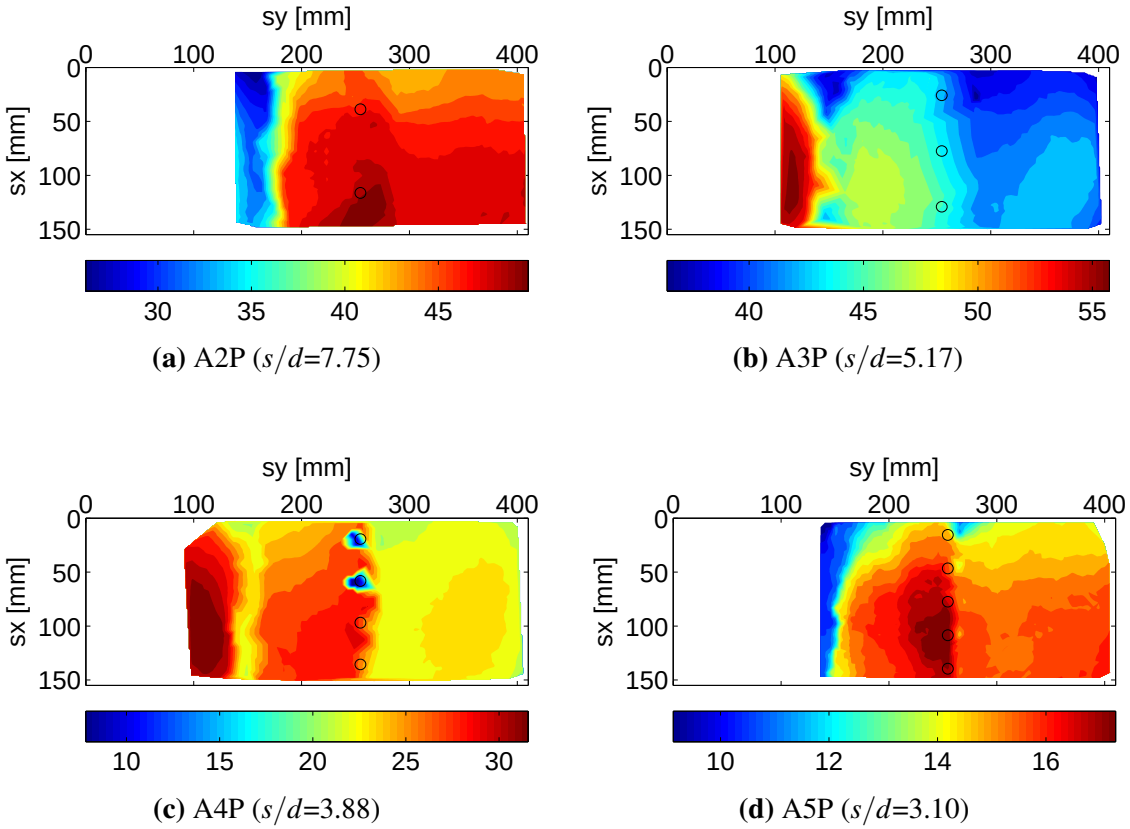

(a) A2P (s/d=7.75) **(b)** A3P (s/d=5.17)

(c) A4P (s/d=3.88) **(d)** A5P (s/d=3.10)

Fig. 4.17 PIV computed displacement (unit: mm) of the top-view at 50 g. Different displacement patterns: in (c) and (d) the down-slope displacement (left) is much higher than the up-slope (right). The initial pile location is marked by hollow circles. Note that sub-figure (b) and (c) are produced by single camera PIV.

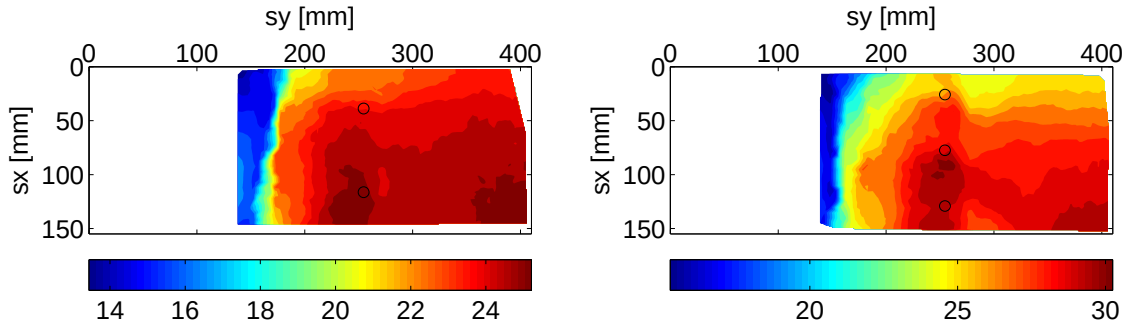

(a) A2P(SG) **(b)** A3P(SG)

(c) A4P(SG) **(d)** A5P(SG)

Fig. 4.18 PIV computed displacement (unit: mm) of the top-view at 50 g. Different displacement patterns: in (c) and (d) the down-slope displacement (left) is much higher than the up-slope (right). The initial pile location is marked by hollow circles.

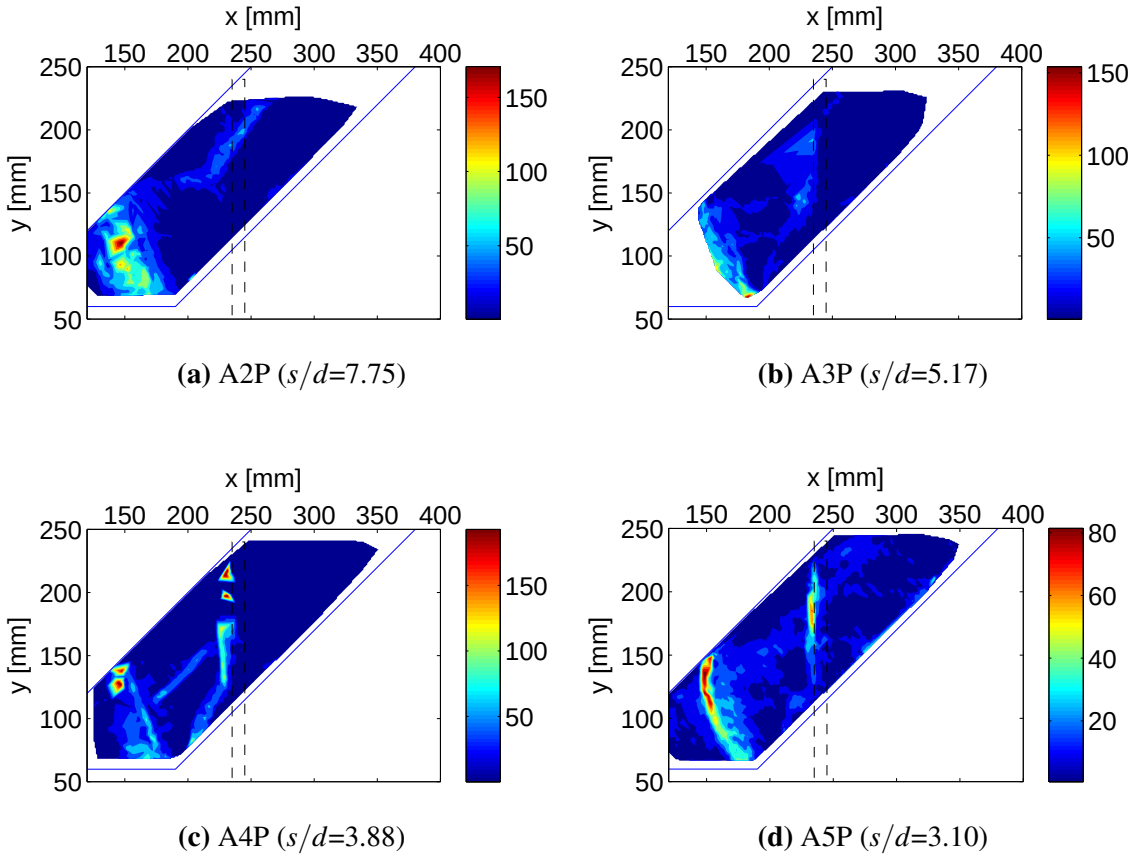

(a) A2P (s/d=7.75) **(b)** A3P (s/d=5.17)

(c) A4P (s/d=3.88) **(d)** A5P (s/d=3.10)

Fig. 4.19 Maximum shear strain (%) of the side-view at 50 g. Large shear strain is obtained at the pile row in (c) and (d). The dashed rectangle indicates the initial pile location.

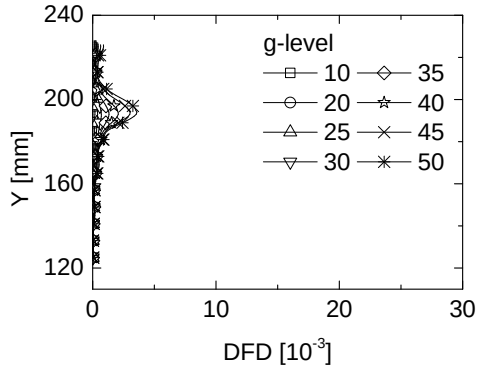

(a) DFD for Δx in test A2P (s/d=7.75)

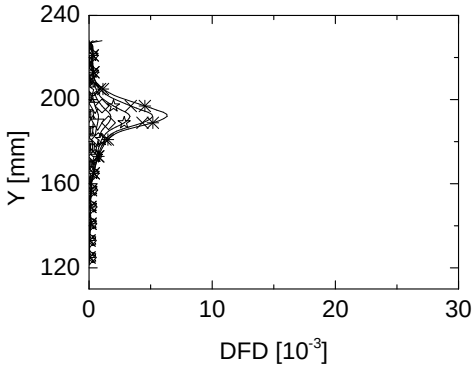

(b) DFD for Δy in test A2P (s/d=7.75)

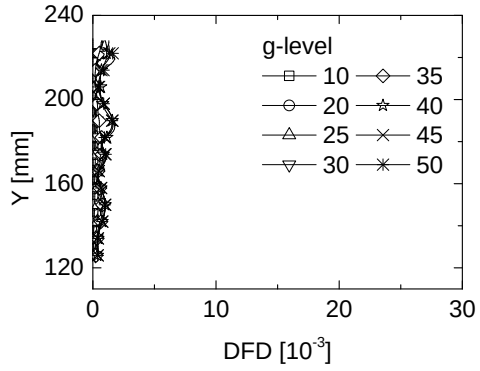

(c) DFD for Δx in test A3P (s/d=5.17)

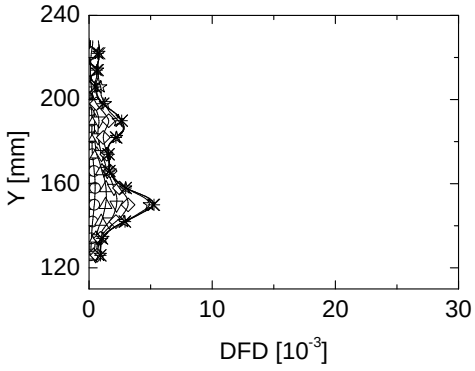

(d) DFD for Δy in test A3P (s/d=5.17)

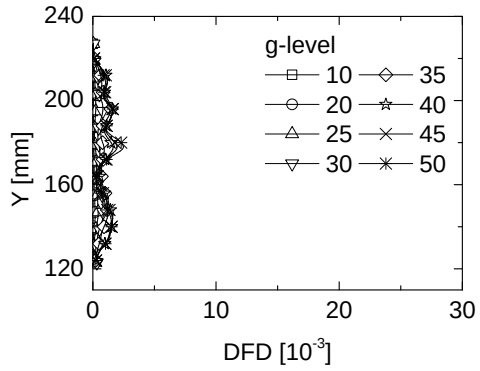

(e) DFD for Δx in test A4P (s/d=3.88)

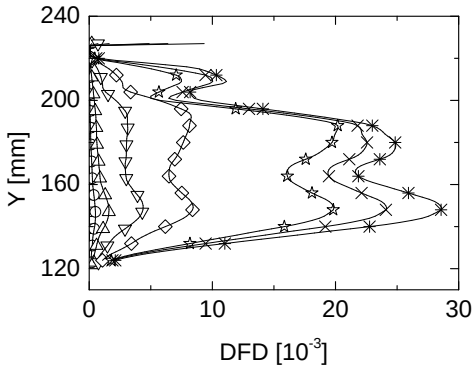

(f) DFD for Δy in test A4P (s/d=3.88)

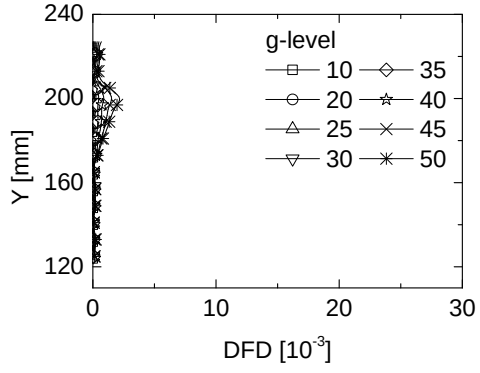

(g) DFD for Δx in test A5P (s/d=3.10)

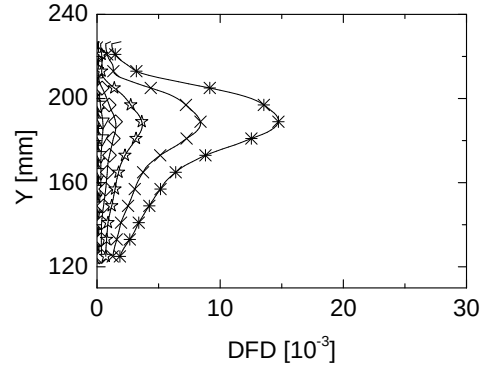

(h) DFD for Δy in test A5P (s/d=3.10)

Fig. 4.20 DFD for x- and y-displacements (Δx and Δy).

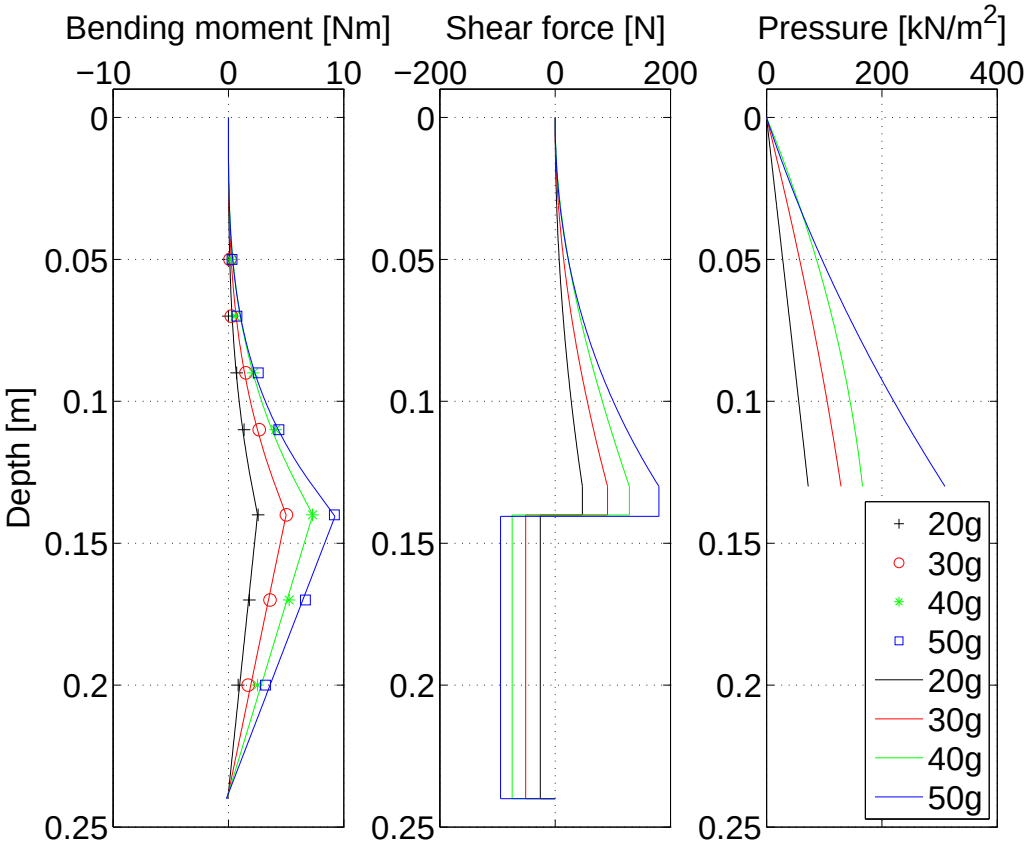

Fig. 4.21 Pile mechanical response from test A5P(SG). Continuous lines in the sub-figure of bending moment are fitting results of the strain gauge measurements. Shear force and pressure are derived from the fitted bending moment.

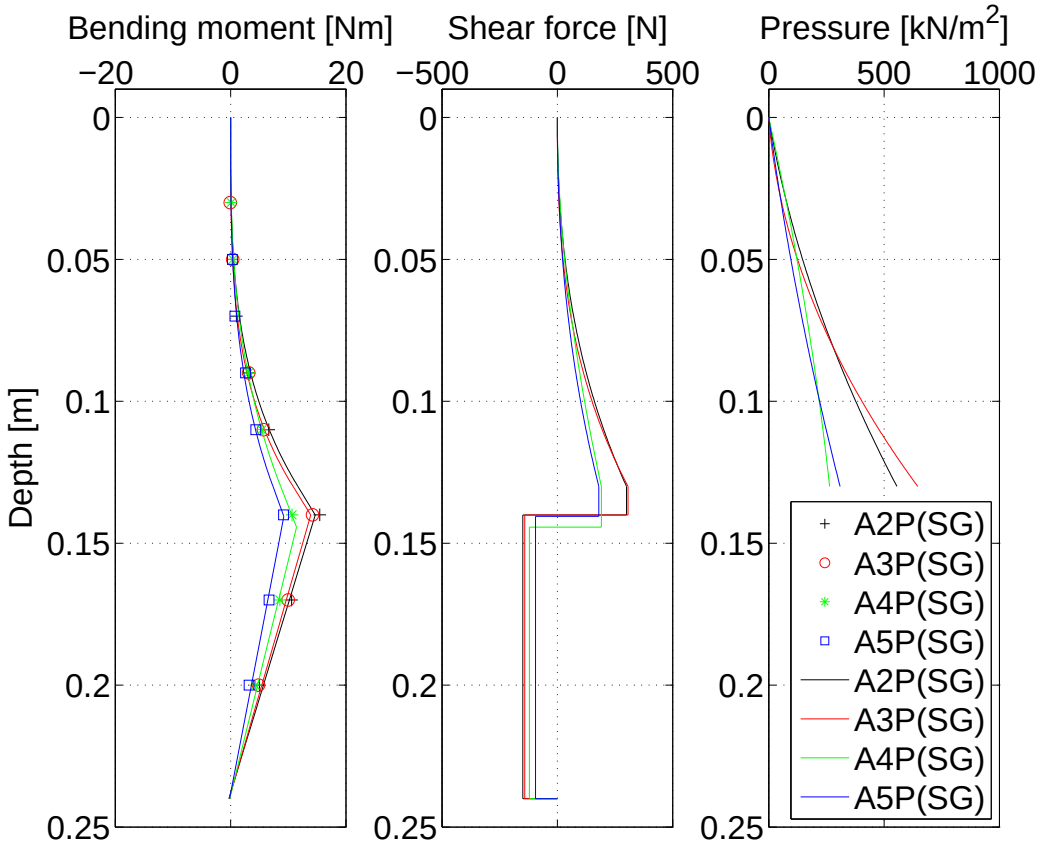

Fig. 4.22 Pile mechanical response from the test series A*i*P(SG) at 50 g. Continuous lines in the sub-figure of bending moment are fitting results of the strain gauge measurements. Shear force and pressure are derived from the fitted bending moment.

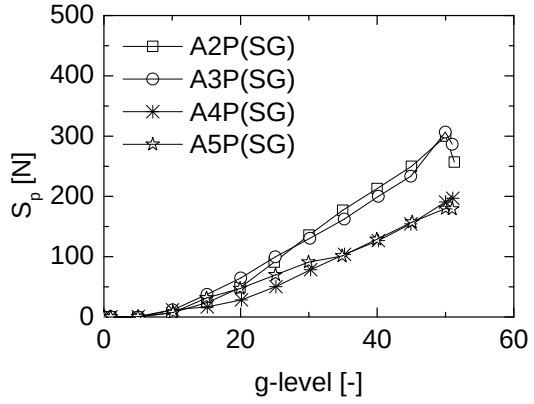

(a) sliding force on the pile

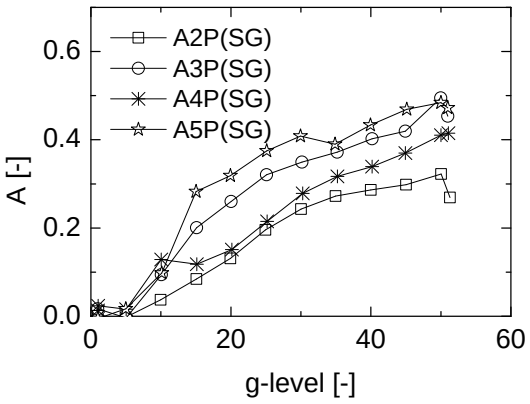

(b) variation of A

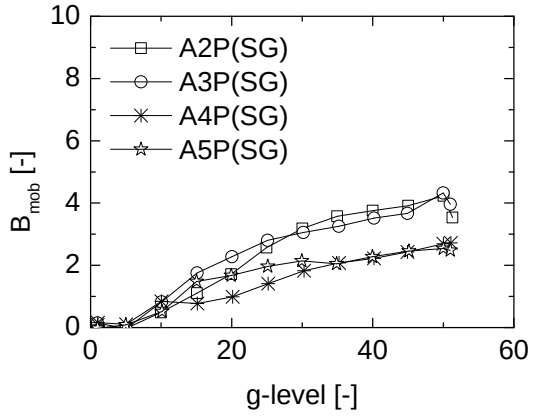

(c) average B_{mob}

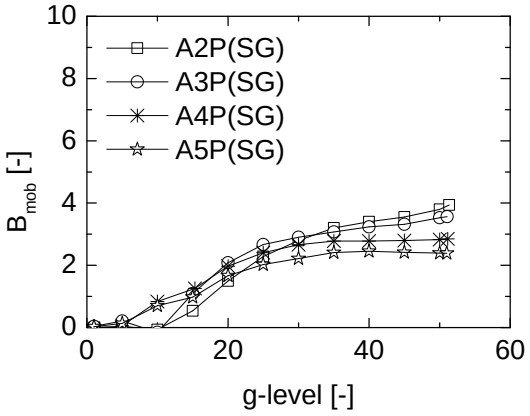

(d) middle B_{mob}

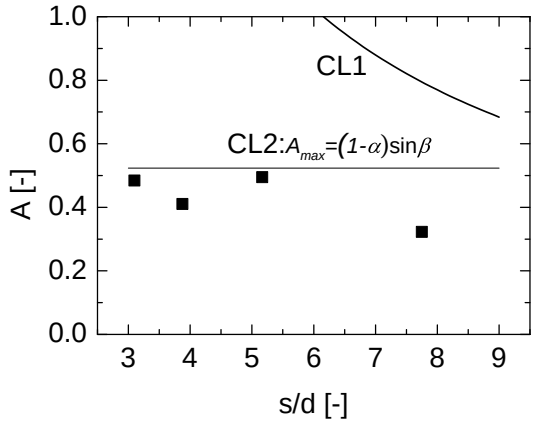

(e) variation of A with s/d

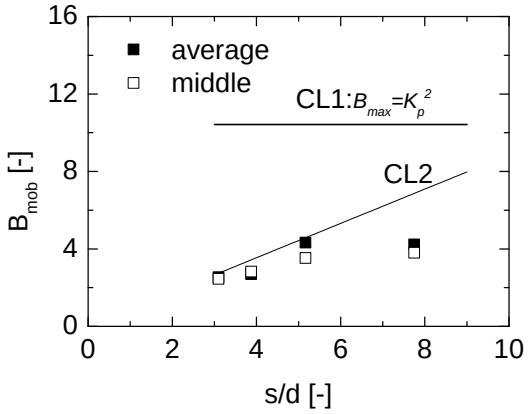

(f) variation of B_{mob} with s/d.

Fig. 4.23 Analysis of the sliding force on the pile. S_p: the sliding force on the pile; A: the ratio of the forces on the piles to the weight of the up-slope soil; B_{mob}: the equivalent soil pressure on the pile normalised by the overburden stress in terms of the average value and the value in the middle of the soil layer. CL1 in (e) and CL2 in (f) are respectively derived from CL1 in (f) and CL2 in (e) through the equation $B_{max} = A_{max} \cdot 2(s/d)(l/h)$.

4.5 The role of pile stiffness EI

Using the same configurations with AiP but with acrylic piles, a test series PiP (i=2, 3, 4, or 5) was conducted in order to examine the role of pile stiffness. All the model piles broke during the tests (except test P3P which was ended just before the breakage).

Displacement analysis

The soil displacements at U1 for all the tests are plotted in Figure 4.24 together with the results from test NP and the test series AiP. Similar to AiP, the soil displacement increases almost linearly with g-level. The larger the pile spacing, the larger the soil displacement. Generally, the soil displacement in the test series PiP is larger than the corresponding test in AiP. With the decrease of pile spacing, the g-level, at which the piles break, has increased from 21.5 g in test P2P to 50.3 g in test P5P. This also implies that the piles carry more force when the pile spacing is larger.

Figure 4.25 shows the displacement of the side-view of the four tests before the breakage of the piles. Different with the test series AiP (Figure 4.16), displacement discontinuity is only observed from nearly half the soil thickness to the slip surface at the pile row. The up-slope failure (over-top failure) and down-slope failure have joined at the pile row from the soil surface to nearly half the soil thickness. The corresponding displacement of the surface is presented in Figure 4.26, which also shows no discontinuity of displacement at the pile row. On the contrary, some small zones in the down-slope near the piles have larger displacements than the surrounding soil due to the large deformation of the acrylic piles. In the perspective of stabilizing the up-slope, the upper section of the pile (from the pile top to nearly half the soil thickness) is ineffective.

Deformation analysis

Figure 4.27 shows the corresponding maximum shear strain of the side-view. As observed in many of the tests, the largest strain value is found in the slope toe area. In the up-slope of tests P3P, P4P and P5P, a shear band parallel to the slip surface is formed. At the pile row, the shear band turns vertical and extends downwards to meet the slip surface. The formation of the shear band is affected by the pile spacing. As the pile spacing becomes smaller, a clearer and more consistent shear band is obtained. Such a shear band is not observed in test P2P.

In order to illustrate the shear deformation in the soil, DFD for the horizontal (x) and vertical (y) displacements (Δx and Δy) along two vertical lines (one at the pile row $x = 240$ mm and the other at $x = 280$ mm in the up-slope) are presented in Figure 4.28 and 4.29. For test P2P, similar to the observation from the shear strain, DFD remains unchanged on both

lines. For the other tests, on the vertical line $x = 240$ mm (also the pile location), the increase of DFD is observed mainly below $y = 200$ mm. The increment of DFD for Δy is larger than that for Δx, especially when the high g-level can be reached (P5P). The location and direction of DFD increment correspond well with the vertical shear band in Figure 4.27. On the vertical line $x = 280$ mm (in the up-slope), the increase of DFD is observed mainly above $y = 220$ mm. The increment of DFD for Δx is slightly larger than that for Δy, which means that the shear direction is about 45° inclined (parallel to the slip surface). The maximum DFD before failure seems not to be affected by the pile spacing. On this vertical line, the location and direction of the DFD increment correspond well with the shear band in the up-slope.

In comparison with A*i*P

Comparing the test series P*i*P with A*i*P, it is concluded that the pile stiffness EI has a great influence on the pile-soil interaction. Under the circumstance that a small pile spacing is adopted to avoid flow failure, the down-slope failure is the main failure mode when stiff piles are used (A*i*P). The up-slope can be well stabilized with more effective reinforcement along the pile length. On the contrary, due to the large deformation of the flexible piles, the top part of the piles becomes ineffective. Only the lower part of the pile in the sliding soil contributes to the reinforcement. The over-top soil movement in the up-slope has merged with the down-slope soil movement. The general stability of the piled slope is reduced.

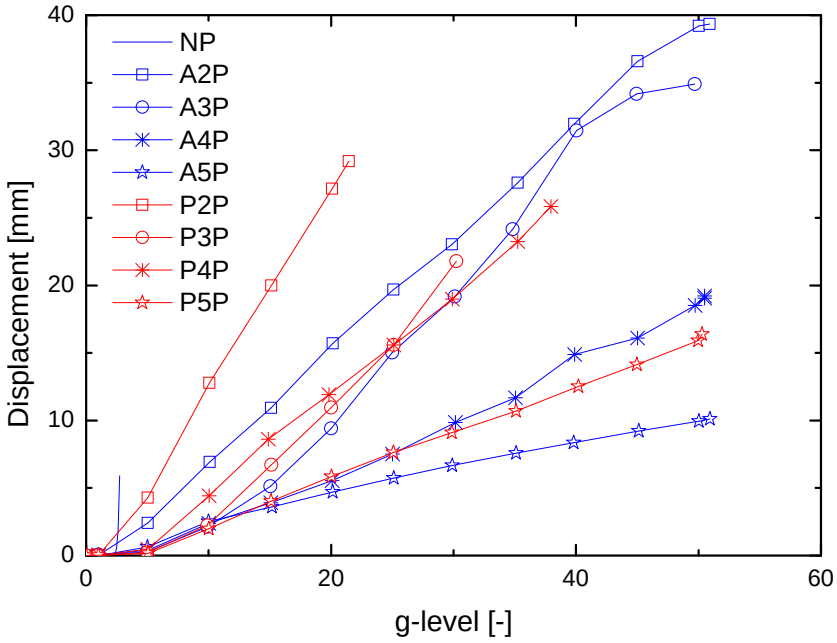

Fig. 4.24 PIV computed soil displacement at U1.

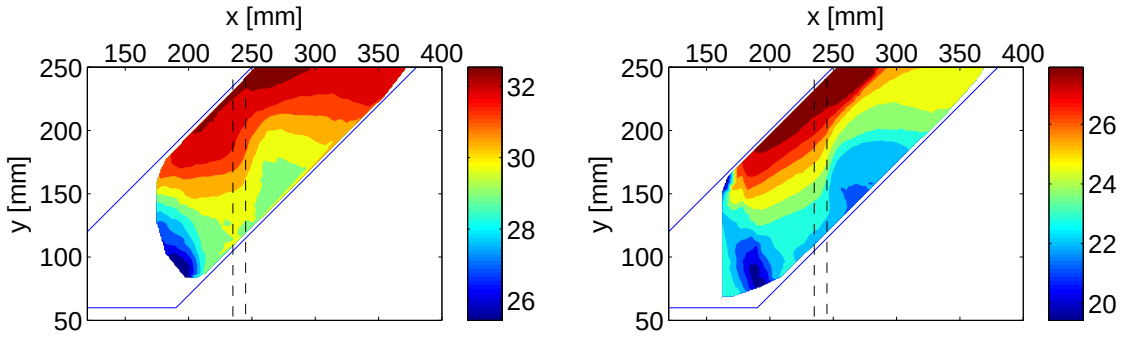

(a) P2P (s/d=7.75) at 21.5 g **(b)** P3P (s/d=5.17) at 30.2 g

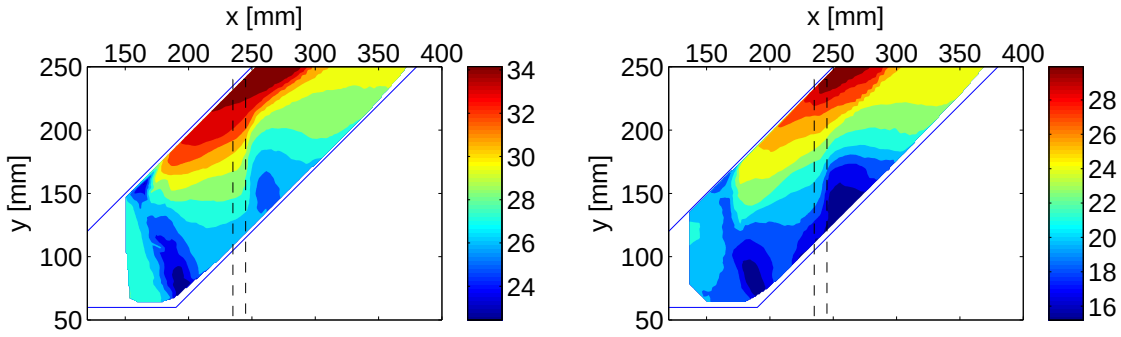

(c) P4P (s/d=3.88) at 37.9 g **(d)** P5P (s/d=3.10) at 50.3 g

Fig. 4.25 PIV computed displacement (unit: mm) of the side-view. Up-slope soil movement and down-slope soil movement have joined at the pile row from the surface to about half the soil thickness. The dashed rectangle indicates the initial pile location.

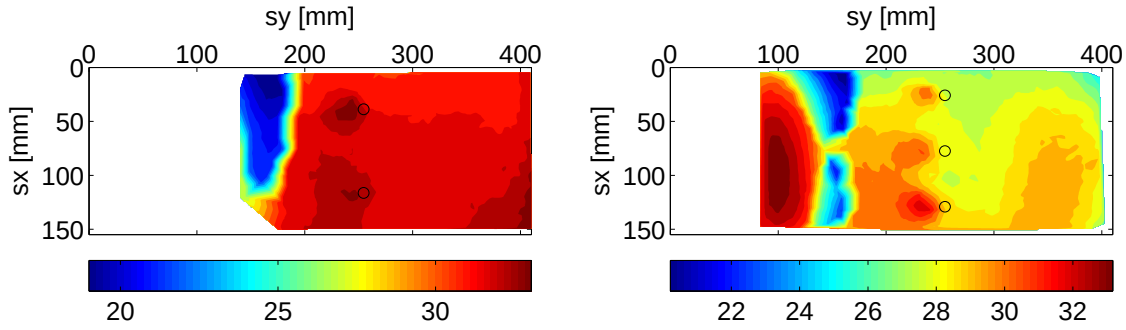

(a) P2P (s/d=7.75) at 21.5 g

(b) P3P (s/d=5.17) at 30.2 g

(c) P4P (s/d=3.88) at 37.9 g

(d) P5P (s/d=3.10) at 50.3 g

Fig. 4.26 PIV computed displacement (unit: mm) of the top-view. Continuous soil displacement at the pile row. Regional larger displacements are observed in the down-slope side (left) of the piles. The initial pile location is marked by hollow circles. Note that (b) and (c) are produced by single camera PIV analysis.

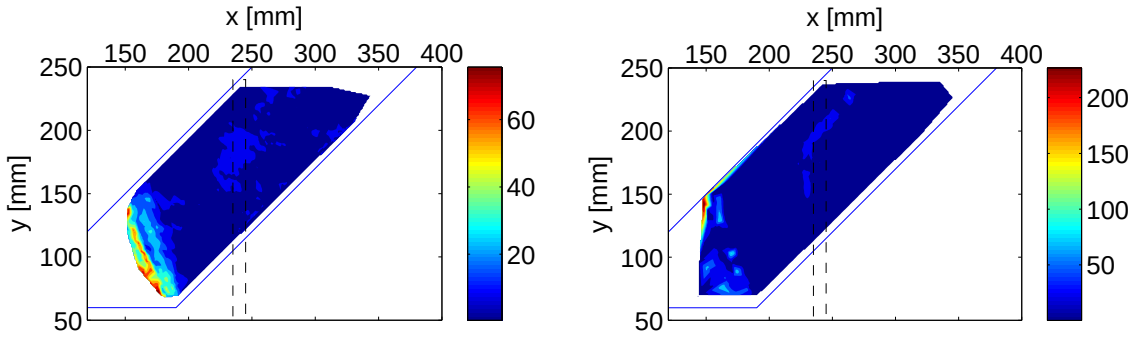

(a) P2P (s/d=7.75) at 21.5 g

(b) P3P (s/d=5.17) at 30.2 g

(c) P4P (s/d=3.88) at 37.9 g

(d) P5P (s/d=3.10) at 50.3 g

Fig. 4.27 PIV computed maximum shear strain (%) of the side-view. Shear band is observed in (b), (c) and (d). The dashed rectangle indicates the initial pile location.

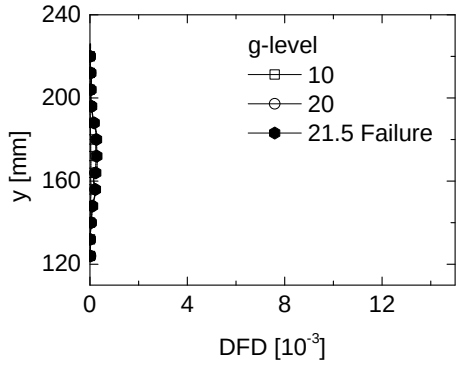

(a) DFD for Δx in test P2P (s/d=7.75)

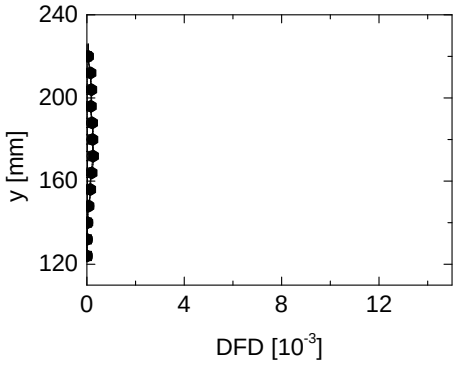

(b) DFD for Δy in test P2P (s/d=7.75)

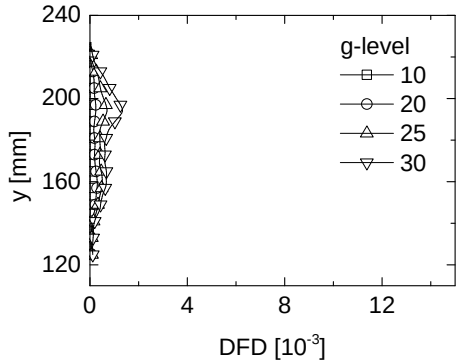

(c) DFD for Δx in test P3P (s/d=5.17)

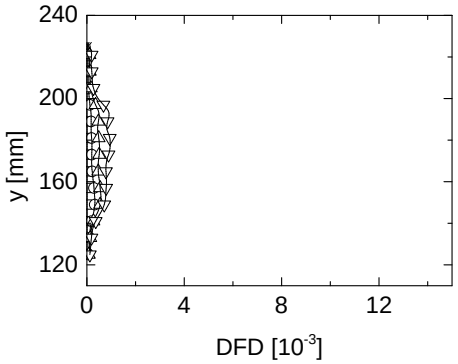

(d) DFD for Δy in test P3P (s/d=5.17)

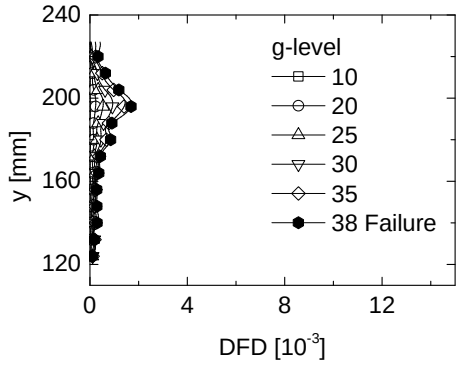

(e) DFD for Δx in test P4P (s/d=3.88)

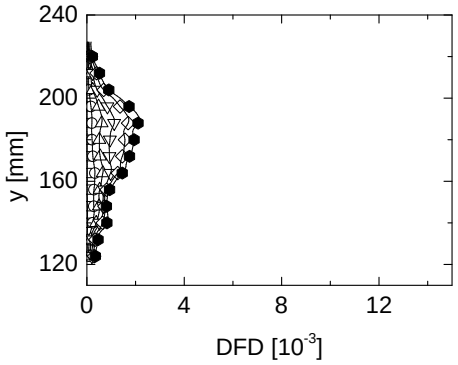

(f) DFD for Δy in test P4P (s/d=3.88)

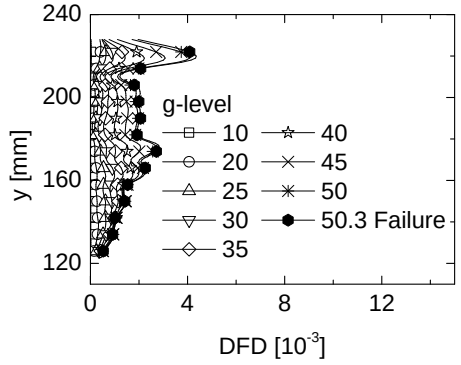

(g) DFD for Δx in test P5P (s/d=3.10)

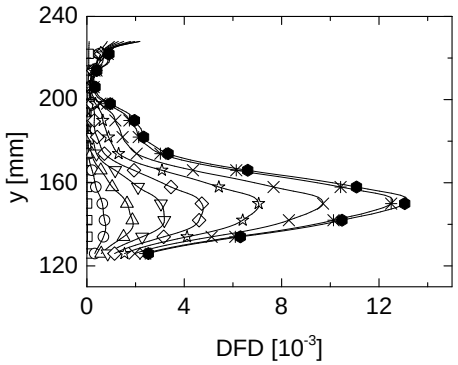

(h) DFD for Δy in test P5P (s/d=3.10)

Fig. 4.28 DFD for x- and y-displacements (Δx and Δy) at $x = 240$ mm.

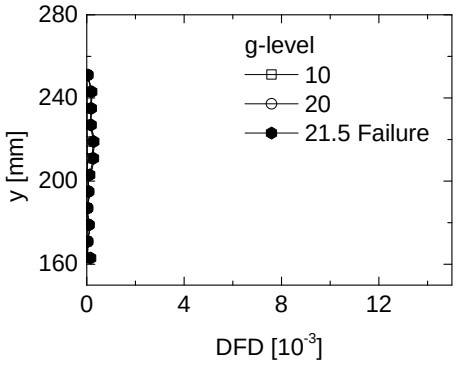

(a) DFD for Δx in test P2P (s/d=7.75)

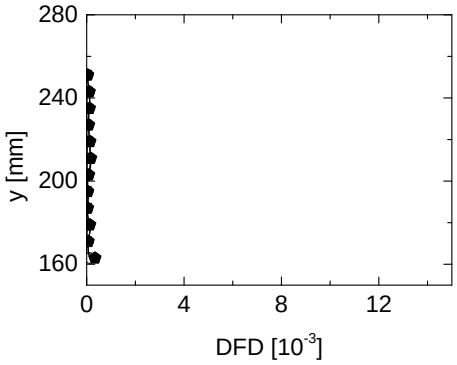

(b) DFD for Δy in test P2P (s/d=7.75)

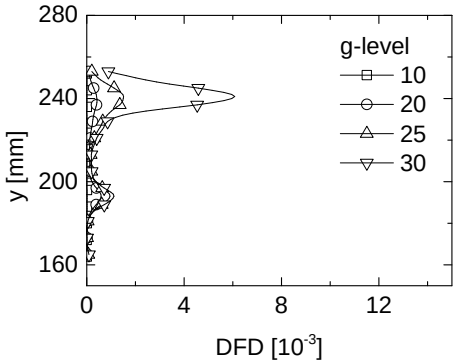

(c) DFD for Δx in test P3P (s/d=5.17)

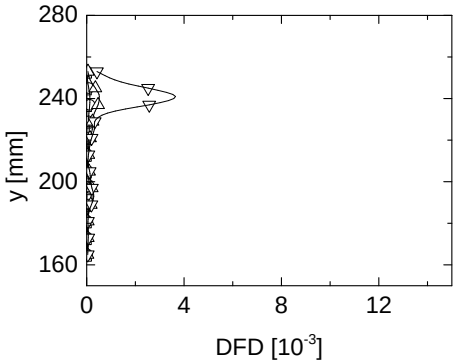

(d) DFD for Δy in test P3P (s/d=5.17)

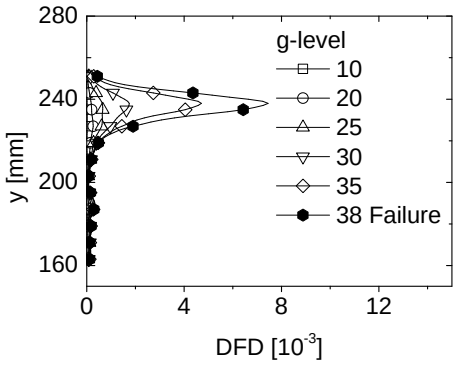

(e) DFD for Δx in test P4P (s/d=3.88)

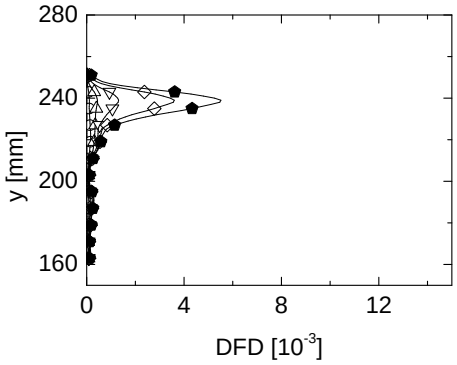

(f) DFD for Δy in test P4P (s/d=3.88)

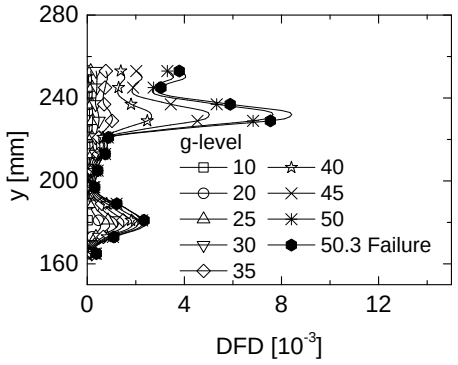

(g) DFD for Δx in test P5P (s/d=3.10)

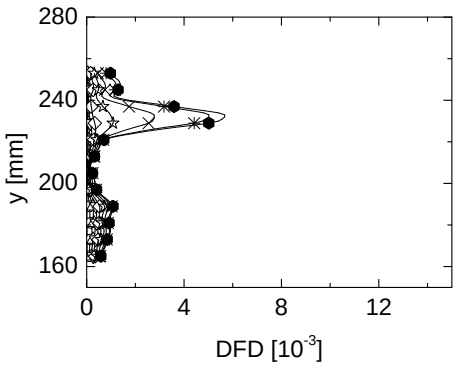

(h) DFD for Δy in test P5P (s/d=3.10)

Fig. 4.29 DFD for x- and y-displacements (Δx and Δy) at $x = 280$ mm.

4.6 The role of pile slenderness h/d

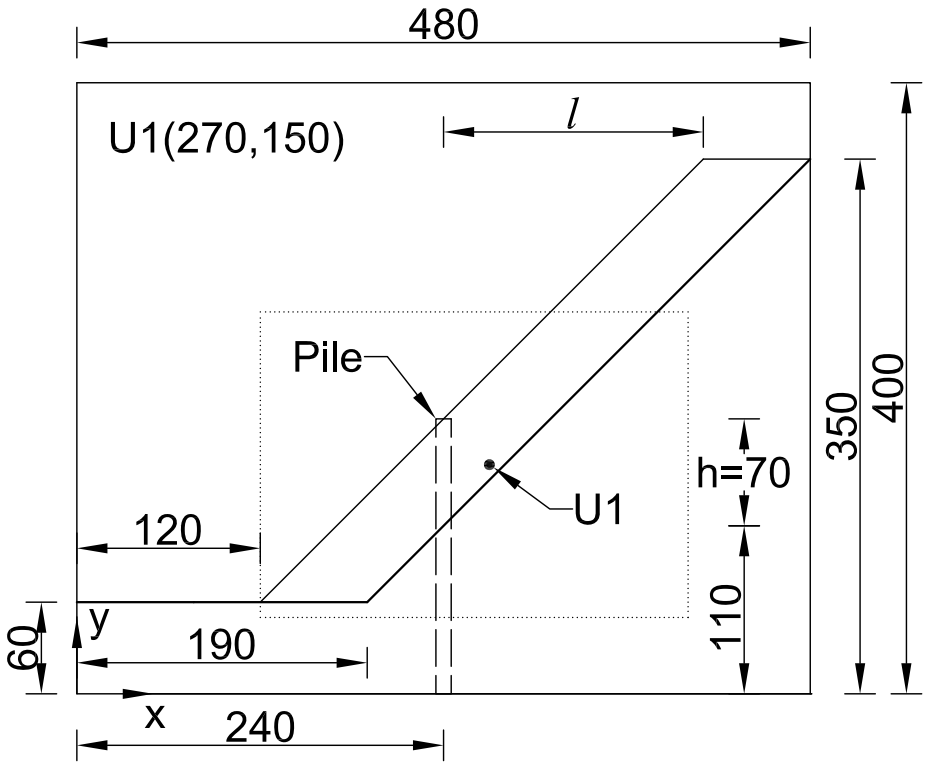

Fig. 4.30 Geometry of the model in the cross-sectional view (unit: mm). The dotted rectangle indicates the area where PIV analysis is applied. U1 is a monitoring point whose displacement is used to represent the movement of the rubber sheet.

Pile slenderness, which in this study means the ratio of the pile length above the slip surface h to the pile diameter d, can also significantly influence the pile-soil interaction. Concerning the flexible pile behaviour in the test series AiP and PiP ($h/d = 13$), two test series (AiPSL where i = 2, 3, 4 or 5, and PiPSL where i = 4 or 5) adopting a smaller pile slenderness ($h/d = 7$) were conducted to study the effect of h/d. Figure 4.30 shows the cross-sectional geometry for this two test series.

Displacement and deformation analysis for AiPSL

The observed failures in the test series AiPSL are similar to the test series AiP, which experienced 'flow failure' at large pile spacings and 'down-slope failure' at small pile spacings. Difference is found in the cases with a small pile spacing, in which the 'over-top failure' in the up-slope has emerged and become the leading soil movement.

Figure 4.31 shows the displacement at U1, which denotes the overall movement of the up-slope soil. The U1 displacement increases almost linearly with g-level before failure. Generally, the larger the pile spacing, the larger the U1 displacement. The turning point at which the U1 displacement starts to increase rapidly is observed in tests A2PSL, A3PSL and A4PSL. However, these tests differ in the failure mechanism.

Figure 4.32 shows the soil displacement in the side-view before failure or at 50 g. The corresponding movement of the soil surface and the maximum shear strain of the side-view are shown in Figure 4.33 and 4.34, respectively. In test A2PSL, no displacement discontinuity is observed between the up-slope and down-slope from both the side and top views. The shear strain (Figure 4.34a) also shows that the soil layer has moved entirely. For the other tests in this series, the up-slope has a much larger displacement than the down-slope, especially in the shallow part of the up-slope. From the side-view, the up-slope soil tends to slide along a second slip surface, which starts at the pile top and extends inwards and upwards to meet the predefined slip surface. This failure mode is defined as the 'over-top failure'. From the maximum shear strain, two shear bands are observed in tests A4PSL and A5PSL. The first shear band extends from the pile top to the slip surface (the deep shear band) while the second one extends from the pile top to the up-slope with a small angle to the slope surface (the shallow shear band). The deep shear band starts to form at a low g-level while the shallow shear band is formed just before failure. As discussed previously, the restriction of the rubber sheet is responsible for this phenomenon. In the down-slope, the tendency of 'down-slope failure' is more visible in test A5PSL, in which a vertical shear band is observed at the pile row (Figure 4.34d). The failure observed in test A4PSL starts with an over-top failure which helps trigger the down-slope failure and finally results in the further large movement of the entire soil layer. This is confirmed by the further analysis of soil deformation using DFD.

Figure 4.35 and 4.36 display the DFD along a vertical line locating at the pile location ($x = 240$ mm, note that for some tests the data at $x = 245$ or 250 mm is used depending on where the maximum DFD is obtained) and $x = 280$ mm, respectively. In test A2PSL, DFD remains unchanged in both directions and on both lines. in test A5PSL, DFD increases slightly before about 40 g, after which the DFD for Δy at the pile location and the DFD for Δx in the upper part of the line at $x = 280$ mm increase significantly. On the line at $x = 245$ mm, the DFD increment for Δy is almost uniform along the depth. Its magnitude is much larger than the corresponding DFD for Δx, which means that the shear deformation is vertically oriented. However, the DFD for Δx has also increased in the pile top region (upper part of the line at $x = 245$ mm) after 40 g due to the soil movement in the up-slope. We can deduce from the magnitude of DFD that the influence of the up-slope movement on the down-slope movement for test A5PSL is at the moment small.

On the contrary, in test A4PSL on the line at the pile row (in this test the line at $x = 250$ mm is chosen), the DFD increment for Δy is much smaller than the corresponding increment for Δx. The DFD increments for both Δx and Δy before failure are more focused in the shallow soil. Besides, the DFD for Δx in test A4PSL on the line at $x = 280$ mm is even larger than in test A5PSL, which is reasonable since failure is observed in test A4PSL at 48.9 g. It is concluded that the occurrence of failure in test A4PSL is due to the over-top failure in the up-slope. Similar failure is expected for test A5PSL if the g-level goes higher than 50 g. For test A3PSL, even though a large increment of DFD for Δx in the pile head region is observed, neither the vertical shear deformation at the pile location nor a clear direction of shear deformation in the up-slope is detected. This result is expected since the 'flow failure' occurs with this pile spacing as analysed previously. However, the soil deformation detected in test A3PSL also distinguishes this test from A2PSL. The influence of the up-slope movement cannot be ignored.

Comparing the test series A*i*PSL with A*i*P, it is observed that when the pile spacing is small, the dominant failure mode in the test series A*i*PSL is over-top failure while in the test series A*i*P is down-slope failure. However, it can be argued that the emergence of the over-top failure mode can also be due to the relatively larger up-slope length ratio l/h, which will be discussed in the next section. The decrease in h/d has increased the relative pile rigidity. In order to confirm the influence of the relative pile rigidity on the over-top failure in the up-slope. The test series P*i*PSL (i = 4 and 5) with acrylic piles are useful.

Displacement and deformation analysis for P*i*PSL

The results of the test series P*i*PSL are presented from Figure 4.37 to 4.41. The displacement of the side-view (Figure 4.37) shows that the up-slope has mainly experienced large compaction along the slip surface instead of moving over the pile top as observed in the test series A*i*PSL. Displacement discontinuity is observed at the pile row,which is also confirmed by the surface soil displacement (Figure 4.38). Large soil displacement is observed in both up- and down-slopes from the surface soil displacement. However, the soil displacement in the up-slope reduces as its location is closer to the pile row. The reinforcement of the piles to the up-slope in test P5PSL is stronger than in test P4PSL. As shown in Figure 4.39, a vertical shear band is formed at the pile row while such shear band in the up-slope, which is observed in the test series A*i*PSL, is not formed. DFD results have also confirmed the observations above. Figure 4.40 shows the DFD along the vertical line at $x = 245$ mm (5 mm to the up-slope direction). Large increment of DFD for Δy is observed for both tests, which corresponds to the vertical shear band in Figure 4.39. Note that large increment of DFD for Δx is also observed in the pile head region (shallow part of the line at $x = 245$ mm),

which could be caused by the large l/h. Figure 4.41 shows the DFD along the vertical line at $x = 280$ mm. DFD increment is small compared to the DFD observations at the pile row or at the same position in tests A4PSL and A5PSL.

It can be concluded that 'down-slope failure' is the main failure mode for the test series P*i*PSL. By comparing P*i*PSL with P*i*P, the role of pile slenderness is revealed. From the slenderness ratio of 13 in P*i*P to 7 in P*i*PSL, the pile behaviour has jumped into the category of rigid piles. The slenderness ratio has significant influence on the relative pile rigidity. The definition of the pile flexibility factor K_R in equation 4.1 is confirmed because the test series A*i*P and P*i*PSL (*i*=4 and 5), which shares the similar values of K_R, have the similar soil movements. By comparing P*i*PSL with A*i*PSL, which has a higher pile bending stiffness, a conclusion about the effect of pile stiffness can be drawn: the over-top failure mode is more likely to occur when stiffer piles are placed with a small spacing.

Analysis of strain gauge measurements in A*i*PSL

Figure 4.42 shows the analysis of the sliding forces on the pile of the test series A*i*PSL. As shown in Figure 4.42a, for test A5PSL, A4PSL and A3PSL, the sliding force on the pile (S_p) increases almost linearly with g-level after about 20 g. As observed in the soil displacement, test A5PSL did not fail before 50 g and tests A4PSL, A3PSL and A2PSL failed at 48.9 g, 46.7 g and 21.5 g, respectively. However, only the failure of test A2PSL is reflected in the S_p curve, which is interrupted at about 30 g and is about 8.5 g delayed to the observation of displacement. This relates to the failure mode of soil. For the tests with the over-top failure mode (A4PSL and A5PSL, note that the soil movement in test A3PSL is also influenced by the tendency of over-top failure), although a part of the soil in the up-slope has moved across the pile row, the soil-pile interaction remains in a state that has not reached the critical. For test A2PSL, the flow failure is bound to affect the soil-pile interaction. With respect to the magnitude, the sliding force becomes larger as the pile spacing increases. This does not apply to test A3PSL, which shows no difference to test A4PSL. The reason could be the transition of failure mode from the flow failure to the over-top failure.

The variations of A, average and middle B_{mob} throughout the tests are displayed in Figure 4.42b, 4.42c and 4.42d, respectively. For test A5PSL, these three parameters increase continuously throughout the test, which implies that the soil-pile interaction has not reached a stable state and is being mobilized. For the other tests, stable values can be observed at the high g-level. As the soil layer thickness is much smaller than the test series A*i*P, the influence of soil boundaries (the ground surface and the slip surface) on the soil pressure distribution has become larger. It is observed that the middle B_{mob} varies less than the average B_{mob}.

The values of A and B_{mob} before failure or at 50 g are plotted against s/d in Figure 4.42e and 4.42f, respectively. The estimation for the maximum A and B_{mob} and their derivations to each other are also plotted as lines and curves in the figures. CL1 and DL1 in Figure 4.42f coincide with each other and represent the soil failure criteria: $B_{max} = {K_p}^2$; CL2 and DL2 in Figure 4.42e represent the estimation $A_{max} = (1-\alpha)\sin\beta$ for the test series AiP and AiPSL, respectively; CL1, DL1 in Figure 4.42e and CL2, DL2 in Figure 4.42f are respectively derived from CL1, DL1 in Figure 4.42f and CL2, DL2 in Figure 4.42e through the equation $B_{max} = A_{max} \cdot 2(s/d)(l/h)$. Different from A$i$P, for the test series A$i$PSL, the soil failure line (DL1) is below the line of the theoretical A_{max} (DL2), which allows the ultimate soil pressure to be reached in tests A4PSL, A3PSL and A2PSL. However, it is observed that only the middle B_{mob} of test A2PSL (s/d=7.75) is above the soil failure line (DL1), which corresponds to the observation of flow failure. For test A4PSL, the failure mode is over-top failure, in which the soil failure does not cause the failure of soil-pile interaction. For test A3PSL, the reason for a small B_{mob} could also be the the soil deformation in the up-slope as described previously.

Summary

By adopting a smaller pile slenderness h/d (from 13 to 7), the relative pile stiffness K_R is increased. The piles have less displacement, therefore a stronger arching effect between the piles is formed and relative higher soil pressure is mobilised. Besides, over-top failure mode is observed when aluminium piles are placed with a small spacing. However, arguments can be made that the emergence of the over-top failure mode is due to the large l/h, which will be confirmed in the next section.

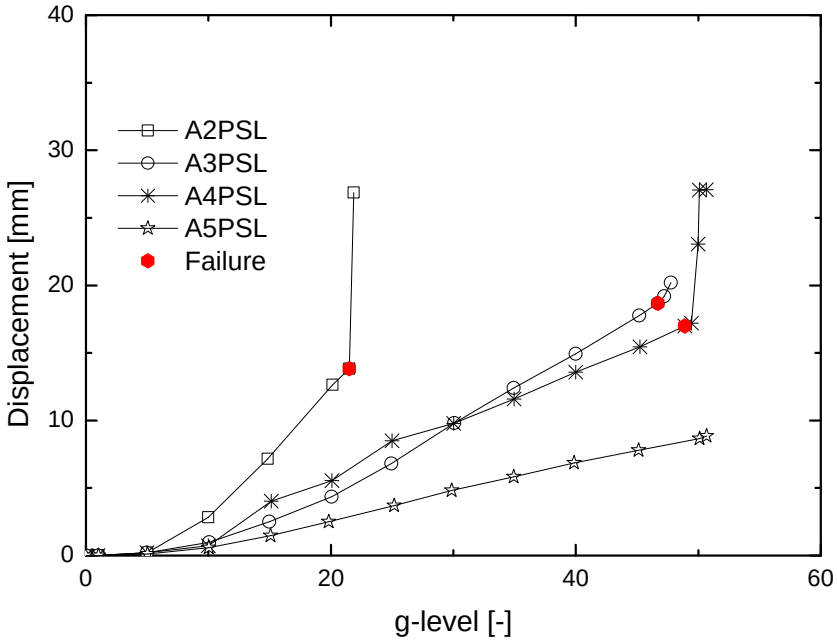

Fig. 4.31 PIV computed soil displacement at U1.

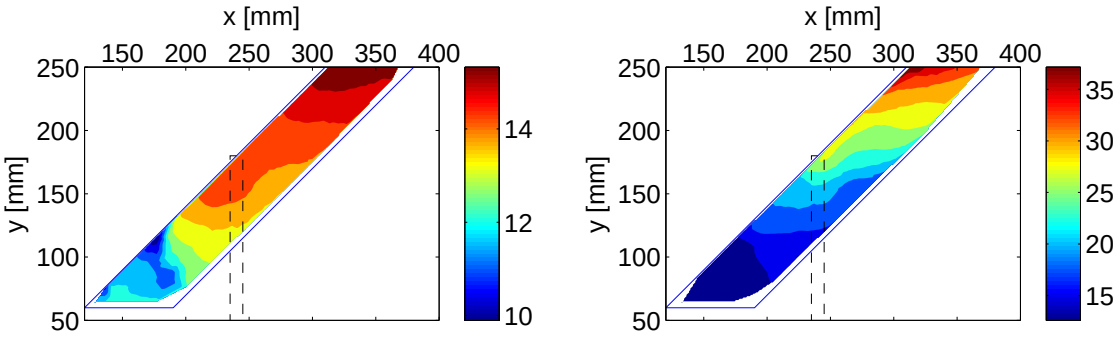

(a) A2PSL (s/d=7.75) at 21.5 g

(b) A3PSL (s/d=5.17) at 46.7 g

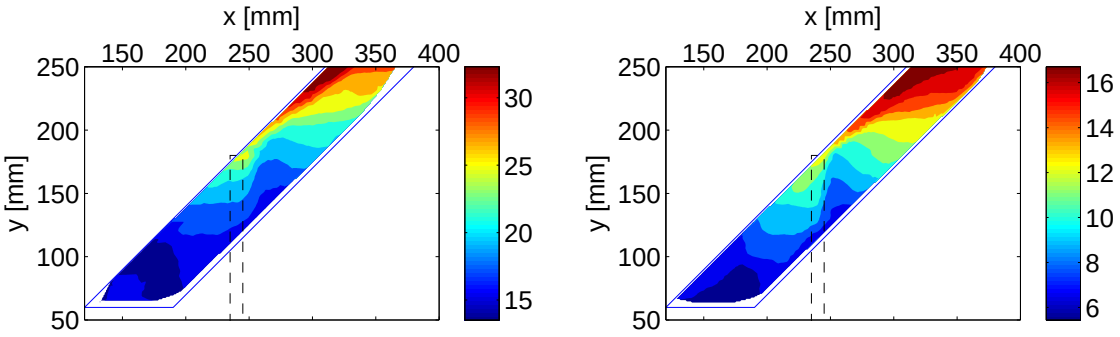

(c) A4PSL (s/d=3.88) at 48.9 g

(d) A5PSL (s/d=3.10) at 50 g

Fig. 4.32 PIV computed displacement (unit: mm) of the side-view. Soil movement pattern varies from flow failure (a) to over-top failure (d). The dashed rectangle indicates the initial pile location.

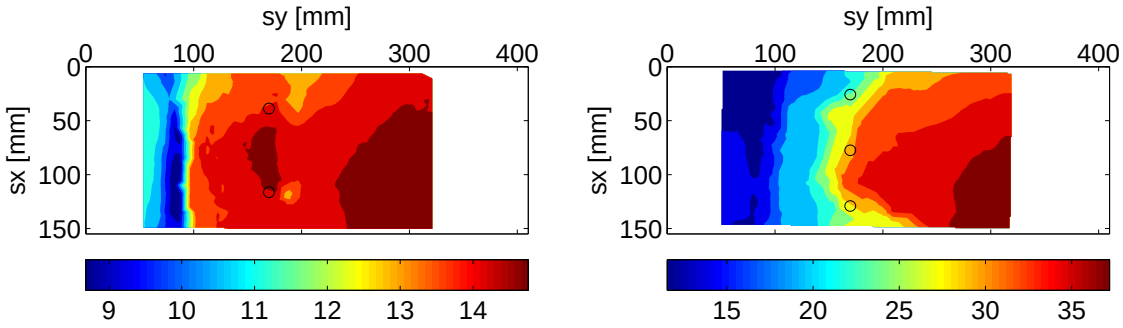

(a) A2PSL (s/d=7.75) at 21.5 g **(b)** A3PSL (s/d=5.17) at 46.7 g

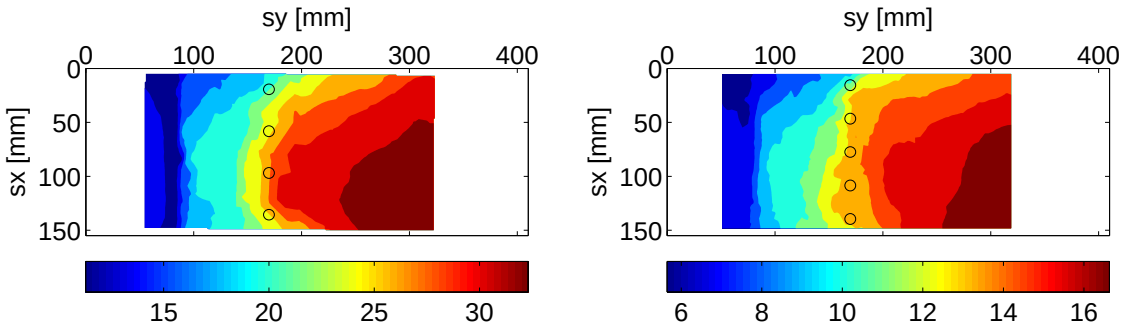

(c) A4PSL (s/d=3.88) at 48.9 g **(d)** A5PSL (s/d=3.10) at 50 g

Fig. 4.33 PIV computed displacement (unit: mm) of the top-view. Larger surface soil displacement in the up-slope (right) is observed in (b), (c) and (d). The initial pile locations are marked by hollow circles.

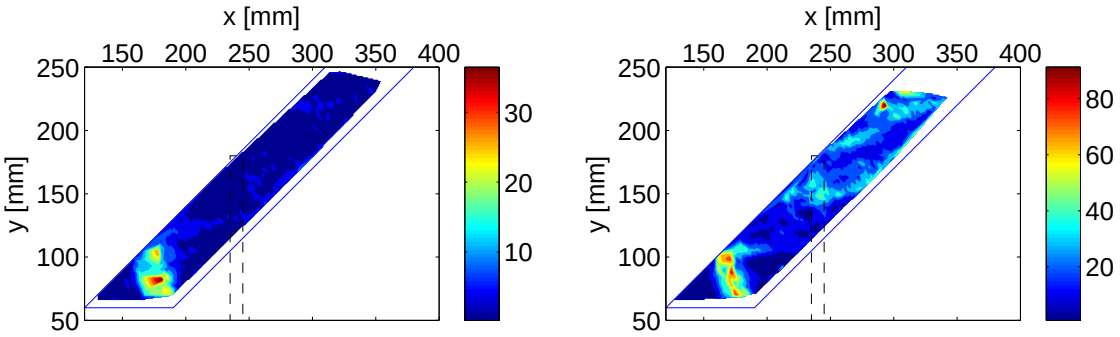

(a) A2PSL (s/d=7.75) at 21.5 g **(b)** A3PSL (s/d=5.17) at 46.7 g

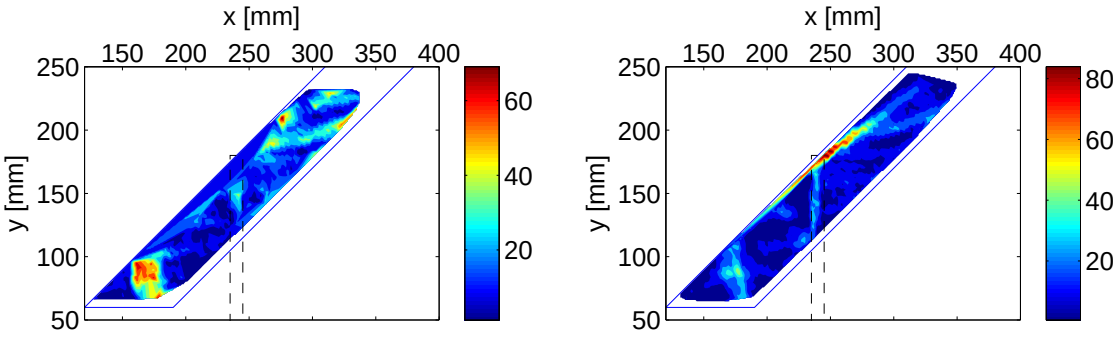

(c) A4PSL (s/d=3.88) at 48.9 g **(d)** A5PSL (s/d=3.10) at 50 g

Fig. 4.34 PIV computed maximum shear strain (%) of the side-view. Continuous shear bands in the up-slope (right) are observed in (c) and (d). The dashed rectangle indicates the initial pile location.

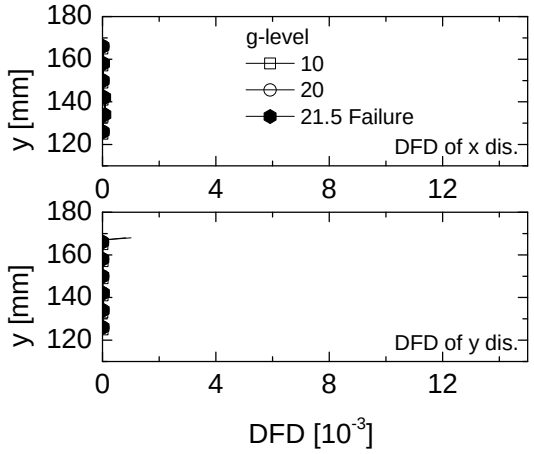

(a) DFD at $x = 240$ mm in A2PSL (s/d=7.75)

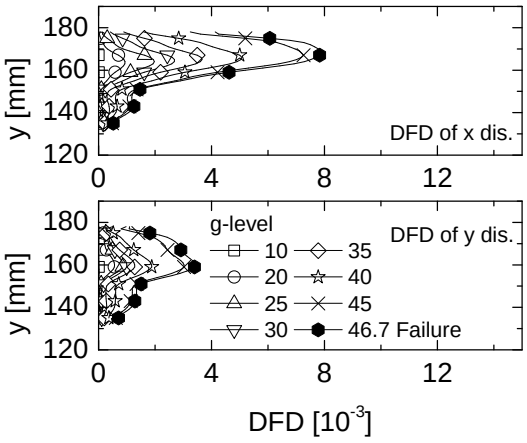

(b) DFD at $x = 250$ mm in A3PSL (s/d=5.17)

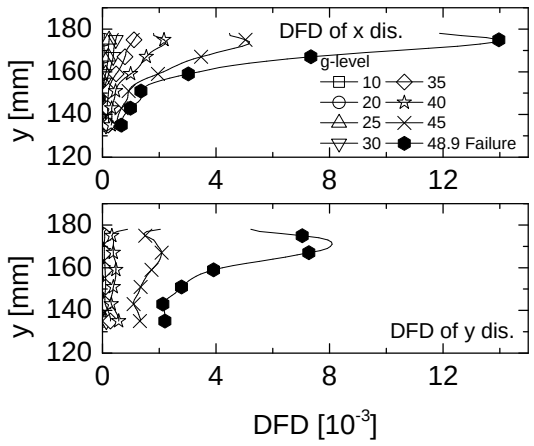

(c) DFD at $x = 250$ mm in A4PSL (s/d=3.88)

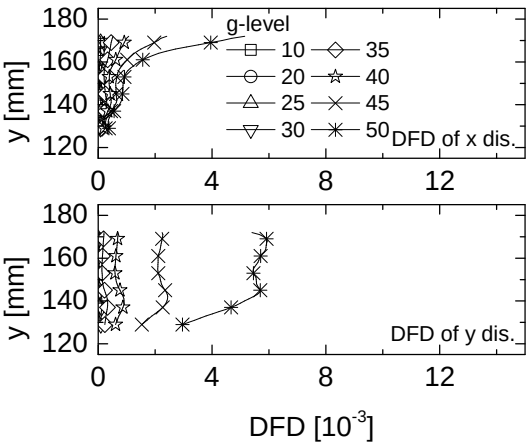

(d) DFD at $x = 245$ mm in A5PSL (s/d=3.10)

Fig. 4.35 DFD at the pile row for the test series AiPSL.

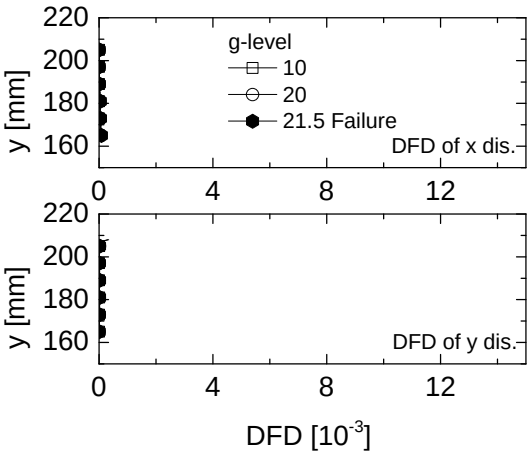

(a) A2PSL (s/d=7.75)

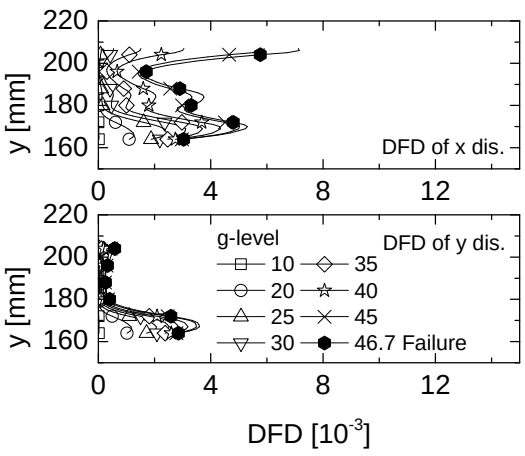

(b) A3PSL (s/d=5.17)

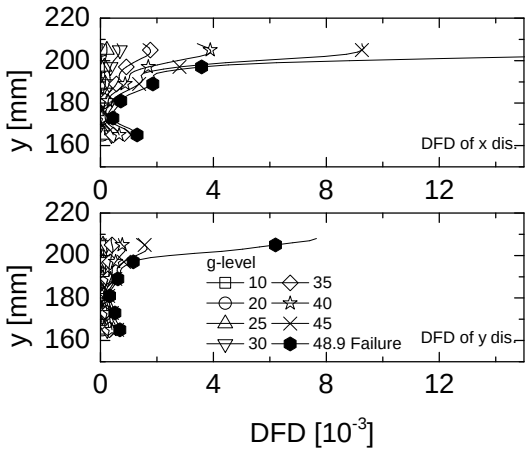

(c) A4PSL (s/d=3.88)

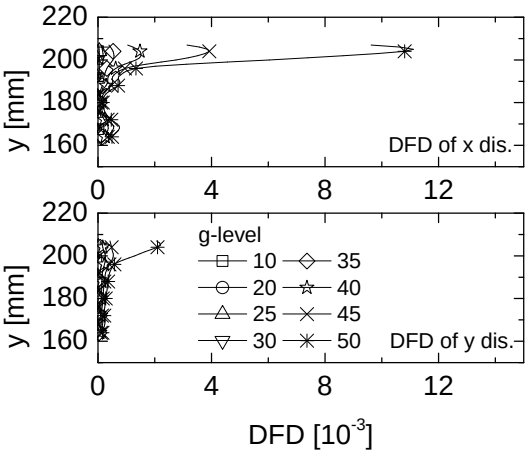

(d) A5PSL (s/d=3.10)

Fig. 4.36 DFD at $x = 280$ mm for the test series A*i*PSL.

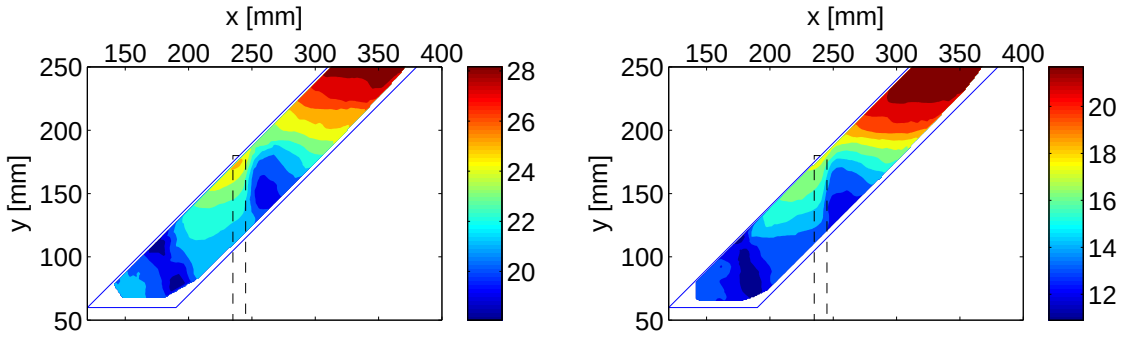

(a) P4PSL (s/d=3.88) at 36.7 g **(b)** P5PSL (s/d=3.10) at 50 g

Fig. 4.37 PIV computed displacement (unit: mm) of the side-view. Soil compaction along the slip surface. The dashed rectangle indicates the initial pile location.

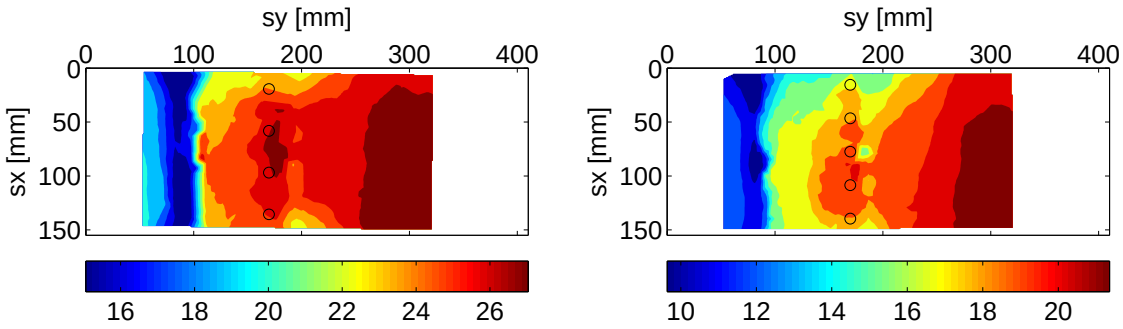

(a) P4PSL (s/d=3.88) at 36.7 g **(b)** P5PSL (s/d=3.10) at 50 g

Fig. 4.38 PIV computed displacement (unit: mm) of the top-view. Displacement discontinuity at the pile row. The initial pile locations are marked by hollow circles.

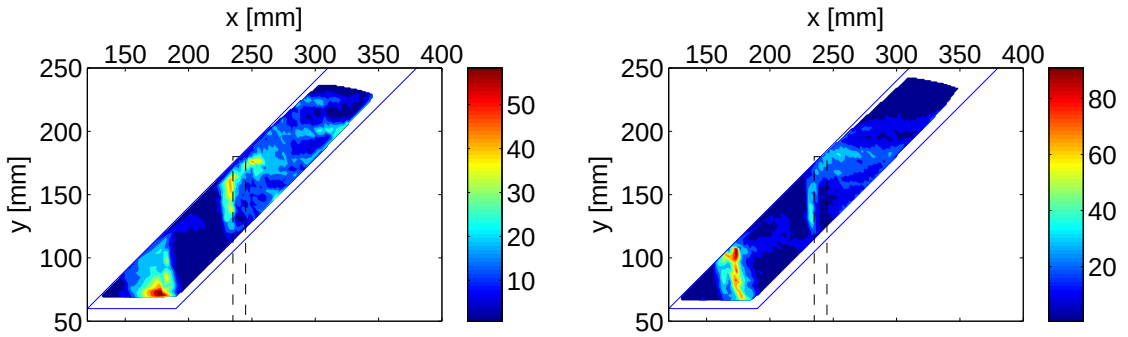

(a) P4PSL (s/d=3.88) at 36.7 g **(b)** P5PSL (s/d=3.10) at 50 g

Fig. 4.39 PIV computed maximum shear strain (%) of the side-view. Vertical shear band at the pile location and no such clear shear band in figure 4.34 in the up-slope (right) are observed. The dashed rectangle indicates the initial pile location.

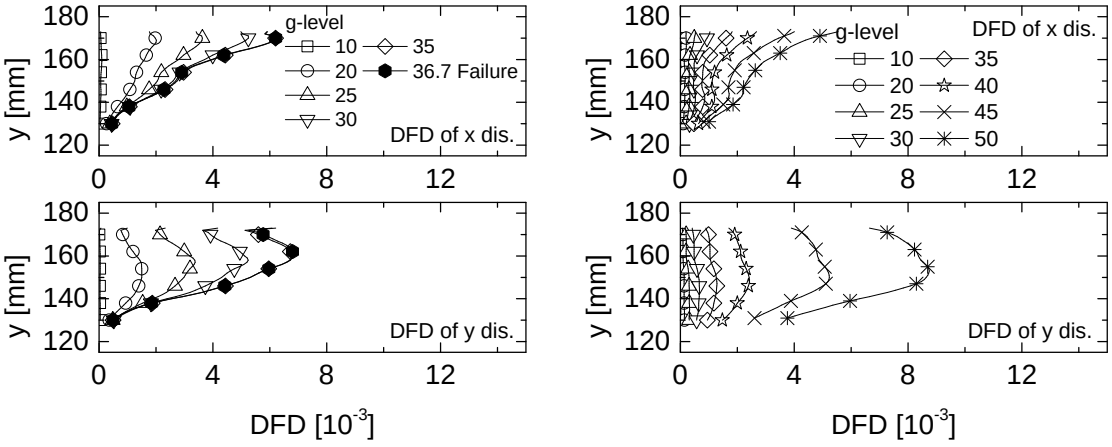

(a) P4PSL (s/d=3.88) **(b)** P5PSL (s/d=3.10)

Fig. 4.40 DFD at $x = 245$ mm for the test series P*i*PSL.

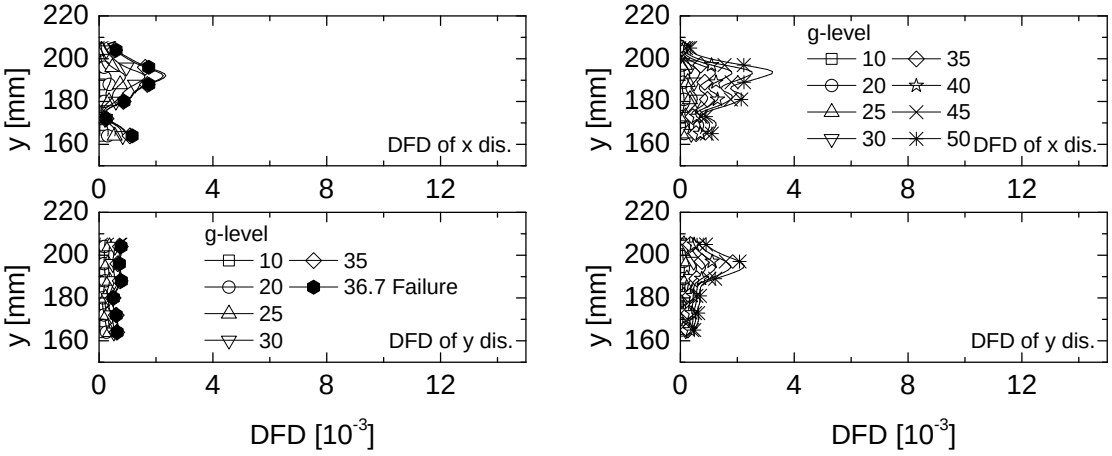

(a) P4PSL (s/d=3.88) **(b)** P5PSL (s/d=3.10)

Fig. 4.41 DFD at $x = 280$ mm for the test series P*i*PSL.

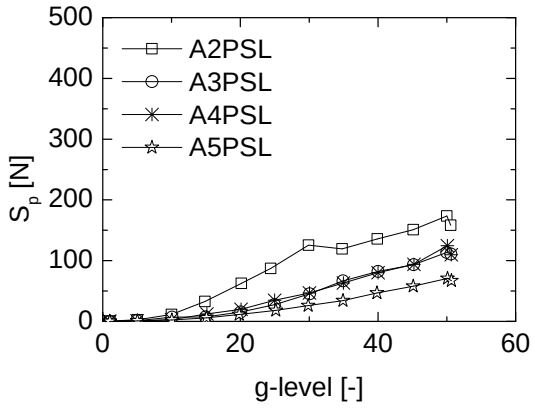

(a) sliding force on the pile

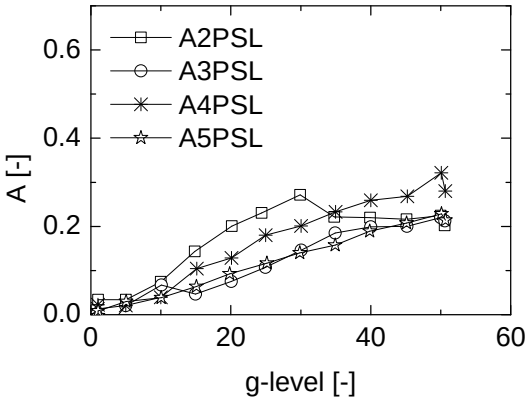

(b) variable A

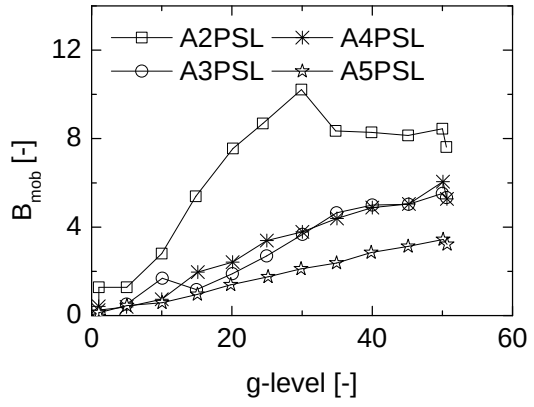

(c) average B_{mob}

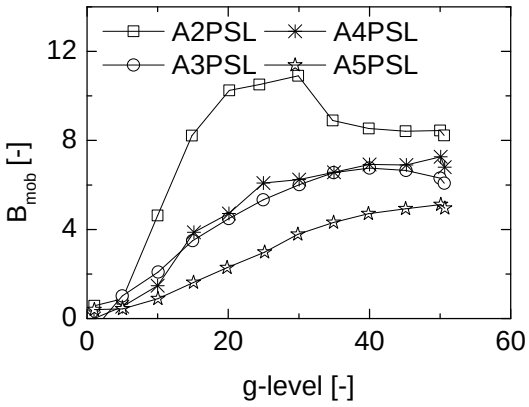

(d) middle B_{mob}

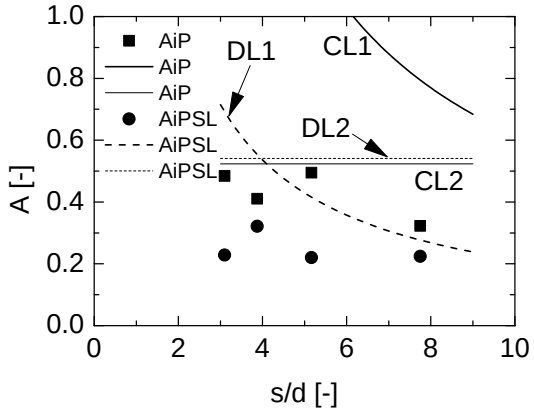

(e) variation of A with s/d

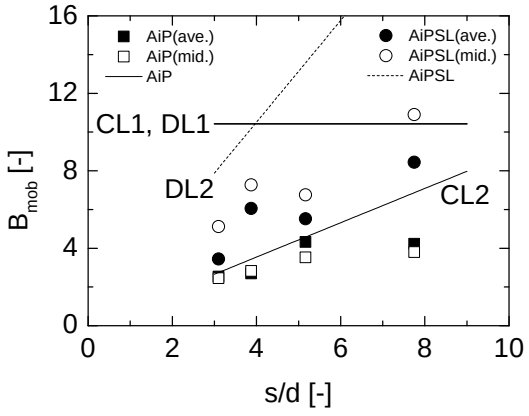

(f) variation of B_{mob} with s/d.

Fig. 4.42 Analysis of the sliding force on the pile. S_p: the sliding force on the pile; A: the ratio of the forces on the piles to the weight of the up-slope soil; B_{mob}: the equivalent soil pressure on the pile normalised by the overburden stress in terms of the average value and the value in the middle of the soil layer. CL1 and DL1 in (f) represent the estimation $B_{max} = {K_p}^2$; CL2 and DL2 in (e) represent the estimation $A_{max} = (1-\alpha)\sin\beta$; CL1, DL1 in (e) and CL2, DL2 in (f) are respectively derived from CL1, DL1 in (f) and CL2, DL2 in (e) through the equation $B_{max} = A_{max} \cdot 2(s/d)(l/h)$.

4.7 The role of l/h

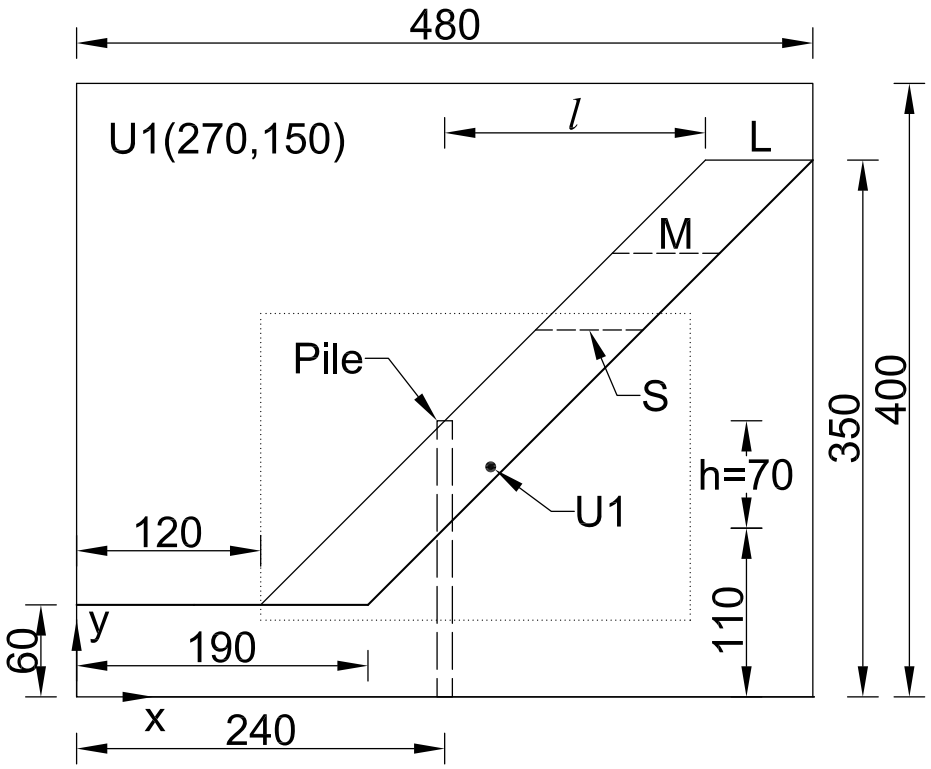

Fig. 4.43 Geometry of the model with a thin soil layer in the cross-sectional view (unit: mm). The dotted rectangle indicates the area where PIV analysis is applied. U1 is a monitoring point whose displacement is used to represent the movement of the rubber sheet. Lines L, M and S denote the crest for long, middle and short slopes, respectively.

As discussed previously in the last section, the emergence of the over-top failure in the test series A*i*PSL could be due to the large ratio of the up-slope length to the soil layer thickness l/h, which is the maximum value (2.43) in the current model box. Tests with two smaller ratios of l/h, 1.56 and 0.85, were conducted with aluminium piles considering two pile spacings: $s/d = 5.17$ and $s/d = 3.10$, which correspond to 3 piles and 5 piles in the test, respectively. The locations of the slope crest of the tests with smaller l/h are shown in Figure 4.43 using dashed lines. The pile location remains the same.

Displacement analysis for A3PS* and A5PS*

Figure 4.44 shows the soil displacement of the side-view at 50 g or just before failure. Figure 4.45 shows the corresponding soil displacement of the top-view. For the test series A5PS* (the symbol ' * ' can be replaced by 'S' for 'short', 'M' for 'medium' or 'L' for

'long' to represent the l/h of 0.85, 1.56 and 2.43 , respectively), displacement discontinuity is observed at the pile row. In the case of small l/h (test A5PSS), the maximum soil displacement is observed in the down-slope, therefore this test is prone to 'down-slope failure'. In the case of large l/h (test A5PSL), 'over-top failure' is observed as the large soil displacement concentrates in the up-slope. In the case of medium l/h (test A5PSM), the signs of both failure modes can be seen. In contrast to A5PS*, soil displacement is continuous at the pile row in the test series A3PS*. The main failure mode is 'flow failure'. However, the increase of l/h has also resulted in additional soil movement, especially in the up-slope in test A3PSL.

In order to compare the soil displacements between the tests, the soil displacement at the point U1 and the average displacement of the down- and up-slopes (using the displacement results in the ranges $x = 200 \sim 240$ mm and $x = 240 \sim 280$ mm, respectively) are plotted against the g-level in Figure 4.46. For the test series A5PS*, the soil displacement at U1 is less than 10 mm and it is not influenced by the increase of l/h. This is because the point U1 is located in the soil zone that is directly stabilised by the pile row. The extra soil in the up-slope due to the increase of l/h only accelerates the movement of the soil part that can move above the pile top. This also implies that the support of the pile row to the up-slope soil with this spacing is solid. In contrast, the displacement level at U1 increases in the test series A3PS* due to the increase of l/h. Note that this observation does not apply to test A3PSL because of local deformation. Figure 4.46b shows that the difference is small between the average displacements of the up- and down-slopes in the test series A3PS*, which is also a characteristic of 'flow failure'. Figure 4.46c shows that the average displacements are similar not only between the up- and down-slopes, but also between the tests in the test series A5PS*. As explained earlier, the contribution of a larger l/h to the soil displacement is limited to the soil with higher elevation, most of which, however, is not counted in the calculation (the average displacement is calculated using the data in the range of $x = 240 \sim 280$ mm for the up-slope). Even though, the difference between the tests can still be seen. The result of the displacement of the up-slope minus the down-slope is shown in Figure 4.46d. In general, the differences are small (less than 4.5 mm). In the test series A5PS*, minus values are observed in tests A5PSS and A5PSM, which corresponds to the 'down-slope failure'. As l/h becomes larger, the curve tends to go back to zero and become positive.

Deformation analysis for A3PS* and A5PS*

The observations of displacement are further verified by the soil deformation. Figure 4.47 shows the maximum shear strain of the side view at 50 g or just before failure. Figure 4.48 and 4.49 present the DFD along the vertical line $x = 240$ mm and $x = 280$ mm, respectively.

The soil strain in the slope toe area is caused by the sudden change of slip surface inclination and is, therefore, neglected here. In the test series A3PS*, a clear shear band is not observed. Some local shear deformations are observed in the up-slope in test A3PSL. They tend to form a shear band that could lead to over-top failure. However, the pile reinforcement is obviously not adequate since similar shear deformation is also observed at the pile row. Correspondingly, DFD increments are also only observed in test A3PSL in the test series A3PS*. However, they do not indicate any specific failure mode. For instance, at $x = 240$ mm (pile row), the DFD for Δx is much larger than DFD for Δy, which is the opposite to the outcome when soil separates at the pile row. At $x = 280$ mm for test A3PSL, the increment of DFD for Δx is observed for the whole depth instead of focusing on a certain depth, which implies that a stable over-top movement has not been formed. However, the shear deformation in the soil has affected the soil movement as mentioned previously. The soil failure mechanism of test A3PSL can be regarded as a flow failure with over-top soil movement. In the test series A5PS*, the soil deformation is much more apparent than A3PS*. In test A5PSS, a vertical shear band is observed at the pile row, indicating a down-slope failure. Correspondingly, large increments of DFD for Δy at $x = 240$ mm (pile row) is observed. In test A5PSM, besides the vertical shear band at the pile row, a second horizontal shear band in the up-slope has emerged. However, DFD shows that the main deformation is still located at the pile row. In test A5PSL, the shear strain at the pile row is smaller compared to the other two tests. An inclined shear band is formed in the up-slope which will lead to an over-top failure. DFD also shows that the main deformation is horizontal in the up-slope. In the test series A5PS*, apparent tendency is observed: As l/h increases from 0.85 to 2.43, the increment of DFD at the pile row becomes smaller while in the up-slope it becomes larger.

Displacement and deformation analysis for P5PS*

A test series P5PS* was conducted using acrylic piles and the same configurations with the test series A5PS*. Figure 4.50 and 4.51 show the soil displacement and maximum shear strain of the side-view. Similar to A5PS*, displacement discontinuity and a vertical shear band at the pile row are observed. In the up-slope, however, a horizontal shear band is formed instead of an inclined one as in test A5PSL. DFD (Figure 4.51) also shows some differences from A5PS*. For instance, as l/h increases from 0.85 to 2.43, the increment of DFD for Δy at the pile row has increased, which is opposite to the test series A5PS*. In the up-slope, the DFD for Δx at $x = 280$ mm increases with l/h. However, its magnitude remains smaller than the DFD at the pile row, which means that over-top failure in the up-slope is not formed. The reason for these differences between P5PS* and A5PS* must be the reduction of pile

bending stiffness by using the acrylic piles. The reinforcement from the acrylic piles in this case is not adequate to cause an over-top failure.

Analysis of strain gauge measurements in A3PS* and A5PS*

Figure 4.52 shows the analysis of the sliding forces on the pile for the test series A3PS* and A5PS*. As shown in Figure 4.52a, for the test series A5PS*, the sliding force on the pile S_p remains unchanged when l/h increases from 0.85 (A5PSS) to 1.56 (A5PSM) while a large increase is observed when l/h increases to 2.43 (A5PSL). For the test series A3PS*, S_p has increased considerably when l/h increases from 0.85 (A3PSS) to 1.56 (A3PSM) while it remains unchanged when l/h increases from 1.56 to 2.43 (A3PSL).

The variations of A, average and middle B_{mob} throughout the tests are displayed in Figure 4.52b, 4.52c and 4.52d, respectively. In the test series A5PS*, as l/h increases, the stable values of these three factors tend to appear in a higher g-level, the middle B_{mob} increases. Test A5PSS has the largest value of A among all the six tests. In the test series A3PS*, the stable value of these three parameters in test A3PSS is the latest to be obtained. As l/h increases, the stable value of A decreases and the stable values of the average and the middle B_{mob} increase. In comparison with the average B_{mob}, the middle B_{mob} is less affected by the soil boundaries during the tests.

The stable values of A and B_{mob} are plotted against l/h in Figure 4.52e and 4.52f, respectively. The estimations of the maximum A and B_{mob} and their conversion to each other are also plotted as lines and curves in the figures. CL1 and DL1 in Figure 4.52f represent the soil failure criteria $B_{max} = {K_p}^2$. CL2 and DL2 in Figure 4.52e represent the estimation $A_{max} = (1-\alpha)\sin\beta$. CL1, DL1 in Figure 4.52e and CL2, DL2 in Figure 4.52f are respectively derived from CL1, DL1 in Figure 4.52f and CL2, DL2 in Figure 4.52e through the equation $B_{max} = A_{max} \cdot 2(s/d)(l/h)$. Generally, A decreases and B_{mob} increases with the increase of l/h, which means that the resistance from the boundaries has increased and the soil-pile interaction has also been enhanced. For the test series A5PS*, in the current range of l/h, the line of the theoretical maximum force on the pile (DL2) is always lower than the line of soil failure criteria (DL1). The maximum soil pressure on the pile is not likely to be reached and so is the observation. It can also be predicted that the maximum soil pressure on the pile cannot be reached with even a higher l/h because of the over-top failure for this pile spacing. For the test series A3PS*, the intersection point of CL1 and CL2 has moved to the left compared to the intersection of DL1 and DL2. This allows the maximum soil pressure on the pile p_u to be reached in test A3PSL theoretically. However, as discussed previously, the appearance of over-top movement in the up-slope has influenced the pile-soil interaction. As the pile spacing becomes larger, the p_u can be reached since it is already confirmed by test

P2PSL. Similar observation is made in the study of Yoon (2008), in which p_u is not reached in the test with a pile spacing of 5.9 when $l/h = 2.5$ but is reached when $l/h = 3.0$.

Summary

The relative up-slope length l/h has a large influence on the soil behaviour. By increasing l/h (from 0.85 to 2.43), larger overall soil displacement and sliding force on the pile are obtained. However, the mechanism varies with the pile spacing s/d. When s/d is small (3.1), the increase of l/h changes the failure mode from down-slope failure to over-top failure. For a large s/d (5.17), a larger l/h can accelerate the flow failure and also bring additional deformation in the up-slope. The influence of l/h can be reduced when flexible piles are used.

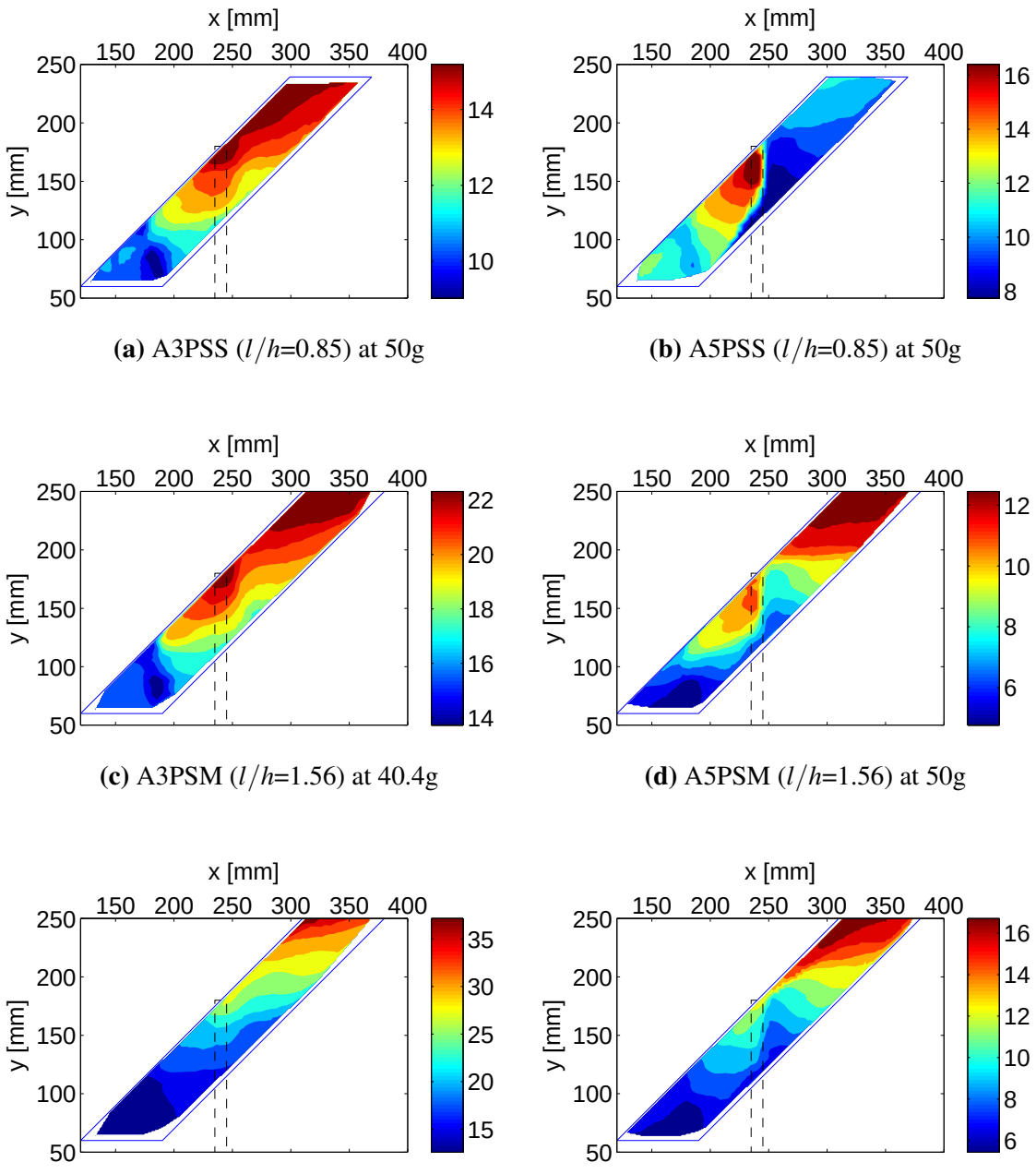

(a) A3PSS (l/h=0.85) at 50g

(b) A5PSS (l/h=0.85) at 50g

(c) A3PSM (l/h=1.56) at 40.4g

(d) A5PSM (l/h=1.56) at 50g

(e) A3PSL (l/h=2.43) at 46.7g

(f) A5PSL (l/h=2.43) at 50g

Fig. 4.44 PIV computed displacement (unit: mm) of the side-view. Different soil movement pattern: flow failure for (a), (c) and (e); down-slope failure for (b); over-top failure for (f). The dashed rectangle indicates the initial pile location.

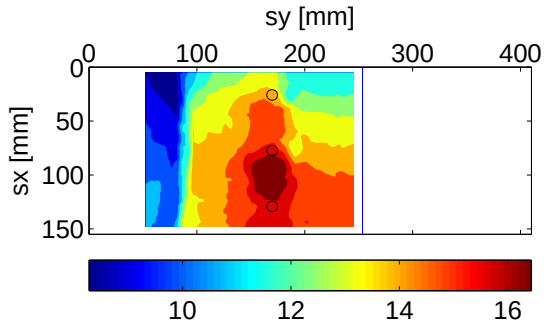

(a) A3PSS (l/h=0.85) at 50 g

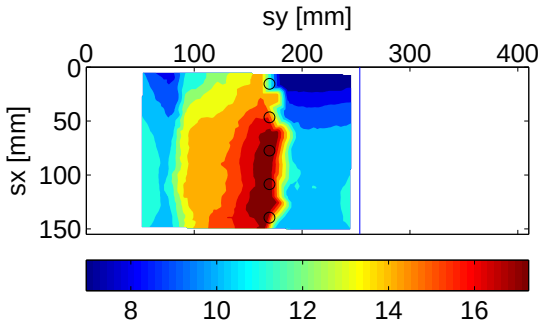

(b) A5PSS (l/h=0.85) at 50 g

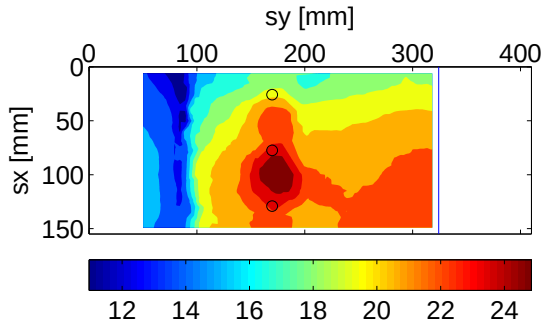

(c) A3PSM (l/h=1.56) at 40.4 g

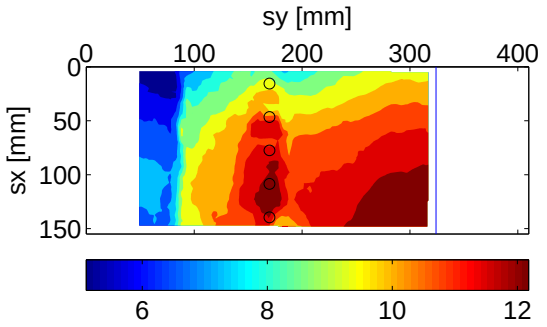

(d) A5PSM (l/h=1.56) at 50 g

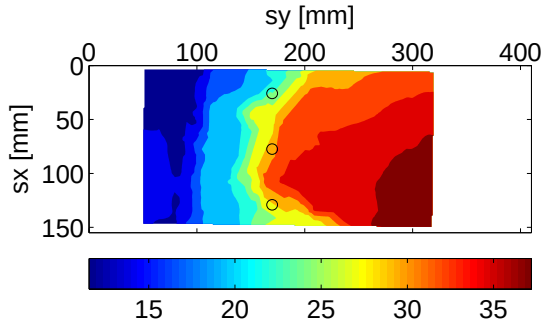

(e) A3PSL (l/h=2.43) at 46.7 g

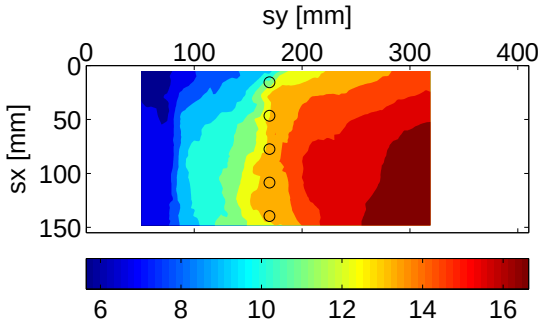

(f) A5PSL (l/h=2.43) at 50 g

Fig. 4.45 PIV computed displacement (unit: mm) of the top-view. Different soil movement pattern: flow failure for (a), (c) and (e); down-slope failure for (b); over-top failure for (f). The blue lines in (a)~(d) denote the initial slope crest. The initial pile locations are marked by hollow circles.

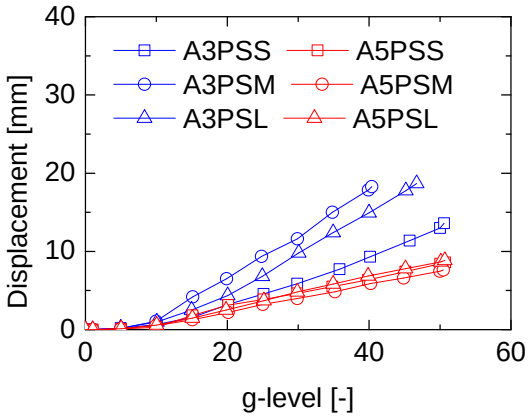

(a) U1 displacement

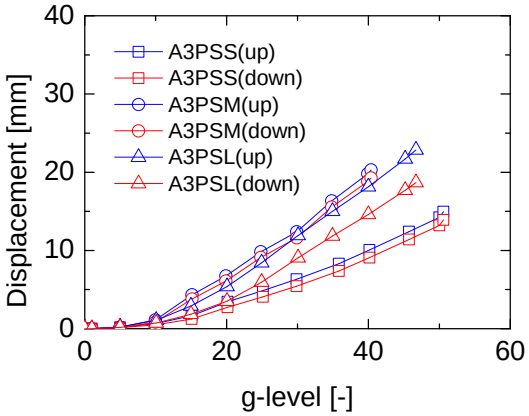

(b) average dis. of the up- and down-slope

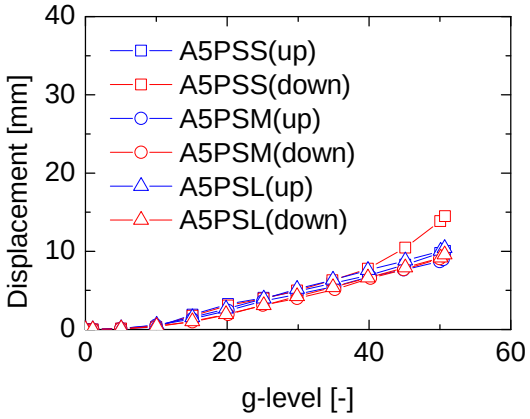

(c) average dis. of the up- and down-slope

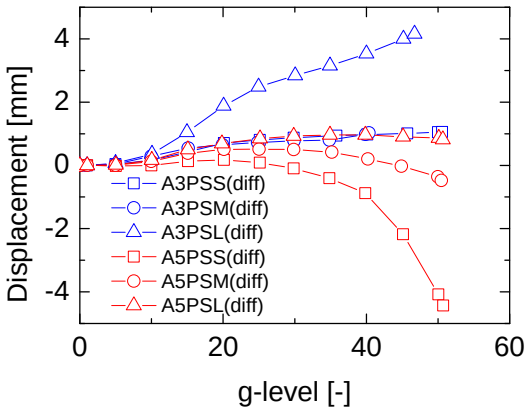

(d) difference of the up- and down-slope dis.

Fig. 4.46 Analysis of the PIV computed soil displacement. In the figure captions, 'dis.' denotes displacement.

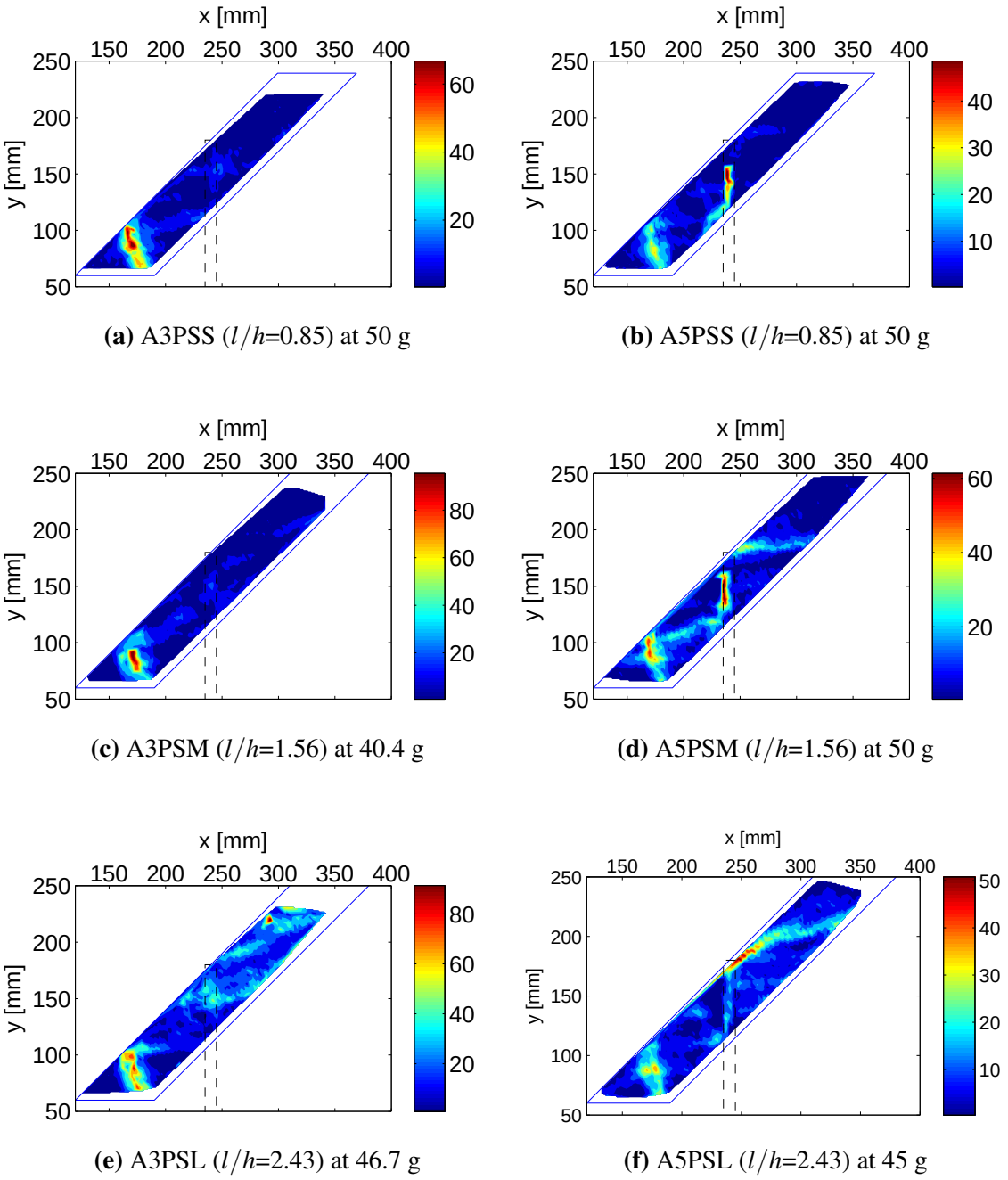

(a) A3PSS (l/h=0.85) at 50 g

(b) A5PSS (l/h=0.85) at 50 g

(c) A3PSM (l/h=1.56) at 40.4 g

(d) A5PSM (l/h=1.56) at 50 g

(e) A3PSL (l/h=2.43) at 46.7 g

(f) A5PSL (l/h=2.43) at 45 g

Fig. 4.47 PIV computed maximum shear strain (%) of the side-view. Continuous shear band is not observed in (a), (c) and (e). Vertical shear band is observed in (b) and (d). Continuous shear band in the up-slope (right) is observed in (f). The dashed rectangle indicates the initial pile location.

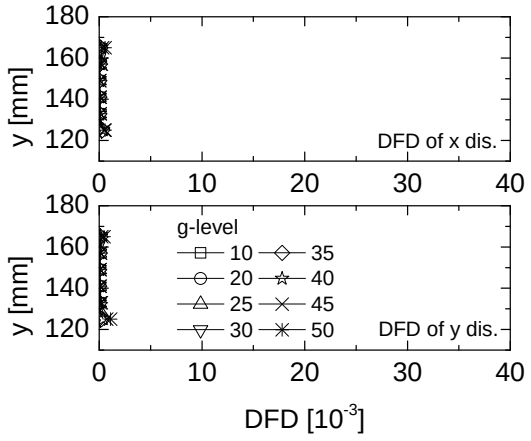

(a) A3PSS (l/h=0.85)

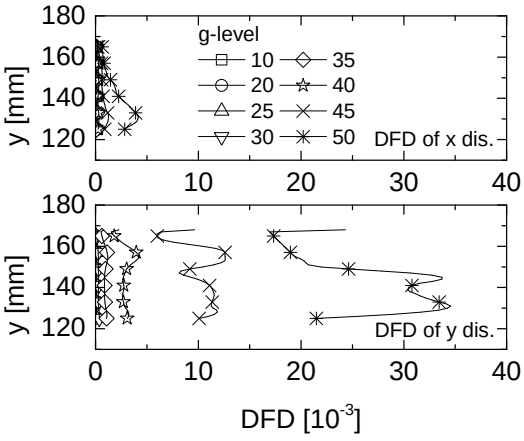

(b) A5PSS (l/h=0.85)

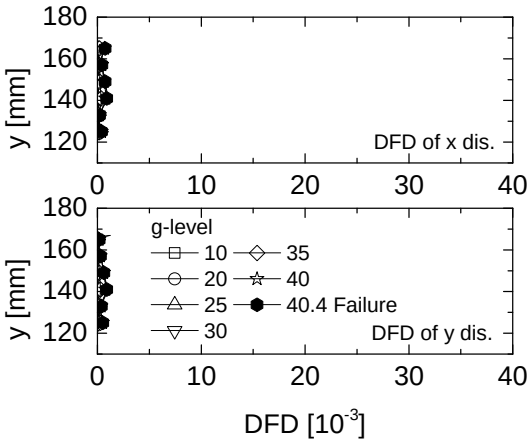

(c) A3PSM (l/h=1.56)

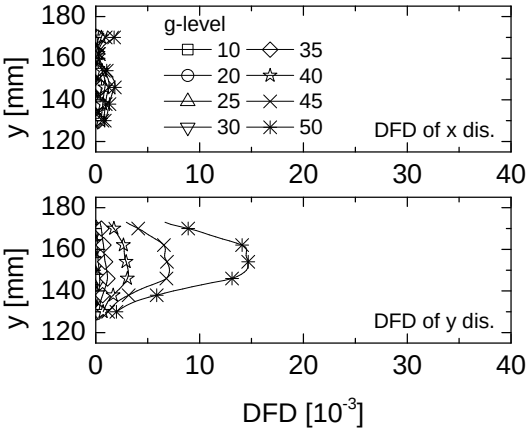

(d) A5PSM (l/h=1.56)

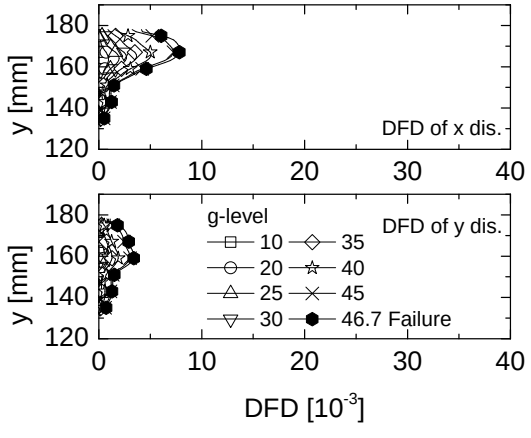

(e) A3PSL (l/h=2.43)

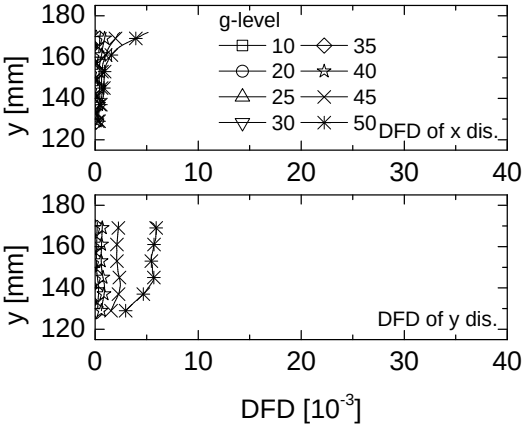

(f) A5PSL (l/h=2.43)

Fig. 4.48 The DFD for x- and y-displacements at $x = 240$ mm.

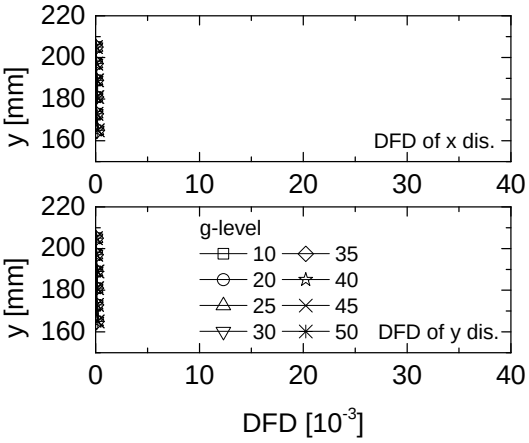

(a) A3PSS (l/h=0.85)

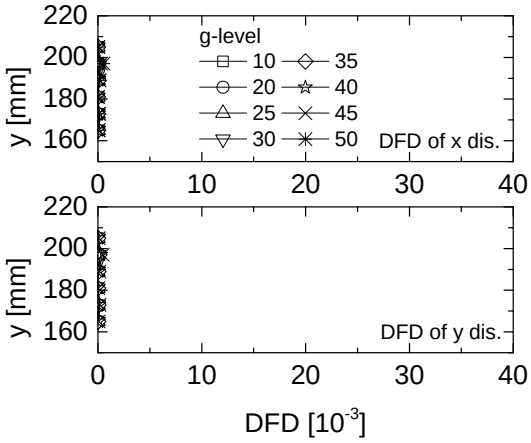

(b) A5PSS (l/h=0.85)

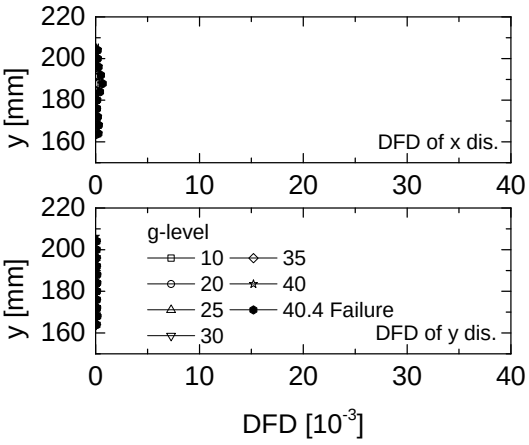

(c) A3PSM (l/h=1.56)

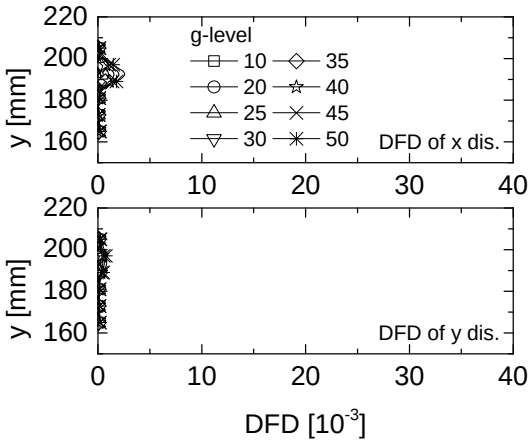

(d) A5PSM (l/h=1.56)

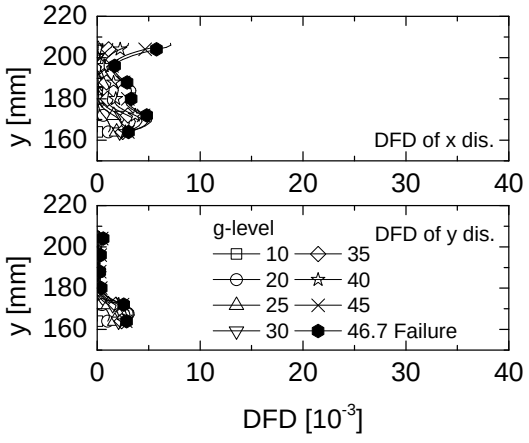

(e) A3PSL (l/h=2.43)

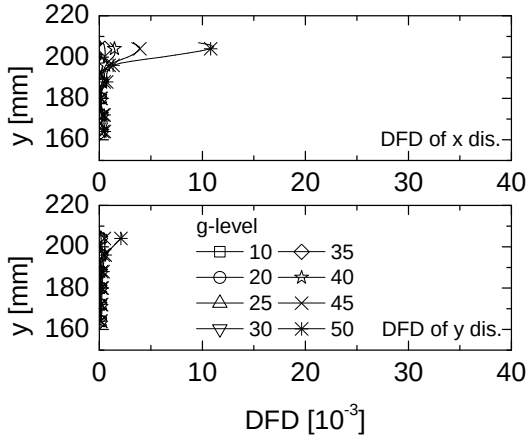

(f) A5PSL (l/h=2.43)

Fig. 4.49 The DFD for x- and y-displacements at $x = 280$ mm

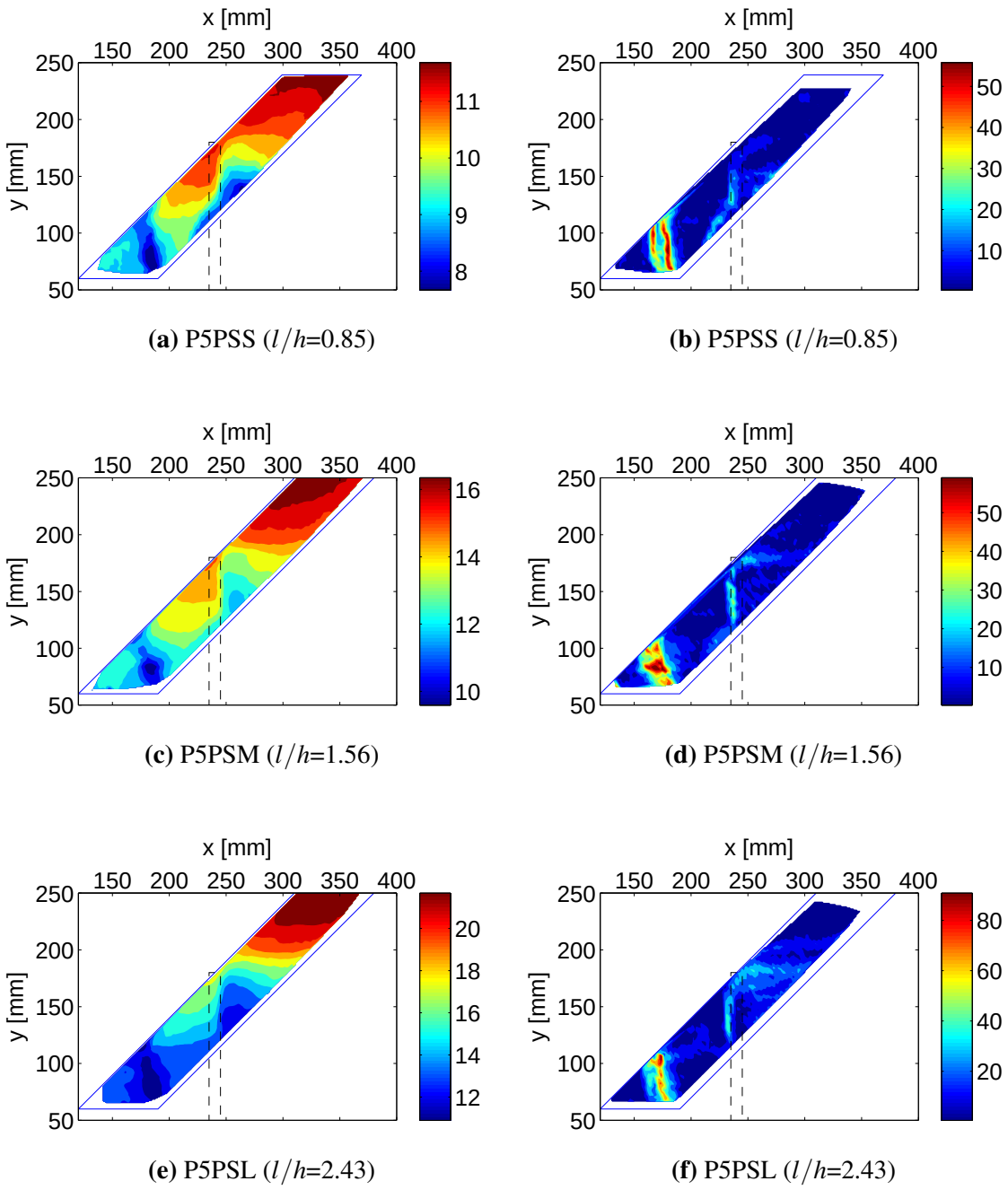

(a) P5PSS (l/h=0.85) **(b)** P5PSS (l/h=0.85)

(c) P5PSM (l/h=1.56) **(d)** P5PSM (l/h=1.56)

(e) P5PSL (l/h=2.43) **(f)** P5PSL (l/h=2.43)

Fig. 4.50 PIV computed displacement (unit: mm) and strain (%) of the side-view at 50 g. The soil displacement discontinuity is observed at the pile row. Continuous shear band in the up-slope (right) is not observed. The dashed rectangle indicates the initial pile location.

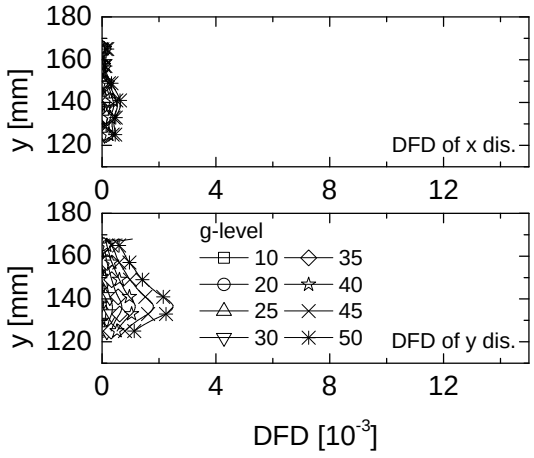

(a) DFD at $x = 240$ mm in P5PSS (l/h=0.85)

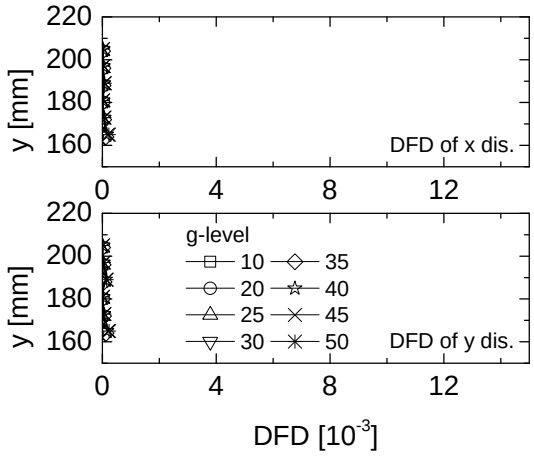

(b) DFD at $x = 280$ mm in P5PSS (l/h=0.85)

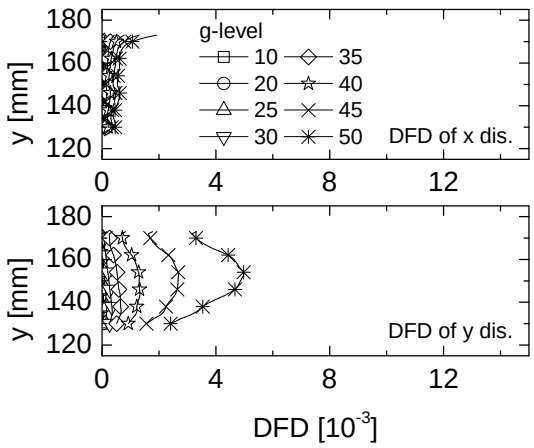

(c) DFD at $x = 245$ mm in P5PSM (l/h=1.56)

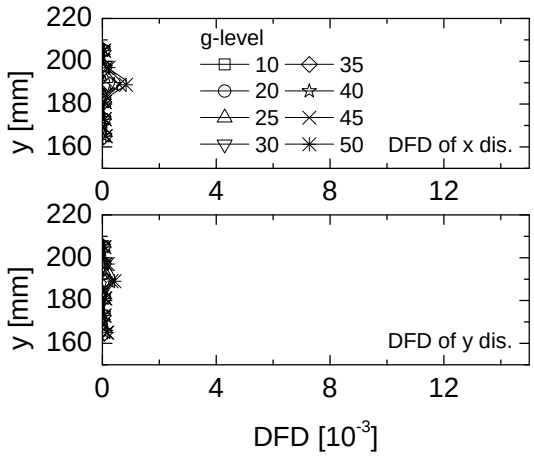

(d) DFD at $x = 280$ mm in P5PSM (l/h=1.56)

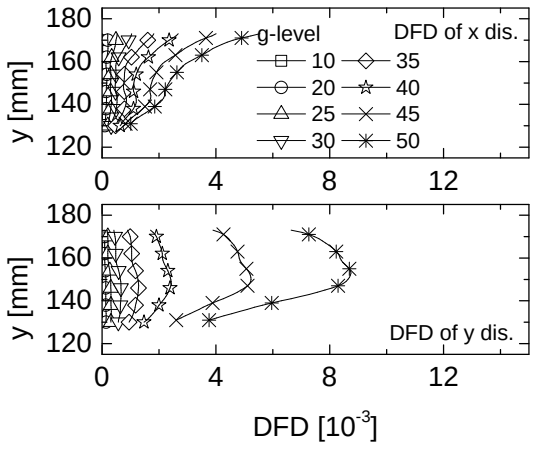

(e) DFD at $x = 245$ mm in P5PSL (l/h=2.43)

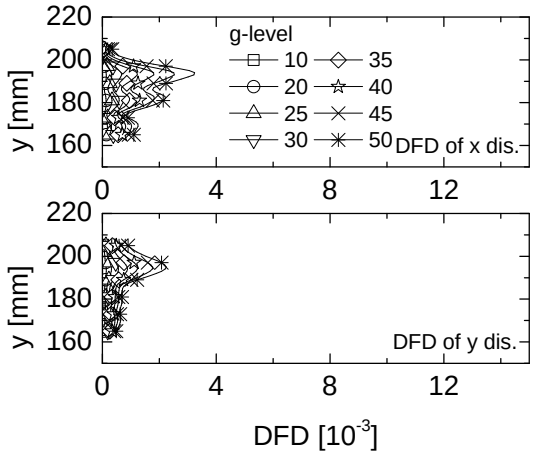

(f) DFD at $x = 280$ mm in P5PSL (l/h=2.43)

Fig. 4.51 The DFD for x- and y-displacements for the test series P5PS*.

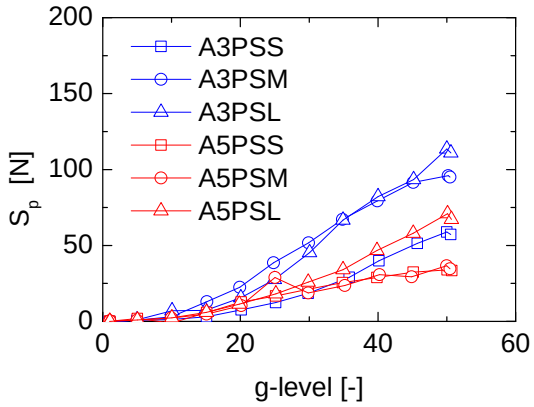

(a) sliding force on the pile

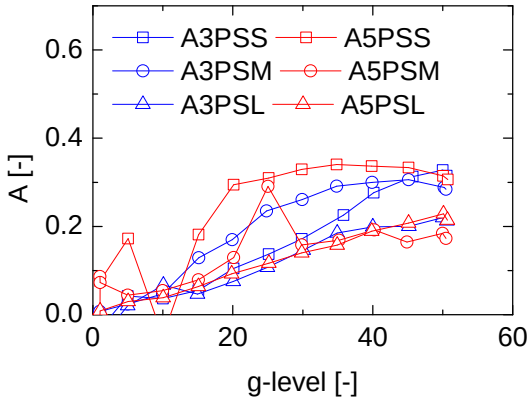

(b) variable A

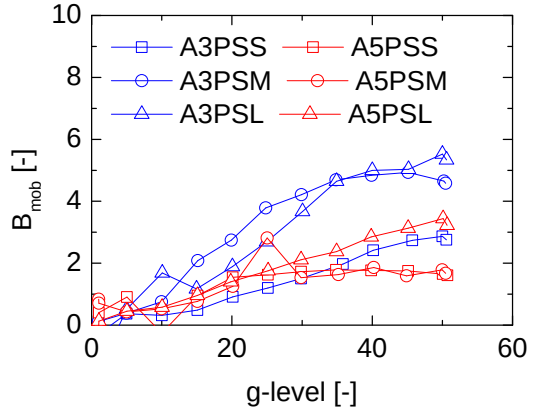

(c) average B_{mob}

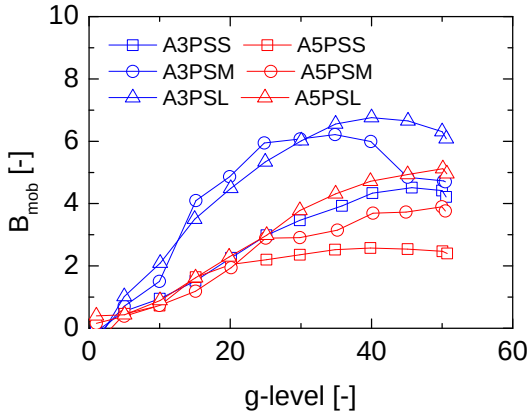

(d) middle B_{mob}

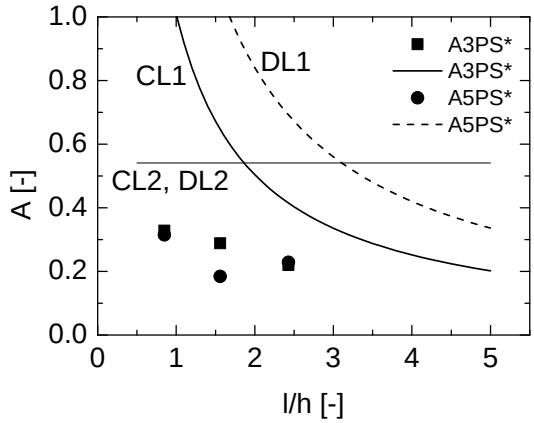

(e) variation of A with l/h

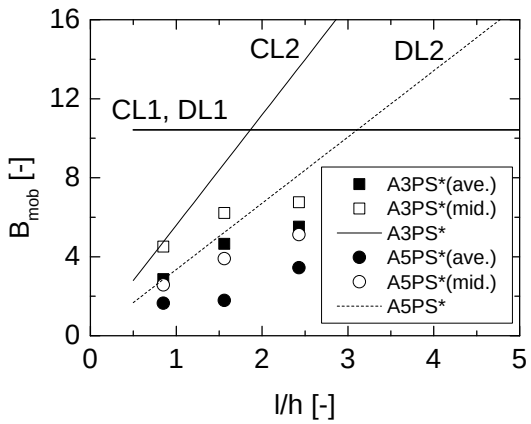

(f) variation of B_{mob} with l/h.

Fig. 4.52 Analysis of the sliding force on the pile. S_p: the sliding force on the pile; A: the ratio of the forces on the piles to the weight of the up-slope soil; B_{mob}: the equivalent soil pressure on the pile normalised by the overburden stress in terms of the average value and the value in the middle of the soil layer. CL1 and DL1 in (f) represent the estimation $B_{max} = {K_p}^2$; CL2 and DL2 in (e) represent the estimation $A_{max} = (1-\alpha)\sin\beta$; CL1, DL1 in (e) and CL2, DL2 in (f) are respectively derived from CL1, DL1 in (f) and CL2, DL2 in (e) through the equation $B_{max} = A_{max} \cdot 2(s/d)(l/h)$.

4.8 The use of deep-buried piles

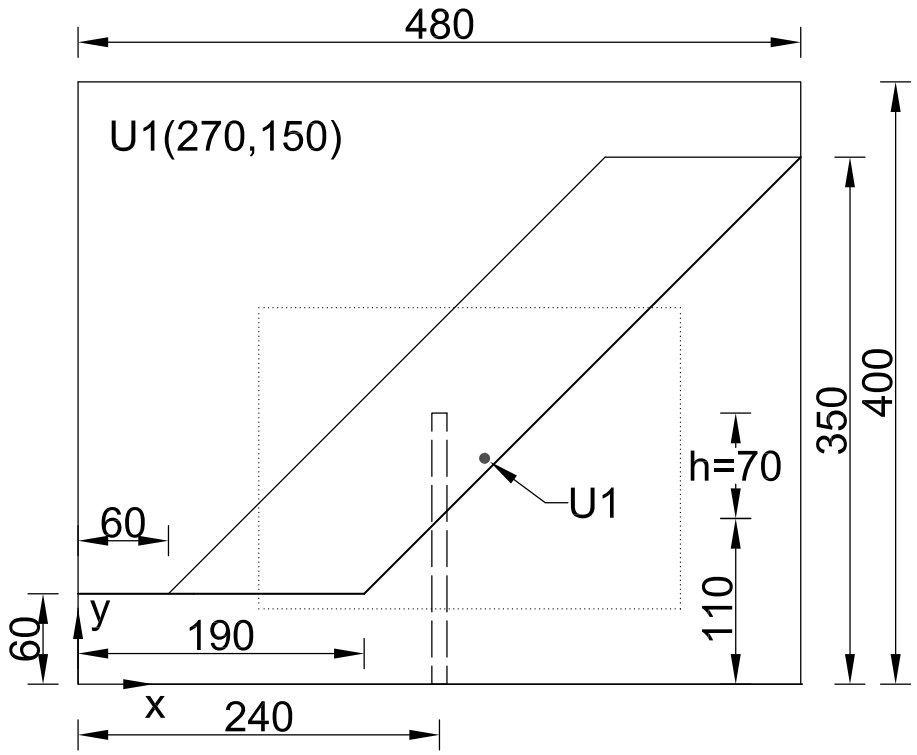

Fig. 4.53 Geometry of the model with deep-buried piles in side-view (unit: mm). The pile head is 60 mm below the soil surface. The dotted rectangle indicates the area where PIV analysis is applied. U1 is a monitoring point whose displacement is used to represent the movement of the rubber sheet.

It is deduced in the test series A*i*P that the reason why the soil pressure on the pile is not fully mobilised even though the observed flow failure is the large pile deformation in the pile top region. The study of the pile bending stiffness also shows that the ineffectiveness of the top part of the pile can significantly reduce the reinforcement of the piles. However, the study of the pile slenderness ratio h/d shows that a rigid pile-soil interaction using acrylic piles can be obtained when the pile slenderness ratio is small. For the cases with a thicker sliding soil layer (the test series A*i*P and P*i*P), a way to reduce the slenderness without changing the pile diameter is to use deep-buried piles. As shown in Figure 4.53, the pile top is located below the soil surface. The embedded length in the stable layer remains the same with the previous tests. Two series of tests, A*i*PB and P*i*PB (*i*=1, 2, 3, 4), are conducted to reveal the behaviour of deep-buried piles.

Displacement and deformation analysis for P*i*PB

The comparisons of the displacements at the point U1 between the test series A*i*PB, P*i*PB and the corresponding test series using full length piles are made in Figure 4.54. In the test series P*i*PB, the soil displacement at U1 shows that the soil layer movement is smaller when the deep-buried piles are used except that the soil displacement of test P5PB ($s/d = 3.10$) is similar to test P5P.

Figure 4.55 shows the displacement and maximum shear strain of the side-view before failure or at 50 g when failure is not observed. It is seen that the displacement of the deep soil, which is reinforced by the piles, is smaller than the shallow soil. With large pile spacing (P2PB), flow failure is expected. The difference between the displacement of deep and shallow soils is small. The displacement difference increases when the pile spacing becomes smaller and over-top failure is observed. The contours of soil displacement show that almost all the soil in the up-slope is mobilized in the over-top movement. However, only the shallower soil has failed due to the restriction of the rubber layer to the deeper soil. As shown by the maximum shear strain, a shear band parallel to the slip surface is observed just above the pile top. Figure 4.56 shows the DFD for both x- and y-displacements (Δx and Δy) in the side-view along a vertical line coinciding with the pile row ($x = 240$ mm). In tests P2PB and P3PB, DFD remains unchanged below the pile top which implies that soil flows around the piles. The pile reinforcement is stronger in test P3PB because the deformation above the pile top has emerged. In tests P4PB and P5PB, large increments of DFD are observed above the pile top. The increment of DFD for Δx is slightly larger than that for Δy, which corresponds well to the orientation of the observed shear band. Besides, in tests P4PB and P5PB, the increment of DFD for *Deltay* is also observed below the pile top while the DFD for Δx remains unchanged, which means that a slight separation effect has appeared due to the small pile spacing.

Displacement and deformation analysis for A*i*PB

In the test series A*i*PB, the soil displacement at U1 is shown in Figure 4.54b. In comparison with A*i*P(SG), smaller soil displacement is obtained when the pile spacing is small (A4PB and A5PB) while larger displacement is observed in tests A2PB and A3PB. Figure 4.57 shows the displacement and the maximum shear strain of the side-view. The side-view of test A3PB is only available before 27.2 g due to a technical problem. The soil movement pattern is similar to the test series P*i*PB. However, a distinct difference of the soil displacement is observed between the up- and down-slopes at the pile location when the pile spacing is small. Besides the shear band parallel to the slip surface, the vertical shear deformation is

also observed at the pile row. DFD analysis along a vertical line at the pile row (Figure 4.58) provides better comparisons. Some small increments of DFD are observed in test A2PB. They may not be fully due to the soil-pile interaction because of the additional resistance from the rubber sheet when the soil displacement approaches the designed maximum (about 35 mm). In tests A4PB and A5PB, on the contrary, the maximum displacement at U1 is less than 20 mm, the calculated DFD should represent the soil deformation due to the soil-pile interaction. Unlike tests P4PB and P5PB, the major soil deformation in tests A4PB and A5PB is observed below the pile top along the y direction. The soil deformation above the pile top has also increased significantly. These observations confirm the shear bands described previously.

The soil displacement at U1 is compared between the test series A*i*PB and P*i*PB in Figure 4.54c. The soil displacements from both test series are similar when the pile spacing is large. With small pile spacing, the soil displacement is smaller in the tests with aluminium piles (A4PB and A5PB). As concluded previously, the acrylic piles can also be regarded as rigid piles with this slenderness ratio. Nevertheless, a higher pile rigidity still contributes to the reinforcement.

Comparing the test series A*i*PB and P*i*PB to A*i*P and P*i*P, it can be concluded that the use of deep-buried piles can raise the risk of over-top failure. However, when flexible piles are intended to be used, a shorter pile length above the slip surface can improve the pile behaviour.

Analysis of strain gauge measurements in A*i*PB

Figure 4.59 shows the analysis of the sliding forces on the pile for the test series A*i*PB. As shown in Figure 4.59a, the magnitude of the sliding force on the pile S_p increases with the increase of the pile spacing. Comparing with the test series A*i*P(SG), S_p in tests A4PB and A5PB is smaller than the corresponding tests in A*i*P(SG) while S_p is, on the contrary, larger in tests A2PB and A3PB. These observations are consistent with the observations from the U1 displacements. It may be interpreted as follows: when the pile spacing is small, both slopes in these two test series are stable. Logically, the shorter piles carry less forces. On the contrary, when the pile spacing is large, the slope with deep-buried piles is less stable and therefore higher soil pressure on the pile is produced, which results in a higher sliding force on the shorter piles.

The variations of A, average and middle B_{mob} throughout the tests are displayed in Figure 4.59b, 4.59c and 4.59d, respectively. Different from the long piles, the calculation of

the average B_{mob} for the buried piles is given by:

$$B_{mob}(z) = \frac{S_p}{\gamma(h^2 - h_1^2)d/2} \tag{4.5}$$

where h_1 is the buried depth of the piles (6cm). Similar to the test series A*i*P(SG), the relatively constant values of the three parameters are reached at about 20 g. The middle B_{mob} is less affected by the soil layer boundaries during the tests.

The maximum value of A and B_{mob} in the stable period are plotted against s/d in Figure 4.59e and 4.59f, respectively. Note that the rapid increase of the sliding force in test A2PB after 40 g is not considered because the maximum relative soil movement has already been reached and the rubber layer has direct contact with the piles, which transfers all the sliding force to the piles. The soil failure criteria, the theoretical maximum A and their derivations to each other are also plotted as lines and curves in the figures. CL1 and DL1 in Figure 4.59f represent the soil failure criteria: $B_{max} = K_p^2$; CL2 and DL2 in Figure 4.59e represent the estimation $A_{max} = (1-\alpha)\sin\beta$; CL1 in Figure 4.59e and CL2 in Figure 4.59f are respectively derived from CL1 in Figure 4.59f and CL2 in Figure 4.59e through the equation $B_{max} = A_{max} \cdot 2(s/d)(l/h)$. DL1 in Figure 4.59e and DL2 in Figure 4.59f are respectively derived from DL1 in Figure 4.59f and DL2 in Figure 4.59e through the following equation:

$$B_{max} = A_{max} \cdot 2(s/d)(\frac{lh}{h^2 - h_1^2}) \tag{4.6}$$

Both B_{mob} generally increase with the increase of s/d. As seen in both figures, in the current range of s/d, the line of the theoretical maximum force on pile (DL2) is always lower than the line of soil failure criteria (DL1), which means that the maximum soil pressure on the pile is not likely to be reached. However, the middle B_{mob} of test A2PB and A3PB, especially A2PB, are already very close to DL1, which agrees with the observation of flow failure. Note that the maximum pile force line (DL2) is the limit for the average B_{mob}. Due to the influence of the large sliding angle, B_{mob} could be non-uniform along the pile length especially the regions close to the ground surface and the slip surface. The middle B_{mob} is less affected and is usually larger than the average B_{mob}. As a result, the middle B_{mob} goes above the maximum pile force line (DL2). Comparing with the test series A*i*P, the middle B_{mob} of the test series A*i*PB is much higher especially when s/d is large ($s/d > 4$). This has also confirmed the mechanism proposed for the test series A*i*P.

Summary

Deep-buried piles can be used when the sliding soil is relatively thick. With smaller pile length in the sliding soil, the relative pile stiffness K_R is increased, higher soil pressure on the pile is mobilised. The use of deep-buried piles can raise the risk of over-top failure. However, when flexible piles are used, the adoption of deep-buried piles produces even higher slope stability than the full length pile.

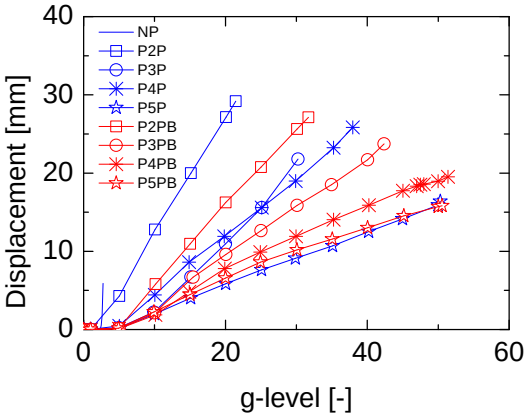

(a) P*i*PB vs. P*i*P

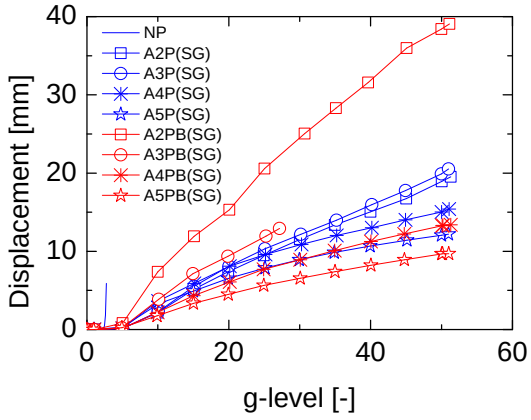

(b) A*i*PB vs. A*i*P

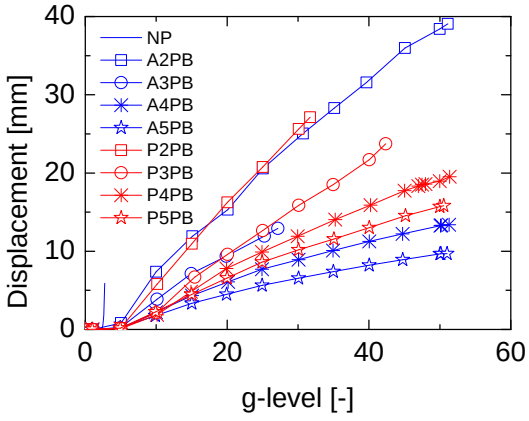

(c) A*i*PB vs. P*i*PB

Fig. 4.54 Comparison of U1 displacement for the deep-buried piles.

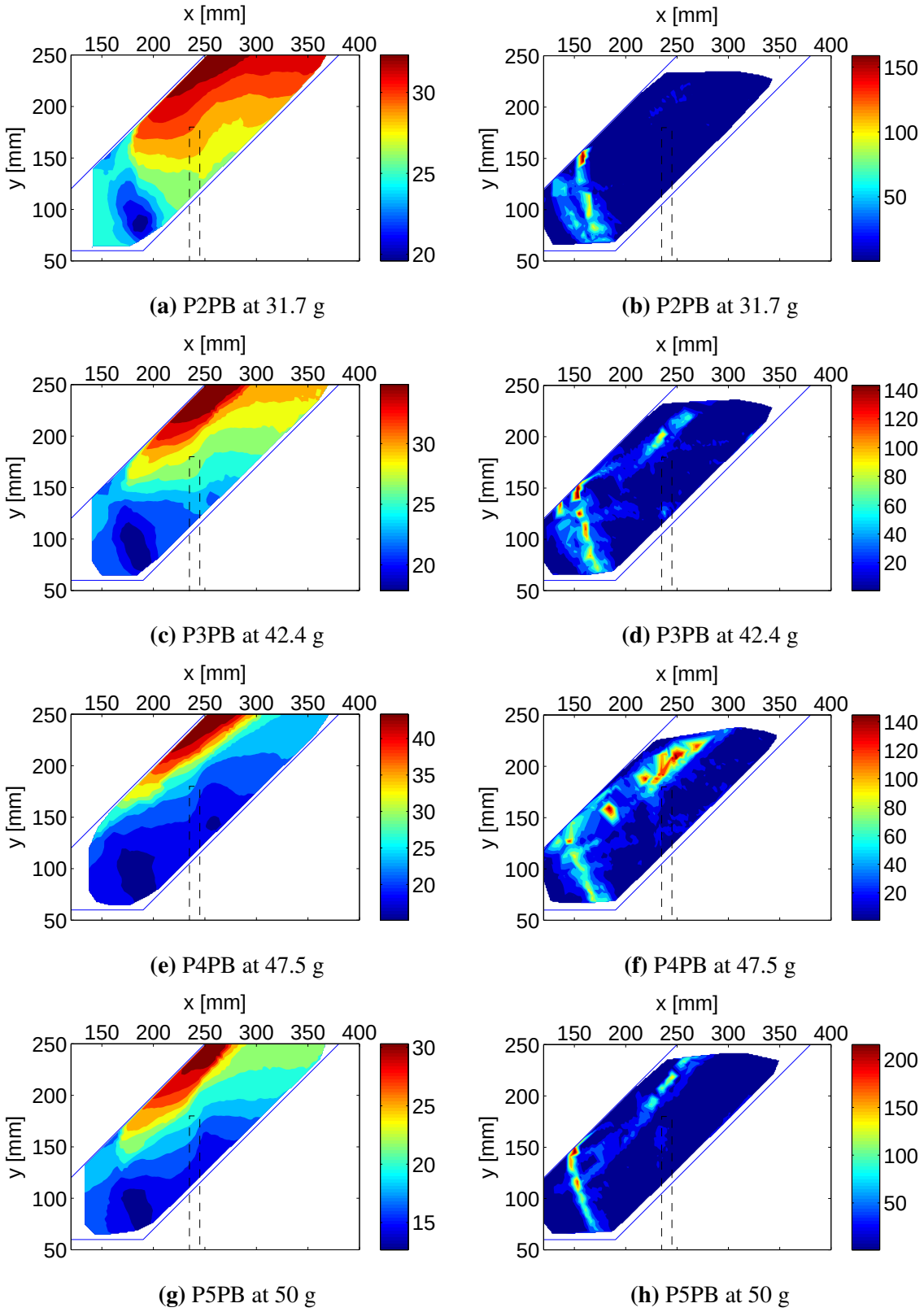

(a) P2PB at 31.7 g

(b) P2PB at 31.7 g

(c) P3PB at 42.4 g

(d) P3PB at 42.4 g

(e) P4PB at 47.5 g

(f) P4PB at 47.5 g

(g) P5PB at 50 g

(h) P5PB at 50 g

Fig. 4.55 PIV computed displacement (subfigures a, c, e, g; unit: mm) and maximum shear strain (subfigures b, d, f, h; unit: %) of the side-view for the test series P*i*PB. Different movement pattern: flow failure in (a) and over-top failure in (c), (e) and (g). Shear band above the pile top is formed in (d), (f) and (h). The dashed rectangle indicates the initial pile location.

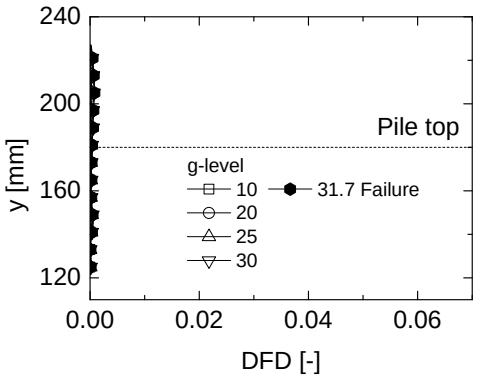

(a) DFD for Δx in test P2PB

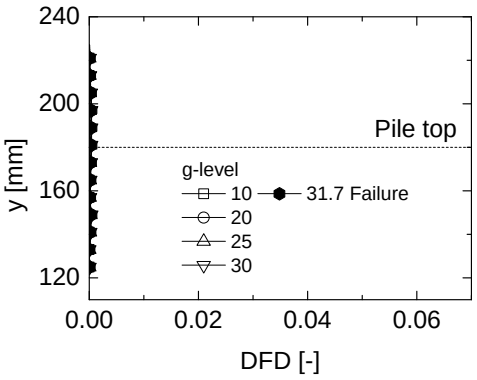

(b) DFD for Δy in test P2PB

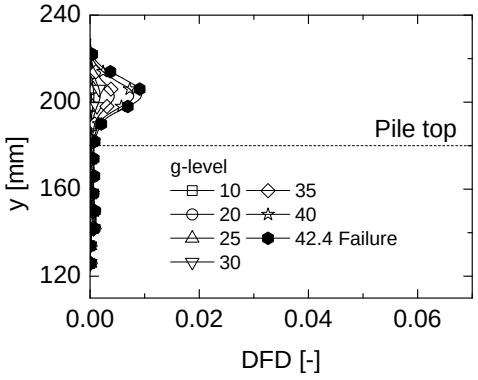

(c) DFD for Δx in test P3PB

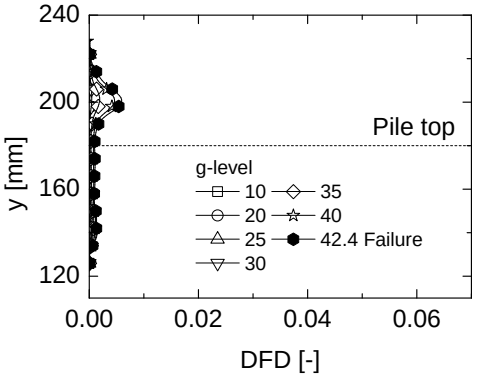

(d) DFD for Δy in test P3PB

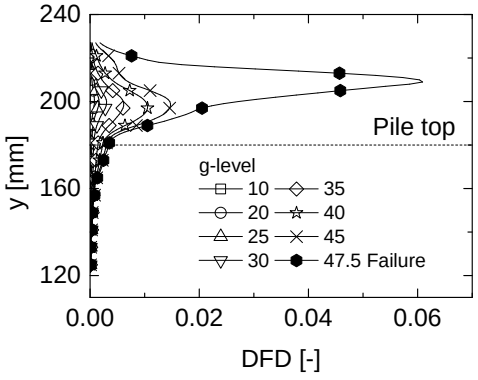

(e) DFD for Δx in test P4PB

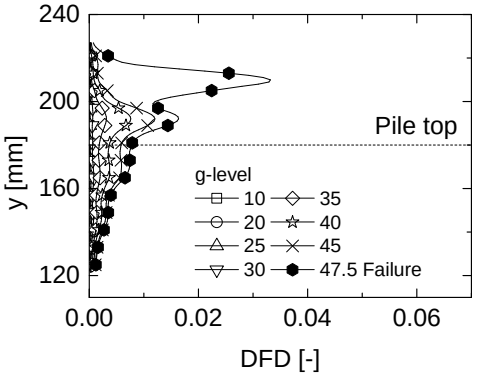

(f) DFD for Δy in test P4PB

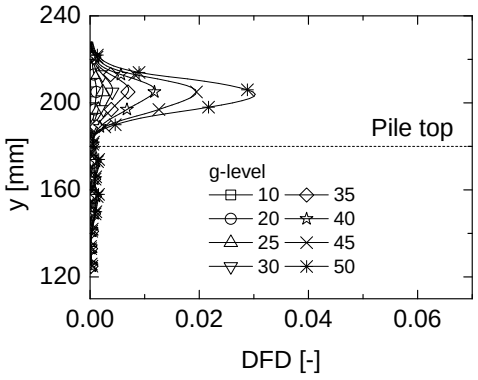

(g) DFD for Δx in test P5PB

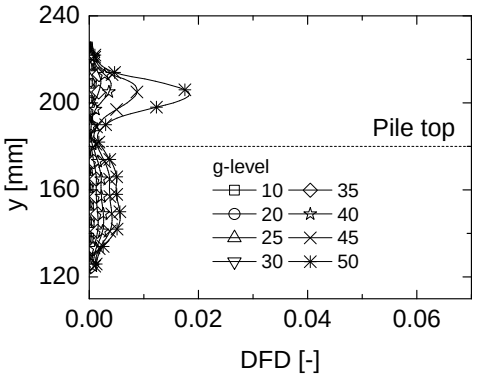

(h) DFD for Δy in test P5PB

Fig. 4.56 DFD for x- and y-displacements (Δx and Δy) at the pile row for P*i*PB.

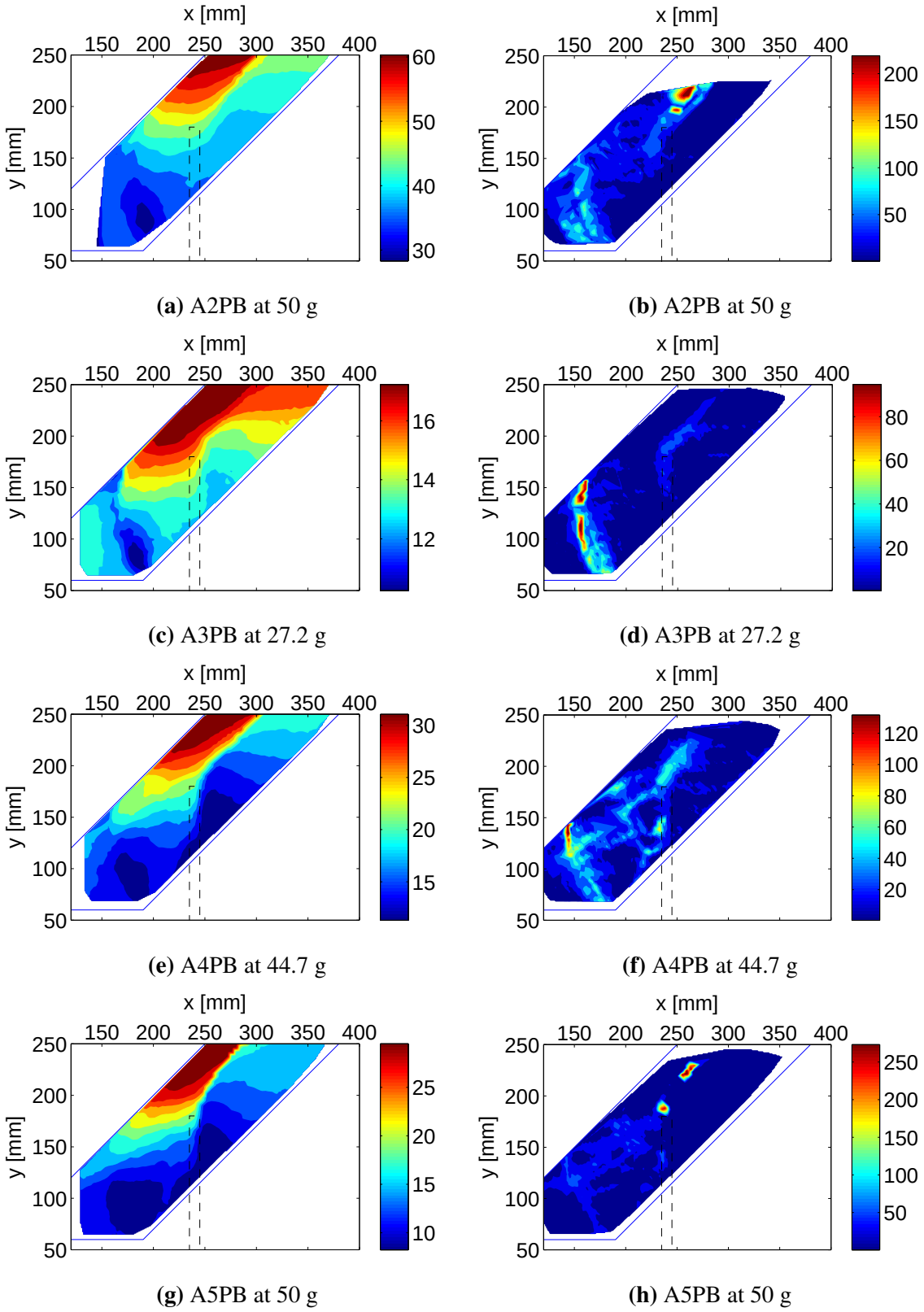

(a) A2PB at 50 g **(b)** A2PB at 50 g

(c) A3PB at 27.2 g **(d)** A3PB at 27.2 g

(e) A4PB at 44.7 g **(f)** A4PB at 44.7 g

(g) A5PB at 50 g **(h)** A5PB at 50 g

Fig. 4.57 PIV computed displacement (subfigures a, c, e, g; unit: mm) and maximum shear strain (subfigures b, d, f, h; unit: %) of the side-view for the test series A*i*PB. Mode of over-top failure is observed. Shear bands above the pile top and along the pile depth tend to form in (d), (f) and (h). The dashed rectangle indicates the initial pile location.

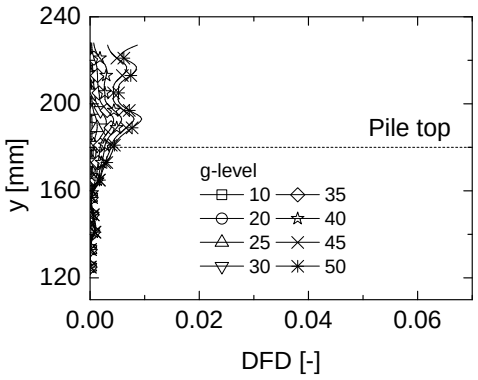

(a) DFD for Δx in test A2PB

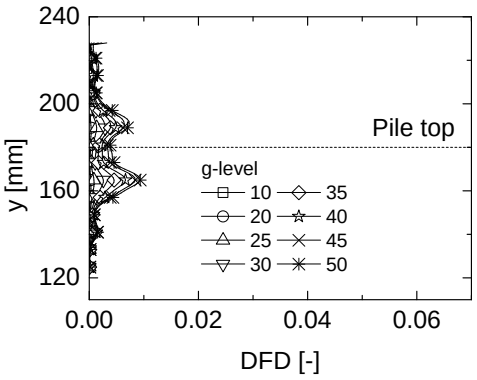

(b) DFD for Δy in test A2PB

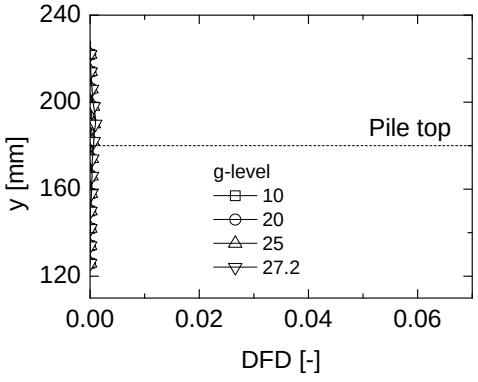

(c) DFD for Δx in test A3PB

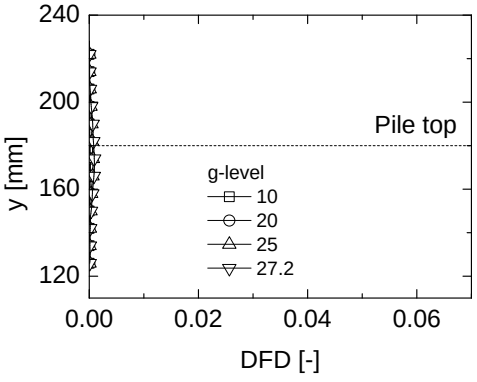

(d) DFD for Δy in test A3PB

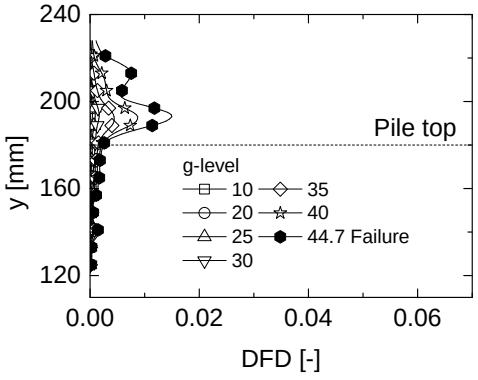

(e) DFD for Δx in test A4PB

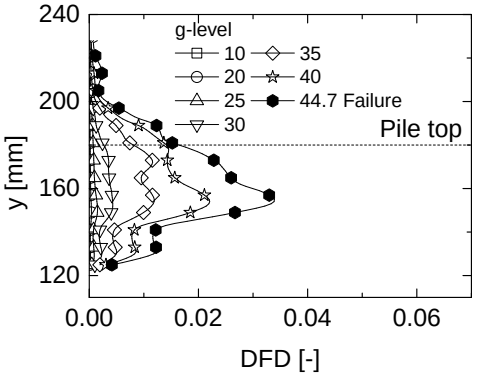

(f) DFD for Δy in test A4PB

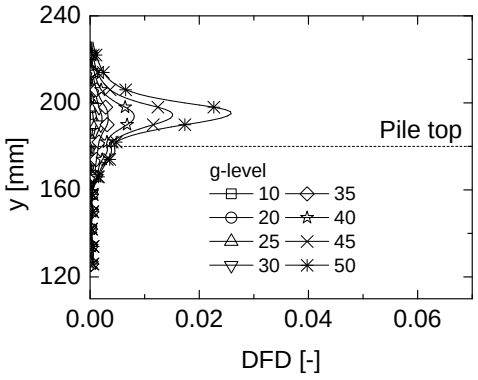

(g) DFD for Δx in test A5PB

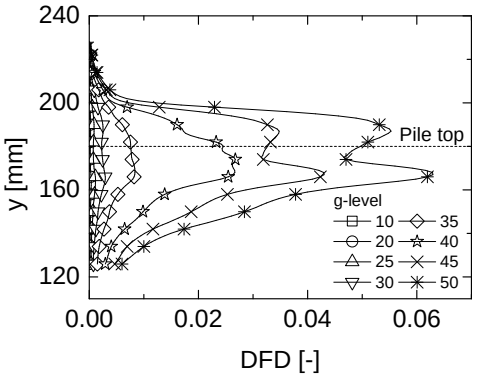

(h) DFD for Δy in test A5PB

Fig. 4.58 DFD for x- and y-displacements (Δx and Δy) at the pile location for A*i*PB.

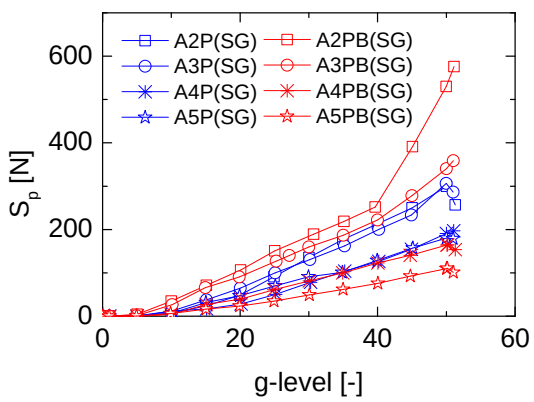

(a) sliding force on the pile

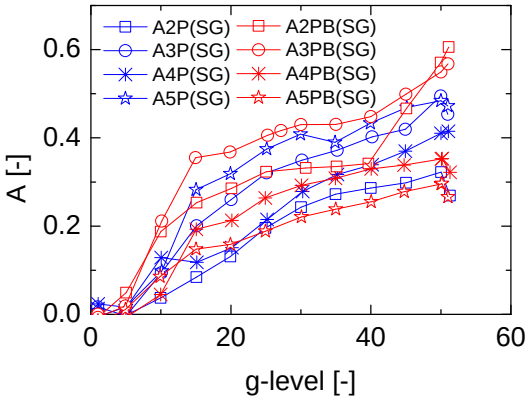

(b) variable A

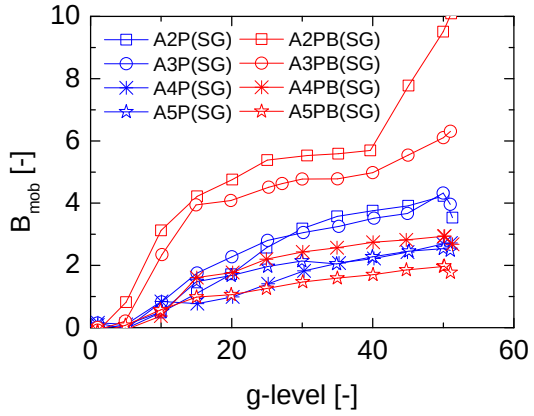

(c) average B_{mob}

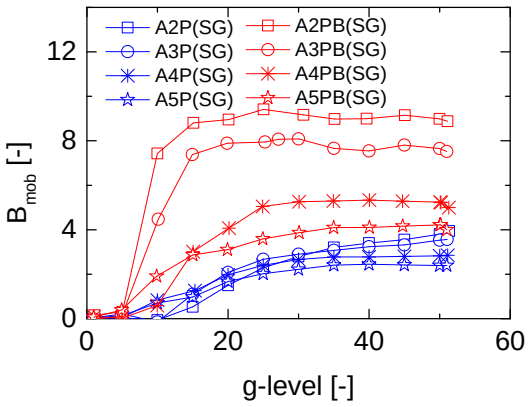

(d) middle B_{mob}

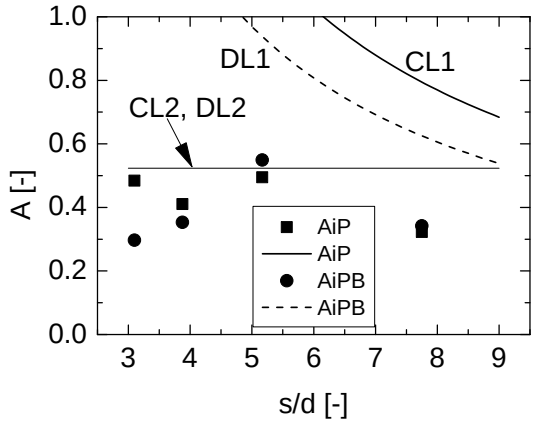

(e) variation of A with s/d

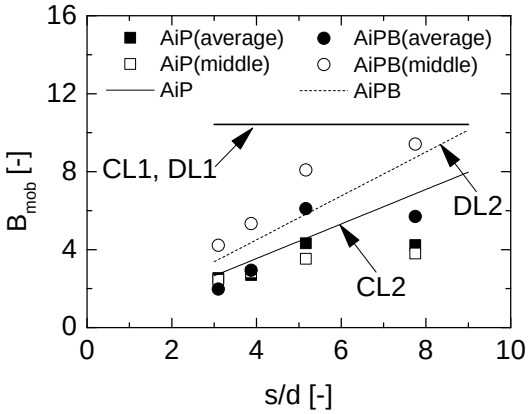

(f) variation of B_{mob} with s/d.

Fig. 4.59 Analysis of the sliding force on the pile. S_p: the sliding force on the pile; A: the ratio of the forces on the piles to the weight of the up-slope soil; B_{mob}: the equivalent soil pressure on the pile normalised by the overburden stress in terms of the average value and the value in the middle of the soil layer. CL1 and DL1 in (f) represent the estimation $B_{max} = {K_p}^2$; CL2 and DL2 in (e) represent the estimation $A_{max} = (1-\alpha)\sin\beta$; CL1 in (e) and CL2 in (f) are respectively derived from CL1 in (f) and CL2 in (e) through the equation $B_{max} = A_{max} \cdot 2(s/d)(l/h)$. DL1 in (e) and DL2 in (f) are respectively derived from DL1 in (f) and DL2 in (e) through equation 4.6.

4.9 Concluding remarks

The effect of pile spacing s/d, bending stiffness EI, slenderness h/d and the relative up-slope soil length l/h on slope stabilization using piles was examined through centrifuge tests. The results were analysed in this chapter. Four failure modes were identified:

- *Flow failure*: Soil flows around the piles when piles are arranged with large spacing (s/d>3.88).
- *Down-slope failure*: Local soil failure tends to occur in the down-slope area while the up-slope soil is stabilized by high stiffness piles arranged with small spacing ($s/d \leq$3.88).
- *Over top failure*: A part of the up-slope soil moves above the pile top. This failure mode is expected when the large l/h (2.43) and small s/d ($\leq$3.88) are adopted. The over-top and down-slope failure movements can merge at the pile row when flexible piles are used.
- *Pile structural failure*: The pile breakage and plastic hinges are observed at a small depth below the slip surface. This failure mode occurs when the ultimate bending moment is reached. The tests with large s/d (>3.88) are prone to this failure mode.

The following conclusions are drawn from the parametric studies:

- As the pile spacing s/d becomes larger (from 3.1 to 7.75), the overall soil displacement and the sliding force on the piles become larger. The failure mode changes from down-slope failure to flow failure.
- When piles with smaller bending stiffness EI are used, the top part of the piles becomes ineffective, at which the over-top movement from the up-slope soil merges with the down-slope soil movement. The overall stability of the slope is reduced.
- By adopting a smaller pile slenderness h/d (from 13 to 7), the relative pile stiffness K_R is increased. The piles have less displacement, therefore a stronger arching effect between the piles is formed and relative higher soil pressure is mobilised.
- By increasing the relative up-slope soil length l/h (from 0.85 to 2.43), a larger overall soil displacement and a larger sliding force on the pile are obtained. However, the mechanism varies with the pile spacing s/d. When s/d is small (3.1), the increase of l/h changes the failure mode from down-slope failure to over-top failure. For large s/d (5.17), a larger l/h can accelerate the flow failure. The influence of l/h can be reduced when flexible piles are used.

- Deep-buried piles can be used when the sliding soil is relatively thick. With a smaller pile length in the sliding soil, the relative pile stiffness K_R is increased, higher soil pressure on the pile is mobilised. The use of deep-buried piles can raise the risk of over-top failure. However, when flexible piles are used, the adoption of deep-buried piles produces even higher slope stability than the full length pile.

Chapter 5

Numerical simulation

5.1 Introduction

In this chapter the pile-soil interaction is further studied using the finite-difference program $FLAC^{3D}$, which is the acronym for Fast Lagrangian Analysis of Continua in three dimensions. It is an explicit finite-difference program for engineering mechanics computation, which is able to simulate the behaviour of three-dimensional structures built of soil, rock or other material that undergo plastic flow when their yield limits are reached. Materials are represented by polyhedral elements within a three-dimensional grid that is adjusted by the user to fit the shape of the object to be modelled. Each element behaves according to a prescribed linear or non-linear stress/strain law in response to applied forces or boundary restraints. The explicit, Lagrangian calculation scheme and the mixed-discretization zoning technique used in $FLAC^{3D}$ ensure that plastic collapse and flow are modelled very accurately. Because no matrices are formed, large three-dimensional calculations can be made without excessive memory requirements. The drawbacks of the explicit formulation (i.e., small time step limitation and the question of required damping) are overcome by automatic inertia scaling and automatic damping that does not influence the model of failure. $FLAC^{3D}$ offers an ideal analysis tool for solution of three-dimensional problems in geotechnical engineering. (ITASCA (2009))

As structures to increase the slope stability, the resistance force from the piles should be maximized. To achieve this aim, the piles should be designed with less deformation to obtain higher soil pressure on the piles. As revealed by the centrifuge study, the pile spacing (s/d), pile bending stiffness (EI) and pile slenderness (h/d) have significant influence on the pile-soil interaction. The advantages of numerical simulation over laboratory tests are its flexibility in defining the geometry and the properties and its accessibility to the soil stress. The intention of the numerical simulation in this chapter is to investigate the pile-

Table 5.1 Mechanical parameters for pile bending test

Elastic modulus E [Pa]	Poisson's ratio μ [-]	Unit weight γ [kN/m^3]	Force along z-axis [N/m]
25×10^9	0.2	2500	1.96×10^4

soil interaction in a more fundamental way rather than to simulate a specific engineering case or experiment. Material properties and geometry simplifications from the literature (Kourkoulis et al. (2010), Kanagasabai et al. (2011), Pan et al. (2012), etc.) are used here. Two horizontal layers (a sliding layer above a stable layer) are modelled. The mechanism of pile-soil interaction, the aforementioned influencing factors as well as the soil properties are examined. Lastly, the plastic deformation theory for the ultimate soil pressure on the pile (p_u) is modified based on the observations in the numerical analysis. The numerically obtained p_u is compared with some empirical estimations and the results from the centrifuge tests.

5.2 Numerical Modelling

Pile is usually simplified as an elastic beam in the analytic and numerical studies. In numerical modelling, it is a generally accepted principle that a finer mesh can generate results with higher accuracy. However, using fine mesh is also time-consuming. An investigation of the suitable mesh size is performed.

Mesh size in two dimensions are the major concerns of this study:

- Mesh size along the pile axis.
- Mesh size between the piles.

5.2.1 Mesh size along the pile axis

A 16 m long vertical pile with a diameter of 1 m is modelled using linear elastic constitutive model. The bottom of the pile is fixed in all the directions. Uniform distributed body force along the lateral direction is applied to induce bending moments in the pile. The mechanical parameters used in this simple pile bending test are listed in Table 5.1.

Figure 5.2.1 shows the pile axis displacement and the internal forces using different number of elements along the pile axis. Corresponding analytical calculations are also presented in the figure. It is seen that the pile displacement and bending moment are sensitive

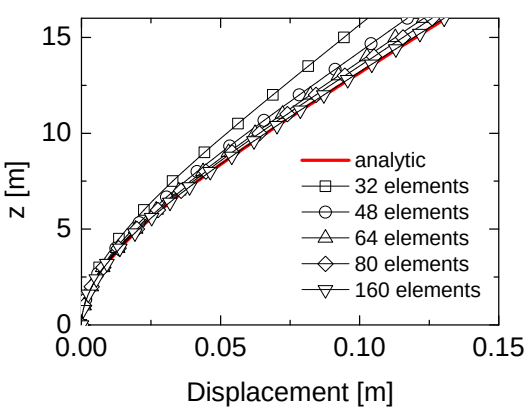

(a) pile axis displacement

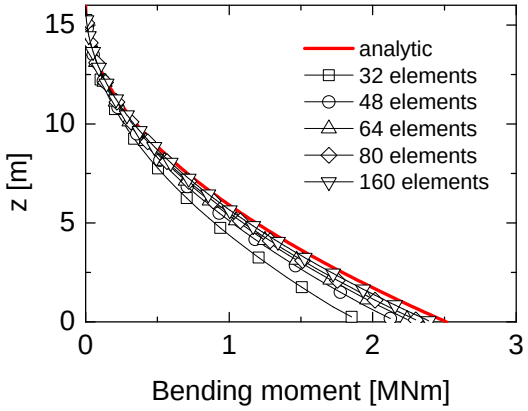

(b) pile bending moment

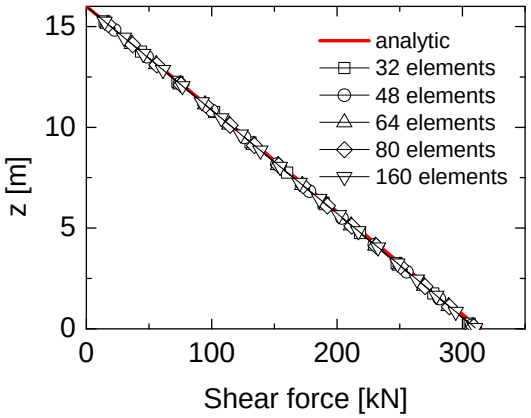

(c) pile cross-sectional shear force

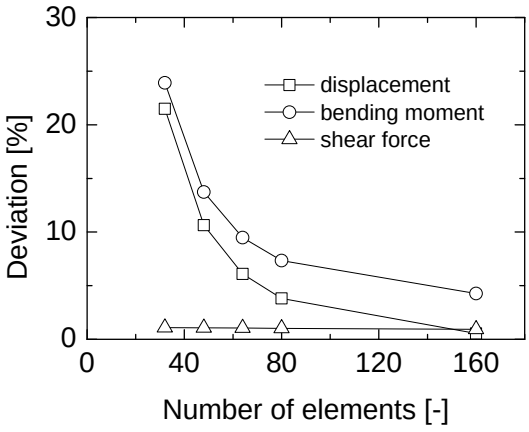

(d) deviation between analytical and numerical results

Fig. 5.2.1 Pile displacement and internal forces with different mesh size. In (d), the deviation of displacement refers to the displacement at the pile top ($z = 16$ m); the deviations of bending moment and shear force refer to the results at the pile tip ($z = 0$ m).

to the mesh size. The deviations of the pile displacement at the pile head (z = 16 m) and the internal forces at the pile tip (z = 0 m) are plotted against the number of elements in Figure 5.2.1d. Improvement of the calculation accuracy can be clearly observed as the number of elements increases. The improvement becomes less effective when the number of elements is larger than 80. Taking the calculation time into consideration, a mesh of 80 elements along the pile axis (element size = 0.2 m) is chosen.

Table 5.2 Soil parameters.

Soil type	Loose silty sand	Dence sand	Soft rock	Rock
Elatic modulus E [Pa]	4.0×10^7	8.0×10^7	3.0×10^9	9.6×10^9
Poisson's ratio μ [-]	0.25	0.3	0.25	0.2
Density γ [kg/m^3]	1900	2000	2200	2400
Friction angle ϕ [°]	28	38	45	45
Cohesion c [Pa]	3.0×10^3	3.0×10^3	5.0×10^4	1.0×10^5
Dilation angle ψ [°]	2	2	5	5

5.2.2 Mesh size between the piles

The arching effect between the adjacent piles is of major concern to this study, a mesh sensitive test along the pile row direction is necessary. As shown in Figure 5.2.2, two horizontal earth layers are modelled: a stationary layer and a sliding layer. The front and rear boundaries are located within a distance of $10d$ (d is the pile diameter) to the pile axis. The side boundaries are symmetrical cross-sectional planes going through the pile axis or the middle point between two adjacent piles. For the side boundaries of both layers and the pile, as well as the front, rear and bottom boundaries of the stationary layer, the movement along the direction which is perpendicular to the boundary plane is fixed. The surface of the sliding layer is free. For the front and rear boundaries of the sliding layer, a continuously increased horizontal displacement is applied to generate the movement of the sliding layer. The interaction between the pile and the surrounding soil is implemented through an intrinsic interface model in $FLAC^{3D}$. Mohr-Coulomb constitutive model and linear elastic model are used for the earth layers and the pile, respectively. The soil properties used in this chapter are listed in Table 5.2.

In this calculation, the sliding layer of loose silty sand and the stable layer of rock are adopted. The pile axis-to-axis distance (s) is equal to $4d$. The frictionless interface between the stable and sliding layers is assumed. Calculations using different mesh densities between the piles are performed. Figure 5.2.3 shows a part of the aerial view of the 3D mesh with the mesh size of 0.2 m along the pile row direction. The mesh size along the sliding direction (y direction) remains constant within the distance of $1d$ from the pile row. It increases with a constant ratio to the mesh size of 1 m at the front and rear boundaries. Several mesh sizes (namely, 0.167 m, 0.2 m, 0.25 m, 0.333 m and 0.5 m) are considered.

The calculation results with different mesh size are shown in Figure 5.2.4. The total force on the pile is not sensitive to the mesh size. The force distribution along the pile depth gives the same conclusion except that abnormal result is obtained when the mesh size is 0.5 m. The displacements of a group of grid nodes, located in the cross-section AA' (Figure 5.2.3)

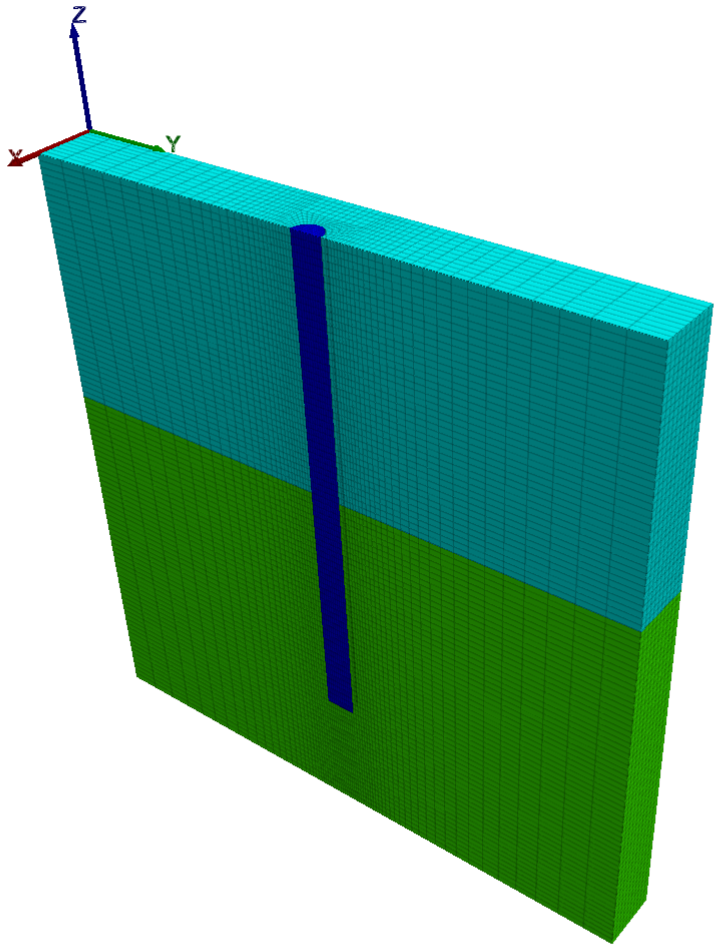

Fig. 5.2.2 3D mesh. Green: stable layer; Cyan: sliding layer; Blue: pile.

at the depth of 8 m (at the sliding surface) when the boundary displacement (*BD*) is 50 cm, are plotted in Figure 5.2.4c. It also shows that the mesh size has no influence on the soil movement when it is not larger than 0.333 m. Taking into account the calculation time, the mesh size of 0.25 m between the piles is chosen.

5.2.3 The effect of friction at pile-soil interface

The friction of the interface between the pile and the soil can also affect the pile response. As shown in Figure 5.2.5, the same model is calculated using different friction angle for the pile-soil interface. The total force applied on the pile increases as the friction angle increases. The interface friction is mainly affected by factors such as the pile material and the construction method, which, however, are not considered in this study. In the following

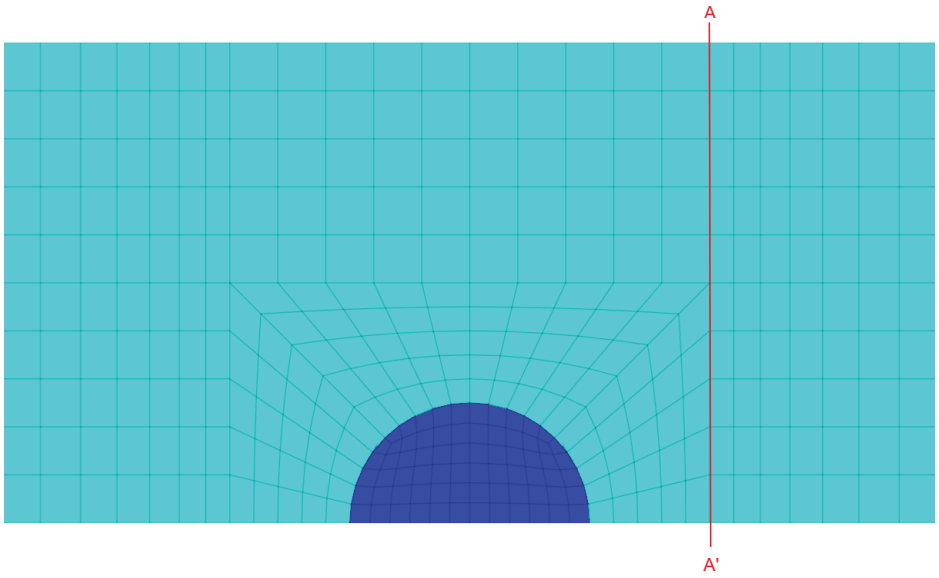

Fig. 5.2.3 Part of the mesh in aerial view. Blue: pile; Cyan: sliding layer. AA': a cross-section with a distance of d to the pile row.

calculation the friction angle of the pile-soil interface is set to be half of the soil internal friction angle.

5.2.4 The effect of at-rest lateral earth pressure coefficient K_0

The at-rest lateral earth pressure is the in-situ lateral pressure, which can be measured directly by a dilatometer test (DMT) or a borehole pressuremeter test (PMT). As these are rather expensive tests, empirical equations are usually adopted. One of the most commonly used equations is proposed by Jaky (1948) for normally consolidated soil:

$$K_{0(NC)} = 1 - \sin\phi' \tag{5.1}$$

where K_0 is the at-rest lateral earth pressure coefficient; ϕ' is the effective friction angle of soil. For over consolidated soil, Mayne and Kulhawy (1982) proposed the following relation:

$$K_{0(OC)} = K_{0(NC)} OCR^{\sin\phi'} \tag{5.2}$$

where OCR is the over consolidated ratio of soil.

As for the at-rest lateral pressure coefficient for rock, measured data (Hoek and Brown (1980)) shows that for the rock layer in the uppermost earth crust, the ratio of lateral stress

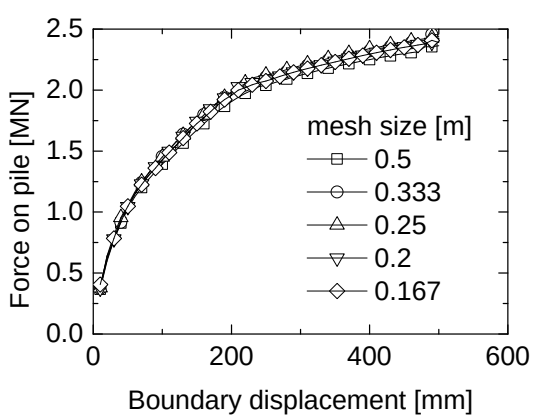

(a) total force applied on the pile

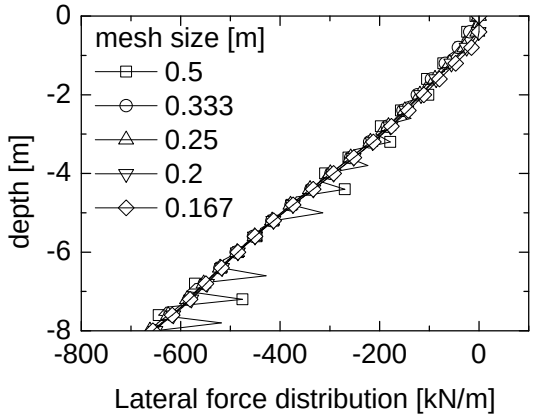

(b) force on the pile

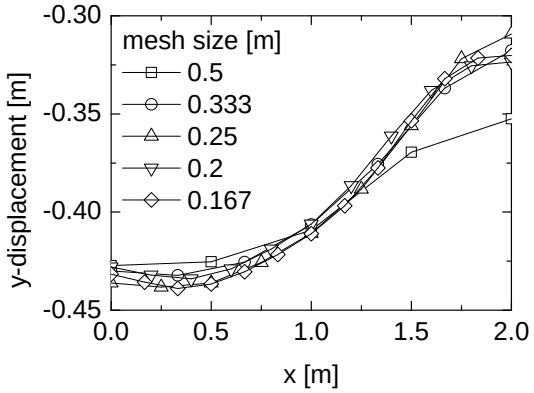

(c) soil movement of the grid points in the cross-section AA' at the depth of 8 m

Fig. 5.2.4 Comparison of the calculation results for different mesh size along the pile row. The force values in (a) and (b) are results for the half pile model when $BD = 50$ cm. In (c), x is the coordinate of the grid points in the cross-section AA' in Figure 5.2.3.

to vertical stress is most likely to be higher than 1. For the bed rock in the calculation, the initial lateral stress is set equal to the vertical stress (i.e., $K_0 = 1$).

For the unstable soil layer, two cases ($K_0 = 1$ and $K_0 = 1 - \sin\phi'$) are calculated to study the effect of K_0. Figure 5.2.6 shows the total force on the pile (P) plotted against the soil boundary displacement (BD) for various s/d and h/d (h is the thickness of the unstable layer). It can be concluded that K_0 has no influence on the ultimate lateral force on the pile. However, the soil boundary displacement, at which the total force on the pile reaches its ultimate, becomes larger when a smaller K_0 is used. It is reasonable since the lateral stress in the soil is gradually increased to be the maximum principle stress due to the pile resistance. A larger initial lateral stress in soil can therefore reduce the soil displacement that is needed

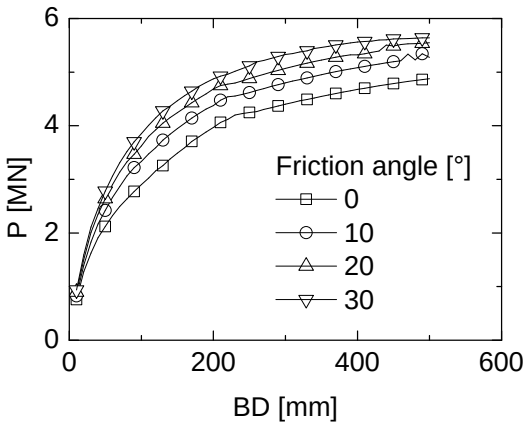

Fig. 5.2.5 Effect of the friction at the pile-soil interface. P: total force on the pile. BD: boundary displacement.

for P to reach its maximum. Considering that the lateral soil stress in an unstable slope is usually larger than the lateral soil stress in the horizontal ground and the ultimate force on the pile is the major concern of this chapter, $K_0 = 1$ is adopted in the following calculations.

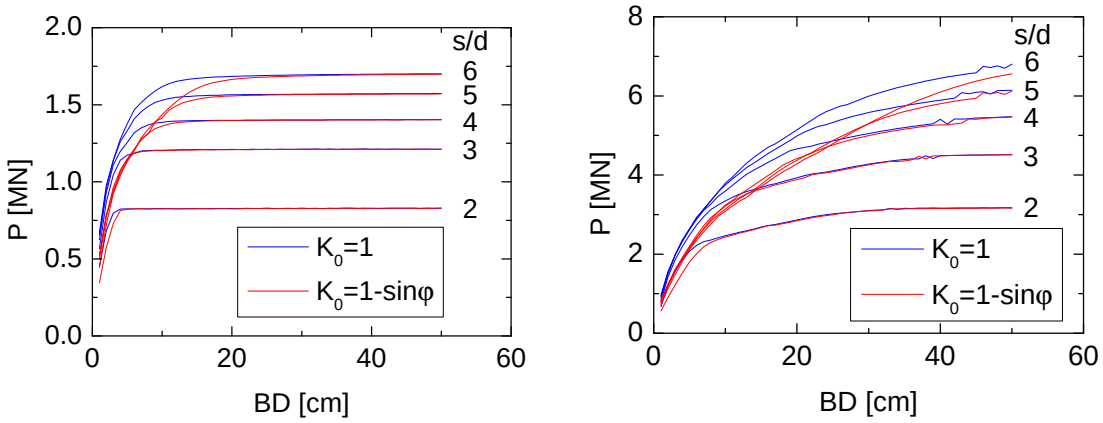

(a) $h/d = 4$ **(b)** $h/d = 8$

Fig. 5.2.6 Comparison of the total force on the pile (P) for different K_0.

5.3 The mechanism of pile stabilizing

The result of a calculation (s/d=4, h/d=8) is presented here to reveal the mechanism of pile stabilizing. The total force (P) applied on the pile and its depth are plotted against the soil boundary displacement (BD) in Figure 5.3.1. The depth of the turning point, at which the lateral pressure changes its direction, is also plotted in the figure. The depth of 0 m for the turning depth means that the lateral pressure has only one direction i.e. the direction of soil movement. As shown in the figure, P increases rapidly in the first 20 cm soil movement. Afterwards, P increases slightly and reaches its ultimate value gradually. Meanwhile, when BD is small (< 20 cm), the top part of the pile pushes the sliding soil and generates a negative lateral force, which disappears after about 20 cm BD. In the whole loading process, the depth of P increases gradually and reaches a constant value.

Figure 5.3.2 shows the increase of the soil pressure p on the pile at different depth during the calculation. For the pile part near the sliding surface (depth = 4 $\sim$ 8 m), p reaches its ultimate quickly before about 20 cm BD. For the top part of the pile (depth < 3 m), negative soil pressure is observed. As the application of soil movement continues, p increases slowly to a positive value and then reaches an ultimate value gradually. Figure 5.3.3 shows the relative soil-pile displacement along the depth at various BD values. The displacement corresponds with the observation of p. The negative relative displacement is observed from the ground surface to about the depth of 2 m, and it disappears totally after about 30 cm BD.

Figure 5.3.4 shows the maximum shear stress in the soil at various BD values. Each sub-figure consists of a upper contour diagram of the yz cross-section going through the pile axis and a lower contour diagram of the xy cross-section at the sliding surface. It is seen that the large shear stresses, which are observed in an area with a cone shape, have emerged in the first 20 cm of BD. As the soil moves further, the area of the large shear stresses spreads upwards to the soil surface, i.e., the cone is enlarged to reach the soil surface.

The mechanism of pile stabilizing can be concluded into two stages: The first stage is the quick mobilization of the soil near the sliding surface. The second stage is the slow mobilization of the soil close to the ground surface. The mobilization of the shallow soil starts also at the beginning of the soil movement. It becomes the main contribution to the further increase of P in the second stage.

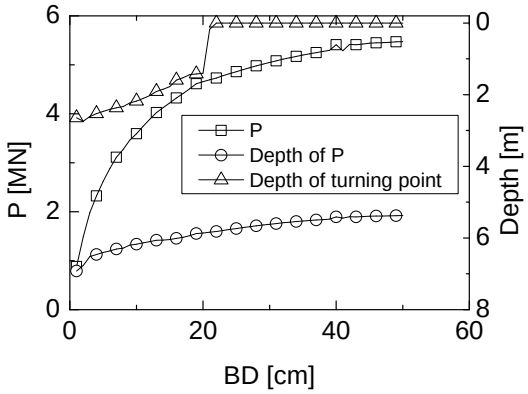

Fig. 5.3.1 Total force P on the pile with $s/d = 4$ and $h/d = 8$. Depth of 0 m is the pile top.

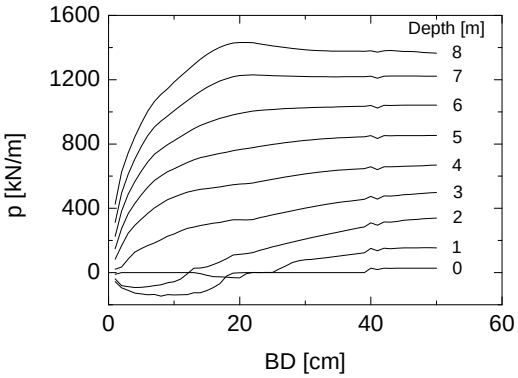

Fig. 5.3.2 Variation of the soil pressure p with depth and BD. Depth of 0 m is the pile top.

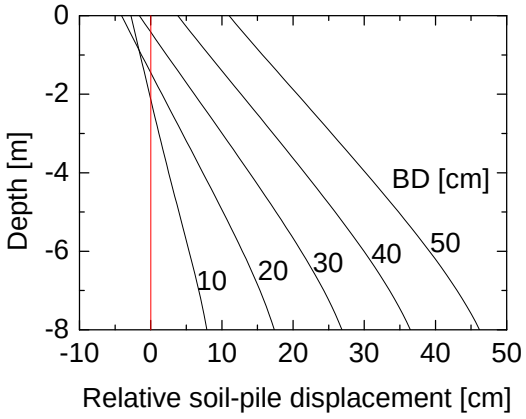

Fig. 5.3.3 Relative soil-pile displacement. Depth of 0 m is the pile top.

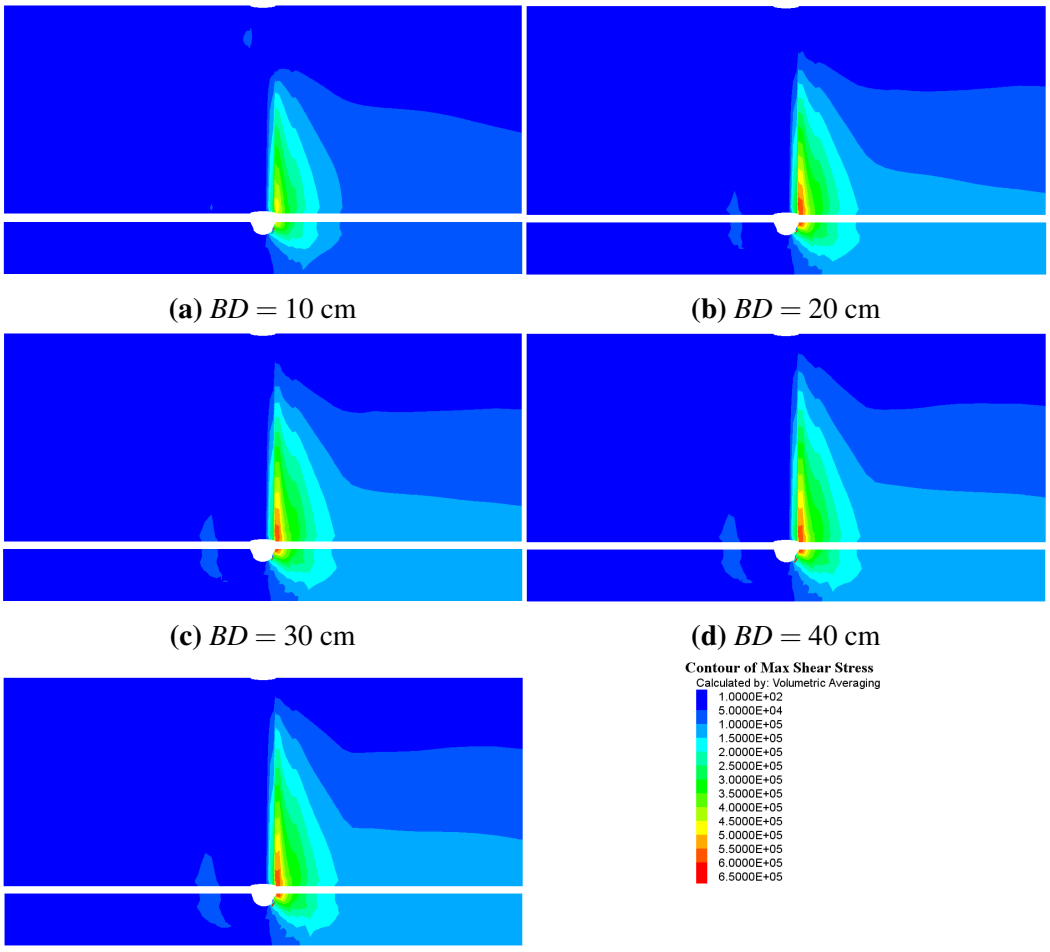

(a) $BD = 10$ cm **(b)** $BD = 20$ cm

(c) $BD = 30$ cm **(d)** $BD = 40$ cm

(e) $BD = 50$ cm

Fig. 5.3.4 Maximum shear stress [Pa]. In each sub-figure, the upper contour diagram denotes the yz cross-section going through the pile axis and the lower contour diagram denotes the xy cross-section at the sliding surface.

5.4 The role of pile spacing s/d

The calculations are performed with integer values of pile spacing (s/d = 2, 3, 4, 5 and 6). In order to facilitate the analysis, the soil pressure on the pile (p) is normalised by the initial vertical stress (σ_{v0}) and the total force on the pile (P) is normalised by the integration of the initial vertical stress along the depth $I_{v0} = \int_0^h \sigma_{v0}\,\mathrm{d}z$. The increases of P/I_{v0} with the soil boundary displacement (BD) for various s/d are plotted in Figure 5.4.1. In this series of calculation ($h/d = 8$), the material in the sliding layer and the stable layer are loose silty sand (loose sand in the following text) and rock, respectively. The pile embedded length is equal to the cantilever part (i.e., the pile length in total is 16m). For each calculation, P/I_{v0} has experienced two stages of increasing. In the first stage, P/I_{v0} increases rapidly for a small soil movement. This part of the curves tends to coincide. As s/d becomes larger, the duration of this stage extends. In the second stage, P/I_{v0} only increases slightly, which indicates that the ultimate value is being reached. In this study the P at the soil boundary displacement of 50 cm ($0.5d$) is regarded as the ultimate force on the pile (P_u). The corresponding soil pressure p distributed along the pile depth is considered as the ultimate soil pressure on the pile (p_u).

Figure 5.4.2 shows the distribution of the normalised p_u along the depth and the increase of the normalised P_u with s/d. The distribution of the normalised p_u is nearly uniform along the depth except the shallow soil part (about 0~2 m). In this case, the soil pressure can be considered as fully mobilised along the depth. With the increase of s/d, p_u becomes larger and so is the normalised P_u. However, the increasing rate reduces gradually with the increase of s/d. In theory, P_u should remain constant and be equal to the P_u of the single pile case when s/d is large enough. Due to the constraints of the prescribed mesh, when a extremely large s/d is adopted, the large soil pile relative displacement may cause an additional calculation error. Therefore, s/d larger than 6 is not calculated.

Figure 5.4.3 shows the displacement of the pile axis and the soil profile located in the middle of two adjacent pile axes. Both the pile displacement and the soil displacement increase with the application of boundary displacement. The difference between the soil and pile displacement is small when $s/d = 2$. The effect of the piles on the soil displacement becomes much smaller when s/d increases to 3 and the piles becomes nearly ineffective for even larger s/d. This observation is very clear in Figure 5.4.3f where all the displacements at $BD = 50$ cm are plotted. $s/d = 4$ or a value between 3 and 4 can be considered as the critical s/d, at which the soil arching effect can be considered to be fully mobilised and will reduce with a higher s/d. This agrees well with the observation in Figure 5.4.2 that the increasing rate of P_u reduces after about $s/d = 4$.

The soil normal stresses *Sxx*, *Syy* and *Szz* on the *xy* cross-section at the depth of 8 m (the slip surface) normalised by the initial vertical soil stress $\sigma_{vo} = \gamma z$ are shown in Figure 5.4.4, 5.4.5 and 5.4.6, respectively. As the soil moves through the gap between the piles, a certain region in the up-slope (right side of the pile) has experienced a rapid increase of stresses while stress decrease is observed in a certain region in the down-slope (left side of the pile). A larger increase of stresses and a larger amount of mobilised soil in the up-slope are observed when the pile spacing becomes larger.

Three representative elements (#1, #2 and #3), are chosen to reveal the stress paths in the different regions of the soil. They are located on the symmetry cross-sections and therefore their principle stresses coincide with the normal stresses along the coordinate axes. Figure 5.4.7 shows the stress paths of the three elements in the case of $s/d = 4$. The failure surface is represented by the 3D surface OABCDEF according to the Mohr-Coulomb criteria for cohesionless soil. Element #1 is located in the up-slope side with a distance of d to the pile axis. For this element, the normal stresses in all the directions have increased multiple times, in which Syy^N heads the list with a maximum of about 8. With the large increase of Syy^N, the stress status has moved from the initial status ($Sxx^N = Syy^N = Szz^N = 1$) towards the failure surface near OF. Element #2 lies in the symmetry cross-section between the piles with a distance of $2d$ to the up-slope side. For this element, the main variation in stresses is the increase of Sxx^N, which leads the stress status towards the failure surface near OB. However, the stress growth rate in this region is small (about 2.5 times). Element #3 is located in the down-slope side with a distance of $1d$ to the pile axis. In this region the stresses have all decreased, in which Syy^N has the largest decrease. As a result, the stress status has moved towards the failure surface near OC.

Among these three normal stresses, *Syy* is the one with the most interest. As for the distribution of Syy^N, Figure 5.4.8 shows Syy^N on the *xz* cross-section that goes through the pile row ($y = 10$ m). For each case, Syy^N is not homogeneous along x axis: the further the soil is located from the pile (right side of the figure), the larger the Syy^N value. However, along z axis Syy^N is almost homogeneous. As the at-rest lateral soil pressure coefficient of 1.0 is chosen in the modelling, the initial value of Syy^N is 1.0. In the cases of $s/d = 2$ and $s/d = 3$, Syy^N is smaller than 1, which means that the soil stress from the up-slope soil is effectively transferred to the piles. In the case of $s/d = 4$, the value of Syy^N around 1 has appeared at about $x = 0m$ (the middle between two piles). As s/d becomes even larger, more soil between the piles with larger Syy^N is observed. The observations from the soil stress at the pile row confirms the previous conclusion that the soil arching between the piles is fully mobilised at about $s/d = 4$ or a value between 3 and 4.

The average Syy^N of the xz cross-section at the pile row (without the part from the surface to one diameter depth) is plotted in Figure 5.4.9 against the soil boundary displacement (BD). For each test, with the application of BD, the average Syy^N first decreases rapidly from 1 to a minimum value at about $BD = 10$ cm, then it increases in the next 15 cm to 20 cm BD and at last it either decreases ($s/d = 2,3$) or increases slightly ($s/d = 4,5,6$) to reach an approximately constant value. This is also an evidence for the different level of arching effect with various s/d. In general, the larger the s/d, the larger the average Syy^N, which is already observed in Figure 5.4.8.

Figure 5.5.8 shows the average Syy^N along the x axis at several depths ($z = 1,2,...,8$) with 50 cm BD. In the up-slope ($y > 10$ m), the average Syy^N is close to K_p (the Rankine passive lateral earth pressure coefficient). It decreases rapidly at about the pile row ($y = 10$ m) to a value near K_a (the Rankine active lateral earth pressure coefficient) in the down-slope ($y < 10$). With the increase of s/d, Syy^N is reduced in the up-slope but increased in the down-slope, which is clearly compared in Figure 5.4.10f where the Syy^N at $z = -8$ m of all the cases are plotted. When s/d is larger than 4, the variation becomes relatively smaller.

To sum up, the pile spacing s/d has significant influence on the arching effect between the piles. As s/d increases to a critical value (between 3 and 4), the arching effect is fully mobilised. For further increase of s/d, the arching effect becomes weaker, soil flows through the piles and more soil pressure is transferred to the down-slope.

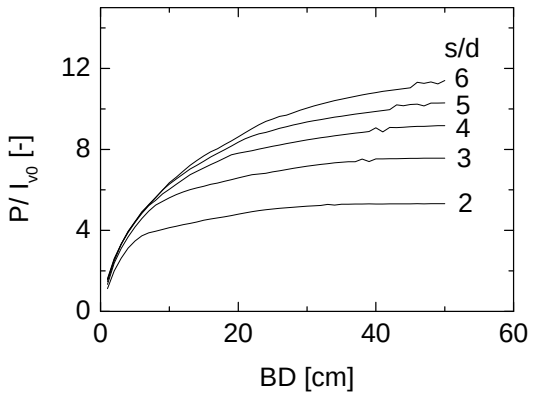

Fig. 5.4.1 Increase of the normalised P with BD and s/d ($h/d = 8$, $I_{v0} = \int_0^h \sigma_{v0}\,dz$).

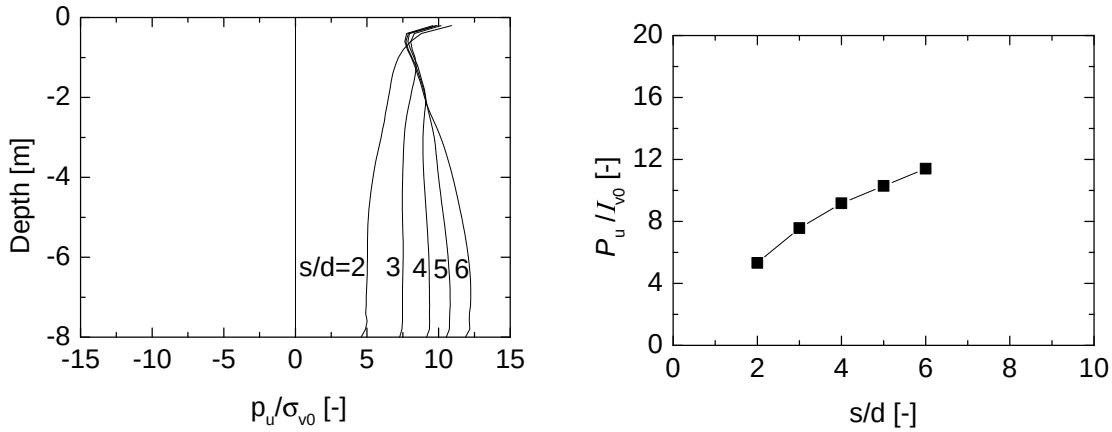

(a) normalised p_u **(b)** normalised P_u

Fig. 5.4.2 Soil pressure and total force on the pile for different s/d.

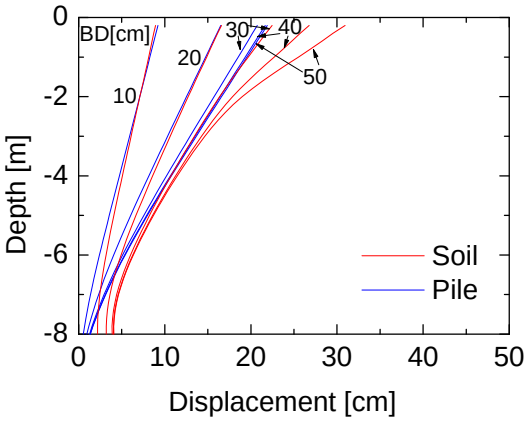

(a) $s/d = 2$

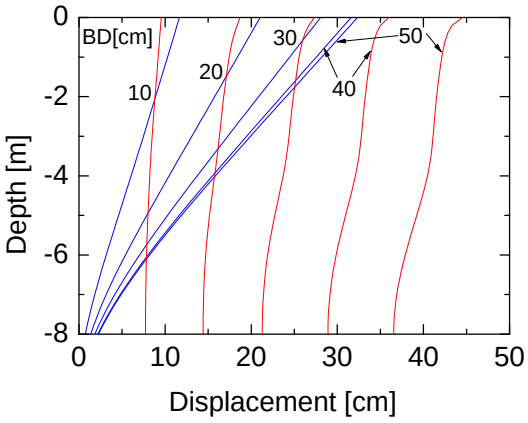

(b) $s/d = 3$

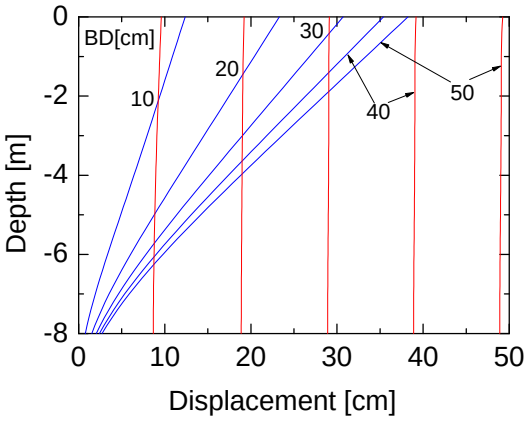

(c) $s/d = 4$

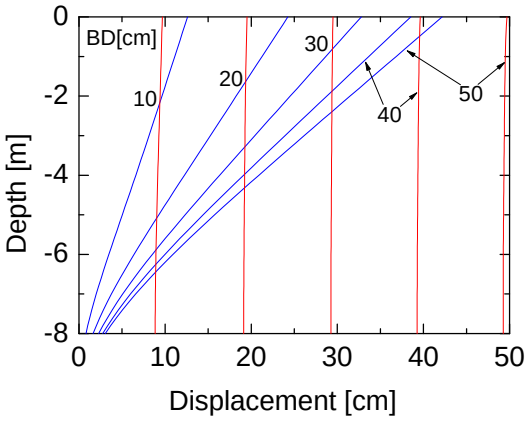

(d) $s/d = 5$

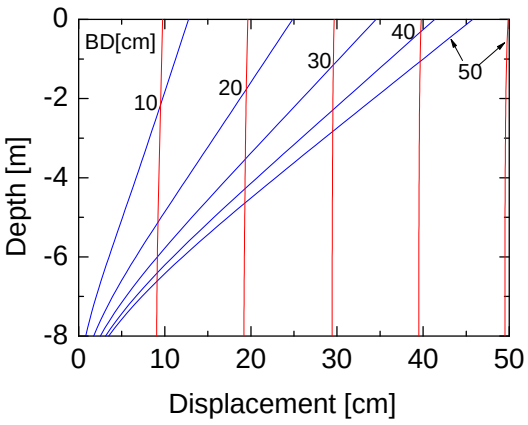

(e) $s/d = 6$

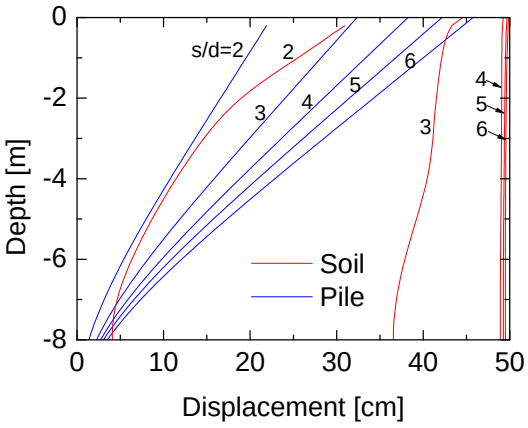

(f) $BD = 50$ cm

Fig. 5.4.3 Pile and soil displacements. The soil profile is located in the middle between two adjacent piles. Sub-figure (f) plots the displacements for different s/d when $BD = 50$ cm.

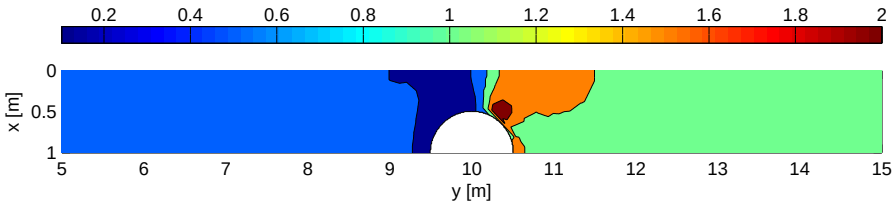

(a) $s/d = 2$

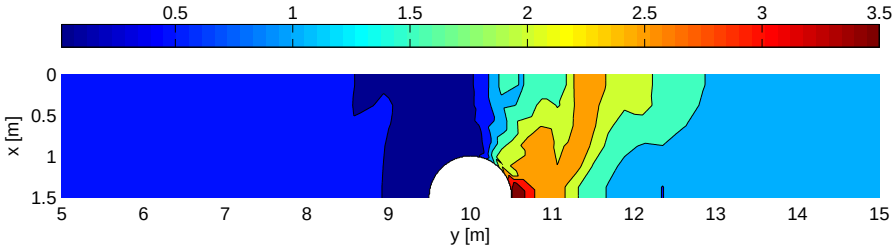

(b) $s/d = 3$

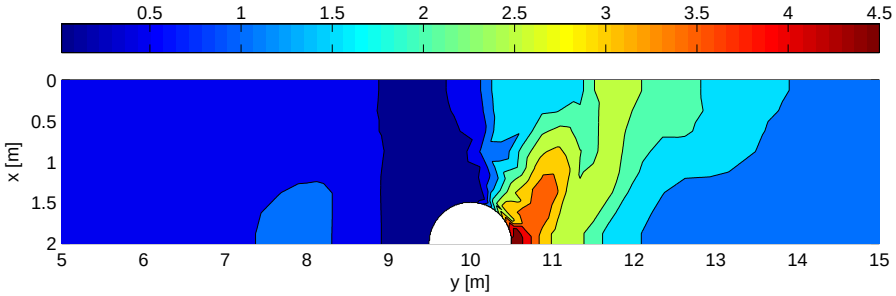

(c) $s/d = 4$

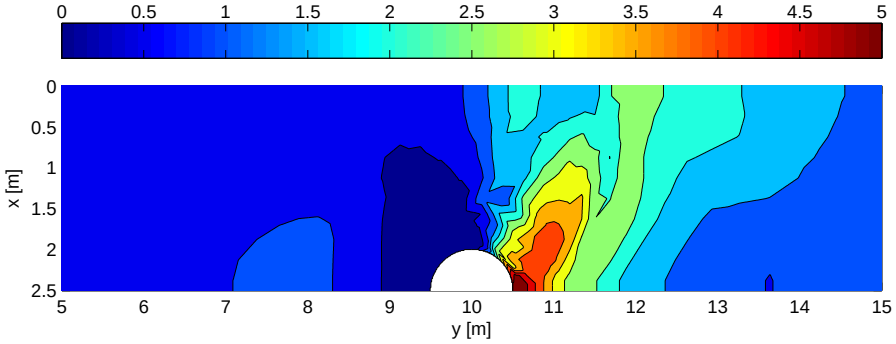

(d) $s/d = 5$

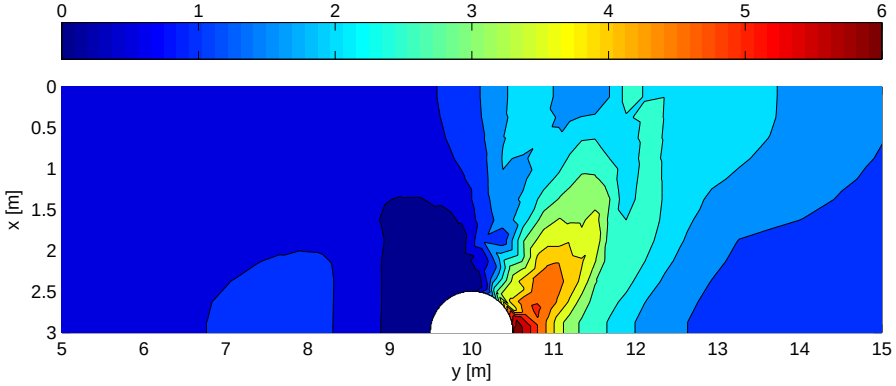

(e) $s/d = 6$

Fig. 5.4.4 Sxx^N on the xy cross-section at the slip surface ($z = -8$ m). Stress increases in the up-slope side (right) and decreases in the down-slope side (left). Value of 1 means the current stress is equal to the initial stress level.

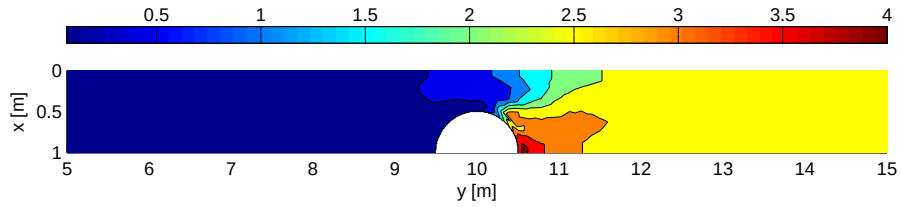

(a) $s/d = 2$

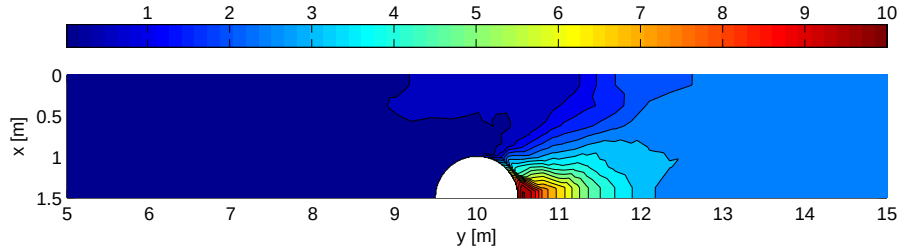

(b) $s/d = 3$

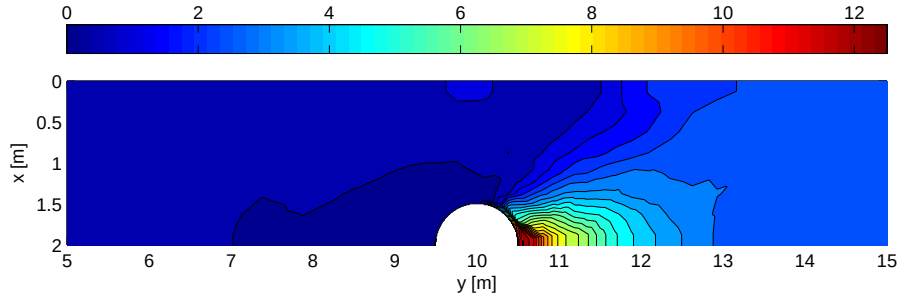

(c) $s/d = 4$

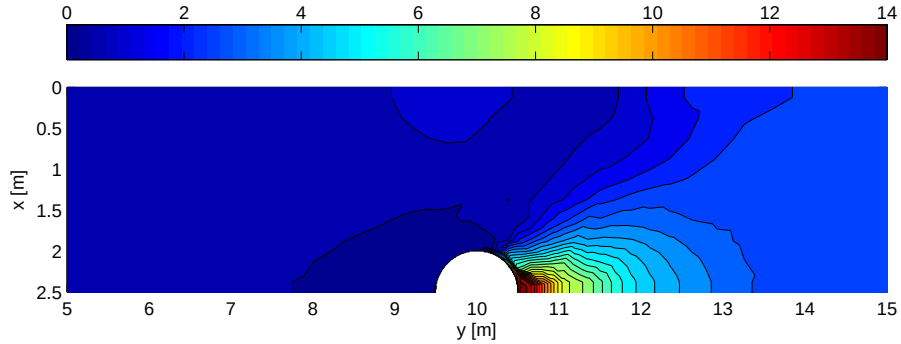

(d) $s/d = 5$

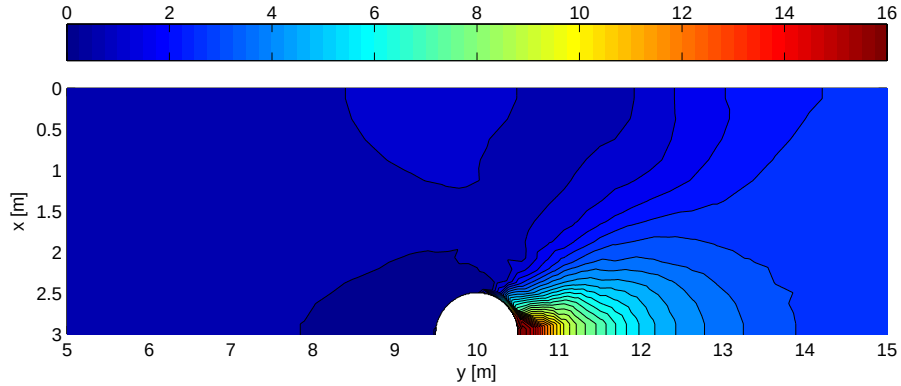

(e) $s/d = 6$

Fig. 5.4.5 Syy^N on the xy cross-section at the slip surface ($z = -8$ m). Stress increases in the up-slope side (right) and decreases in the down-slope side (left). Value of 1 means the current stress is equal to the initial stress level.

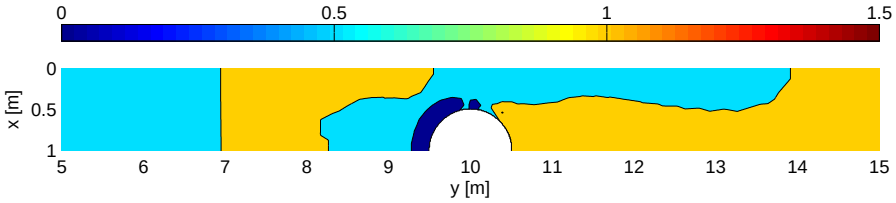

(a) $s/d = 2$

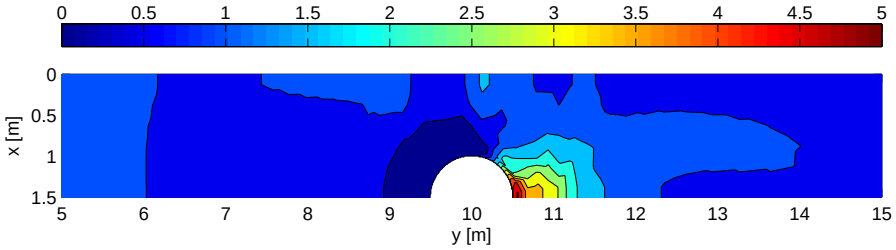

(b) $s/d = 3$

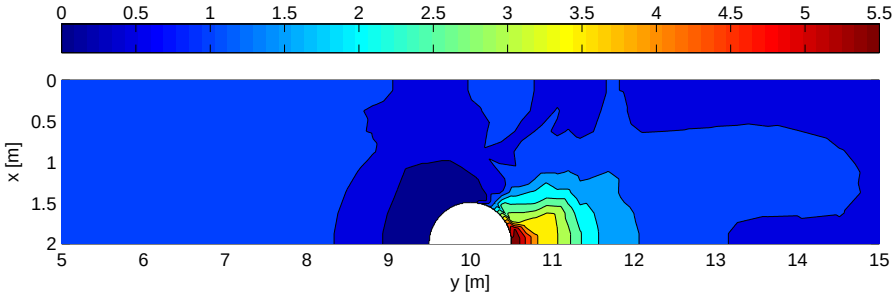

(c) $s/d = 4$

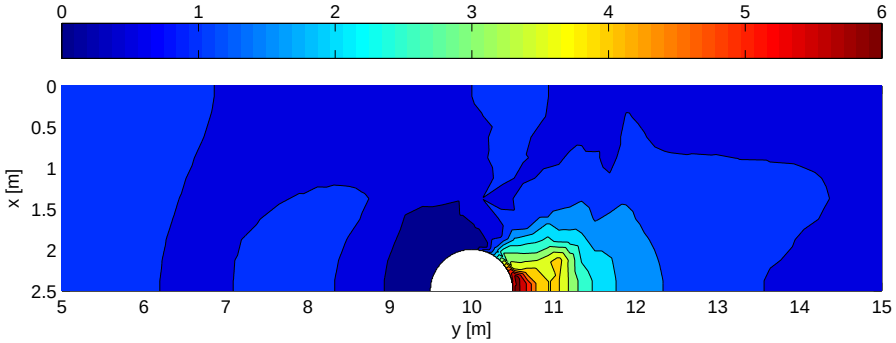

(d) $s/d = 5$

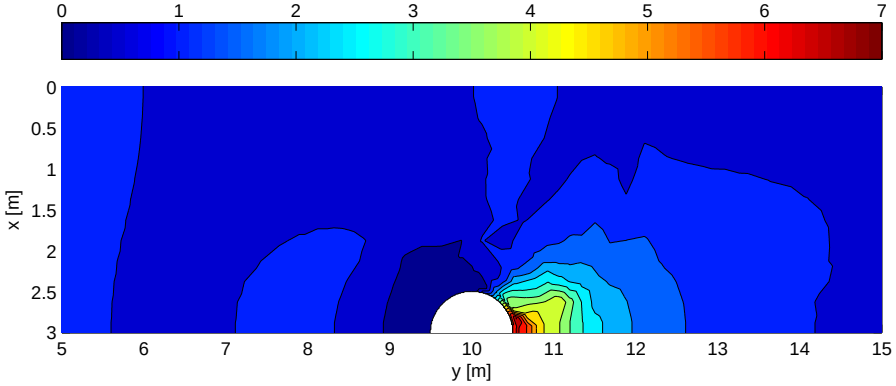

(e) $s/d = 6$

Fig. 5.4.6 Szz^N on the xy cross-section at the slip surface ($z = -8$ m). Stress increases in the up-slope side (right) and decreases in the down-slope side (left). Value of 1 means the current stress is equal to the initial stress level.

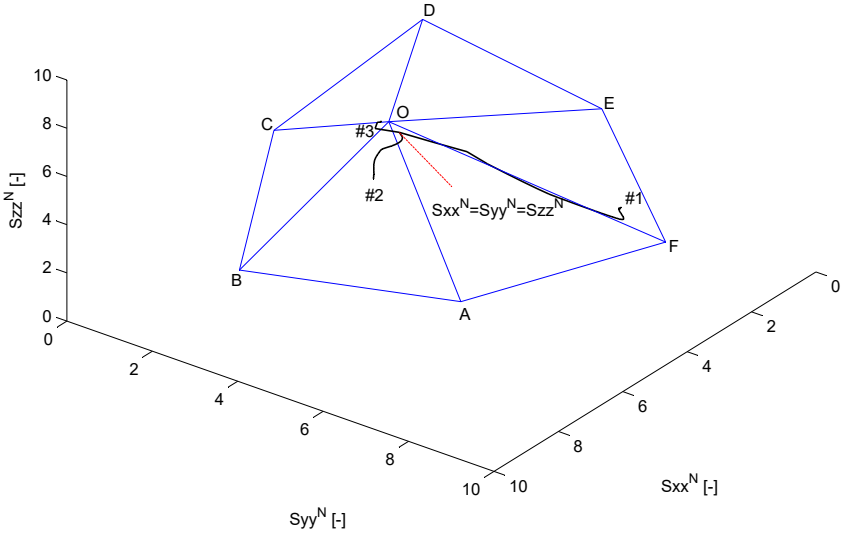

Fig. 5.4.7 Stress paths of the representative elements.

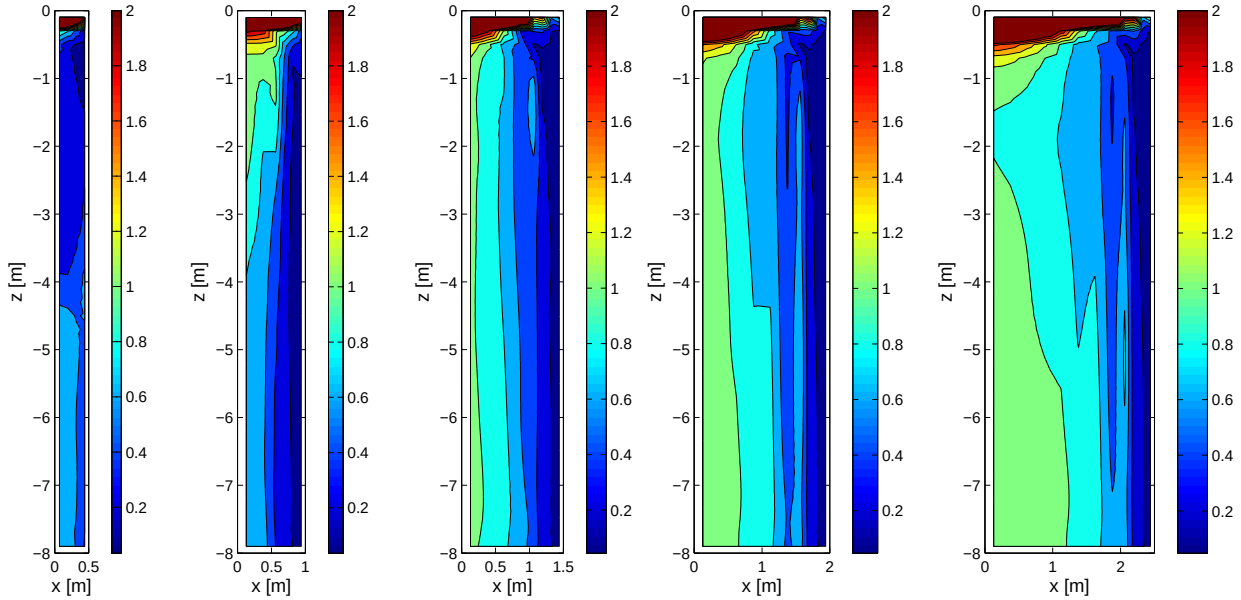

(a) $s/d = 2$ **(b)** $s/d = 3$ **(c)** $s/d = 4$ **(d)** $s/d = 5$ **(e)** $s/d = 6$

Fig. 5.4.8 Syy^N on the xz cross-section at the pile row ($y = 10$ m). $x = 0$ m is the middle point between the piles. The pile-soil interface is located at the maximum of x axis. Syy^N value of 1 means the current stress is equal to the initial stress level.

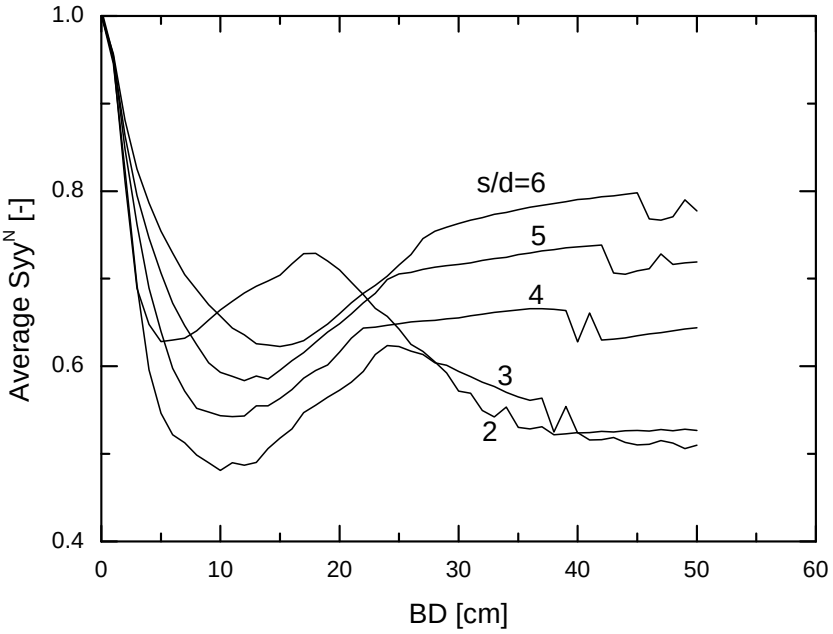

Fig. 5.4.9 Average Syy^N of the XZ cross-section at the pile row ($y = 10$ m).

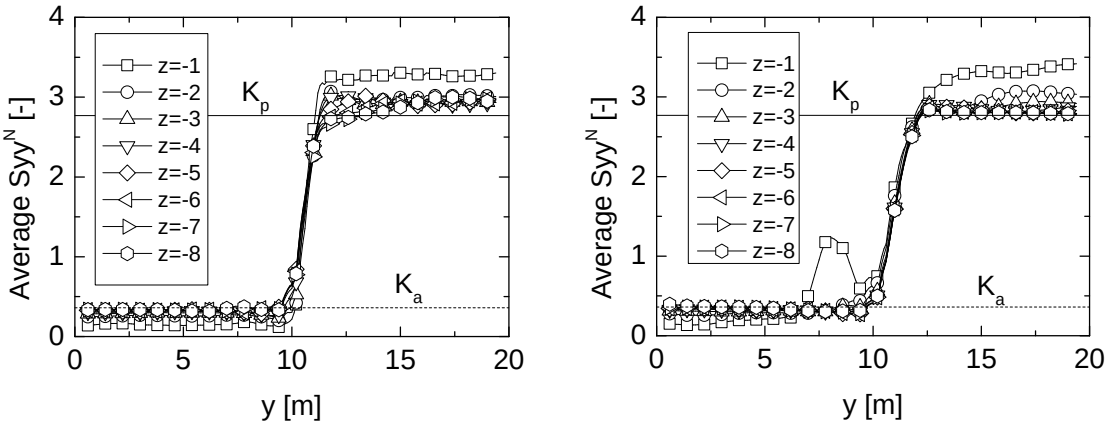

(a) $s/d = 2$ **(b)** $s/d = 3$

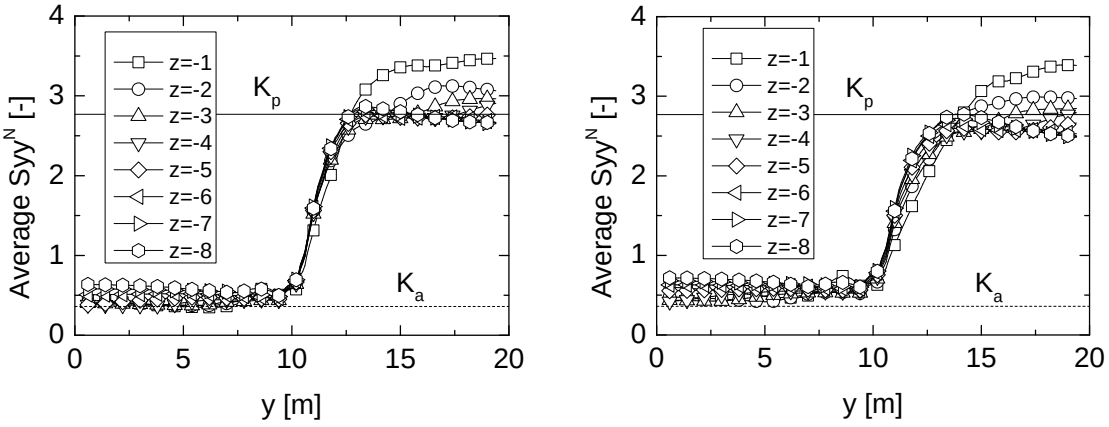

(c) $s/d = 4$ **(d)** $s/d = 5$

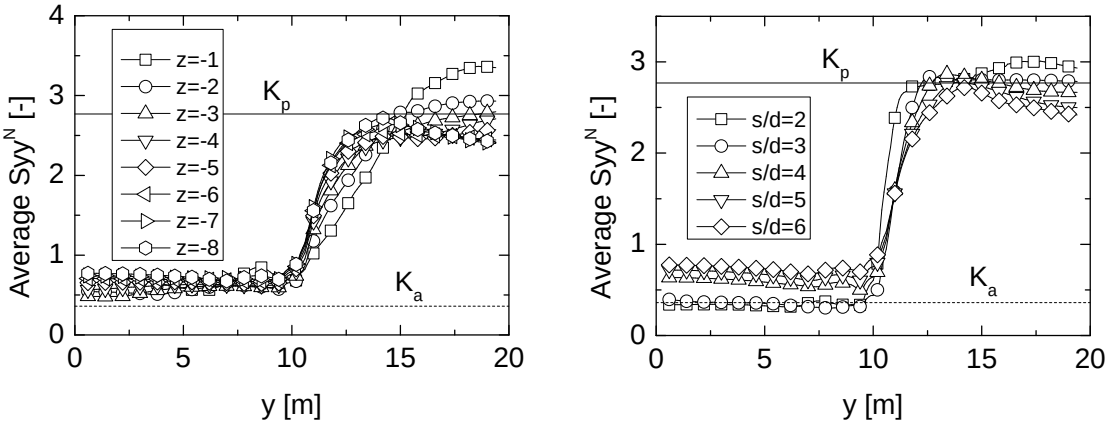

(e) $s/d = 6$ **(f)** at $z = -8$ m

Fig. 5.4.10 Syy^N averaged along the x axis. The piles are located at $y = 10$ m. $y > 10$ m is the up-slope side.

5.5 The role of h/d and EI

As revealed in the centrifuge tests, both the pile slenderness h/d and the pile bending stiffness EI have a great impact on the pile behaviour. It is observed in the last section that the current EI and h/d can already produce a rigid pile behaviour, in which the soil pressure is fully mobilised along the whole depth. Therefore, two smaller EI ($0.5EI$ and $0.1EI$) are selected to study the influence of the pile stiffness on the pile behaviour. Two smaller h/d (6 and 4) are adopted to illustrate the role of slenderness.

Figure 5.5.1 shows the normalised total force on the pile (P/I_{v0}) increasing with the soil boundary displacement (BD) for all the calculations. It is observed that the BD that is needed for the normalised P to reach a stable value is smaller when larger EI and smaller h/d are adopted. The normalised P at 50 cm BD is considered as the ultimate value (P_u), which is plotted in Figure 5.5.2. When $h/d = 4$, P_u is not affected by the pile stiffness. When $h/d = 6$, P_u remains unchanged until $0.1EI$ is applied. A large decrease of P_u is observed when smaller stiffness is combined with $h/d = 8$. Compare the case of $h/d = 4$ with $0.1EI$ to the case of $h/d = 8$ with EI , it seems that the decrease of the relative pile stiffness by changing EI to $0.1EI$ is neutralized by reducing h/d from 8 to 4.

Figure 5.5.3 shows the normalised p_u along the depth. It is observed that p_u is significantly reduced in the upper part of the piles for the following three configurations: $h/d = 8$ with $0.5EI$, $h/d = 8$ with $0.1EI$, and $h/d = 6$ with $0.1EI$. In the case of $h/d = 8$ with $0.1EI$, large negative p_u is obtained in the region from the ground surface to about $1/3$ of the soil thickness. Obviously, it is because of the relatively larger pile displacement than the soil displacement in this region. It can be concluded that losing reinforcement of the shallow soil is responsible for the reduction of P_u. In this chapter, the pile response is defined as flexible when the upper part of the pile is ineffective and otherwise the pile response is rigid. Note that the definition of rigid pile behaviour in this chapter is based on the soil pressure, which may be a higher standard than the definition in the last chapter based on the soil displacement. The distribution of different type of pile response in the dimensions of EI and h/d is shown in Figure 5.5.4. Based on the observations in this section, a line can be roughly drawn to represent the boundary between the rigid and flexible pile behaviours.

Figure 5.5.5 and 5.5.6 show the normalised Syy (Syy^N) on the xz cross-section at the pile row (y=10m) for the calculation of $h/d = 8$ with $0.5EI$ and $h/d = 8$ with $0.1EI$, respectively. The major difference is the distribution along the depth compared to Figure 5.4.8. It is seen that the soil area, in which Syy^N is equal or larger than 1, has shrunk to about half the thickness or even smaller as the pile bending stiffness decreases. This agrees well with the observation from the distribution of p_u along the depth.

Figure 5.5.7 shows the Syy^N averaged over the xz cross-section at the pile row ($y = 10$ m) varying with the boundary displacement BD. Similar to the curves of P (Figure 5.5.1), the BD that is needed for the average Syy^N to reach a relative constant value is smaller when larger EI and smaller h/d are adopted. The average Syy^N at $BD = 50$ cm is considered as the final stable value and is compared in Figure 5.5.8. It is seen that the average Syy^N remains unchanged with the decrease of EI when $h/d = 4$ while large variations are observed in the other two cases. In the cases of $h/d = 8$ and $h/d = 6$, especially when $h/d = 8$, Syy^N at high s/d ($\geq$4) has reduced significantly when flexible piles are used. Considering the fact that smaller P_u is applied on the piles with smaller EI, we can conclude that the sliding forces from the up-slope are transferred to the down-slope more through the piles other than through the soil between the piles. In other words, the soil pressure on the pile from the down-slope soil has increased to a lever similar to or in some cases in the pile head region even higher than the soil pressure level from the up-slope. This agrees with the illustration in Figure 5.5.3 that p_u is not fully mobilised in the shallow soil or even negative p_u is produced when flexible piles with large h/d are used. In these cases, the arching effect between the piles is only mobilised in the deeper soil.

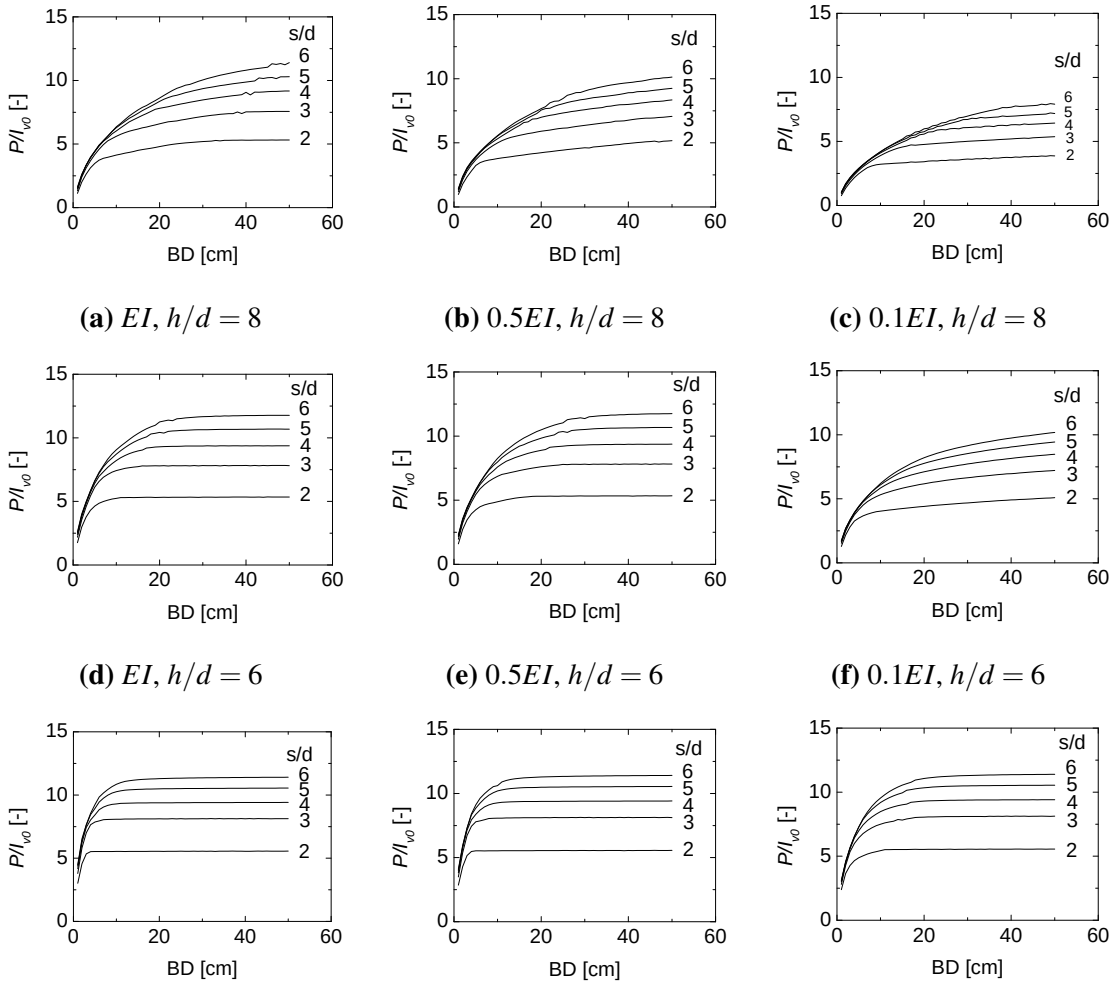

(a) EI, $h/d = 8$ **(b)** $0.5EI$, $h/d = 8$ **(c)** $0.1EI$, $h/d = 8$

(d) EI, $h/d = 6$ **(e)** $0.5EI$, $h/d = 6$ **(f)** $0.1EI$, $h/d = 6$

(g) EI, $h/d = 4$ **(h)** $0.5EI$, $h/d = 4$ **(i)** $0.1EI$, $h/d = 4$

Fig. 5.5.1 Increase of the normalised P with the soil boundary displacement (BD). The BD that is needed for the normalised P to reach a stable value is smaller when larger EI and smaller h/d are adopted.

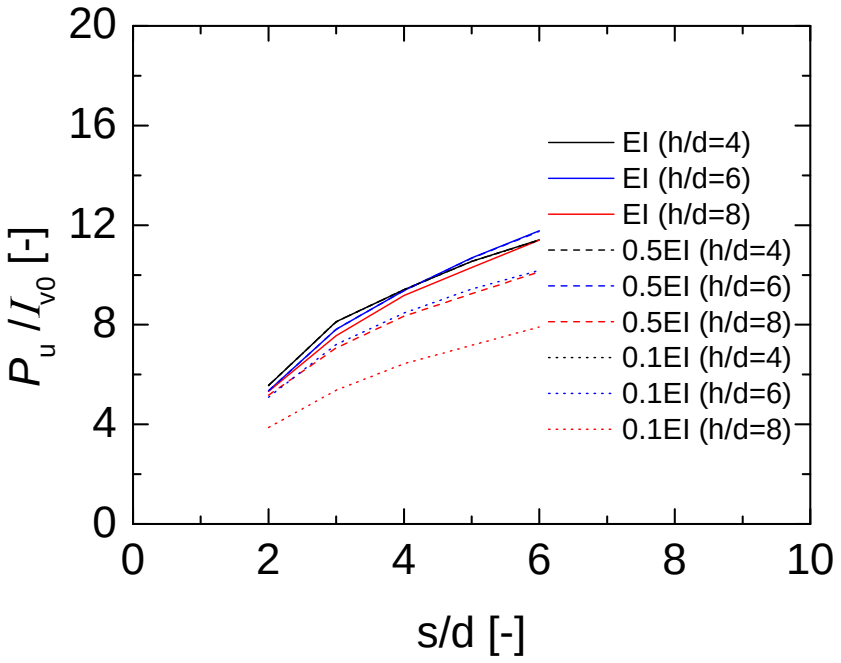

Fig. 5.5.2 Normalised P_u for various EI and h/d. Large reduction of the normalised P_u for the combinations $0.5EI$ with h/d=8, $0.1EI$ with h/d=6 and $0.1EI$ with h/d=8.

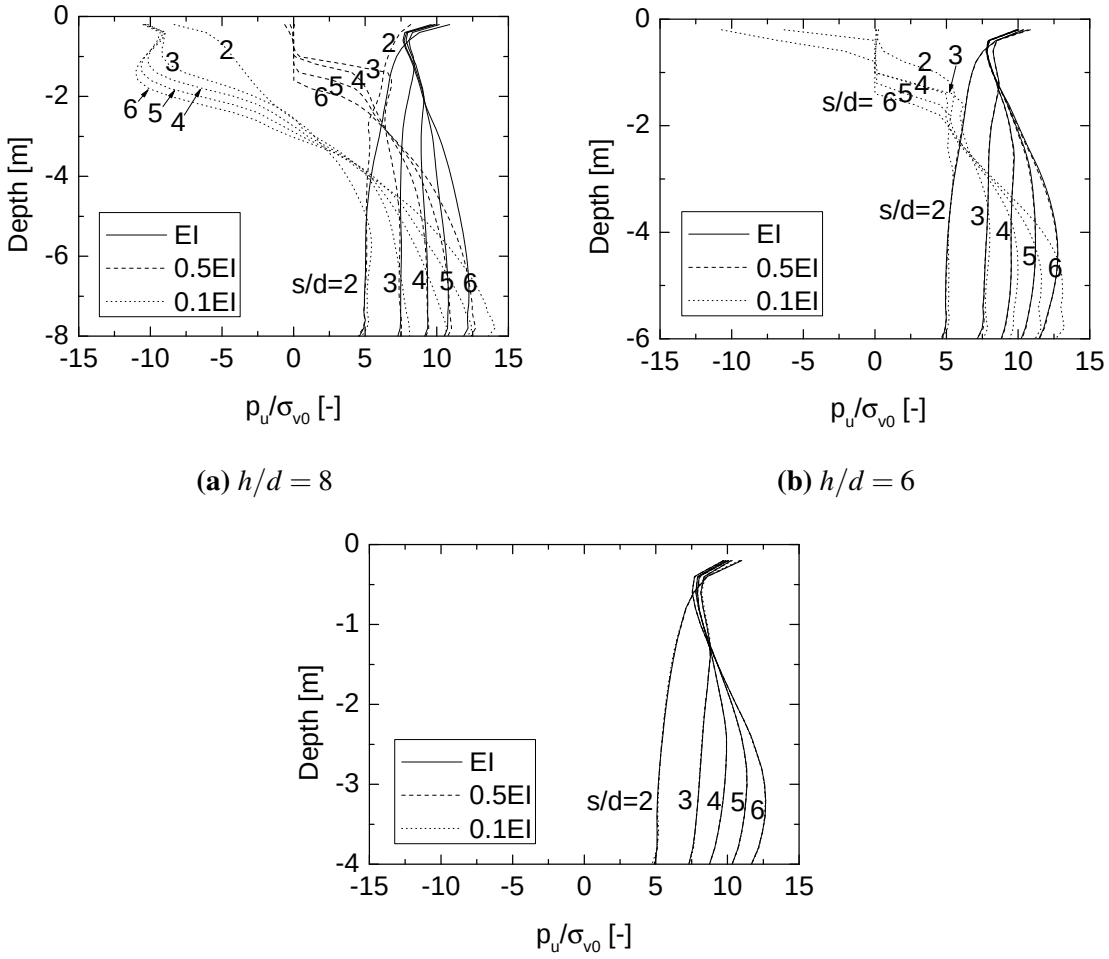

(a) $h/d = 8$

(b) $h/d = 6$

(c) $h/d = 4$

Fig. 5.5.3 Distribution of the normalised p_u along depth. p_u is not fully mobilised along the whole pile length for the combinations $0.5EI$ with h/d=8, $0.1EI$ with h/d=8, and $0.1EI$ with h/d=6.

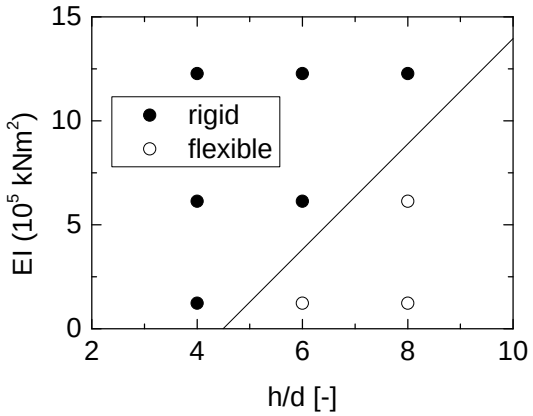

Fig. 5.5.4 Distribution of pile response.

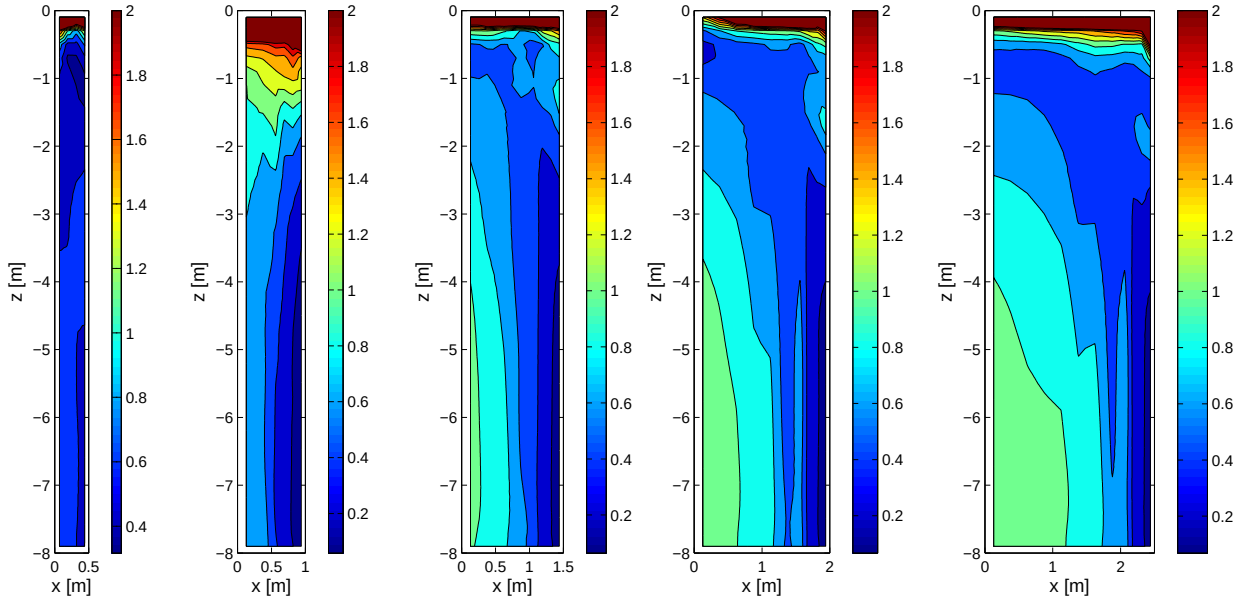

(a) $s/d = 2$ **(b)** $s/d = 3$ **(c)** $s/d = 4$ **(d)** $s/d = 5$ **(e)** $s/d = 6$

Fig. 5.5.5 Syy^N on the xz cross-section at the pile row ($y = 10$ m) for the calculation of $h/d = 8$ with $0.5EI$. Non-uniform distribution of Syy^N along depth is observed from the depth of about -1 m to -4 m.

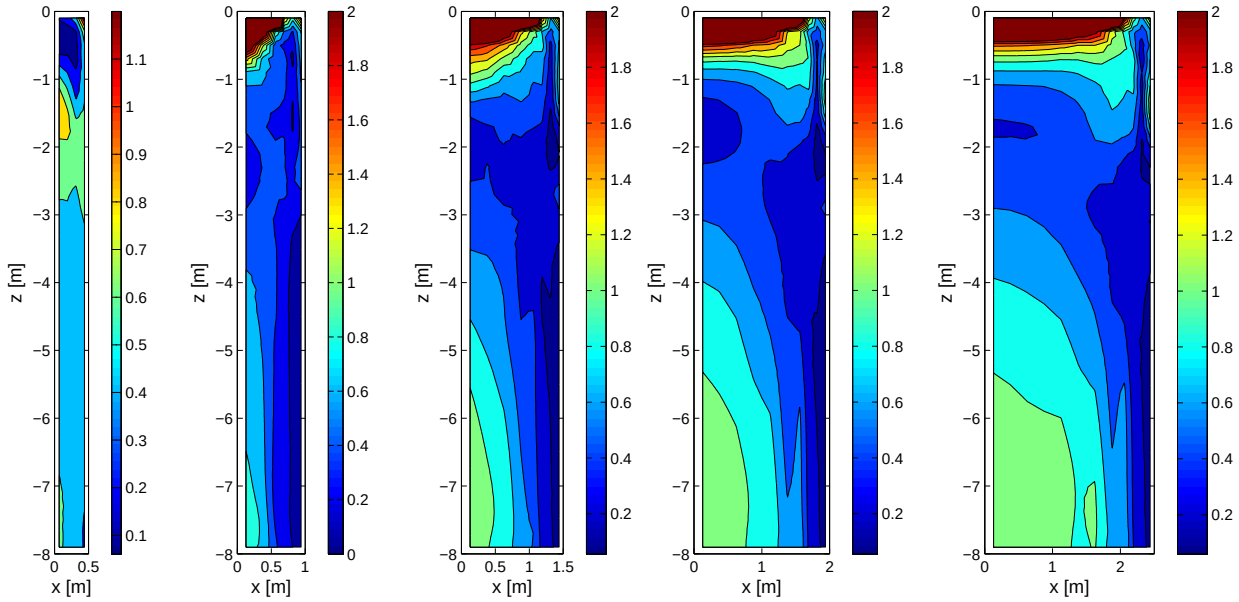

(a) $s/d = 2$ **(b)** $s/d = 3$ **(c)** $s/d = 4$ **(d)** $s/d = 5$ **(e)** $s/d = 6$

Fig. 5.5.6 Syy^N on the XZ cross-section at the pile row ($y = 10$ m) for the calculation of $h/d = 8$ with $0.1EI$. Non-uniform distribution of Syy^N along depth is observed from the depth of about -1 m to -5 m.

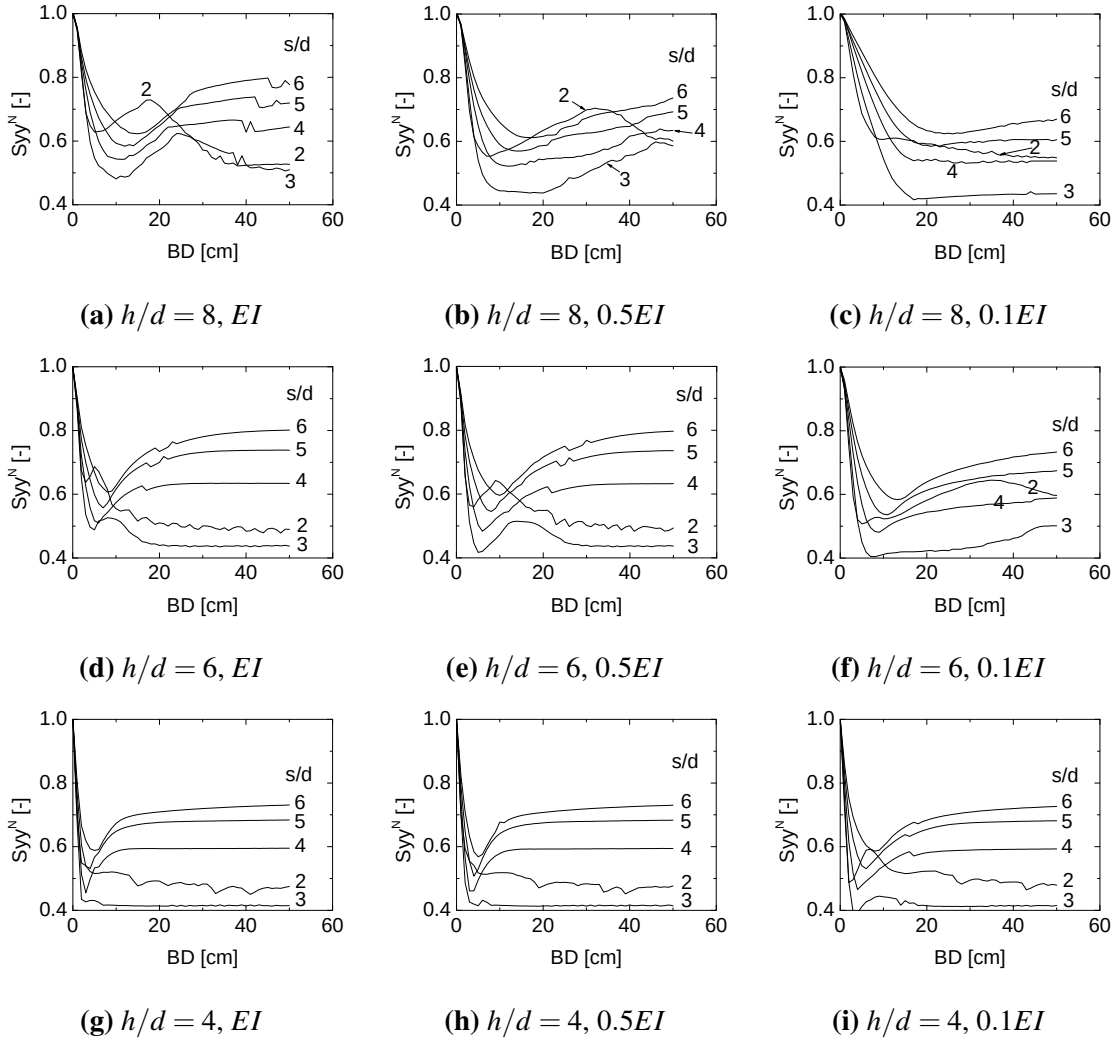

(a) $h/d = 8$, EI **(b)** $h/d = 8$, $0.5EI$ **(c)** $h/d = 8$, $0.1EI$

(d) $h/d = 6$, EI **(e)** $h/d = 6$, $0.5EI$ **(f)** $h/d = 6$, $0.1EI$

(g) $h/d = 4$, EI **(h)** $h/d = 4$, $0.5EI$ **(i)** $h/d = 4$, $0.1EI$

Fig. 5.5.7 Average Syy^N of the xz cross-section at the pile row ($y = 10$ m). The BD that is needed for Syy^N to reach a stable value is smaller when larger EI and smaller h/d are adopted.

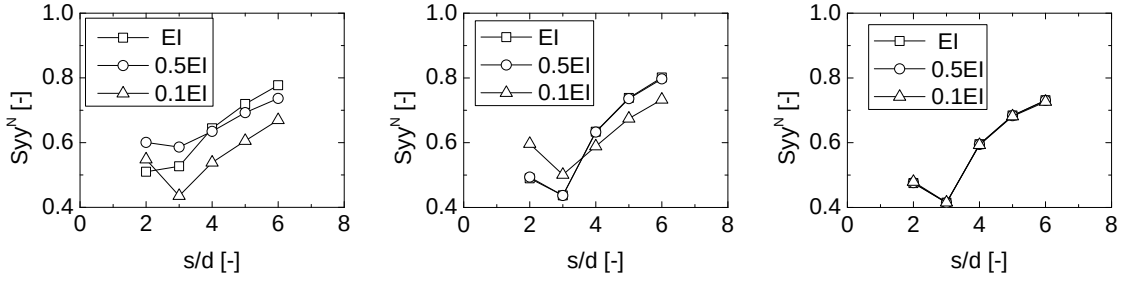

(a) $h/d = 8$ **(b)** $h = 6$ **(c)** $h/d = 4$

Fig. 5.5.8 Average Syy^N of the xz cross-section at the pile row ($y = 10$ m) when $BD = 50$ cm. Reduction of Syy^N for large s/d ($\geq$4) in (a) and (b).

5.6 The role of sliding soil parameters

The previous calculations use the stratigraphic combination that a loose sand layer sliding on a rock layer. In this section the calculations of a dense sand layer sliding on a rock layer are presented.

Figure 5.6.1 compares the normalised P_u from a dense sand layer with the case of a loose sand layer for various h/d and s/d. A much larger P_u is observed in the case of dense sand than the case of loose sand, which is reasonable since the internal friction angle of dense sand is much higher. Unlike the case of loose sand, which is not affected by h/d with the current EI, the normalised P_u of the dense sand case has been clearly reduced when $h/d = 8$. The distribution of the normalised p_u in the case of dense sand with $h/d = 8$ and $h/d = 4$ is shown in Figure 5.6.2, which apparently shows that p_u is not fully mobilised along the depth when $h/d = 8$. Further calculations adopting smaller EI are performed to obtain the distribution of pile response (Figure 5.6.3). Comparing to the case of loose sand, for a stronger sliding soil, more flexible pile responses are observed and the boundary of the pile behaviours has rotated counter-clockwise.

Figure 5.6.4 shows the normalised Syy (Syy^N) on the xz cross-section at the pile row for the calculation of dense sand with $h/d = 8$. It can be seen from the contour that Syy^N is reduced compared to the corresponding calculation using loose sand (Figure 5.4.9). With respect to the distribution of Syy^N along the depth, the large values are more concentrated in the lower part of the sliding layer, which is in line with the conclusion from the p_u distribution that the soil pressure is fully mobilised only in the lower part, similar to the cases with smaller EI (Figure 5.5.5 and 5.5.6).

Figure 5.6.5 shows the average Syy^N on the xz cross-section at the pile row ($y = 10$ m) when $BD = 50$ cm. It shows that Syy^N is clearly reduced when the sliding soil is made of dense sand. However, the difference of the magnitude of the average Syy^N between loose sand and dense sand does not correspond to the mobilisation level of soil arching because the dense sand produces a stronger soil arching between the piles. Comparing the average Syy^N of the dense sand between the cases of different h/d, it is observed that the curve has less variation with s/d when $h/d = 8$, which is also a feature of relative flexible pile behaviour.

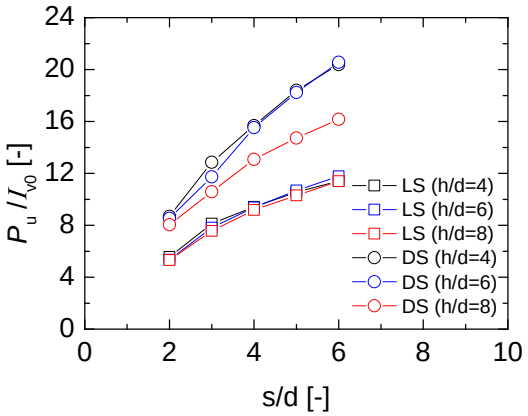

Fig. 5.6.1 Normalised P_u. LS: loose sand; DS: dense sand. Reduction of P_u is observed for dense sand when $h/d = 8$.

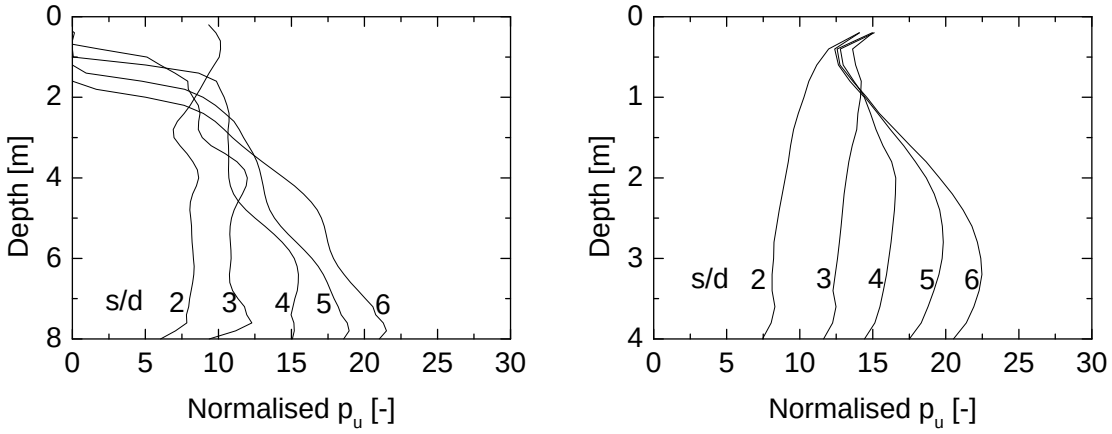

(a) $h/d = 8$ **(b)** $h/d = 4$

Fig. 5.6.2 Distribution of the normalised p_u along depth in the case of dense sand. p_u is not fully mobilised along the whole depth when $h/d = 8$.

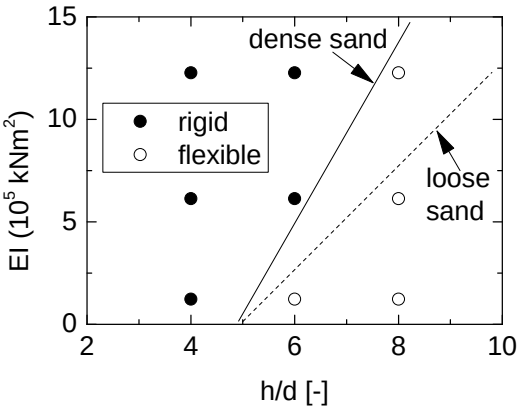

Fig. 5.6.3 Distribution of pile response.

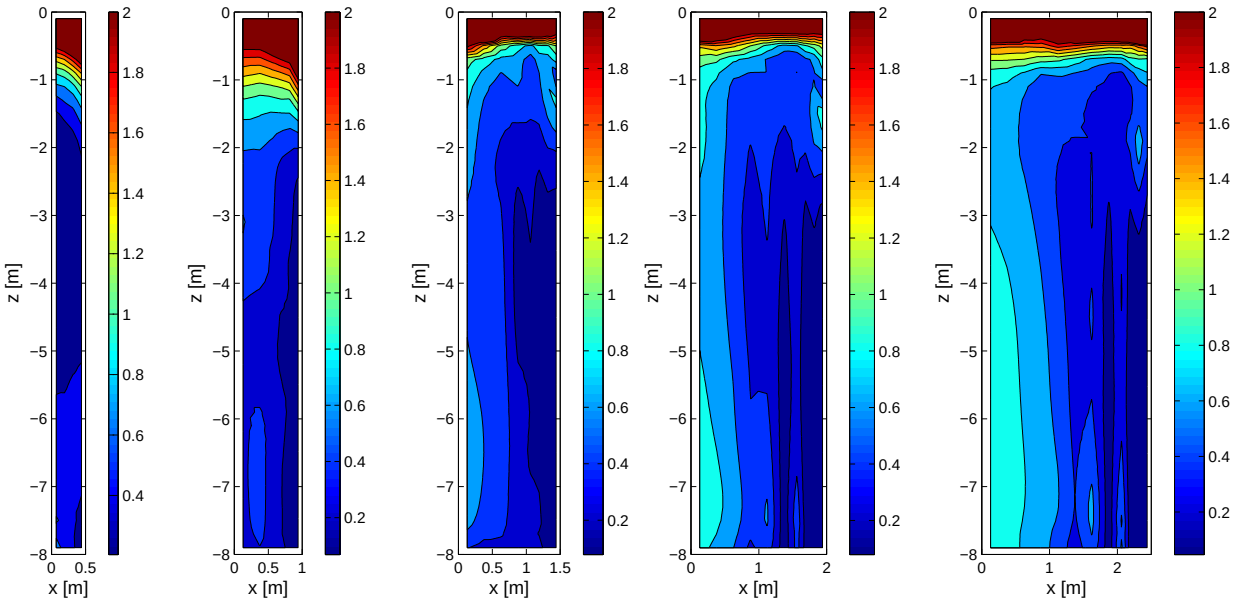

(a) $s/d = 2$ **(b)** $s/d = 3$ **(c)** $s/d = 4$ **(d)** $s/d = 5$ **(e)** $s/d = 6$

Fig. 5.6.4 Syy^N on the xz cross-section at the pile row ($y = 10$m) for the calculations of dense sand.

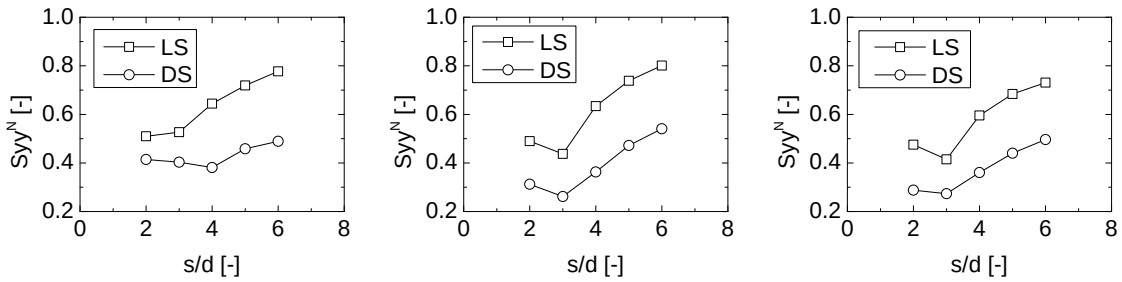

(a) $h/d = 8$ **(b)** $h/d = 6$ **(c)** $h/d = 4$

Fig. 5.6.5 Average Syy^N of the xz cross-section at the pile row ($y = 10$ m) when $BD = 50$ cm. LS: loose sand; DS: dense sand. Less variation of Syy^N with s/d is observed for dense sand when $h/d = 8$.

5.7 The role of stable layer parameters

In order to study the influence of the stable layer parameters, two additional models (loose sand sliding on soft rock, loose sand sliding on dense sand) are calculated.

Figure 5.7.1 compares the normalised P_u for different material of stable layer. Large reduction in the normalised P_u is observed in the case of dense sand with $h/d = 8$. The normalised p_u along the pile depth for all the related calculations is plotted in Figure 5.7.2. It shows that only a small shallow part is affected when soft rock is used as the stable layer and $h/d = 8$. However, according to the definition in this study, this case still belongs to the category of flexible pile behaviour. Great influence is observed when dense sand is adopted as the stable layer and $h/d \geq 6$. Almost half the soil along the depth cannot be mobilised to form an effective arching effect. Another observation, which is not found in the previous calculations, is that the soil pressure on the pile has been reduced clearly in the region from the slip surface to about 1 m above when dense sand is used as the stable layer. Due to the weak confinement of dense sand as the stable layer, the pile displacement is also large in the stable layer, which causes stress release in the stable layer opposite to the pile movement direction. Accordingly, the vertical stress, which is critical for the lateral soil pressure on the pile, is reduced in the relevant region in the sliding soil. More calculations are also performed with various EI to obtain the distribution of pile response. As shown in Figure 5.7.3, more flexible pile responses are observed and the boundary of the pile behaviours rotates counter-clockwise when stable layer becomes relatively weaker.

The normalised Syy (Syy^N) on the xz cross-section at the pile row ($y = 10$ m) when $BD = 50$ cm in the case of dense sand as the stable layer and $h/d = 8$ is shown in Figure 5.7.4. The large values of Syy^N concentrate in the lower half of the soil layer. There is also a tendency that Syy^N reduces at the bottom of the soil layer, which corresponds to the reduction of p_u near the slip surface. The average Syy^N on the xz cross-section at the pile row ($y = 10$m) when $BD = 50$ cm for various stable layer materials is shown in Figure 5.7.5. It is seen that the average Syy^N in the case of dense sand as the stable layer with $h/d = 8$ is apparently smaller when $s/d \geq 4$. The variation of Syy^N with s/d is also smaller than the other cases. This observation corresponds to the previous analysis.

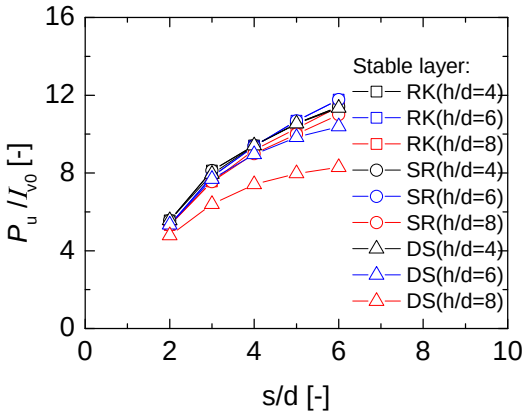

Fig. 5.7.1 Normalised P_u for different stable layer materials: RK: rock; SR: soft rock; DS: dense sand.

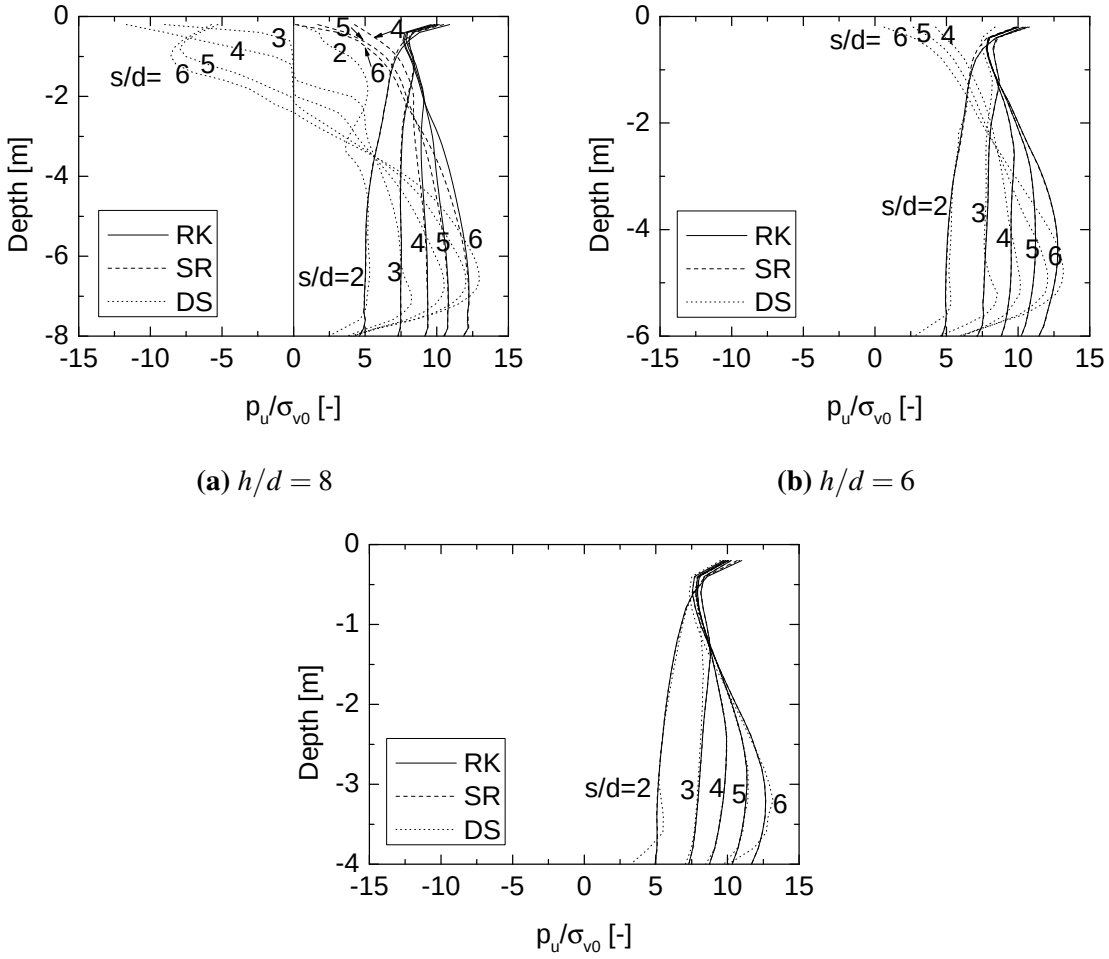

(a) $h/d = 8$

(b) $h/d = 6$

(c) $h/d = 4$

Fig. 5.7.2 Distribution of the normalised p_u along depth for different stable layer materials. RK: rock; SR: soft rock; DS: dense sand. p_u is not fully mobilised along the depth for the following cases: SR with $h/d = 8$, DS with $h/d = 6$ and $h/d = 8$.

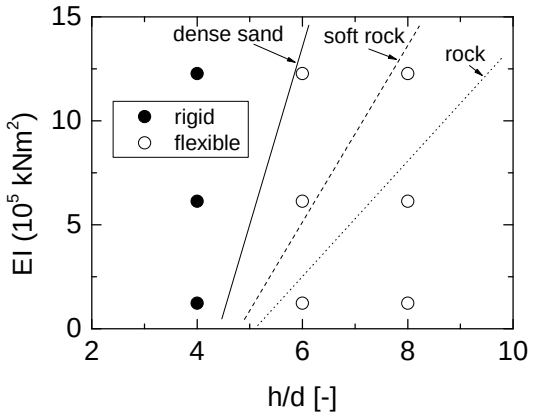

Fig. 5.7.3 Distribution of pile response for different stable layer.

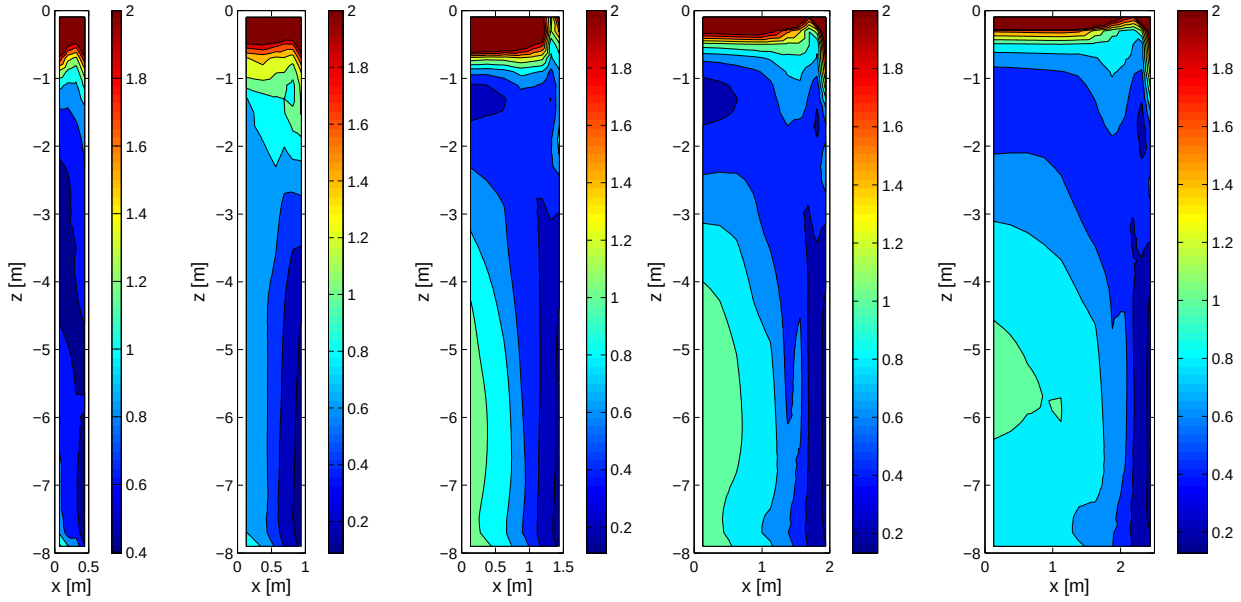

(a) $s/d = 2$ **(b)** $s/d = 3$ **(c)** $s/d = 4$ **(d)** $s/d = 5$ **(e)** $s/d = 6$

Fig. 5.7.4 Syy^N on the xz cross-section at the pile row ($y = 10$ m) when $BD = 50$ cm for the calculation using dense sand as the stable layer and $h/d = 8$. The large values of Syy^N concentrate in the lower half of the soil layer.

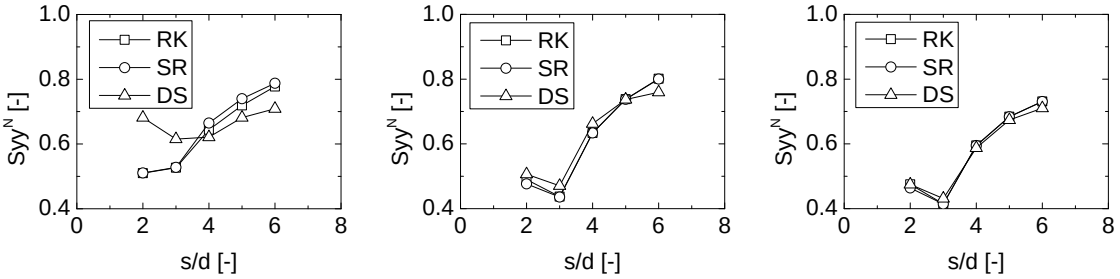

(a) $h/d = 8$ **(b)** $h/d = 6$ **(c)** $h/d = 4$

Fig. 5.7.5 Average Syy^N of the xz cross-section at the pile row ($y = 10$ m) when $BD = 50$ cm for different stable layer: RK – rock; SR – soft rock; DS – dense sand. Smaller Syy^N for dense sand with $h/d = 8$ when $s/d \geq 4$.

5.8 The ultimate lateral pressure p_u

In the literature, various theories or empirical equations were proposed for the ultimate lateral pressure p_u on the pile. For sandy soil, the simplest approach is to use the suggestion of Broms (1964):

$$p_u = aK_p\sigma'_{vo} \tag{5.3}$$

where $K_p = tan^2(45+\frac{\phi}{2})$ is the Rankine passive pressure coefficient; ϕ is the internal friction angle of soil; σ'_{vo} is the effective overburden pressure and a is a coefficient ranging between 3 and 5. The equation was initially proposed for the laterally loaded piles in the stable soil. For the piles in the sliding soil, $\frac{a}{2}$ can be taken into account (Poulos (1995)).

Barton (1982) found from lateral pile tests that the simple variation given by

$$p_u = K_p^2\sigma'_{vo} \tag{5.4}$$

could be used.

Reese et al. (1974) proposed a wedge failure mechanism in front of the pile, which leads to a variation of p_u with depth that is initially proportional to K_p, but at greater depths becomes proportional to k_p^3 (Fleming et al. (2008)). Norris (1986) proposed a strain wedge model to predict the response of a flexible pile under lateral loading. The model was later applied in the analysis of stabilizing piles by Ashour and Ardalan (2012a). The theory assumes a conceptualized three-dimensional wedge, in which the soil is in critical state.

Considering the arching effect between the adjacent piles, Ito and Matsui (1975) have developed a theory for the flow of soil through a row of piles. Their equations show that the limiting pressure developed on a pile by the soil that is flowing through the pile row depends on the strength properties of the soil, the overburden pressure, and the spacing between the piles relative to their diameter. Their equations are meant to apply to the portion of the piles in the unstable or moving soil. However, Poulos (1995) stated that the equations are only valid over a limited range of spacings, since, at large spacings or at very close spacings, the mechanism of flow through the piles assumed by Ito and Matsui (1975) is not the critical mode. Nevertheless, this theory has provided a physical meaningful alternative to the empirical equations. According to the observations from the numerical study in this chapter, when the pile spacing increases to the critical value ($s/d = 3$ to 4), the soil pressure on the pile is fully mobilised and the arching effect is established. As the pile spacing increases further, the soil flows through the piles and more pressure is transferred to the down-slope, which in return strengthens the arching effect to enable more pressure on the pile. Consequently, a question now arises to an assumption in the plastic deformation theory,

which is that the normal stress at the pile row is represented by the active earth pressure:

$$\sigma_{yy} = \gamma z K_p^{-1} - 2cK_p^{-1/2} \tag{5.5}$$

where, z is the soil depth, γ is the unit weight of soil, and c is the cohesion. This assumption serves as a boundary condition to solve the differential equation. However, it does not hold for very small or large pile spacings. A new parameter K_f is introduced into the plastic deformation theory to evaluate the normal soil stress at the pile row:

$$\sigma_{yy} = K_f \gamma z \tag{5.6}$$

The derivation of the p_u with the proposed parameter is given in Appendix B.

The analysis in this chapter has revealed that several parameters have an impact on whether the ultimate soil pressure p_u can be fully mobilised or not. However, the combinations of a 4 m thick layer of loose sand or dense sand sliding on the stable layer of rock stabilised by the full EI piles are believed to produce the p_u. These two calculation series are used to back calculate the parameter K_f.

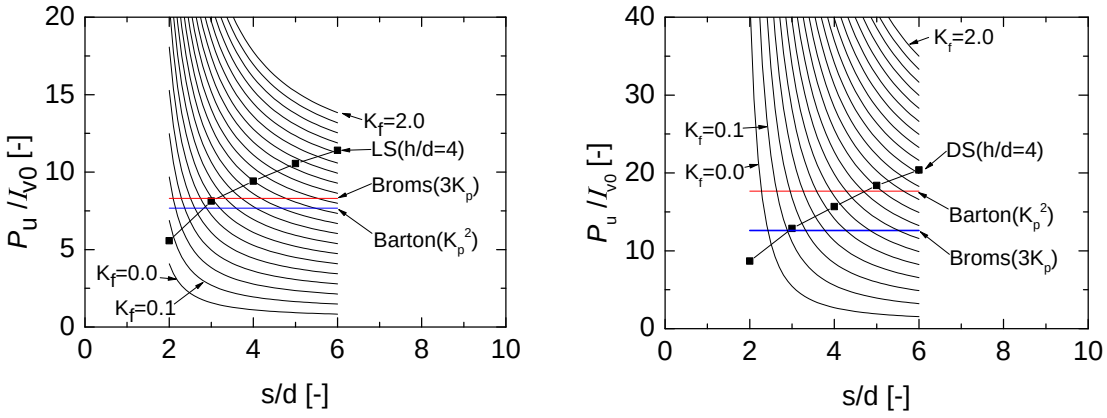

(a) loose sand **(b)** dense sand

Fig. 5.8.1 Normalised P_u compared with several predictions. The lines with filled squares (LS: loose sand; DS: dense sand) are results from $FLAC^{3D}$.

Figure 5.8.1 shows the normalised P_u of loose sand and dense sand compared with several predictions. Curves from the modified plastic deformation theory using a series of K_f values (i.e.,0.0, 0.1,..., 2.0) are also plotted in the figure. It is seen that the empirical predictions intersect with the curve from $FLAC^{3D}$ with a large angle, which implies that the empirical predictions could be precise in a small range of s/d. On the contrary, the curves using the proposed theory with various K_f intersect with the curve from the numerical calculation in

the whole range of s/d. K_f is back calculated using the numerical results and is shown in Figure 5.8.2. The average of the normalised *Syy* at the pile row in the numerical model, which is equivalent to K_f, and the Rankine active soil pressure coefficient K_a, which is adopted in the original plastic deformation theory, are also shown in the figure. With the increase of s/d, the normalised *Syy* has experienced a small decrease until $s/d = 3$ and a small increase afterwards. As analysed previously, the arching effect between the piles is fully mobilised at about $s/d = 3$ to 4, which results in the maximum difference of soil stress at the pile row. As s/d becomes even larger, the arching effect becomes weaker and the soil stress between the piles becomes larger. The back-calculated K_f increases approximately linearly with the increase of s/d. Some unrealistic values of K_f (larger than 1 at a large s/d and smaller than 0 at a small s/d) are observed. This has also reflected the limitation of the plastic deformation theory. However, the proposed modification has extended the applicable pile spacing range of the theory.

Numerical calculations ($h/d = 4$) are also performed using the soil parameters of the centrifuge tests. Considering that the relative displacement between the pile and soil is observed in the early stage of the centrifuge test, frictionless pile surface is adopted in the numerical calculation. Since equation 5.4 is based on the assumption of cohesionless soil, an additional calculation is performed using zero cohesion. The results are compared in Figure 5.8.3. Good agreement is obtained between the empirical equations and the numerical calculation without cohesion while difference is observed between the centrifuge tests and the corresponding numerical calculations. According to the analysis of the centrifuge tests, the centrifuge results may be underestimated. The pile-soil interaction is significantly affected by the soil deformation and failure mode. In the cases of small spacings, higher soil pressure may be obtained by raising the relative up-slope length. Underestimation may also be due to the modelling of the centrifuge tests. For example, during the centrifuge test, deeper soil has relatively larger g-level than the shallow soil. In this thesis, the g-level is calculated according to the slope toe. Consequently, the soil g-level around the piles are overestimated, which can result in an increase of up to 7.4% for the results of A*i*PSL and A*i*PB when considered. The inclination of the centrifuge model and neglecting the pore water pressure may also cause the overestimation of the vertical soil stress around the piles. Note that the overestimation of g-level and the vertical soil stress result in the underestimation of the normalised P_u. As for the numerical calculations, the normalised P_u at a high spacing could be overestimated due to the restriction of the mesh and the interface elements in the model. It seems that the cohesion has a large influence on the P_u. This should be further studied using mesh-independent methods and suitable soil constitutive models.

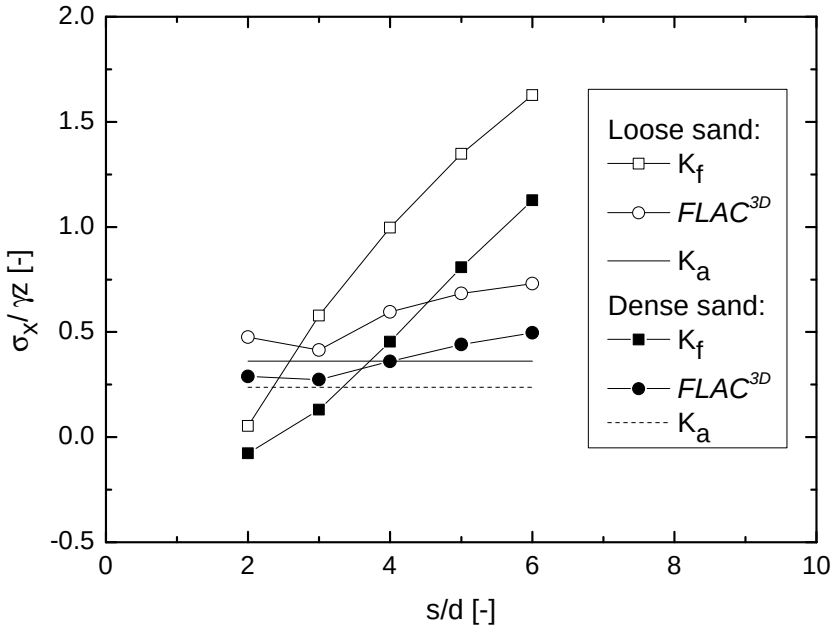

Fig. 5.8.2 Parameter K_f compared with numerical results and empirical equations. K_a is the Rankine active soil pressure coefficient.

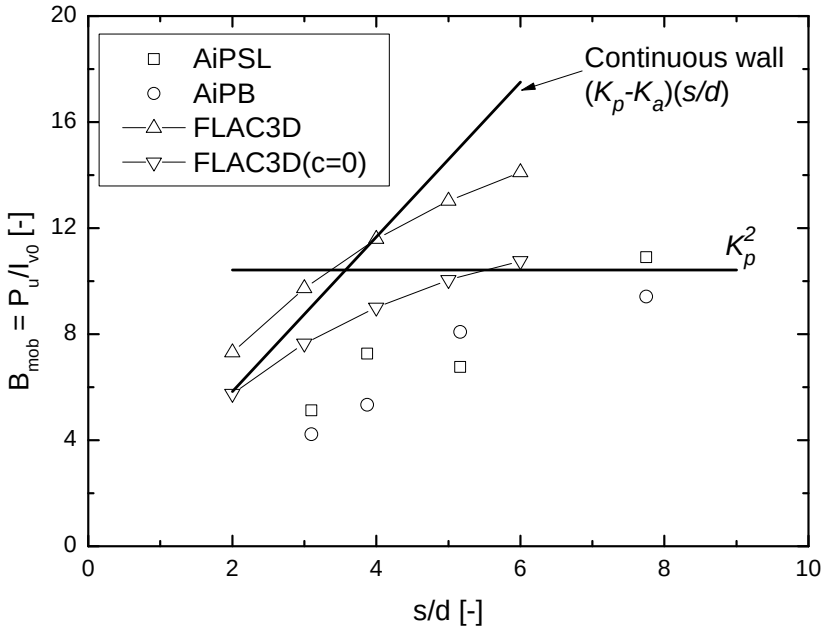

Fig. 5.8.3 Comparison between the numerical results and the centrifuge results. Numerical calculations are performed using the soil parameters in the centrifuge tests: $c = 6$ kPa, $\phi' = 31.8$ °. K_a and K_p are the Rankine active and passive soil pressure coefficients, respectively. A*i*PSL and A*i*PB are series name of the centrifuge tests.

5.9 Concluding remarks

The pile-soil interaction is studied using the numerical model of a soil layer sliding above a stable layer. The sliding layer is reinforced by a row of piles spaced discretely. The pile-soil interaction mechanism is studied and several parameters are examined by analysing the soil stress. The following conclusions are drawn:

- A two-stage mechanism is observed for the mobilisation of the soil pressure on the pile. In the first stage the soil pressure from the lower part of the sliding soil is quickly mobilised. In the second stage, the soil pressure from the upper part of the sliding soil is gradually mobilised.

- As the pile spacing s/d becomes larger, the first stage for the mobilisation of soil pressure on the pile has extended and the ultimate force on the pile P_u has increased. The influence of s/d becomes effective when it is larger than a critical value (between 3 and 4), at which the soil stress that transfers to the down-slope soil at the pile row is minimum and the arching effect is fully mobilised. As the pile spacing increases further, the soil flows through the piles and more soil pressure is transferred to the down-slope soil.

- The pile slenderness h/d and the pile stiffness EI have significant influence on the pile-soil interaction. With a smaller h/d (4), the soil stress transmission at the pile row is less affected by the variation of EI. On the other hand when a large h/d (8) and a smaller EI are adopted, flexible pile behaviour, in which the arching effect and the soil pressure in the upper part of the pile can not be fully mobilised, is obtained.

- The material parameters of the sliding layer and the stable layer can also affect the pile-soil interaction. As the sliding soil becomes stronger (from loose sand to dense sand) or the stable layer becomes weaker (from rock to dense sand), more flexible pile behaviour tends to appear and the pressure from the shallow soil becomes more difficult to be fully mobilised.

- A parameter K_f, which can be back calculated using the P_u obtained in the numerical analysis, is proposed to modify the plastic deformation theory to predict the ultimate pressure p_u on the pile in practice. Comparing with the centrifuge results, P_u from the numerical calculations is higher.

Chapter 6

Analytical method

6.1 Introduction to Strain Wedge Model

The Strain Wedge Model (SWM) was developed by Norris (1986) to predict the response of flexible pile under lateral load. It is based on the assumption of a theoretical passive soil wedge on the pile. Later on, the applicability of SWM has been extended from piles in uniform sand to piles in different ground conditions and configurations, e.g., in layered soil (Ashour et al. (1998), Ashour and Norris (2000), Xu et al. (2013)), in liquefied sand (Ashour and Ardalan (2012b)) and from a single pile to pile groups (Ashour et al. (2004)). The first attempt to apply the strain wedge model to slope stabilizing piles was made by Ashour and Ardalan (2012a), in which the complex pile-soil interaction is modelled by a single mobilized strain wedge above the slip surface (Fig. 6.1.1a). However, large difference is observed between the predicted results and the measurements, because the single wedge model ignores the interaction between the pile top and the down-slope soil. Ardalan (2013) attempted to resolve this problem by introducing the soil-pile relative displacement. However, the shape of the wedge remained unchanged. This similar problem was encountered by He et al. (2015).

In this chapter, the pile-soil interaction above the slip surface is modelled by an inverted 'stabilized strain wedge' in the up-slope and a 'mobilized strain wedge' in the down-slope (Fig. 6.1.1b). The 'stabilized strain wedge' refers to the soil zone in the up-slope, where the movement is blocked by the pile and hence the term 'stabilized', while the 'mobilized strain wedge' refers to the soil zone in the down-slope, where the soil is pushed by the pile and hence the term 'mobilized'. Note that the tip angle of the stabilized wedge points upwards. The reason is that the pile segment above the slip surface can be seen as a cantilever beam with the minimum lateral deflection $y_p = y_{min}$ at the slip surface and the maximum lateral deflection $y_p = y_{max}$ at the pile top. As a result the soil movement y_s and the pile movement

y_p have the largest positive difference at the slip surface and the largest negative difference at the pile top if $y_s < y_{max}$. By taking the relative soil-pile displacement as the reference, the shape of the wedges adopted here is consistent with the strain wedges used in the laterally loaded pile analyses (Norris (1986), Ashour et al. (1998)).

The proposed approach is supported by some observations in the literature and previous studies in this thesis. For instance, the stabilized wedge is similar to the 'Zone C' in the pile stabilizing mechanism proposed by Wang and Zhang (2013), in which the horizontal displacement of the soil is reduced by the piles significantly. Wei and Cheng (2009) concluded that the critical slip surface of a piled slope is usually shallower than that of a slope without pile. Kanagasabai et al. (2011) observed in the numerical analysis that the soil in front of the pile (corresponds to the up-slope soil here) tends to move upward. Similarly, the development of the stabilized wedge can be regarded as the uplifting of the slip surface and therefore the soil moves upward. 'Over-top failure", in which the up-slope soil slides above the pile head, has been observed in the centrifuge tests and also reported in the literature (Tang et al. (2014), Stefania et al. (2015), Li et al. (2016)). This failure mode can be considered as an extreme case, in which the thickness of the stabilized wedge is equal to or even larger than the sliding layer.

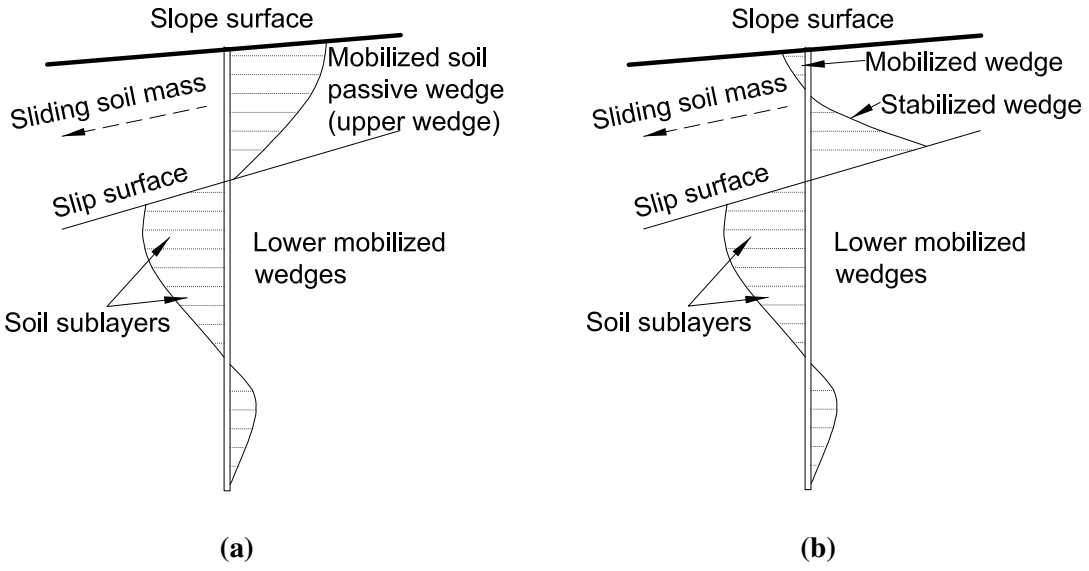

Fig. 6.1.1 Strain wedge induced by lateral soil movement. (a) Soil wedges adopted by Ashour and Ardalan (2012a); (b) Soil wedges adopted in this study.

6.2 Model characterization

According to the soil wedge in Figure 6.1.1b, the driving force induced by the soil movement is shown in Figure 6.2.1. The purpose of the proposed model is to estimate the distribution of the driving force.

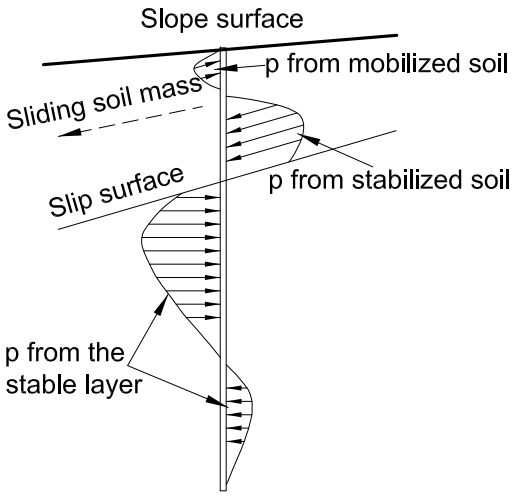

Fig. 6.2.1 Driving force p induced by lateral soil movement.

6.2.1 Strain wedge in the soil

As seen in Figure 6.2.2a, a stabilized three-dimensional soil wedge is developed due to the sliding force from the up-slope. The thickness of the stabilized strain wedge (h_w) is a variable which is normally smaller than the depth of the slip surface (h). As illustrated by Figure 6.2.2b, the wedge angle (β_s and β_m) and the width of wedge face (BC) can be calculated by:

For the stabilized wedge,

$$(\overline{BC})_i = d + (h_w - x_i)2(\tan\beta_s)_i(\tan\phi_s)_i \tag{6.1}$$

$$(\beta_s)_i = 45 + \frac{(\phi_s)_i}{2} \tag{6.2}$$

For the mobilized wedge

$$(\overline{BC})_i = d + (x_i - h_w)2(\tan\beta_m)_i(\tan\phi_m)_i \tag{6.3}$$

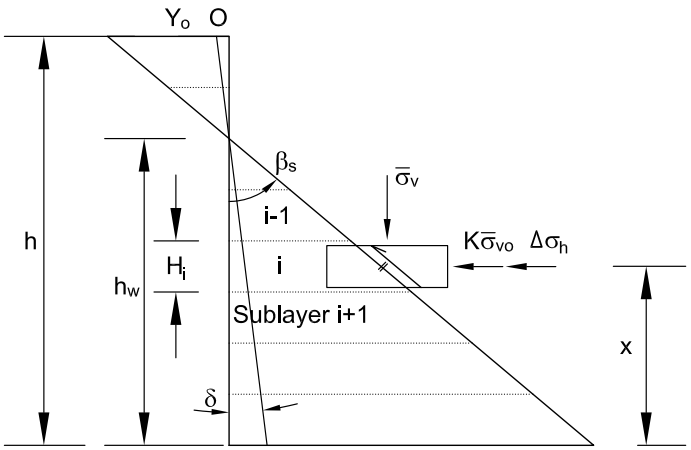

(a) linearized deflection pattern

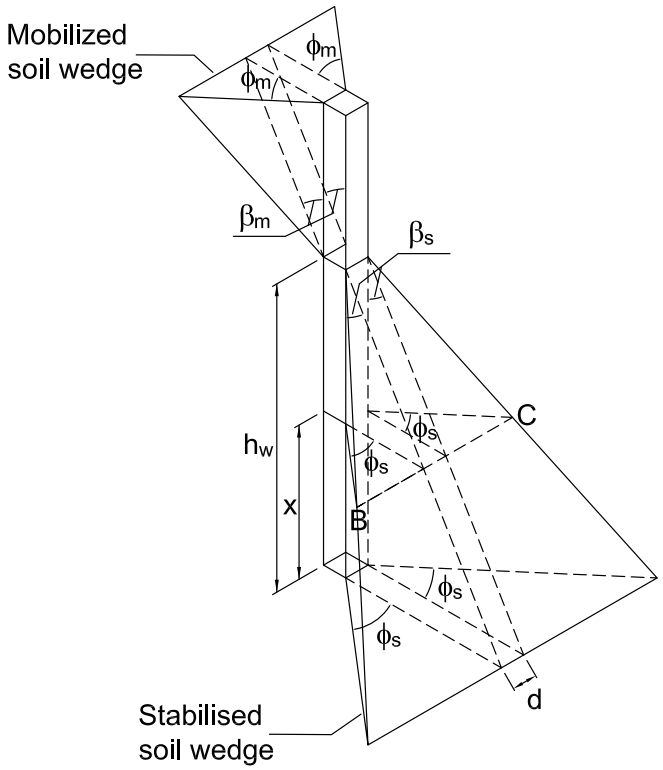

(b) strain wedges in 3D

Fig. 6.2.2 Strain wedges above the slip surface.

$$(\beta_m)_i = 45 + \frac{(\phi_m)_i}{2} \tag{6.4}$$

where i indicate the number of the sub-layer, d is the width of the pile cross-section for a rectangular pile or the diameter of a circular pile, x_i is the distance between the sub-layer and the slip surface, h is the depth of the stabilized wedge, ϕ_s and ϕ_m are the fanning angle of the stabilized and mobilized wedges, respectively.

The linear deflection pattern is only valid for the case of short piles, in which the soil strain can be assumed to remain unchanged along the pile length (Ashour and Ardalan (2012a)). For the deflected long and intermediate piles (flexible piles), the soil strains may vary between the sub-layers. Therefore, a multi-wedge model is employed as shown in Figure 6.2.3. For each sub-layer the shear strain of the wedge δ_i is given by

$$\delta_i = \frac{\Delta y_i}{H_i} \tag{6.5}$$

where Δy_i is the absolute difference of the lateral deflection of the pile at the top and the bottom of the i^{th} sub-layer, H_i is the thickness of the sub-layer.

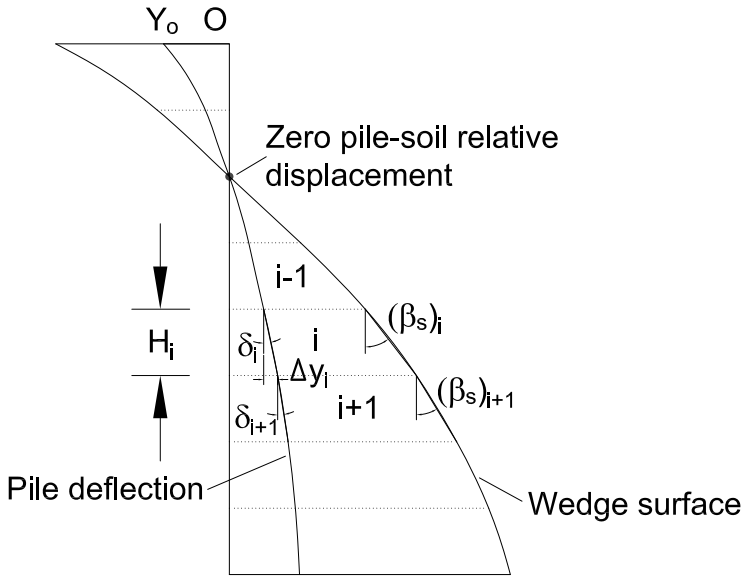

Fig. 6.2.3 Multi-wedge model

The multi-wedge model is also applied to the wedges below the slip surface. Compared to the derivation of δ_i in the research of Ashour and Ardalan (2012a), the advantage of the

multi-wedge model is its adaptability to more complicated cases, e.g., when more than one zero-crossing points below the slip surface exist.

6.2.2 Soil stress-strain relationship

In the strain wedge model, the horizontal strain (ε) is the predominant parameter. The stress-strain relationship is defined based on the results of the isotropically consolidated drained (sand) or undrained (clay) triaxial test (Ashour et al. (1998)). The horizontal stress change ($\Delta\sigma_h$) is equivalent to the deviatoric stress increment in the triaxial test and the vertical stress and the perpendicular horizontal stress are assumed to be constant similar to the compression pressure in the triaxial test. Using the Mohr strain circle illustrated in Figure 6.2.4, the shear strain (γ) is defined by

$$\frac{\gamma}{2} = \frac{1}{2}(\varepsilon - \varepsilon_v)\sin 2\Theta_s = \frac{1}{2}\varepsilon(1+\nu)\sin 2\Theta_s \tag{6.6}$$

Where ε and ε_v are the horizontal strain (ε_1) and the vertical strain (ε_3) of the soil, respectively; ν is the Poisson's ratio of the soil; Θ_s is calculated by $\Theta_s = 90 - \beta_s = 45 - \varphi_s/2$ (Figure 6.2.4).

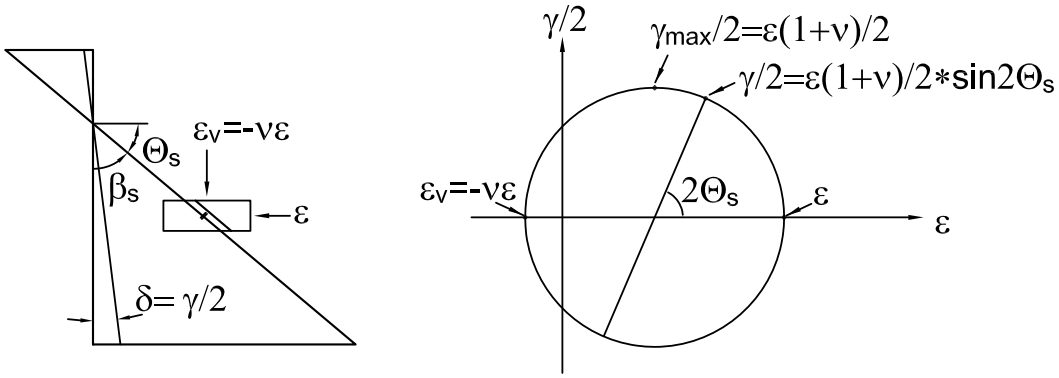

Fig. 6.2.4 Distortion of the wedge and the associated Mohr circle of strain (after Ashour et al. (1998))

In the strain wedge model, the soil shear strain and the local pile deflection angle in the i^{th} sub-layer (δ_i) have the following relationship:

$$\delta_i = \frac{\gamma_i}{2} \tag{6.7}$$

Using equation 6.6, equation 6.7 can be rewritten into

$$\delta_i = \frac{\varepsilon_i(1+\nu_i)\sin 2(\Theta_s)_i}{2} = \frac{\varepsilon_i}{\Psi_s} \tag{6.8}$$

where Ψ_s varies with the Poisson's ratio of the soil and the wedge angle Θ_s. According to Ashour et al. (1998), for a possible range of Poisson's ratio and wedge angle, the value of Ψ_s only varies slightly with an average value of 1.77 for sand and 1.4 for clay. The average value is used to simplify the calculation.

The horizontal soil stress increment $\Delta\sigma_h$ is normalised into a variable called Stress Level (SL), which is equal to zero when $\Delta\sigma_h = 0$ and one when soil fails. SL is defined by

$$SL = \frac{\Delta\sigma_h}{\Delta\sigma_{hf}} \tag{6.9}$$

where $\Delta\sigma_{hf}$ indicates the horizontal stress increment at failure (or the deviatoric stress at failure in the triaxial test) and is given by (Ashour and Ardalan (2012a)):

$$\begin{aligned} \text{sand} &: \Delta\sigma_{hf} = \bar{\sigma}_{vo}[\tan^2(45+\frac{\varphi}{2})-1] \\ \text{clay} &: \Delta\sigma_{hf} = 2S_u \\ c-\varphi \text{ soil} &: \Delta\sigma_{hf} = (\frac{c}{\tan\varphi}+\bar{\sigma}_{vo})[\tan^2(45+\frac{\varphi}{2})-1] \end{aligned} \tag{6.10}$$

where S_u is the undrained shear strength of clay; c and φ are the cohesion and the internal friction angle of soil, respectively.

To assess SL as a function of ε, Norris (1986) employed a hyperbolic stress-strain relationship, which was modified by Ashour et al. (1998) and also adopted by Ashour and Ardalan (2012a).

As shown in Figure 6.2.5, the soil stress-strain relationship is divided into three stages, which correspond to the following equations:

$$\begin{aligned} \text{Stage I} &: SL_i = \frac{3.19\varepsilon_i}{(\varepsilon_{50})_i}\exp(-3.707SL_i) \\ \text{Stage II} &: SL_i = \frac{\lambda\varepsilon_i}{(\varepsilon_{50})_i}\exp(-3.707SL_i) \\ \text{Stage III} &: SL_i = \exp(\ln 0.2+\frac{100\varepsilon_i}{m\varepsilon_i+q_i}) \end{aligned} \tag{6.11}$$

where λ varies linearly from 3.10 at $SL = 0.5$ to 2.14 at $SL = 0.8$; $m = 59.0$ and $q_i = 95.4\varepsilon_{50}$.

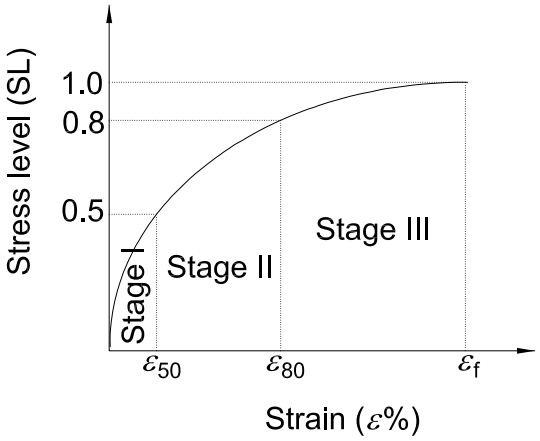

Fig. 6.2.5 Soil stress-strain relationship developed by Ashour et al. (1998)

6.2.3 Shear stress along the pile sides

Shear stress (τ) along the pile sides in the strain wedge model is determined according to the soil type by (Ashour and Ardalan (2012a)):

$$\begin{aligned} \text{sand} &: \tau_i = (\overline{\sigma}_{vo})_i \tan(\phi_s)_i \\ \text{clay} &: \tau_i = (SL_t)_i (\tau_{ult})_i \\ c-\varphi \text{ soil} &: \tau_i = (\overline{\sigma}_v o)_i \tan(\phi_s)_i + 2c_s \end{aligned} \tag{6.12}$$

where $\tan\phi_s = 2\tan\phi_m$ and $\tan\phi_s \leq \tan\phi$; SL_t is the stress level of the shear stress along the pile sides in clay (Ashour et al. (1998)), τ_{ult} is a function of S_u; $c_s = 2c_m$ and c_m is the mobilized cohesion which is limited to the cohesion of the soil.

6.2.4 Interaction between adjacent piles

The response of a single pile is usually affected by the adjacent piles, which is known as the group effect. The group effect is of great importance for the stabilising piles because it forms a soil arch between the piles to prevent the flow failure. However, it also reduces the lateral capacity of the pile embedment (i.e., the pile segment below the slip surface). Pilling et al. (2001) considered the group effect by modifying the soil strain according to the interference between the soil wedges. Ashour et al. (2004) used an empirical equation to calculate the average stress level in each soil layer using the overlap of the wedge faces as input. Essentially, both the solutions estimate the pile response in a group by modifying the parameters in the single pile analysis. In the proposed model, the soil strain is related to the local pile deformation and is calculated through an iterative scheme. Therefore, instead of

modifying the parameters, a simple solution is adopted here. As illustrated in Figure 6.2.6, when overlap between the wedges occurs, $BC = s$ is applied, where s is the axis-to-axis pile distance.

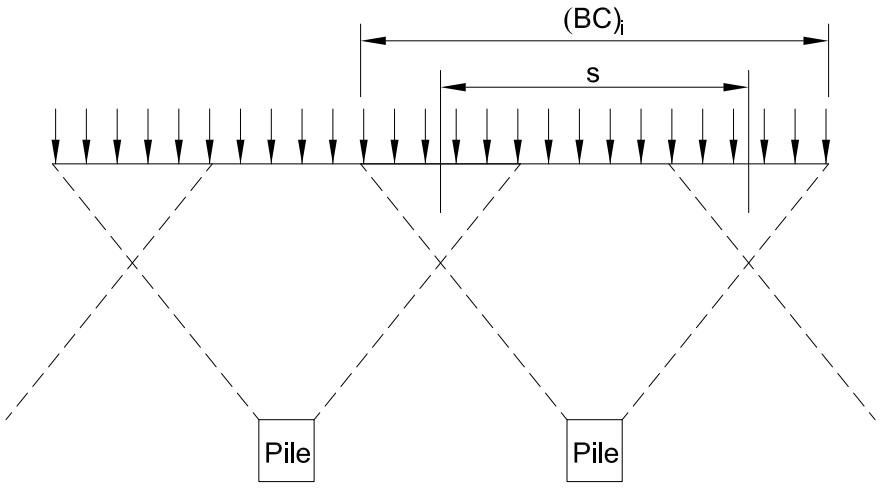

Fig. 6.2.6 Wedge overlap between adjacent piles

6.2.5 Pile response calculation

Pile response is calculated by solving the following differential equation:

$$EI(\frac{d^4y}{dx^4}) + E_s(x)y = 0 \tag{6.13}$$

where EI is the bending stiffness of the pile; y is the relative pile-soil displacement; and E_s can be considered as the secant slope at any point on the $p-y$ curve, i.e.

$$E_s = \frac{p}{y} \tag{6.14}$$

where p is the force per unit length exerted on the pile.

Consider a horizontal slice (a soil sub-layer) of the strain wedge as shown in Figure 6.2.7, the horizontal equilibrium of the horizontal and shear stresses is expressed as

$$p_i = (\Delta\sigma_h)_i\overline{BC}_iS_1 + 2\tau_i dS_2 \tag{6.15}$$

where S_1 and S_2 are equal to 0.75 and 0.5, respectively, for a circular pile cross section, and 1.0 for a square pile.

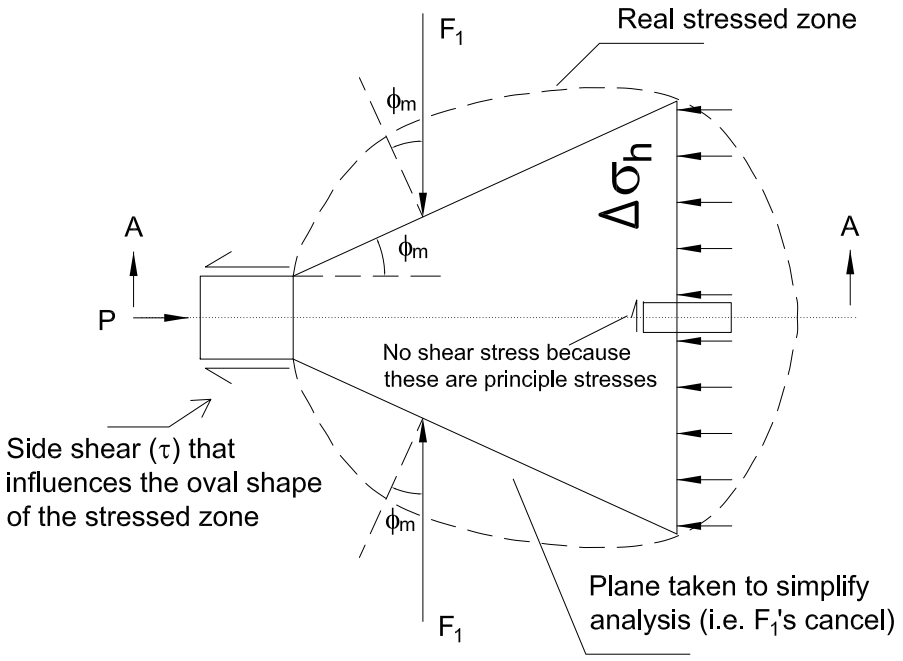

Fig. 6.2.7 Horizontal equilibrium of stresses (after Ashour and Ardalan (2012a))

As observed in the numerical analysis, the lateral soil stress in the down-slope tends to decrease to the level of passive lateral soil stress, which means that not only the increment of the lateral soil stress in the up-slope but also the reduction of the lateral soil stress in the down-slope are taken by the piles. Equation 6.15 is derived for the pile segment in the stable soil. For the pile segment in the sliding soil, equation 6.15 is modified as:

$$p_i = (SL\sigma_{h0} + \Delta\sigma_h)_i \overline{BC}_i S_1 + 2\tau_i dS_2 - SL\sigma_h^p dS_1 \tag{6.16}$$

where σ_{h0} and σ_h^p are the initial and passive lateral soil stress, respectively.

The modulus of the subgrade reaction is expressed as

$$(E_s)_i = \frac{p_i}{y_i} \tag{6.17}$$

In the analysis of the pile response under lateral soil movements, a uniform lateral soil movement with a 'drag zone' is usually presumed (Poulos (1995), Kourkoulis et al. (2010)). As shown in Figure 6.2.8a, it is assumed that a large volume of soil (the upper portion) moves downwards as a rigid body. Below the unstable soil is a relatively thin 'drag zone' undergoing intense shearing, which can be determined from the inclinometer data. The

underlying 'stable zone' is stationary. The 'drag zone' between the slide zone and the stable zone can be regarded as a transition layer, in which the slip surface is determined by the sudden change of displacement (6.2.8b).

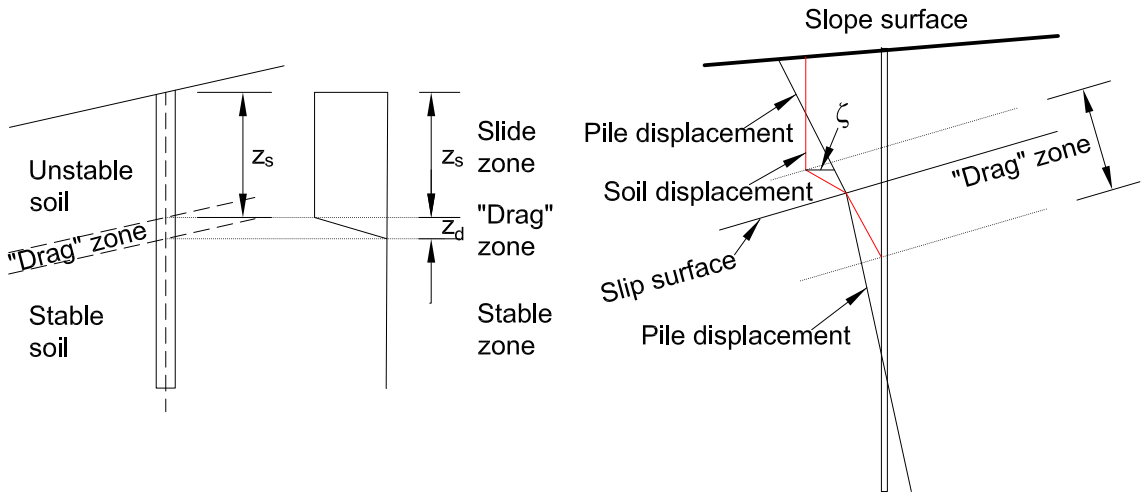

(a) soil movement pattern by Poulos (1995) **(b)** assumed soil movement pattern

Fig. 6.2.8 Soil movement pattern.

The purpose of the strain wedge model is to relate the relative pile-soil movement to the soil stress variations. However, the soil in the 'drag zone' has a non-uniform soil movement due to the shear deformation. The soil movement is assumed to change gradually in the sliding part and stable part of the 'drag zone' while the soil movement equals the global soil movement at the top of the 'drag zone', equals the pile displacement at the slip surface and vanishes at the bottom of the 'drag zone'. Since the soil deformation in the 'drag zone' is caused by the shear stress on the slip surface, the stress increment due to this deformation should not be related to the piles. By adopting the soil movement pattern in Figure 6.2.8b, the net pressure $(p_n)_i$ on the pile can be determined by:

$$(p_n)_i = (E_s)_i \times \zeta \tag{6.18}$$

where ζ is the relative displacement between the soil and the pile (Figure 6.2.8b).

6.2.6 The ultimate lateral pressure on the pile

The ultimate soil pressure on the pile p_u above the slip surface can be calculated from the modified plastic deformation theory according to the research in Chapter 5. For p_u in the stable layer, the simplest approach suggested by Barton (1982) (equation 5.4) is adopted for

sandy soils. For clay soils, as suggested by Poulos (1995), it is usual to adopt a total stress approach in which p_u is related to the undrained shear strength S_u as follows:

$$p_u = N_p S_u \tag{6.19}$$

where N_p is the lateral capacity factor and is assumed to increase linearly from 2 at the ground surface to a limiting value of 9 at a depth of 3.5 times the pile diameter (or the pile width) and beyond for a single pile. For pile groups in a purely cohesive soil, according to the numerical analysis of Chen and Poulos (1993), the reduction of N_p is not significant if the piles are arranged in a row that is perpendicular to the direction of the pile movement while a substantial reduction is observed for piles in two rows. The reduction of N_p is not considered in this study since only one row of piles is used. The $(p_n)_i$ from the strain wedge model is further compared with p_u when the pile spacing is larger than or equal to four times of the pile diameter or width. p_u is adopted if it is exceeded.

6.3 Iteration in the analysis

The calculation procedure based on the proposed model is explained in Figure 6.3.1. Two iterations are essential: the first iteration determines ε_i and h_w for the strain wedges in the sliding zone for the given F_D and M_D; the second iteration determines M_D using the continuity of the pile deformation at the slip surface. Note that the procedure to determine the E_s of the sub-layers below the slip surface is not included in the flowchart. In this study the strain wedge method introduced by Ashour et al. (1998) combined with the multi-wedge method is employed to analyse the pile response below the slip surface with the same F_D and M_D.

To begin with, a small initial soil strain ε_i and an initial height of the stabilized wedge h_w (normally half the thickness of the landslide) are assumed to determine the E_s distribution along the pile above the slip surface, which is essential for the pile analysis using the one-dimensional finite difference method (FDM). The current pile deflection Y_{SWM} obtained from the SW model is compared with the pile deflection Y_{FDM} obtained from FDM. The strains of the wedges are updated through equation 6.5 and h_w is updated by comparing Y_{FDM} with the assumed soil movement until an acceptable difference (5% of the relative pile-soil movement at slip surface for instance) between Y_{SWM} and Y_{FDM} is achieved.

In order to obtain the M_D corresponding to the given F_D, a possible series of M_D is selected for the above iteration to obtain a series of the rotation angle θ_s of the pile cross-section at the slip surface. Another series of θ_s is calculated through the analysis of the pile segment below the slip surface using the same combination of F_D and M_D. The target M_D

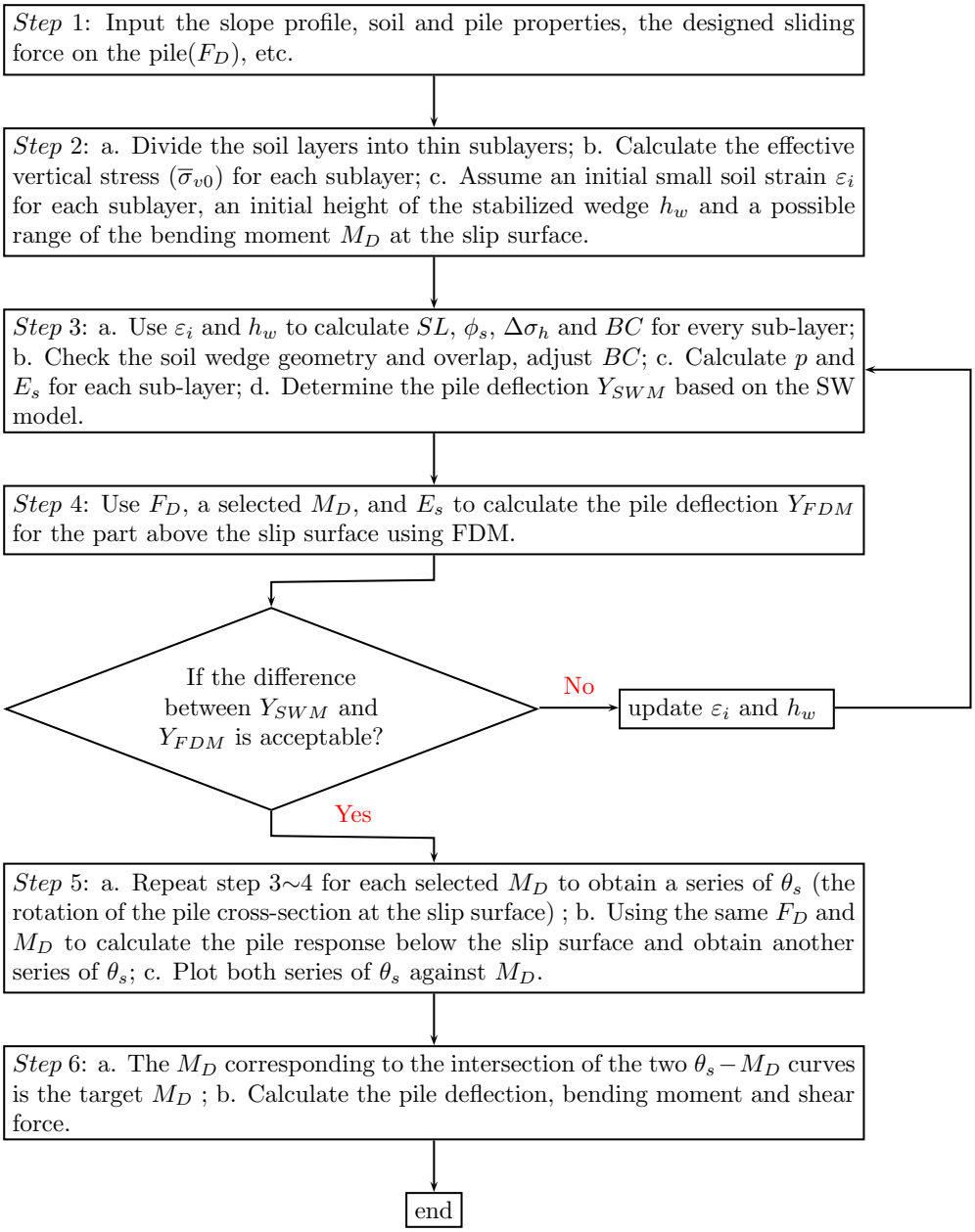

Fig. 6.3.1 Flowchart of the calculation process.

can be obtained by plotting both series of θ_s against M_D. The M_D at the intersection of the two curves is the target value. A Matlab toolbox is created for this purpose.

6.4 In comparison with numerical examples

The proposed approach is compared with some numerical examples to demonstrate its ability to capture the primary features of stabilizing piles. Since the analysis of piles in rock is not included in the approach, the numerical results of a loose sand layer sliding on a dense sandy layer in chapter 5 are used here as references. Another reason to compare with this soil combination is that the ultimate lateral soil pressure is not fully mobilised in the cases of $h/d = 6$ and $h/d = 8$.

Figure 6.4.1 shows the comparison between the numerical and analytical approaches. It is observed that the proposed approach is able to produce good predictions when $s/d = 4$. For higher s/d values, more rigid curves and slightly larger ultimate value P_u are obtained. On the contrary, less rigid curves and smaller P_u are obtained for lower s/d values. The P_u is normalised and compared in Figure 6.4.1d. Except for the cases when s/d equals 2 and 3, the proposed approach is able to capture the reduction of P_u due to the flexible response of the piles.

A characteristic of a relatively flexible pile is the existence of negative soil pressure distributed from the pile top to a certain depth h_c. The decrease of h_c with the increase of the soil displacement is presented in Figure 6.4.2. In the cases with smaller slenderness ($h/d = 4$, 6), the negative soil pressure disappears at a small level of soil displacement, while it still exists even at an extraordinary high level of soil displacement when $h/d = 8$. Pile spacing has also an influence on the negative pressure: h_c tends to reduce faster with a smaller spacing. Comparing h_c between the proposed approach and the numerical method, the initial values are in line with each other. However, the h_c from the proposed approach decreases faster with the increase of the soil displacement. A reason for that could be the non-accurate prediction of the pile response in the stable layer from the proposed approach. Figure 6.4.3 shows the distribution of the soil pressure on the pile at 0.5 m soil displacement with $s/d = 4$. Good comparisons of the soil pressure in the sliding layer are obtained despite the less accurate predictions in the stable layer. It is not further investigated since the pile response in the stable layer is not the research object of this study.

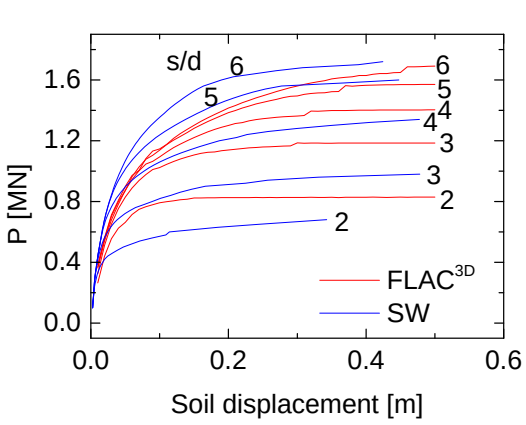

(a) $h/d = 4$

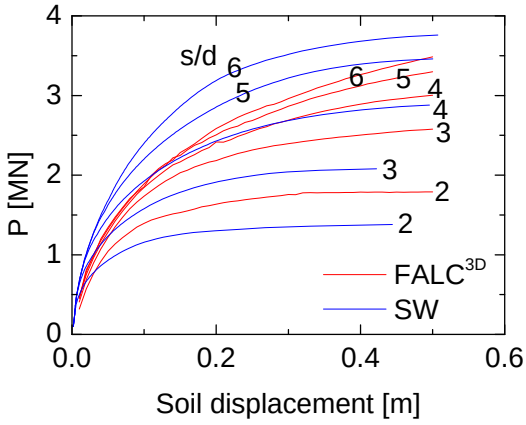

(b) $h/d = 6$

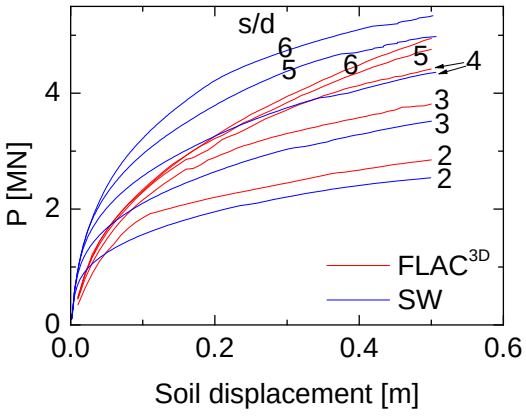

(c) $h/d = 8$

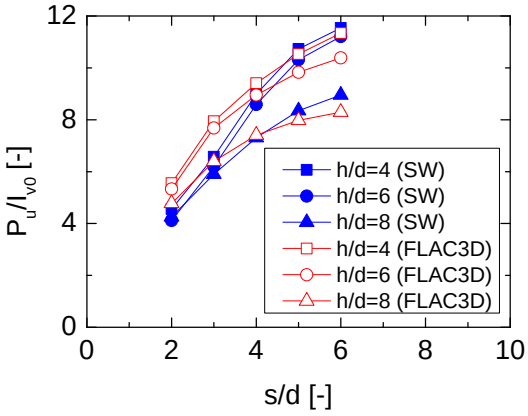

(d) normalised P_u

Fig. 6.4.1 Comparison between numerical method and the proposed SW approach. $P = F_D$, is the the total driving force on the pile; P_u is the ultimate force on the pile; I_{v0} is the integration of the initial vertical stress in the soil over the depth.

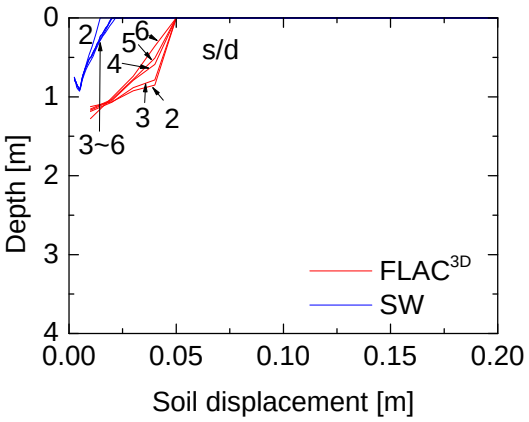

(a) $h/d = 4$

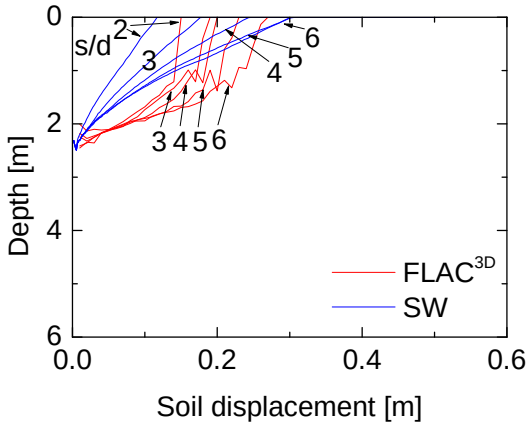

(b) $h/d = 6$

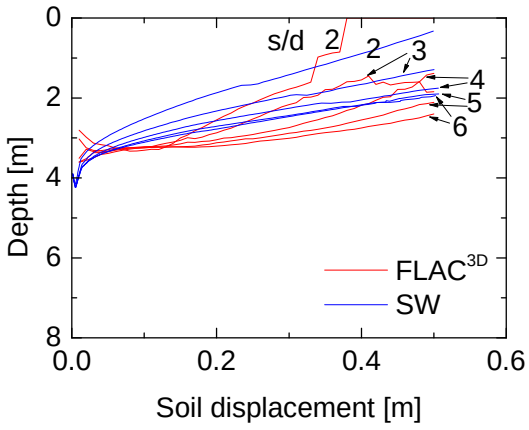

(c) $h/d = 8$

Fig. 6.4.2 Variation of h_c with soil displacement. h_c: the depth of the turning point of soil pressure on the pile, above which the negative soil pressure is obtained.

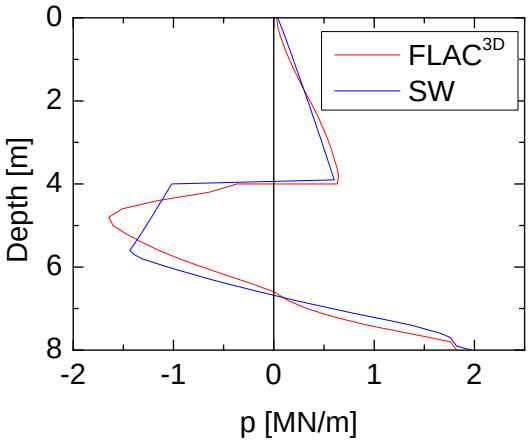

(a) $h/d = 4$, $s/d = 4$

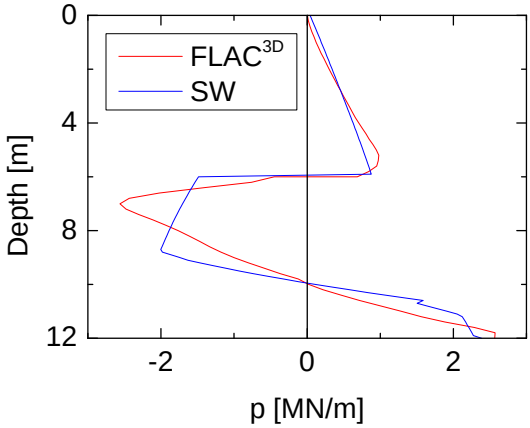

(b) $h/d = 6$, $s/d = 4$

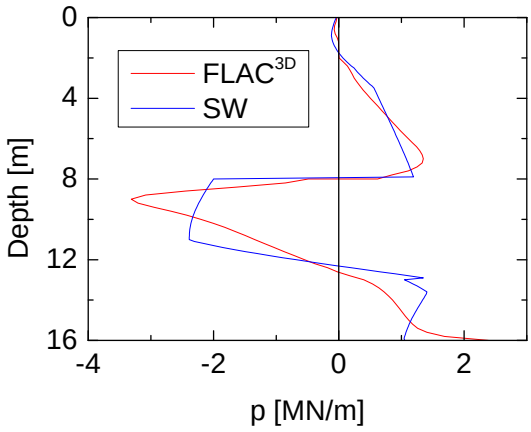

(c) $h/d = 8$, $s/d = 4$

Fig. 6.4.3 Distribution of soil pressure on the pile when soil displacement is 0.5 m.

Table 6.1 Material properties used in the analyses of stabilizing piles in Masseria Marino mudslide (Italy)

	Sliding body	Shear zone	Stable layer	Pile
$\gamma(kN/m^3)$	19	19	19	-
$E(Pa)$	2e7	1e7	5e7	2e11
μ	0.34	0.34	0.34	0.25
$c(kPa)$	0	0	1000	14e4
$\phi(^\circ)$	28	25	30	-
$\psi(^\circ)$	0	0	0	0

6.5 Case study

Two reported cases are studied in order to validate the proposed analysis method. Piles in both cases are well instrumented. The calculation results from the proposed method are compared with the measurements and also other analyses.

6.5.1 Case 1

Lirer (2012) reported a situ experiment of stabilizing piles in the Masseria Marino landslide (Italy). Five steel tube piles with a wall thickness of 6 mm, a length of 10 m, a diameter of 0.4 m and a pile spacing of 0.9 m were installed in the middle of the mudslide. The thickness of the sliding body is 4.6 m with a 11° inclined slip surface. The water level is located at a depth of 2.0 m below the ground surface. Inclinometers were used to monitor the displacement of both the piles and the sliding soil. Vibrating wire gauges were used to measure the local strain. The parameters used in the analyses are listed in Table 6.1. The moment of inertia of the tube pile is $1.44 \times 10^{-4}\ m^4$ as calculated.

Similar to the numerical analysis performed by Lirer (2012), the calculation results from the proposed model are compared with the inclinometer measurement made in June 2000 (Figure 6.5.1). The soil pressure distribution, bending moment and shear force are derived from the measured pile displacement. The observation of zero soil pressure at the depth of 4.6 m confirms the location of the slip surface. The pile shear force at the slip surface indicates that the resultant lateral load exerted on the pile is 71 kN. The numerically calculated pile displacement and soil pressure on the pile from Lirer (2012) and an inclinometer measurement in the soil locating 1.5 m away from the pile row in the direction against the slope (P1 in Lirer (2012)) are also plotted in Figure 6.5.1 for comparison.

The P1 measurement shows that the soil near the slip surface is strongly deformed, which leads to a 'drag zone' from the depth of 3.1 m to 6 m. The soil displacement distribution adopted in the calculation is given as a blue dashed line in Figure 6.5.1a. Good agreement can be observed between the measured and computed pile displacements, lateral soil pressures, bending moments, and shear forces of the pile segment above the slip surface.

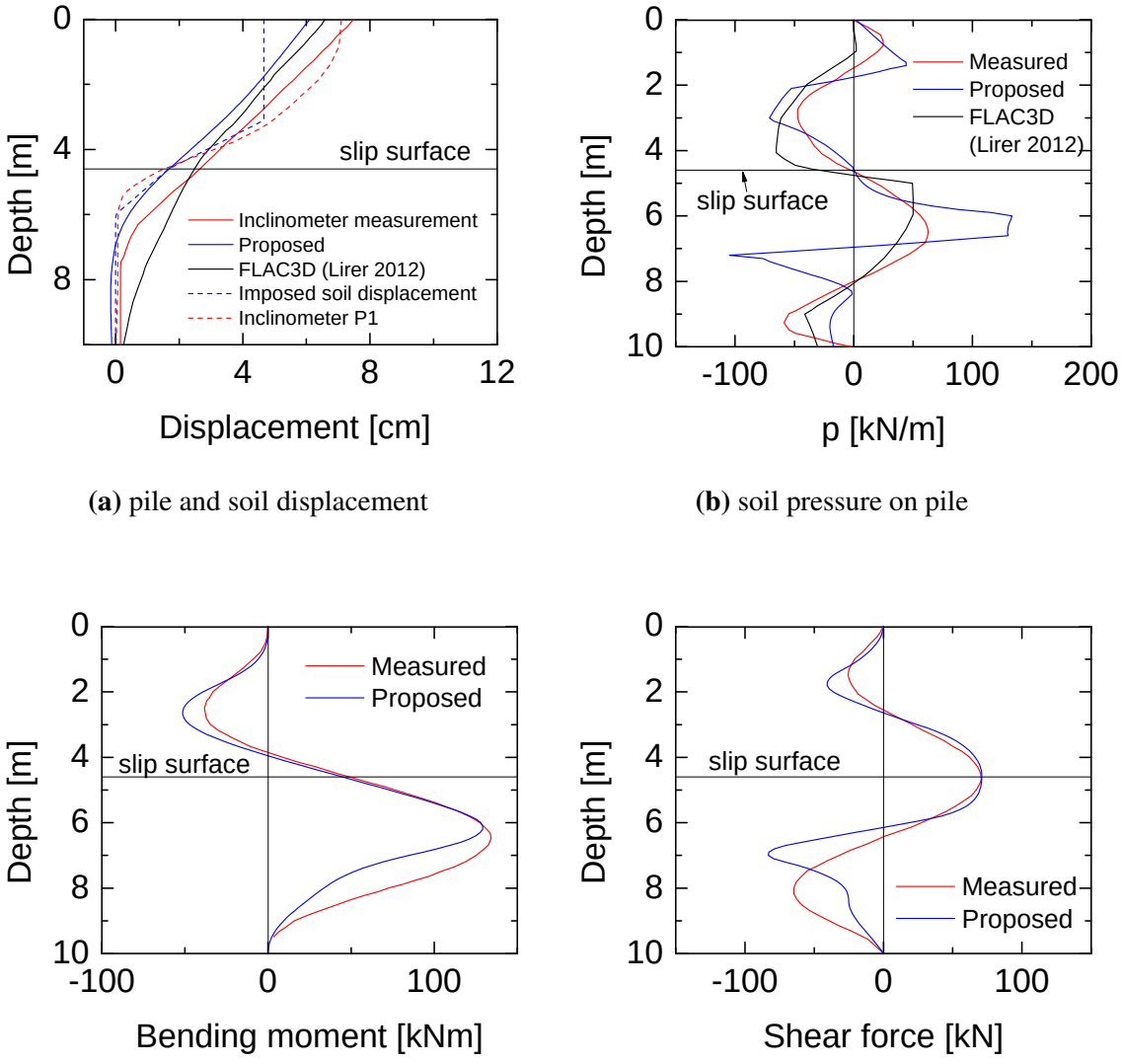

(a) pile and soil displacement

(b) soil pressure on pile

(c) bending moment

(d) shear force

Fig. 6.5.1 Comparison between the experimented data in June 2000 (Lirer (2012)) and the calculated results. Good predictions are obtained for the pile segment above the slip surface.

6.5.2 Case 2

A number of bored concrete piles were used to stabilize a railway embankment at Hildenborough, Kent, UK (Smethurst and Powrie (2007)). The piles are 10 m long with a diameter of 0.6 m and a spacing of 2.4 m. Strain gauges were installed in three adjacent piles to measure the bending moments induced in the piles by the slope movements. Inclinometer measurements were made both in the strain-gauged piles and in the soil between the instrumented piles. The bending stiffness (EI) is $187 \times 10^3 kNm^2$ for the lower 7 m of the pile and $171 \times 10^3 kNm^2$ for the upper 3 m. As suggested by Smethurst and Powrie (2007), the pile stiffness is assumed to increase smoothly from the depth of 2 m to 4 m, rather than increasing suddenly at the depth of 3 m. To consider the structural cracks in the concrete, $75\%EI$ is applied over a pile section from the depth of 4.5 m to 8.5 m with a smooth transition of 0.5 m at the top and the bottom of the section. The section profile of the embankment after the regraded construction platform is shown in Figure 6.5.2 and the corresponding soil parameters for the pile design are listed in Table 6.2. The pore pressure is assumed to be hydrostatic below and zero above the depth of 3.5 m.

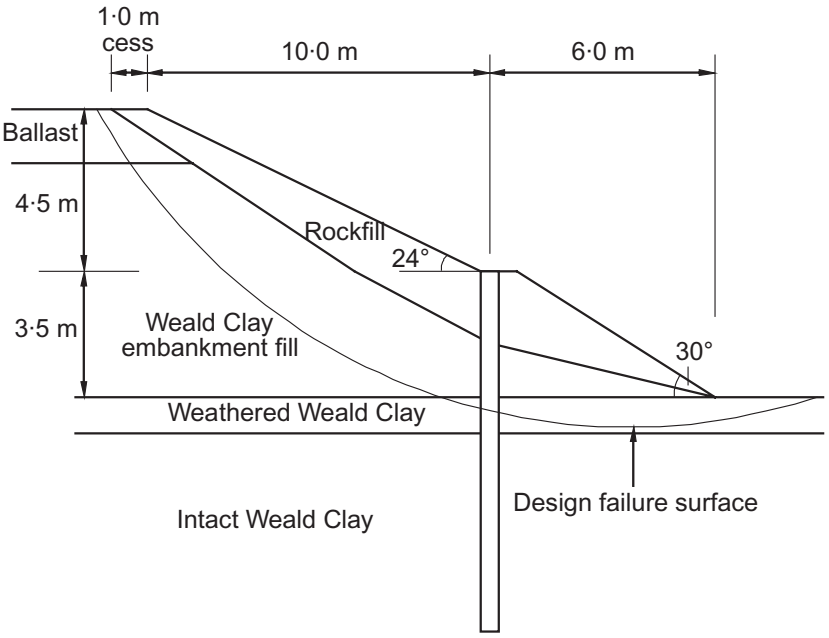

Fig. 6.5.2 Embankment profile after regrading (Smethurst and Powrie (2007)).

The measured data on day 1345 after the pile installation is used here for comparison. As suggested by Smethurst and Powrie (2007), the strain gauge measurement gives a better indication of the true bending moments and soil pressures than the inclinometer. Therefore,

Table 6.2 Design soil parameters of the railway embankment at Hildenborough, Kent, UK (Smethurst and Powrie (2007)).

Soil type	Unit weight, $\gamma(kN/m^3)$	Friction angle, $\phi(^\circ)$	Effective cohesion, $c(kPa)$
Weald Clay embankment fill	19	25	1
Softened Weald Clay embankment fill	19	19	1
Weathered Weald Clay	19	25	1
Weald Clay	20	30	5
Rockfill	19	35	0

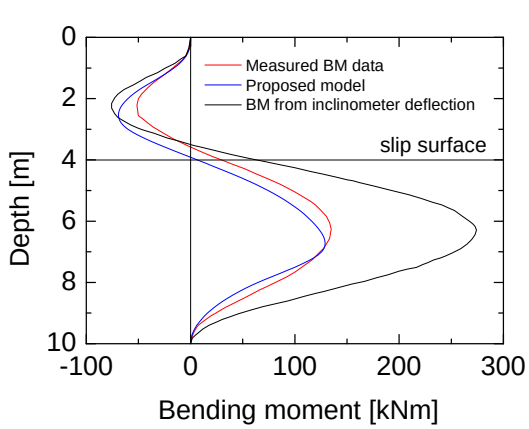

(a) bending moment

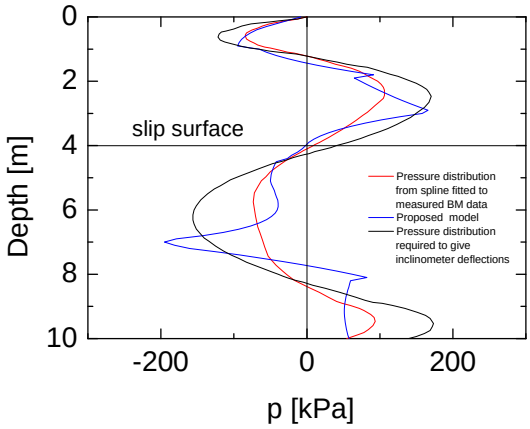

(b) soil pressure on pile

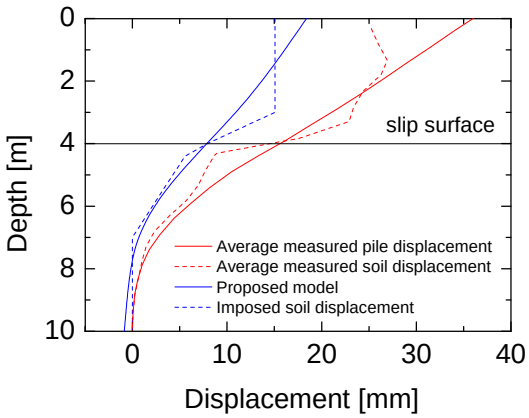

(c) displacement

Fig. 6.5.3 Comparison between the measurements on day 1345 (Smethurst and Powrie (2007)) and the calculated results. The computed bending moment and pressure fit well with the measured data for the pile segment above the slip surface.

the pressure distribution derived from the strain gauge measurement (the red line in Figure 6.5.3b) is used here to calculate the sliding force, which is 75 kN and is calculated by integrating the pressure from the depth of 0 m to 4 m. The computed pile bending moment, soil pressure and displacement are plotted in Figure 6.5.3 together with the corresponding results derived from the strain gauge and inclinometer measurements. The computed bending moment and soil pressure fit well with the measured data for the pile segment above the slip surface. From the comparison of the pile displacement (Figure 6.5.3c), it is clear that the resistance from the stable soil stratum is overestimated. This could be improved by providing further knowledge of the cracked flexural rigidity of the pile.

6.6 Concluding remarks

In this chapter, based on the stabilizing mechanism of piles revealed in the previous chapters, a generalized strain wedge model for flexible piles subjected to lateral soil movement is introduced. The modified plastic deformation theory from chapter 5 is combined with the strain wedge model to provide the ultimate soil pressure in the sliding soil since the failure mode that soil flows between the piles is not considered in the strain wedge model. The proposed approach is able to calculate the pile response at small soil movement and capture the characteristic of negative soil pressure at the pile top for relatively flexible piles. Some numerical models from chapter 5 are calculated using the proposed approach. Good agreement of results comparison is obtained. The validity of the proposed approach is also demonstrated by two case studies.

Chapter 7

Conclusions and future work

7.1 Centrifuge model tests

Centrifuge model tests of a total of 29 cases were conducted to study the interaction of stabilizing piles and a failing slope. The failing slope was modelled by a sliding soil layer above a stable wood layer with a predefined slip surface in between. Two types of piles (acrylic and aluminium) were applied with four different intervals to investigate the effect of pile stiffness and pile spacing. The stabilizing mechanism of deep-buried piles was studied by installing 6 cm shorter piles in the same slope. A shallower sliding soil layer with shorter piles was used to study the influence of pile slenderness and relative up-slope length. An aluminium model pile was instrumented with strain gauges at eight locations throughout the depth to measure the bending moment during the tests. In-flight photography and digital image processing were used to measure the pile top displacement and the soil displacement on the slope surface and the exposed cross-section.

Four failure modes were identified in the centrifuge tests:

- *Flow failure*: Soil flows around the piles when piles are arranged with large spacing (s/d>3.88).

- *Down-slope failure*: Local soil failure tends to occur in the down-slope area while the up-slope soil is stabilized by high stiffness piles arranged with small spacing ($s/d \leq$3.88).

- *Over-top failure*: A part of the up-slope soil moves above the pile top. This failure mode is expected when the large l/h (2.43) and small s/d ($\leq$3.88) are adopted. The over-top and down-slope failure movements can merge at the pile row when flexible piles are used.

- *Pile structural failure*: The pile breakage and plastic hinges are observed at a small depth below the slip surface. This failure mode occurs when the ultimate bending moment is reached. The tests with large s/d (>3.88) are prone to this failure mode.

The following conclusions are drawn from the parametric studies:

- As the pile spacing s/d becomes larger (from 3.1 to 7.75), the overall soil displacement and the sliding force on the piles become larger. The failure mode changes from down-slope failure to flow failure.

- When piles with smaller bending stiffness EI are used, the top part of the piles becomes ineffective, at which the over-top movement from the up-slope soil merges with the down-slope soil movement. The overall stability of the slope is reduced.

- By adopting a smaller pile slenderness h/d (from 13 to 7), the relative pile stiffness K_R is increased. The piles have less displacement, therefore a stronger arching effect between the piles is formed and higher soil pressure is mobilised.

- By increasing the relative up-slope soil length l/h (from 0.85 to 2.43), a larger overall soil displacement and a larger sliding force on the pile are obtained. However, the mechanism varies with the pile spacing s/d. When s/d is small (3.1), the increase of l/h changes the failure mode from down-slope failure to over-top failure. For large s/d (5.17), a larger l/h can accelerate the flow failure. The influence of l/h can be reduced when flexible piles are used.

- Deep-buried piles can be used when the sliding soil is relatively thick. With a smaller pile length in the sliding soil, the relative pile stiffness K_R is increased, higher soil pressure on the pile is mobilised. The use of deep-buried piles can raise the risk of over-top failure. However, when flexible piles are used, the adoption of deep-buried piles produces even higher slope stability than the full length pile.

7.2 Numerical simulation

The intention of conducting numerical simulation is to study the pile-soil interaction in a more fundamental way rather than to simulate a specific engineering case or experiment. Similar to the centrifuge tests, a two-layer system consisting of a soil layer sliding above a stable layer was adopted. A limited geometry of soil was modelled since the soil movement is triggered by the boundary soil movement instead of soil gravity. In the centrifuge tests, the topic was studied mostly using the measurements of soil displacement and the pile bending

moment. In the numerical simulation, the pile-soil interaction was investigated using the soil stress data. The effect of pile spacing, slenderness ratio, stiffness and soil parameters were studied. The plastic deformation theory to predict the ultimate soil pressure on the pile was modified by adding a parameter K_f according to the soil stress analysis.

The following conclusions are drawn:

- A two-stage mechanism is observed for the mobilisation of the soil pressure on the pile. In the first stage the soil pressure from the lower part of the sliding soil is quickly mobilised. In the second stage, the soil pressure from the upper part of the sliding soil is gradually mobilised.

- As the pile spacing s/d becomes larger, the first stage for the mobilisation of the soil pressure on the pile has extended and the ultimate force on the pile P_u has increased. The influence of s/d becomes effective when it is larger than a critical value (between 3 and 4), at which the soil stress that transfers to the down-slope soil at the pile row is minimum and the arching effect is fully mobilised. As the pile spacing increases further, the soil flows through the piles and more soil pressure is transferred to the down-slope soil.

- The pile slenderness h/d and the pile stiffness EI have significant influence on the pile-soil interaction. With a smaller h/d (4.0), the soil stress transmission at the pile row is less affected by the variation of EI. On the other hand when a large h/d (8.0) and a smaller EI are adopted, flexible pile behaviour, in which the arching effect and the soil pressure in the upper part of the pile can not be fully mobilised, is obtained.

- The material parameters of the sliding layer and the stable layer can also affect the pile-soil interaction. As the sliding soil becomes stronger (from loose sand to dense sand) or the stable layer becomes weaker (from rock to dense sand), more flexible pile behaviour tends to appear and the pressure from the shallow soil becomes more difficult to be fully mobilised.

- A parameter K_f, which can be back calculated using the P_u obtained in the numerical analysis, is proposed to modify the plastic deformation to predict the ultimate pressure p_u on the pile in practice. Comparing with the centrifuge results, P_u from the numerical calculations is higher.

7.3 Analytical method

Based on the pile-soil interaction mechanism revealed through the centrifuge tests and numerical simulation. An analytical method, the strain wedge method, was modified to consider the relative pile-soil displacement of the flexible piles. Combined with the modified plastic deformation theory, the proposed approach is able to take into account the flow failure between the piles. The pile response at small soil movement can be calculated and the characteristic of negative soil pressure at the pile top for relatively flexible piles can be captured. The validity of the proposed approach was demonstrated by comparing with the numerical results and two case studies. Good agreement was obtained.

7.4 Future work

Slope stabilized by piles, which can be influenced by a large amount of parameters, is a complex geotechnical topic. Based on the achievements of this study, some areas of this topic and also the experimental technologies can be further investigated and improved:

- The Stereo PIV was successfully applied in the centrifuge analysis. However, it still can be improved by considering the relative lens movement between the cameras due to the centrifugal force.
- In the current study, the slip surface is predefined, which could be not true for a currently stable but potentially endangered slope. How the installation of piles influences the critical slip surface needs to be examined.
- In the numerical simulation using $FLAC^{3D}$, the soil is modelled by continuous mesh, which allows limited deformation and can not model the tensile failure in the soil. A further study using discrete element method or meshless method is recommended.
- The relative pile rigidity K_R is used in the analysis of centrifuge tests to distinguish the pile behaviour, while in the numerical analysis more parameters are observed to have influence on the pile behaviour. The usage of K_R can be further investigated.
- The variation of pore water pressure is not considered in the study. Its effect on the soil pressure on the pile needs to be studied since hydrological variations (rainfall, reservoir water, etc.) are also the triggering factors of slope failure.

References

Abdoun, T., Dobry, R., O'Rourke, T. D., and Goh, S. (2003). Pile response to lateral spreads: centrifuge modeling. *Journal of Geotechnical and Geoenvironmental engineering*, 129(10):869–878.

Ardalan, H. (2013). *Analysis of slopes stabilized using one row of piles based on soil-pile interaction*. PhD thesis, The University of Alabama in Huntsville.

Ashour, M. and Ardalan, H. (2012a). Analysis of pile stabilized slopes based on soil–pile interaction. *Computers and Geotechnics*, 39:85–97.

Ashour, M. and Ardalan, H. (2012b). p–y curve and lateral response of piles in fully liquefied sands. *Canadian Geotechnical Journal*, 49(6):633–650.

Ashour, M. and Norris, G. (2000). Modeling lateral soil-pile response based on soil-pile interaction. *Journal of Geotechnical and Geoenvironmental Engineering*, 126(5):420–428.

Ashour, M., Norris, G., and Pilling, P. (1998). Lateral loading of a pile in layered soil using the strain wedge model. *Journal of Geotechnical and Geoenvironmental Engineering*, 124(4):303–315.

Ashour, M., Pilling, P., and Norris, G. (2004). Lateral behavior of pile groups in layered soils. *Journal of Geotechnical and Geoenvironmental Engineering*, 130(6):580–592.

Barton, Y. (1982). *Laterally loaded model piles in sand: Centrifuge tests and finite element analyses*. PhD thesis, University of Cambridge.

Beer, E. and Wallays, M. (1972). Forces induced in piles by unsymmetrical surcharges on the soil around the piles. In *Fifth Eur Conf On Soil Proc/Sp/*, number Conf Paper, pages 325–332.

Bezuijen, A. and van der Schrier, J. (2005). The influence of a bored tunnel on pile foundations. *Tunnelling. A Decade of Progress. GeoDelft 1995-2005*, pages 127–132.

Bhattacharya, S., Madabhushi, S., and Bolton, M. (2005). An alternative mechanism of pile failure in liquefiable deposits during earthquakes. *Géotechnique*, 55:259–263.

Bishop, A. W. (1955). The use of the slip circle in the stability analysis of slopes. *Géotechnique*, (5):7–17.

Bouguet, J. (2015). Camera calibration toolbox for Matlab. Online manual.

Brandenberg, S. J., Boulanger, R. W., Kutter, B. L., and Chang, D. (2007). Static pushover analyses of pile groups in liquefied and laterally spreading ground in centrifuge tests. *Journal of Geotechnical and Geoenvironmental Engineering*, 133(9):1055–1066.

Bransby, M. and Springman, S. (1997). Centrifuge modelling of pile groups adjacent to surcharge loads. *Soils and Foundations*, 37(2):39–49.

Broms, B. B. (1964). Lateral resistance of piles in cohesionless soils. *Journal of the Soil Mechanics and Foundations Division*, 90(3):123–158.

Byrne, P. M., Anderson, D. L., and Janzen, W. (1984). Response of piles and casings to horizontal free-field soil displacements. *Canadian Geotechnical Journal*, 21(4):720–725.

Cai, F. and Ugai, K. (2003). Response of flexible piles under laterally linear movement of the sliding layer in landslides. *Canadian Geotechnical Journal*, 40(1):46–53.

Cai, F. and Ugai, K. (2011). A subgrade reaction solution for piles to stabilise landslides. *Géotechnique*, 61(2):143–151.

Carrubba, P., Maugeri, M., and Motta, E. (1989). Esperienze in vera grandezza sul comportamento di pali per la stabilizzaaione di un pendio. *Proceedings of the XVII Convegno Nazionale di Geotechica, Taormina, Italy*, pages 26–28.

Chen, C.-Y. and Martin, G. (2002). Soil–structure interaction for landslide stabilizing piles. *Computers and Geotechnics*, 29(5):363–386.

Chen, L. (1994). *Effect of lateral soil movements on pile foundations*. PhD thesis, University Of Sydney.

Chen, L. and Poulos, H. (1993). Analysis of pile-soil interaction under lateral loading using infinite and finite elements. *Computers and Geotechnics*, 15(4):189–220.

Chen, L. and Poulos, H. (1997). Piles subjected to lateral soil movements. *Journal of Geotechnical and Geoenvironmental Engineering*, 123(9):802–811.

Chiang, K.-H. and Lee, C.-J. (2007). Responses of single piles to tunneling-induced soil movements in sandy ground. *Canadian Geotechnical Journal*, 44(10):1224–1241.

Chow, Y. (1996). Analysis of piles used for slope stabilization. *International Journal for Numerical and Analytical Methods in Geomechanics*, 20(9):635–646.

Dobry, R., Abdoun, T., O'Rourke, T. D., and Goh, S. (2003). Single piles in lateral spreads: Field bending moment evaluation. *Journal of Geotechnical and Geoenvironmental Engineering*, 129(10):879–889.

Durrani, I., Ellis, E., and Reddish, D. (2008). Numerical modelling of lateral pile-soil interaction for a row of piles in a frictional soil. In *Proceedings of the 1st International Conference on Advances in Transportation Geotechnics*, pages 291–298.

Ellis, E., Durrani, I., and Reddish, D. (2010). Numerical modelling of discrete pile rows for slope stability and generic guidance for design. *Géotechnique*, 60(3):185–195.

Ellis, E. and Springman, S. (2001). Full-height piled bridge abutments constructed on soft clay. *Géotechnique*, 51(1):3–14.

Esu, F. and D'Elia, B. (1974). Interazione terreno-struttura in un palo sollecitato da una frana tipo colata. *Rivista Italiana di Geotecnica*, 8(1):27–38.

Finn, W. L. (2005). A study of piles during earthquakes: issues of design and analysis. *Bulletin of Earthquake Engineering*, 3(2):141–234.

Fleming, K., Weltman, A., Randolph, M., and Elson, K. (2008). *Piling engineering*. CRC press, 2nd edition.

Frank, R. and Pouget, P. (2008). Experimental pile subjected to long duration thrusts owing to a moving slope. *Géotechnique*, 58(8):645–658.

Fukuoka, M. (1977). The effects of horizontal loads on piles due to landslides. In *Proceedings of 9th I.C.S.M.F.E., Specialty Session*, volume 10, pages 27–42.

Guo, W. and Ghee, E. (2006). Behavior of axially loaded pile groups subjected to lateral soil movement. In *Foundation Analysis and Design: Innovative Methods*, pages 174–181.

Guo, W., Qin, H., and Ghee, E. (2006). Effect of soil movement profiles on vertically loaded single piles. In *Proceedings of the 6th International Conference on Physical Modelling in Geotechnics, Hong Kong*, pages 4–6.

Guo, W. D. (2006). On limiting force profile, slip depth and response of lateral piles. *Computers and Geotechnics*, 33(1):47–67.

Guo, W. D. and Qin, H. (2010). Thrust and bending moment of rigid piles subjected to moving soil. *Canadian Geotechnical Journal*, 47(2):180–196.

Hassiotis, S., Chameau, J., and Gunaratne, M. (1997). Design method for stabilization of slopes with piles. *Journal of Geotechnical and Geoenvironmental Engineering*, 123(4):314–323.

Hayward, T., Lees, A., Powrie, W., Richards, D., and Smethurst, J. (2000). Centrifuge modelling of a cutting slope stabilised by discrete piles. *Wokingham, GB. Transport Research Laboratory*.

He, Y., Hazarika, H., Yasufuku, N., and Han, Z. (2015). Evaluating the effect of slope angle on the distribution of the soil–pile pressure acting on stabilizing piles in sandy slopes. *Computers and Geotechnics*, 69:153–165.

Heikkilä, J. (2000). Camera calibration toolbox for Matlab. Online manual.

Heikkila, J. and Silven, O. (1997). A four-step camera calibration procedure with implicit image correction. In *Computer Vision and Pattern Recognition, 1997. Proceedings., 1997 IEEE Computer Society Conference on*, pages 1106–1112. IEEE.

Hoek, E. and Brown, E. T. (1980). *Underground excavations in rock*. CRC Press.

Hong, Y., Soomro, M. A., and Ng, C. (2015). Settlement and load transfer mechanism of pile group due to side-by-side twin tunnelling. *Computers and Geotechnics*, 64:105–119.

Idinger, G. (2016). *Experimental study on failure initiation in partially saturated slopes*. PhD thesis, University of Natural Resources and Life Sciences, Vienna.

ITASCA (2009). FLAC3D version 4.0 user's manual. *Itasca Consulting Group, Minneapolis, MN, USA*.

Ito, T. and Matsui, T. (1975). Methods to estimate lateral force acting on stabilizing piles. *Soils and Foundations*, 15(4):43–59.

Ito, T., Matsui, T., and Hong, W. P. (1981). Design method for stabilizing piles against landslide-one row of piles. *Soils and Foundations*, 21(1):21–37.

Jaky, J. (1948). Pressure in silos. In *Proc. 2nd Int. Conf. Soil Mech.*, volume 1, pages 103–107.

Janbu, N. (1957). Earth pressure and bearing capacity calculations by generalized procedure of slices. In *Proc. 4. Int. Conf. SMFE, London*, volume 2, pages 207–212.

Kalteziotis, N., Frank, R., Zervogiannis, H., Seve, G., and Berche, J. (1993). Experimental study of landslide stabilization by large diameter piles. In *International Symposium, Geotechnical Engineering of Hard Soils-Soft Rocks*, volume 2, pages 1115–1124.

Kanagasabai, S., Smethurst, J., and Powrie, W. (2011). Three-dimensional numerical modelling of discrete piles used to stabilize landslides. *Canadian Geotechnical Journal*, 48(9):1393–1411.

Kourkoulis, R., Gelagoti, F., Anastasopoulos, I., and Gazetas, G. (2010). Slope stabilizing piles and pile-groups: parametric study and design insights. *Journal of Geotechnical and Geoenvironmental Engineering*, 137(7):663–677.

Kourkoulis, R., Gelagoti, F., Anastasopoulos, I., and Gazetas, G. (2011). Hybrid method for analysis and design of slope stabilizing piles. *Journal of Geotechnical and Geoenvironmental Engineering*, 138(1):1–14.

Leung, C., Chow, Y., and Shen, R. (2000). Behavior of pile subject to excavation-induced soil movement. *Journal of Geotechnical and Geoenvironmental Engineering*, 126(11):947–954.

Leung, C., Lim, J., Shen, R., and Chow, Y. (2003). Behavior of pile groups subject to excavation-induced soil movement. *Journal of Geotechnical and Geoenvironmental Engineering*, 129(1):58–65.

Leung, C., Ong, D., and Chow, Y. (2006). Pile behavior due to excavation-induced soil movement in clay. II: Collapsed wall. *Journal of Geotechnical and Geoenvironmental Engineering*, 132(1):45–53.

Li, C., Tang, H., Hu, X., and Wang, L. (2013). Numerical modelling study of the load sharing law of anti-sliding piles based on the soil arching effect for Erliban landslide, China. *KSCE Journal of Civil Engineering*, 17(6):1251–1262.

Li, C., Wu, J., Tang, H., Hu, X., Liu, X., Wang, C., Liu, T., and Zhang, Y. (2016). Model testing of the response of stabilizing piles in landslides with upper hard and lower weak bedrock. *Engineering Geology*, 204:65–76.

Liang, R. and Zeng, S. (2002). Numerical study of soil arching mechanism in drilled shafts for slope stabilization. *Soils and Foundations*, 42(2):83–92.

Liang, R. Y. and Yamin, M. (2010). Three-dimensional finite element study of arching behavior in slope/drilled shafts system. *International Journal for Numerical and Analytical Methods in Geomechanics*, 34(11):1157–1168.

Lirer, S. (2012). Landslide stabilizing piles: Experimental evidences and numerical interpretation. *Engineering Geology*, 149:70–77.

Martin, G. and Chen, C.-Y. (2005). Response of piles due to lateral slope movement. *Computers & structures*, 83(8):588–598.

Mayne, P. W. and Kulhawy, F. H. (1982). Ko- OCR relationships in soil. *Journal of the Soil Mechanics and Foundations Division*, 108(6):851–872.

Morgenstern, N. and Price, V. E. (1965). The analysis of the stability of general slip surfaces. *Géotechnique*, 15(1):79–93.

Ng, C. W. W., Hong, Y., and Soomro, M. (2015). Effects of piggyback twin tunnelling on a pile group: 3D centrifuge tests and numerical modelling. *Géotechnique*, 65(1):38–51.

Ng, C. W. W. and Lu, H. (2013). Effects of the construction sequence of twin tunnels at different depths on an existing pile. *Canadian geotechnical journal*, 51(2):173–183.

Norris, G. (1986). Theoretically based BEF laterally loaded pile analysis. In *Proc. 3rd Int. Conf. on Numerical Methods in Offshore Piling*, pages 361–386.

Ong, D., Leung, C., and Chow, Y. (2006). Pile behavior due to excavation-induced soil movement in clay. I: Stable wall. *Journal of Geotechnical and Geoenvironmental Engineering*, 132(1):36–44.

Ong, D., Leung, C., and Chow, Y. (2009). Behavior of pile groups subject to excavation-induced soil movement in very soft clay. *Journal of Geotechnical and Geoenvironmental Engineering*, 135(10):1462–1474.

ÖNORM-EN-ISO-14688-2 (2013). *Geotechnische Erkundung und Untersuchung - Benennung, Beschreibung und Klassifizierung von Boden - Teil 2: Grundlagen von Bodenklassifizierung*.

Paik, K. and Salgado, R. (2003). Estimation of active earth pressure against rigid retaining walls considering arching effects. *Géotechnique*, 53(7):643–654.

Pan, D., Smethurst, J., and Powrie, W. (2012). Limiting pressure on a laterally loaded pile in a frictional soil. *Géotechnique Letters*, 2(2):55–60.

Pan, J., Goh, A., Wong, K., and Selby, A. (2002a). Three-dimensional analysis of single pile response to lateral soil movements. *International Journal for Numerical and Analytical Methods in Geomechanics*, 26(8):747–758.

Pan, J., Goh, A., Wong, K., and Teh, C. (2002b). Ultimate soil pressures for piles subjected to lateral soil movements. *Journal of Geotechnical and Geoenvironmental Engineering*, 128(6):530–535.

Pan, J., Goh, A. T., Wong, K., and Teh, C. (2000). Model tests on single piles in soft clay. *Canadian Geotechnical Journal*, 37(4):890–897.

Pilling, P., Ashour, M., and Norris, G. (2001). Strain wedge model hybrid analysis of laterally loaded pile group. *Transportation Research Record: Journal of the Transportation Research Board*, 1772:115–121.

Poulos, H. G. (1971). Behavior of laterally loaded piles I: single piles. *Journal of Soil Mechanics & Foundations Div*, 97(5):711–731.

Poulos, H. G. (1973). Analysis of piles in soil undergoing lateral movement. *Journal of Soil Mechanics & Foundations Div*, 99(5):391–406.

Poulos, H. G. (1995). Design of reinforcing piles to increase slope stability. *Canadian Geotechnical Journal*, 32(5):808–818.

Poulos, H. G. and Davis, E. H. (1980). *Pile foundation analysis and design*. John Wiley & Sons, Inc.

Reese, L., Wang, S., Isenhower, W., and Arrellaga, J. (2000). LPILE plus 4.0 technical manual. *ENSOFT INC.*

Reese, L. C., Cox, W. R., and Koop, F. D. (1974). Analysis of laterally loaded piles in sand. *Offshore Technology in Civil Engineering Hall of Fame Papers from the Early Years*, pages 95–105.

Reese, L. C., Wang, S.-T., and Fouse, J. L. (1993). Use of drilled shafts in stabilizing a slope. In *Stability and Performance of Slopes and Embankments II*, pages 1318–1332. ASCE.

Sarma, S. (1973). Stability analysis of embankments and slopes. *Géotechnique*, 23(3):423–433.

Smethurst, J. and Powrie, W. (2007). Monitoring and analysis of the bending behaviour of discrete piles used to stabilise a railway embankment. *Géotechnique*, 57(8):663–677.

Song, Y.-S., Hong, W.-P., and Woo, K.-S. (2012). Behavior and analysis of stabilizing piles installed in a cut slope during heavy rainfall. *Engineering Geology*, 129:56–67.

Spencer, E. (1967). A method of analysis of the stability of embankments assuming parallel inter-slice forces. *Géotechnique*, 17(1):11–26.

Springman, S. M. (1989). *Lateral loading on piles due to simulated embankment construction.* PhD thesis, University of Cambridge.

Stefania, L., Massimo, R., and Caterina, T. (2015). Numerical analysis of slopes reinforced with a row of short piles. In *Engineering Geology for Society and Territory*, volume 2, pages 2077–2081. Springer.

Stewart, D. P. (1992). *Lateral loading of piled bridge abutments due to embankment construction*. PhD thesis, University of Western Australia.

Stewart, D. P., Jewell, R. J., and Randolph, M. (1994). Design of piled bridge abutments on soft clay for loading from lateral soil movements. *Géotechnique*, 44(2):277–296.

Tang, H., Hu, X., Xu, C., Li, C., Yong, R., and Wang, L. (2014). A novel approach for determining landslide pushing force based on landslide-pile interactions. *Engineering Geology*, 182:15–24.

Tsuchiya, T., Kakurai, M., Yamashita, K., and Hamada, J. (2001). Large-scale laminar shear box for lateral pile loading tests with ground displacements. *International Journal of Physical Modelling in Geotechnics*, 1(2):43–51.

Viggiani, C. (1981). Ultimate lateral load on piles used to stabilize landslides. In *Proceedings of the 10th International Conference on Soil Mechanics and Foundation Engineering, Stockholm, Sweden*, volume 3, pages 555–560.

Wang, L. and Zhang, G. (2013). Pile-reinforcement behavior of cohesive soil slopes: Numerical modeling and centrifuge testing. *Journal of Applied Mathematics*, 2013:1–15.

Wang, W. L. and Yen, B. C. (1974). Soil arching in slopes. *Journal of Geotechnical Engineering*, 100(gt1):61–78.

Wei, W. and Cheng, Y. (2009). Strength reduction analysis for slope reinforced with one row of piles. *Computers and Geotechnics*, 36(7):1176–1185.

White, D., Take, W., and Bolton, M. (2003). Soil deformation measurement using particle image velocimetry (PIV) and photogrammetry. *Géotechnique*, 53(7):619–631.

White, D. J., Thompson, M. J., Suleiman, M. T., and Schaefer, V. R. (2008). Behavior of slender piles subject to free-field lateral soil movement. *Journal of Geotechnical and Geoenvironmental Engineering*, 134(4):428–436.

Wilson, D. W., Boulanger, R. W., and Kutter, B. L. (2000). Observed seismic lateral resistance of liquefying sand. *Journal of Geotechnical and Geoenvironmental Engineering*, 126(10):898–906.

Xu, L.-Y., Cai, F., Wang, G.-X., and Ugai, K. (2013). Nonlinear analysis of laterally loaded single piles in sand using modified strain wedge model. *Computers and Geotechnics*, 51:60–71.

Yamin, M. and Liang, R. Y. (2010). Limiting equilibrium method for slope/drilled shaft system. *International Journal for Numerical and Analytical Methods in Geomechanics*, 34(10):1063–1075.

Yoon, B. and Ellis, E. (2009). Centrifuge modelling of slope stabilisation using a discrete pile row. *Geomechanics and Geoengineering: An International Journal*, 4(2):103–108.

Yoon, B. S. (2008). *Centrifuge modelling of discrete pile rows to stabilise slopes*. PhD thesis, University of Nottingham.

Yuan, B., Liu, J., Chen, W., and Xia, K. (2011). Development of a robust Stereo-PIV system for 3-D soil deformation measurement. *Journal of Testing and Evaluation*, 40(2):256–264.

Zhang, G. and Wang, L. (2010). Stability analysis of strain-softening slope reinforced with stabilizing piles. *Journal of Geotechnical and Geoenvironmental Engineering*, 136(11):1578–1582.

Zhang, G. and Wang, L. (2016). Integrated analysis of a coupled mechanism for the failure processes of pile-reinforced slopes. *Acta Geotechnica*, 11(4):941–952.

Zhou, C., Shao, W., and van Westen, C. J. (2014). Comparing two methods to estimate lateral force acting on stabilizing piles for a landslide in the Three Gorges Reservoir, China. *Engineering Geology*, 173:41–53.

Appendix A

The effect of boundary conditions

Using the boundary conditions of the model, the sliding force on the piles can be roughly estimated. Figure A.0.1 shows the idealised analysis model adopted by Yoon (2008), which is in line with the current centrifuge model. The forces P_1 and P_2 due to the lateral earth pressure on the planes AD and BC are assumed to cancel each other out. The driving force from the soil block $ABCD$ is given by

$$F_d = W \sin\beta \tag{A.1}$$

where β is the angle of inclination of the slip surface, W is the weight of the soil block which is calculated by

$$W = lhbN\gamma \tag{A.2}$$

where l is the length of the up-slope soil, h is the thickness of the sliding layer, b is the model width, N is the g-level and γ is the soil unit weight.

Besides the support of the piles, the movement of the soil block is resisted by the friction from the side walls T_s and the slip surface at the bottom T_b:

$$T_s = \mu_s N_s = \frac{1}{2}\mu_s K_s \gamma h^2 l = \frac{1}{2}\mu_s K_s \frac{h}{b} W \tag{A.3}$$

$$T_b = \mu_b N_b + c_b \frac{bl}{\cos\beta} = \mu_b W \cos\beta + c_b \frac{bl}{\cos\beta} \tag{A.4}$$

where N_s and N_b are normal forces on the side wall and the slip surface, respectively; μ_s and μ_b are coefficients of friction; K_s is the coefficient of lateral earth pressure and c_b is the cohesion of the slip surface. The total resistance force from the model boundaries F_μ is given by:

$$F_\mu = 2T_s + T_b = \mu_s K_s \frac{h}{b} W + \mu_b W \cos\beta + c_b \frac{bl}{\cos\beta} \tag{A.5}$$

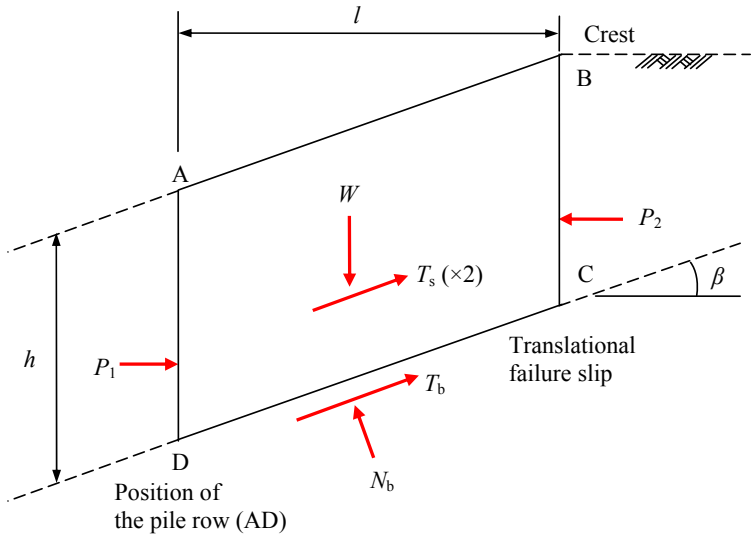

Fig. A.0.1 Idealisation of a piled slope problem for semi-infinite slope (Yoon (2008)).

The sliding force applied on the piles S is calculated by using the driving force F_d to minus the resisting force F_μ:

$$S = F_d - F_\mu = AW \tag{A.6}$$

where A is the ratio of the resistances from the piles to the weight of the up-slope soil:

$$A = \frac{S}{W} = \sin\beta - \mu_s K_s \frac{h}{b} - \mu_b \cos\beta - \frac{c_b}{hN\gamma\cos\beta} \tag{A.7}$$

The coefficients of friction have been determined by direct shear tests:

$$\mu_s = \tan 27.8^\circ = 0.53$$
$$\mu_b = \tan 6.06^\circ = 0.11$$
$$c_b = 4.78kPa$$

The coefficient of lateral earth pressure K_s is estimated using the earth pressure coefficient at rest:

$$K_s = K_0 = 1 - \sin 31.8^\circ = 0.47$$

Substitute the values of the coefficients into equation A.7, the ratio of the resistances from the piles to the weight of the up-slope soil (A) is calculated. With the increase of g-level, the

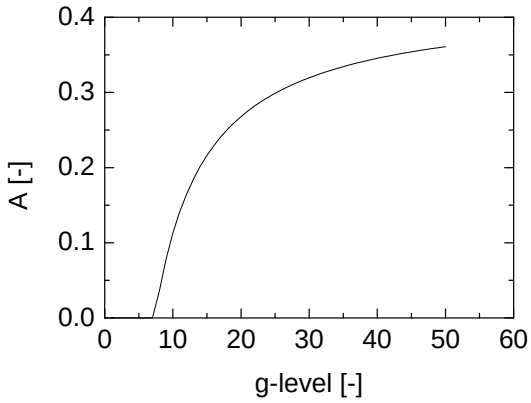

Fig. A.0.2 Increase of A with g-level.

influence of c_b on A reduces, as a result, A increases (as shown in figure A.0.2). A can be used as a reference to the analysis of the strain gauge measurements. Note that the driving force accounts for 70.7% of the soil gravity while the side friction accounts for 20.9%. For the resistance from the bottom sliding surface, the contribution of the friction to the resistance is 7.5% of the soil gravity while the contribution of cohesion is up to 38.7% at 8 g and it reduces to 6.2% at 50 g. The resistance from the side wall and the cohesion from the bottom may be overestimated and must be corrected according to the centrifuge test observations.

The stability of the centrifuge model can be evaluated by a limit equilibrium method (Yamin and Liang (2010)). As shown in figure A.0.3, the sliding soil mass is divided into n vertical slices. The forces acting on each slice under the experimental condition are shown in figure A.0.4. The safety factor (F_s) of the slope is defined as:

$$F_s = \frac{\tau_f}{\tau} \tag{A.8}$$

where τ_f is the available shear strength along the slip surface at failure and τ is the shear force that is required to bring the slope into a state of equilibrium.

Applying equations of force equilibrium for slice i in both perpendicular and parallel directions to the slice bottom, the following equations hold:

$$N_{bi} = W_i \cos\beta_i + R_i \sin(\beta_{i-1} - \beta_i) \tag{A.9}$$

$$T_{bi} = W_i \sin\beta_i + R_i \cos(\beta_{i-1} - \beta_i) - L_i - T_{si} \tag{A.10}$$

where N_{bi} is the force normal to the base of slice i, W_i is the weight of slice i, T_{bi} is the force parallel to the base of slice i, R_i is the right inter-slice force of slice i, L_i is the left inter-slice force of slice i, T_{si} is the friction from the side walls, β_i is the inclination of the base of slice i.

The available shear strength τ_f along the slip surface is assumed to follow the Mohr-Coulomb failure criterion, which gives the following equation:

$$\tau_f = c_b + \sigma' \tan \varphi_b \tag{A.11}$$

where c_b and φ_b are the cohesion and the friction angle of the slip surface, respectively; σ' is the effective stress.

Substituting equation A.10 into equation A.11, the left inter-slice force L_i can be related to the right inter-slice force R_i for a typical slice i as follows:

$$L_i = C_{Ai} + C_{Bi} R_i \tag{A.12}$$

where

$$C_{Ai} = W_i \sin \beta_i - \frac{c_{bi} \Delta x \sec \beta_i}{F_s} - T_{si} - W_i \cos \beta_i \frac{\tan \phi_{bi}}{F_s} \tag{A.13}$$

$$C_{Bi} = \cos(\beta_{i-1} - \beta_i) - \sin(\beta_{i-1} - \beta_i) \frac{\tan \phi_{bi}}{F_s} \tag{A.14}$$

The factor of stability (F_s) of the model slope can be calculated through a searching scheme with the condition that $L_n = 0$. Figure A.0.5 shows the decrease of F_s with g-level. Using the current friction parameters of the model box boundaries, F_s is larger than 1 until about 18 g, which is inconsistent with the observations from the centrifuge tests. As mentioned above, the resistances from the side walls and the cohesion of the sliding surface could be overestimated. A reduction of these resistances is applied to correct the calculation of F_s. It was observed in the centrifuge tests that test *NP* (no piles) started the large soil movement at about 2.7 g. In most tests with piles, the measured soil movement and the sliding force are very small before about 5 g. It is reasonable to choose a reduction ratio for the aforementioned boundary resistances, with which the model slope has a stability factor of 1 at about 5 g. In this case, 0.4 is chosen as shown in figure A.0.5. The increases of A with g-level after the correction are shown in figure A.0.6. It is seen that the influence of g-level on A becomes very small after about 15 g. The values of A at 50 g are used for the analysis of the centrifuge tests.

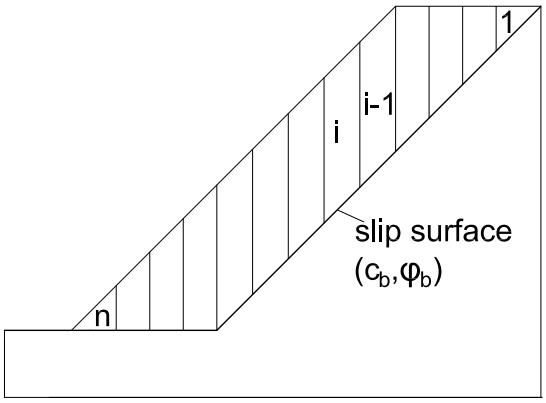

Fig. A.0.3 The sliding soil divided into *n* slices.

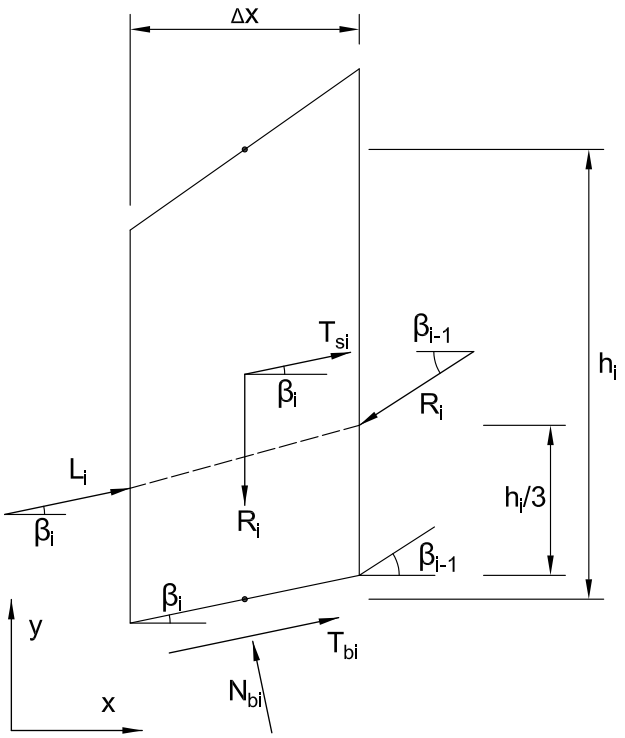

Fig. A.0.4 Forces acting on a typical slice.

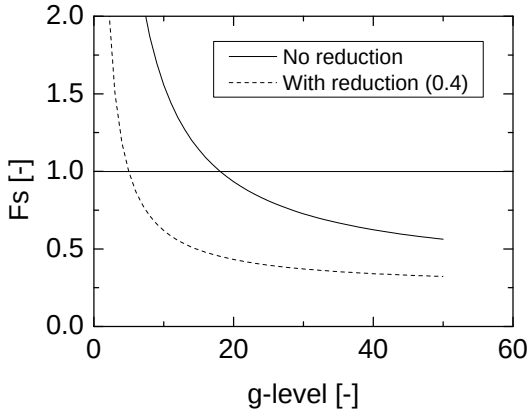

Fig. A.0.5 Factor of stability.

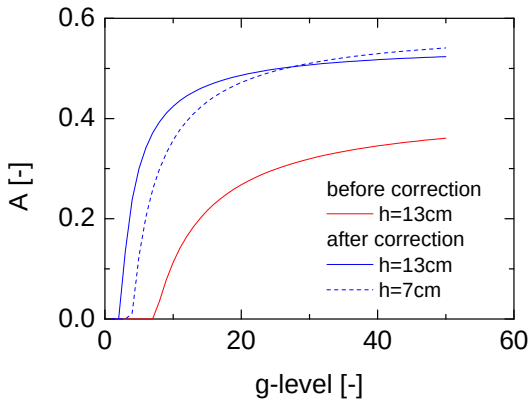

Fig. A.0.6 Increase of A with g-level before and after correction. h is the soil thickness in the centrifuge model.

Appendix B

Modified plastic deformation theory

The derivation of the ultimate soil pressure on the pile p_u in the modified plastic deformation theory is presented in this appendix.

In the plastic deformation theory, two sliding surfaces, which occur along the lines AEB and $A'E'B'$ (Figure B.0.1), are assumed. The soil layer becomes plastic only in the soil zone $AEBB'E'A'$, in which the Mohr-Coulomb's yield criterion is applied.

Figure B.0.2a shows a small element of the plastically deforming soil in the zone $EBB'E'$, the equilibrium of forces in the x direction gives that

$$-D\mathrm{d}\sigma_x - \sigma_x \mathrm{d}D + 2\mathrm{d}x\left[\sigma_\alpha \tan(\frac{\pi}{4}+\frac{\phi}{2}) + \sigma_\alpha \tan(\phi) + c\right] = 0 \tag{B.1}$$

The normal stress σ_α on the surfaces EB and $E'B'$ is given by

$$\sigma_\alpha = \sigma_x N_\phi + 2c\sqrt{N_\phi} \tag{B.2}$$

where $N_\phi = \tan^2(\frac{\pi}{4}+\frac{\phi}{2})$. From the geometrical conditions,

$$\mathrm{d}x = \frac{\mathrm{d}(D/2)}{\tan(\frac{\pi}{4}+\frac{\phi}{2})} \tag{B.3}$$

Substituting equation B.2 and B.3 into equation B.1, the following equation is obtained:

$$\frac{\mathrm{d}\sigma_x}{N_A\sigma_x + cN_B} = \frac{\mathrm{d}D}{D} \tag{B.4}$$

where $N_A = N_\phi^{\frac{1}{2}} \tan\phi + N_\phi - 1$ and $N_B = 2\tan\phi + 2N_\phi^{\frac{1}{2}} + N_\phi^{-\frac{1}{2}}$. The differential equation can be integrated in both sides and the following solution is obtained:

$$\sigma_x = \frac{(C_1 D)^{N_A} - cN_B}{N_A} \tag{B.5}$$

where C_1 is an integration constant.

Similar analysis is implemented for the soil zone $AEE'A'$. Figure B.0.2b shows a small element of the plastically deforming soil. The equilibrium of forces in the x direction gives that

$$D_2 \mathrm{d}\sigma_x = 2(\sigma_\alpha \tan\phi + c)\mathrm{d}x \tag{B.6}$$

which leads to the following solution that:

$$\sigma_x = \frac{C_2 \exp(\frac{2N_C}{D_2}x) - cN_D}{N_C} \tag{B.7}$$

where C_2 is another integration constant, $N_C = N_\phi \tan\phi$ and $N_D = 2N_\phi^{\frac{1}{2}} \tan\phi + 1$.

The lateral soil pressure on the plane AA' ($x = 0$), according to the numerical analysis in this thesis, varies with the pile spacing and is represented by:

$$\left|\sigma_x\right|_{AA'} = K_f \gamma z \tag{B.8}$$

where K_f is a coefficient depending on the pile spacing, z is an arbitrary depth from the ground surface and γ is the unit weight of soil.

Using equation B.8 as boundary condition, the constant C_2 in equation B.7 can be obtained:

$$C_2 = K_f \gamma z N_C + cN_D \tag{B.9}$$

Substituting equation B.9 into equation B.7, the soil stress on plane EE' ($x = \frac{D1-D2}{2} tan(\frac{\pi}{8} + \frac{\phi}{4})$) is obtained by the following equation:

$$\left|\sigma_x\right|_{EE'} = \left(K_f \gamma z + c\frac{N_D}{N_C}\right) \exp\left(N_C \frac{D_1 - D_2}{D_2} \tan(\frac{\pi}{8} + \frac{\phi}{4})\right) - c\frac{N_D}{N_C} \tag{B.10}$$

which can be considered as boundary condition for equation B.5 to obtain the constant C_1:

$$\frac{(C_1 D_2)_A^N}{N_A} = \left(K_f \gamma z + c\frac{N_D}{N_C}\right) \exp\left(N_C \frac{D_1 - D_2}{D_2} \tan(\frac{\pi}{8} + \frac{\phi}{4})\right) + c\left(\frac{N_B}{N_A} - \frac{N_D}{N_C}\right) \tag{B.11}$$

Using equation B.5 and B.11, the lateral soil pressure on the plane BB' is calculated by:

$$\begin{aligned}\left|\sigma_x\right|_{BB'} &= \left(\frac{D_1}{D_2}\right)^{N_A}\left(K_f\gamma z + c\frac{N_D}{N_C}\right)\exp\left(N_C\frac{D_1-D_2}{D_2}\tan(\frac{\pi}{8}+\frac{\phi}{4})\right)\\ &+\left(\frac{D_1}{D_2}\right)^{N_A} c\left(\frac{N_B}{N_A}-\frac{N_D}{N_C}\right)-c\frac{N_B}{N_A}\\ &= K_1 * \left|\sigma_x\right|_{AA'} + K_2 c\end{aligned} \tag{B.12}$$

where

$$\begin{aligned}K1 &= \left(\frac{D_1}{D_2}\right)^{N_A}\exp\left(N_C\frac{D_1-D_2}{D_2}\tan(\frac{\pi}{8}+\frac{\phi}{4})\right)\\ K2 &= \left(\frac{D_1}{D_2}\right)^{N_A}\frac{N_D}{N_C}\exp\left(N_C\frac{D_1-D_2}{D_2}\tan(\frac{\pi}{8}+\frac{\phi}{4})\right)+\left(\frac{D_1}{D_2}\right)^{N_A}\left(\frac{N_B}{N_A}-\frac{N_D}{N_C}\right)-\frac{N_B}{N_A}\end{aligned} \tag{B.13}$$

The lateral force acting on a pile per unit thickness of layer in the x direction is the difference between lateral forces acting on the plane BB' and AA', as:

$$p_u = p_{BB'} - p_{AA'} = D_1\left|\sigma_x\right|_{BB'} - D_2\left|\sigma_x\right|_{AA'} \tag{B.14}$$

When the lateral force on the pile p is known, the coefficient K_f can be back calculated:

$$K_f = \frac{p_u - K_2 D_1 c}{(K_1 D_1 - D_2)\gamma z} \tag{B.15}$$

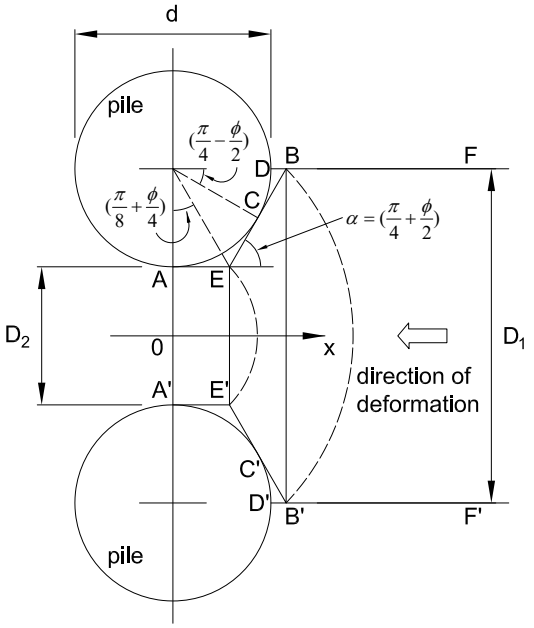

Fig. B.0.1 State of plastic deformation in the ground just around piles.

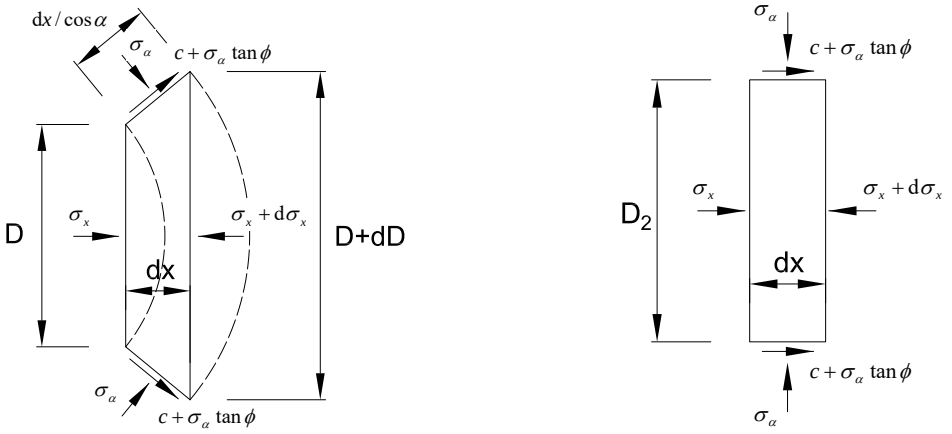

(a) Zone $EBB'E'$ **(b)** Zone $AEE'A'$

Fig. B.0.2 Small element of plastically deforming ground.